

**Contract No:**

This document was prepared in conjunction with work accomplished under Contract No. DE-AC09-08SR22470 with the U.S. Department of Energy (DOE) Office of Environmental Management (EM).

**Disclaimer:**

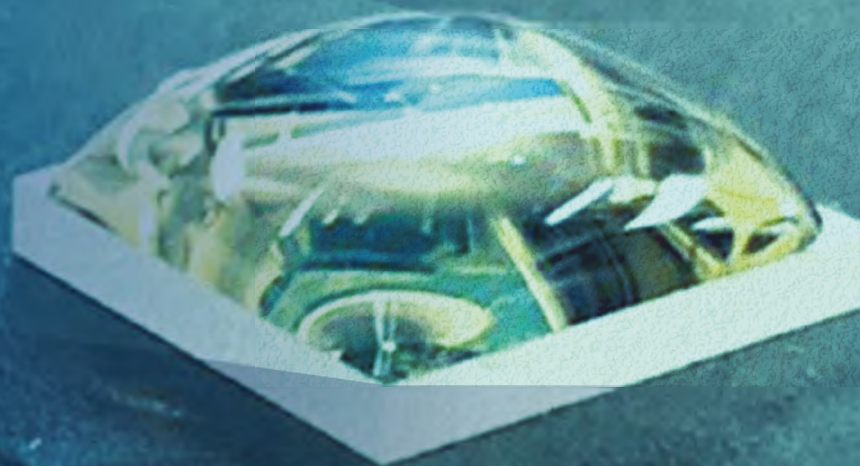
This work was prepared under an agreement with and funded by the U.S. Government. Neither the U. S. Government or its employees, nor any of its contractors, subcontractors or their employees, makes any express or implied:

- 1 ) warranty or assumes any legal liability for the accuracy, completeness, or for the use or results of such use of any information, product, or process disclosed; or
- 2 ) representation that such use or results of such use would not infringe privately owned rights; or
- 3) endorsement or recommendation of any specifically identified commercial product, process, or service.

Any views and opinions of authors expressed in this work do not necessarily state or reflect those of the United States Government, or its contractors, or subcontractors.

# *Savannah River National Laboratory*

## **FY20 LDRD** *Annual Report*



**Legacy Waste Cleanup**  
**Nuclear Deterrent**  
**Nuclear Materials Threat Reduction**  
**Secure Energy & Manufacturing**  
**Pioneering Science**



## **DISCLAIMER**

“This report was prepared by Savannah River Nuclear Solutions, LLC (SRNS) for the United States Department of Energy under Contract No. DE-AC09 - 08SR22470 and is an account of work performed under that contract. Neither the United States Government nor any agency thereof, nor any of their employees, nor any of their contractors, subcontractors or their employees assume any legal liability or responsibility for any third party’s use of the results of such use of any information, apparatus, product, or process disclosed, or represent that its use would not infringe privately owned rights. Reference herein to any specific commercial product, process or services by trademark, name, manufacturer or otherwise does not necessarily constitute or imply endorsement, recommendation, or favoring of same by SRNS or the United States Government or any Agency thereof.”

## MESSAGE FROM THE LABORATORY DIRECTOR

The Laboratory Directed Research and Development (LDRD) Program supports scientific research leading to successful innovations and discovery each year, and FY20 was no exception. Through dedication and determination, the Savannah River National Laboratory (SRNL) team furthered science and technology critical to the nation's energy security.

An example of research success includes a rapid response to the COVID-19 national crisis through the development of a face shield protection technology. I am proud of the way individuals across the laboratory rapidly pulled together to form a unified team and methodically tested an idea that led to follow-on research supported by the Office of Science.

Another great research success includes the High Resolution Actinide Speciation project. By building on SRNL's unique capabilities of handling and characterizing actinides, a device was developed in collaboration with Purdue University based on the properties of tensioned metastable fluids to differentiate between isotopes. This could be a game changer in actinide characterization. The National Nuclear Security Administration believes in the technology's potential and is supporting focused follow-on research.

SRNL LDRD program success has supported creative scientific minds, furthered scientific and technical understanding, and positioned the SRNL to respond to the challenges facing the Department of Energy and the National Nuclear Security Agency. I invite you to learn more about the exciting science supported by the LDRD program ongoing at SRNL in this annual report.



Dr. Vahid Majidi

A handwritten signature in black ink, appearing to read 'V. Majidi', written in a cursive style.

Laboratory Director  
Savannah River National Laboratory

## Overview

The Laboratory Directed Research and Development (LDRD) program funds scientific efforts to build upon the unique knowledge base of Savannah River National Laboratory (SRNL). The program yields foundational scientific research and development (R&D) essential to SRNL's core business areas, while aligning optimally and continuously with SRNL's Strategic Plan and providing long-term benefits to DOE and the National Nuclear Security Administration (NNSA), other customers, and stakeholders. While fiscal year (FY) 2020 presented unprecedented challenges due to the COVID-19 global pandemic, the SRNL research team continued to advance science and further technology through the support of the LDRD program.

The purpose of the LDRD program is three fold:



## FY20 LDRD Program Focus Areas:

The FY20 SRNL LDRD Program included focus areas aligned with SRNL's strategic goals in the areas of legacy waste cleanup, nuclear deterrent, nuclear material threat reduction, and secure energy and manufacturing.

### Legacy Waste Cleanup:

Unique concepts that lead to new approaches and options for critical EM risk reduction challenges and also reduce the life cycle in processing high activity liquid waste and nuclear materials, remediating contaminated soil, groundwater and facilities, as well as validating long-term remediation strategies.

### Nuclear Deterrent:

Unique concepts that ensure a sustainable tritium supply to meet current and future stockpile needs, including gas transfer systems, chemical processing and purification and incorporate of process intensification and advanced manufacturing concepts to the tritium supply chain.

### Nuclear Materials Threat Reduction:

Innovative process technologies to convert excess nuclear materials into useful product or waste forms. Enhancements to the Nation's capabilities to detect, characterize, access, and track nuclear materials and processes across the globe.

### Secure Energy & Manufacturing:

Advanced research in the development, demonstration, and deployment of secure energy and manufacturing technologies. Development of innovative solutions to increase electrical network security, reliability, and resiliency.

### Pioneering Science:

Science-driven research that fosters revolutionary discoveries, expands on our historically significant applied contributions and builds an enduring foundation for future solutions to enhance the long-term security of the Nation.

# LDRD BY THE *NUMBERS*

**54** TOTAL # OF PROJECTS

**\$7.66M** TOTAL PROGRAM COST

## PROJECT TYPES

DISCOVERY SCIENCE: 3  
FOCUSED SCIENCE: 27  
SEEDLINGS: 24

**44%** PROJECTS LED BY EARLY CAREER STAFF

PROJECTS INVOLVING EARLY CAREER STAFF

**70%**

*\*EARLY CAREER IS DEFINED AS WITHIN 10 YEARS OF TERMINAL DEGREE GRADUATION*

**12** PEER-REVIEWED MANUSCRIPTS PUBLISHED ON LDRD SUPPORTED RESEARCH

POSTDOCTORAL RESEARCHERS FUNDED THROUGH THE LDRD PROGRAM **11**

**22** PROJECTS HAD AT LEAST ONE POSTDOC INVOLVED IN THE PROJECT

**6** INVENTION DISCLOSURES

**5** PATENTS

**5** EXTERNAL ENTITIES ENGAGED  
NAVAL RESEARCH LABORATORY  
MAINLAND SOLUTIONS  
CENTER FOR INTEGRATED NANOMATERIALS  
DOUGLAS FLUID & INTEGRATION TECHNOLOGY

## 12 UNIVERSITIES ENGAGED

**PURDUE**  
UNIVERSITY



**AUGUSTA**  
UNIVERSITY

**CLEMSON**  
UNIVERSITY

**UNIVERSITY OF GEORGIA**

**Odum School of Ecology**  
UNIVERSITY OF GEORGIA

**GT**  
GEORGIA TECH

**VT** VIRGINIA TECH

**UNIVERSITY OF CAMBRIDGE**

**ALABAMA A&M**  
UNIVERSITY

California State University  
**Northridge**

**UNIVERSITY OF SOUTH CAROLINA**

## FY20 MOST VALUABLE PROJECT

Each year, the LDRD Program selects a project to recognize as the Most Valuable Project (MVP) Award. The award is granted to a project funded within the last 5 years for exceptional performance resulting in publication of peer-reviewed manuscripts, development of external collaborations, and establishment of R&D programs built from results obtained through a funded LDRD project.

The MVP Award for FY20 was granted to the project:

### Characterization of the Environmentally Induced Chemical Transformation of Uranium Tetrafluoride

Matthew Wellons led the project along side M. A. DeVore II, E. Villa-Aleman, R.M. Rogers, and J.T. Hewitt.

Through their research efforts, a fundamental understanding of UF<sub>4</sub> chemical reactions with water in ambient conditions was developed. The research included a combination of microanalytical and bulk material characterization methods to build a fundamental understanding of the complex microscale reaction and overall hydrolysis kinetics. The researchers developed and implemented advanced analytical strategies for automated particle analysis, in-situ Raman spectroscopy and <sup>19</sup>F NMR of UF<sub>4</sub> hydrates, and transmission electron microscopy coupled with electron energy loss spectroscopy.

The project successes included:

- Follow-on programs supported by the NNSA, U.S. Special Police, and Department of Defense
- 3 peer-reviewed publications
- 6 external presentations
- One post-doc who transitioned to full-service employment
- External collaborations:
  - University of South Carolina
  - Los Alamos National Laboratory
  - Naval Research Laboratory



# LEGACY WASTE CLEANUP

## PROJECTS

Metal-Organic Framework Glasses as Rad Contaminant Sequesters and Nuclear Waste Forms

Process Image Analysis Using Big Data, Machine Learning, and Computer Vision

Thermodynamics of Deuterium Oxide Separations in Aqueous Two-Phase Systems

Non-destructive Imaging of a Liquid Moving Through Porous Media Using a Computed Tomography Scanner

Development of Bio-Compatible Fluorescent Sensor

Quantitative Determination of Total Cesium in SRS Tank Waste by Inductively Coupled Plasma Emission Spectroscopy

Rapid, Inexpensive Analysis of Metal Contaminated Sediment Pore Water Using Combined Techniques

Investigation of Optical, Physical and Corrosion Properties of Gamma-Irradiated International Simple Glass

## Metal-Organic Framework Glasses as Rad Contaminant Sequesters and Nuclear Waste Forms

**Project Team:** Dien Li, Kathryn Taylor-Pashow, Daniel I. Kaplan, Jake Amoroso

**University of South Carolina Collaborator:** Natalia Shustova

**University of Cambridge, UK Collaborator:** Tom Bennett

**Soochow University, China Collaborator:** Shuao Wang

**Project Start Date:** October 1, 2017

**Project End Date:** September 30, 2020

*Remediation of Tc remains an unresolved problem at the Savannah River Site (SRS) and other Department of Energy (DOE) sites. The objective of this project was to develop novel metal organic framework (MOF) glasses for radioactive contaminant sequestration and stabilization. Cetyltrimethylammonium bromide (CTAB)-functionalized MIL-101-Cr was demonstrated to have high  $\text{ReO}_4^-$  removal capacity (139 mg/g sorbent) from artificial groundwater. Re chemical speciation and binding mechanism on MIL-101-CTAB were also revealed as  $\text{ReO}_4^-$  in the pore structure with slightly larger Re-O bond distances than those in  $\text{NaReO}_4$  and binding with the positively charged sites of CTAB. In addition, a new Ni-TIPA MOF was demonstrated to be very stable, selective and effective for  $\text{TcO}_4^-$  removal from the SRS tank waste stream (~90% removal). The Ni-TIPA MOF sample containing  $\text{ReO}_4^-$  was prepared and shipped for*

*pressure-induced vitrification. This research may provide a highly applicable platform for solving critical DOE and industrial problems related to nuclear environmental stewardship and nuclear power production.*

### FY2020 Objectives

- Complete additional experiments and data analysis for CTAB-functionalized, and F<sup>-</sup>, Cl<sup>-</sup>, I<sup>-</sup>, CF<sub>3</sub>SO<sub>3</sub><sup>-</sup>-exchanged MIL-101-Cr
- Complete and submit two manuscripts
- Write a user proposal to Advanced Photo Source (APS)
- Conduct experiments on vitrifying the crystalline Ni-TIPA containing  $\text{ReO}_4^-$

### Introduction

<sup>99</sup>Tc is a major long-lived fission product created during nuclear power generation. Over the years, Tc has been inadvertently introduced into the environment from leaks at waste storage facilities. <sup>99</sup>Tc currently is one of the key risk drivers at the Savannah River Site (SRS) and other DOE environmental management sites (most notably the Hanford Site, Paducah Gaseous Diffusion Plant, and Oak Ridge National Laboratory). The most common chemical form of Tc in liquid nuclear wastes and in the environment is anionic pertechnetate ( $\text{TcO}_4^-$ ).  $\text{TcO}_4^-$  displays limited adsorption onto common sediment minerals and is highly mobile making it difficult to capture or to be immobilized. <sup>1</sup> As the stockpile of <sup>99</sup>Tc-bearing nuclear waste continues to increase rapidly, novel sequestration technologies are needed to reduce its potential contamination of the environmental and living organisms.

With current technologies, quaternary amine-based resins have been used to remove aqueous Tc. <sup>2</sup> However, these resins are expensive and have only modest  $\text{TcO}_4^-$  loading capacities from the raffinate waste streams. Chemical reductants (e.g.,  $\text{Fe}_3\text{S}_4$ , soluble or structural Fe(II))<sup>3</sup> and some bacteria <sup>4</sup> can reduce Tc(VII) to the sparingly soluble Tc(IV). However, the resulting  $\text{Tc(IV)O}_2 \cdot 1.6\text{H}_2\text{O}$  has a solubility of  $1.5 \times 10^{-8}$  M in groundwater, <sup>5</sup> which greatly exceeds the EPA's maximum contaminant level of  $5 \times 10^{-10}$  M, and is readily re-oxidized and re-mobilized under most environmental conditions. <sup>6</sup> Tc reduction to form

sulfides (e.g.,  $Tc_2S_7$ )<sup>7</sup> or embedding into other sulfide phases<sup>8</sup> or iron oxide waste forms<sup>9</sup> have also been investigated. However, these methods are not practical for many applications. There are currently no demonstrated technologies that are highly efficient and cost-effective for separation of Tc-containing nuclear waste streams and remediation of aqueous Tc in the contaminated sites.

The overarching objective of this project was to develop novel metal organic framework (MOF) glasses as radioactive contaminant sequesters and nuclear waste forms. First, we need to develop novel MOF materials of high stability, high capacity and high selectivity for  $TcO_4^-/ReO_4^-$  from groundwater and high pH tank waste streams. Now we have developed two new MOF materials that met these performance criteria. Second, we want to develop high pressure induced technology for vitrification of these MOF materials containing  $ReO_4^-$ , which will potentially lead to the next generation of glass waste forms for nuclear waste stabilization.

## Approach

The chemical formula of MIL-101-Cr (MIL, Matériel Institut Lavoisier) is  $Cr_3NO_3(H_2O)_2O(BDC)_3 \cdot nH_2O$  ( $n \sim 25$ ; BDC = 1,4-benzenedicarboxylate;  $NO_3^-$  can be substituted by  $F^-$ ,  $Cl^-$ ,  $I^-$ , or  $CF_3SO_3^-$ ). The crystal structure of MIL-101-Cr- $NO_3^-$  is shown in Fig. 1.<sup>10</sup> Modified MIL-101-Cr samples with the different exchangeable anions and cetyltrimethylammonium bromide (CTAB)-functionalized MIL-101-Cr- $NO_3^-$  samples were prepared. Powder X-ray diffraction (XRD), BET surface area measurement, thermogravimetric analysis (TGA), energy dispersive X-ray spectroscopy (EDS), and Fourier transform infrared (FTIR) spectroscopy were used for MOF characterization before and after  $ReO_4^-$  adsorption in which  $ReO_4^-$  was used as a non-radioactive surrogate for  $TcO_4^-$ . Synchrotron radiation X-ray absorption spectroscopy was applied to studying Re chemical speciation and molecular binding mechanisms by modified MOFs.

Batch  $ReO_4^-$  adsorption experiments were conducted from AGW using the modified MIL-101-Cr MOFs. The mass of Re sorbed ( $q_e$ , mg/g) was calculated using equation 1:

$$q_e = \frac{(C_0 - C_e) \times V}{M} \quad (1)$$

where  $C_0$  (mg/L) is the initial concentration in the control samples,  $C_e$  (mg/L) is the final concentration remaining in the solution,  $V$  is the volume of the solution (mL), and  $M$  is the mass of the sorbent (g). Adsorption isotherms of  $ReO_4^-$  onto MIL-101-Cr- $NO_3^-$  with and without CTAB functionalization were obtained at an equilibration pH  $\sim 4.0$  and  $\sim 9.0$ . The Langmuir isotherm model (equation 2) was used to describe the data for  $ReO_4^-$  adsorption on MIL-101-Cr- $NO_3^-$ -CTAB:

$$\frac{C_e}{q_e} = \frac{1}{q_{max}} C_e + \frac{1}{K_L \times q_{max}} \quad (2)$$

where  $q_e$  is the mass of  $ReO_4^-$  sorbed onto the sorbent at equilibrium,  $q_{max}$  is the saturation sorption capacity,  $C_e$  is the Re concentration in solution at equilibrium, and  $K_L$  is the Langmuir constant. In addition, factors such as contact time (e.g., 0.5–24 h), solution pH (e.g., 0–10), effect of competing anions (e.g.,

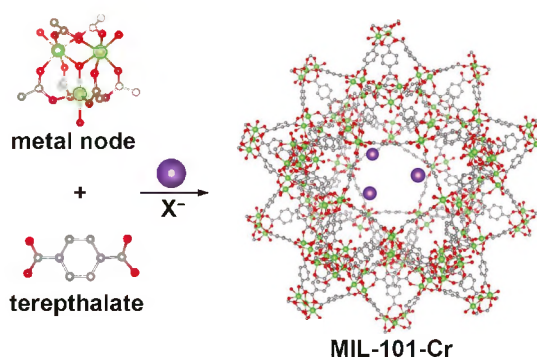


**Figure 1:** The structure of MIL-101-Cr. Atom colors: Cr = green, O = red, C = gray, blue = exchangeable anions (i.e.,  $NO_3^-$ ,  $F^-$ ,  $Cl^-$ ,  $I^-$ , and  $CF_3SO_3^-$ ).

$\text{NO}_3^-$ ,  $\text{CO}_3^{2-}$ ,  $\text{SO}_4^{2-}$ , and  $\text{Cl}^-$ ), and desorption and resorption behavior were evaluated for  $\text{ReO}_4^-$  removal from groundwater.

We also investigated a new Ni-TIPA MOF for Tc removal from the SRS tank waste stream. The Ni-TIPA sample containing  $\text{ReO}_4^-$  was shipped for high pressure induced vitrification experiments at the Advanced Photo Source (APS). The ultimate goal was to develop the next generation of MOF glasses as nuclear waste forms.

## Results/Discussion

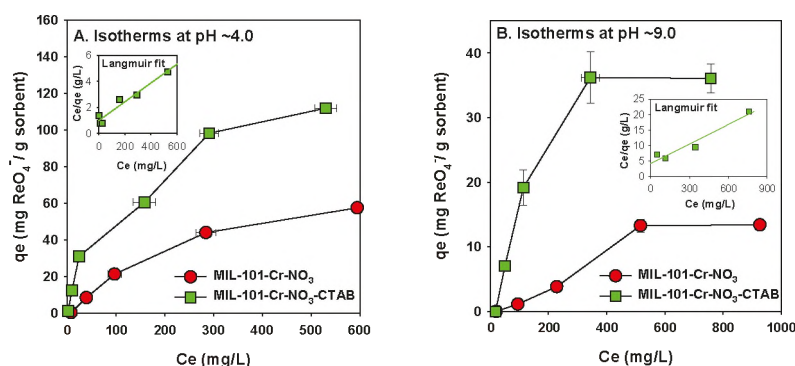
### 1. $\text{ReO}_4^-$ removal of MIL-101-Cr MOFs with different anions

For MIL-101-Cr with different anions, with MIL-101-Cr- $\text{NO}_3$  as a baseline, MIL-101-Cr-F was slightly less effective for  $\text{ReO}_4^-$  removal; while  $\text{Cl}^-$ ,  $\text{I}^-$ , and  $\text{CF}_3\text{SO}_3^-$ -exchanged MIL-101-Cr materials had improved capacity for  $\text{ReO}_4^-$  sequestration. The ranking of anion-exchanged MIL-101-Cr for  $\text{ReO}_4^-$  removal was  $\text{F}^- < \text{NO}_3^- < \text{Cl}^- \approx \text{I}^- \approx \text{CF}_3\text{SO}_3^-$ , which was essentially in agreement with the so-called Hofmeister order for predicting anion partitioning in liquid/liquid systems.<sup>11</sup> These results can be explained in terms of ionic radius and standard Gibbs energies of hydration ( $\Delta G_h^\circ$ )<sup>11-12</sup>.  $\text{I}^-$  and  $\text{CF}_3\text{SO}_3^-$  have a similar ionic radius and  $\Delta G_h^\circ$  to those of  $\text{ReO}_4^-/\text{TcO}_4^-$ , which is favorable for  $\text{ReO}_4^-$  exchange and improves the  $\text{ReO}_4^-$  removal performance. On the other hand, the ionic radius and  $\Delta G_h^\circ$  of  $\text{F}^-$  are much smaller than those of  $\text{ReO}_4^-/\text{TcO}_4^-$ , which is not favorable for  $\text{ReO}_4^-$  exchange into MIL-101-Cr-F.

### 2. $\text{ReO}_4^-$ removal and characterization of CTAB-functionalized MIL-101-Cr- $\text{NO}_3$

**$\text{ReO}_4^-$  Removal Isotherms.** The obtained saturation capacity of MIL-101-Cr- $\text{NO}_3$ -CTAB for  $\text{ReO}_4^-$  removal from AGW was 139 mg  $\text{ReO}_4^-/\text{g}$  sorbent ( $R^2 = 0.948$ ) at the equilibrium pH value of  $\sim 4.0$  and 39 mg  $\text{ReO}_4^-/\text{g}$  sorbent ( $R^2 = 0.942$ ) at the equilibrium pH value of  $\sim 9.0$  (Fig. 2). In addition, we attempted to fit Re isotherm data for MIL-101-Cr- $\text{NO}_3$  (without CTAB functionalization) at pH values of  $\sim 4.0$  and  $\sim 9.0$  to both the Langmuir and Freundlich models, but neither model produces satisfactory results with  $R^2$  values of  $< 0.90$ . However, the capacity of MIL-101-Cr- $\text{NO}_3$  for  $\text{ReO}_4^-$  removal from AGW was estimated to be  $\sim 50$  mg  $\text{ReO}_4^-/\text{g}$  sorbent at pH 4.0 and  $\sim 14$  mg  $\text{ReO}_4^-/\text{g}$  sorbent at pH 9.0 (Fig. 2). Therefore, CTAB functionalization on MIL-101-Cr- $\text{NO}_3$  significantly improved its capacity for  $\text{ReO}_4^-$  removal at pH 4.0 and 9.0 AGW.

**Figure 2:** Adsorption isotherms of  $\text{ReO}_4^-$  on MIL-101-Cr- $\text{NO}_3$  (red) and MIL-101-Cr- $\text{NO}_3$ -CTAB (green) in artificial groundwater at pH  $\sim 4.0$  (A) and  $\sim 9.0$  (B) for 6 d. For MIL-101-Cr- $\text{NO}_3$ -CTAB, Langmuir fits are shown in the insets, but the isotherm curves for MIL-101-Cr- $\text{NO}_3$  were not well fit by the Langmuir model.



**Effect of Contact Time.** The effect of contact time of  $\text{ReO}_4^-$  with these two MOF samples was further investigated to evaluate the anion exchange rate and equilibrium time. As shown in Fig. 3A, under specified experimental conditions,  $\sim 90\%$  of  $\text{ReO}_4^-$  in AGW was removed by MIL-101-Cr- $\text{NO}_3$  within 30 min, while nearly 100% of  $\text{ReO}_4^-$  in AGW was removed by CTAB functionalized MIL-101-Cr- $\text{NO}_3$  within 10 min. These results indicate that CTAB functionalized MIL-101-Cr- $\text{NO}_3$  improves sorption kinetics and provides higher capacity for  $\text{ReO}_4^-$  removal compared to MIL-101-Cr- $\text{NO}_3$ .

**Effect of Solution pH.** As shown in Fig. 3B, the  $\text{ReO}_4^-$  removal percentage diminished to nearly zero for MIL-101-Cr- $\text{NO}_3$  and to  $\sim 15\%$  for MIL-101-Cr- $\text{NO}_3$ -CTAB at pH  $\sim 10.0$ . These results may indicate that the MIL-101-Cr materials have limited applications to  $\text{ReO}_4^-/\text{TcO}_4^-$  sequestration from alkaline media such as legacy liquid nuclear waste. For both MIL-101-Cr- $\text{NO}_3$  samples with and without CTAB functionalization, the  $\text{ReO}_4^-$  removal capacity also diminished with a decreasing pH and its removal rate was reduced to  $\sim 13\%$  in a 3 M nitric acid solution. These results indicate that the MIL-101-Cr- $\text{NO}_3$  samples become less effective for  $\text{ReO}_4^-/\text{TcO}_4^-$  removal in strongly acidic aqueous media. However, it could prove effective for  $\text{ReO}_4^-/\text{TcO}_4^-$  removal from weakly acidic to neutral aqueous media (pH 3-8) like contaminated groundwater.

**Effect of Competing Anions.** For MIL-101-Cr- $\text{NO}_3$ , the presence of 5 mM  $\text{NO}_3^-$ ,  $\text{CO}_3^{2-}$ , or  $\text{Cl}^-$  reduced  $\text{ReO}_4^-$  removal capacity by 32%, 34%, and 23%, respectively, while the presence of 5 mM  $\text{SO}_4^{2-}$  reduced  $\text{ReO}_4^-$  removal capacity by 89% (Fig. 3C). These results indicated that MIL-101-Cr- $\text{NO}_3$  had moderate affinity and selectivity for  $\text{ReO}_4^-$  over  $\text{NO}_3^-$ ,  $\text{CO}_3^{2-}$ , or  $\text{Cl}^-$ , but  $\text{SO}_4^{2-}$  significantly reduced the affinity and selectivity of MIL-101-Cr- $\text{NO}_3$  for  $\text{ReO}_4^-$  removal. On the other hand, for MIL-101-Cr- $\text{NO}_3$ -CTAB, the presence of 5 mM  $\text{NO}_3^-$ ,  $\text{CO}_3^{2-}$ , and  $\text{Cl}^-$  reduced  $\text{ReO}_4^-$  removal capacity by 7%, 5%, and 2%, respectively, while the presence of 5 mM  $\text{SO}_4^{2-}$  reduced  $\text{ReO}_4^-$  removal capacity by only 18%. These results indicate that with CTAB functionalization, MIL-101-Cr- $\text{NO}_3$  substantially improves sorption affinity and selectivity for  $\text{ReO}_4^-$  over all tested competing anions.

**$\text{ReO}_4^-$  Desorption and Resorption Studies.**  $\text{ReO}_4^-$  desorption and resorption behavior of MIL-101-Cr- $\text{NO}_3$  with and without CTAB functionalization was investigated by using 1 M KI solution as an extracting agent. Figure 5D shows  $\text{ReO}_4^-$  removal percentages of MIL-101-Cr- $\text{NO}_3$  and MIL-101-Cr- $\text{NO}_3$ -CTAB during sorption/desorption cycles. For both samples, initially 92–97% of  $\text{ReO}_4^-$  was removed by the sorbent materials, then 60–62% of the anion was eluted during the first desorption step; and then  $\sim 98\%$  of  $\text{ReO}_4^-$  was sorbed by these two MOFs during the subsequent two resorption steps. These results indicate that  $\text{ReO}_4^-$  was not completely eluted by 1 M KI solution, and after the KI desorption step, the materials remained effective for  $\text{ReO}_4^-$  removal until reaching its saturation capacity.

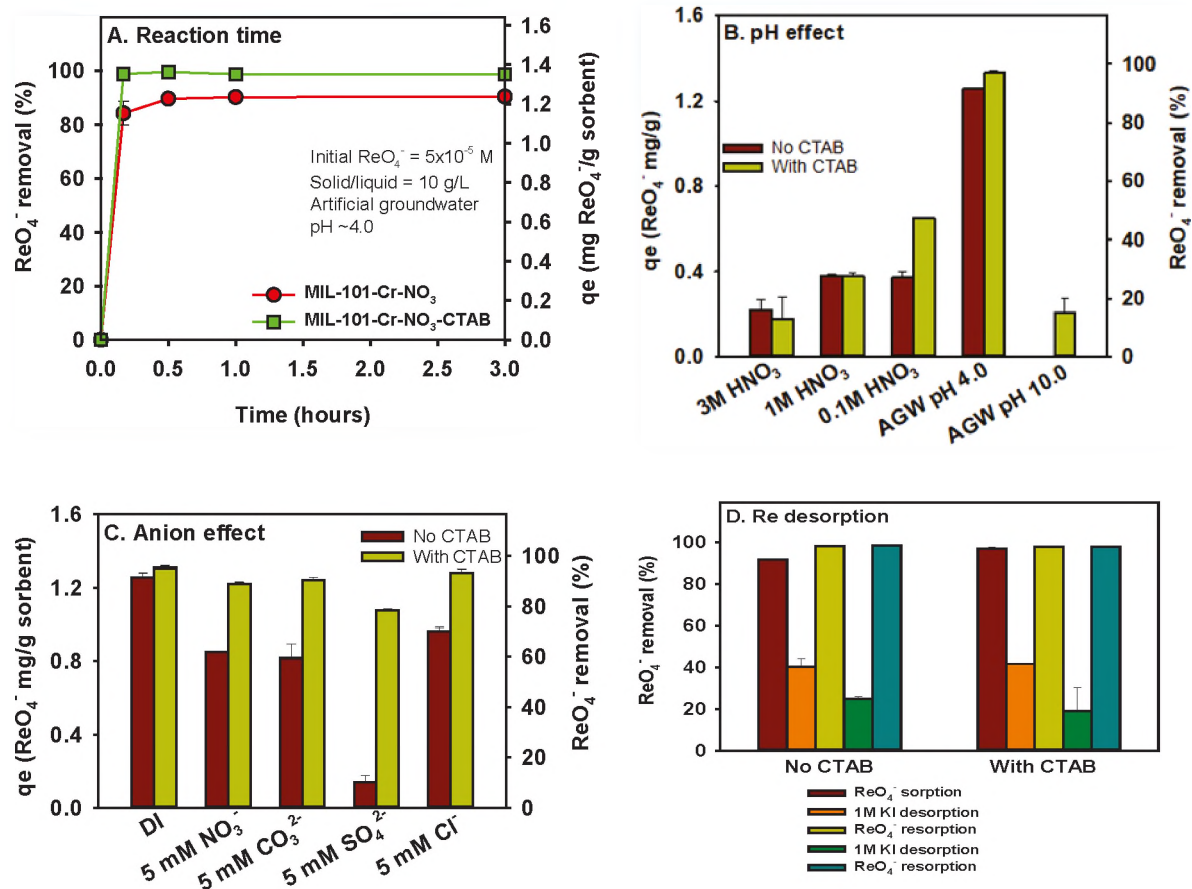


**Figure 3:**  $\text{ReO}_4^-$  adsorption on MIL-101-Cr- $\text{NO}_3$ -CTAB in AGW versus (A) reaction time, (B) pH value, (C) co-existing anions, and (D)  $\text{ReO}_4^-$  desorption/resorption cycles. The experimental conditions were:  $[\text{ReO}_4^-] = 5 \times 10^{-5} \text{ M}$ , solid/liquid = 10g/L, reaction time = 1 d, pH = ~4.0.

**Re  $L_3$ -edge XANES and EXAFS.** The Re  $L_3$ -edge X-ray absorption near edge structure (XANES) spectra of MIL-101-Cr- $\text{NO}_3$ -CTAB after exposure to  $5 \times 10^{-4} \text{ M}$   $\text{ReO}_4^-$  in pH 4.1 and 8.5 AGW are shown in Fig. 4A, in comparison with the spectrum of sodium perrhenate ( $\text{NaReO}_4$ ). The  $L_3$ -edge absorption peaks of this MOF sample exposed to  $\text{ReO}_4^-$  were at 10535.1 eV, with another peak at about 10546.4 eV, which clearly indicated that the sequestered Re species by MIL-101-Cr- $\text{NO}_3$ -CTAB in AGW at an equilibrium pH of 4.1-8.5 was  $\text{ReO}_4^-$ .

Re  $L_3$ -edge extended X-ray absorption fine structure (EXAFS) spectra in Fourier transform plots in R magnitude of these two samples are shown in Fig. 4B, together with the corresponding spectrum of  $\text{NaReO}_4$ . The experimental data are shown as dotted lines, and EXAFS fits are shown as colored lines. The Re  $L_3$ -edge EXAFS data of the MIL-101-Cr- $\text{NO}_3$ -CTAB samples exposed to  $\text{ReO}_4^-$  were fitted with tetrahedral Re-O paths at a Re-O distance of  $1.730 \pm 0.004 \text{ \AA}$  with a coordination number of  $3.8 \pm 0.3$ . Thus, the Re  $L_3$ -edge EXAFS spectra of MIL-101-Cr- $\text{NO}_3$ -CTAB exposed to  $\text{ReO}_4^-$  in both pH 4.1 and 8.5 AGW confirmed that the Re species associated with the sorbents was  $\text{ReO}_4^-$ .

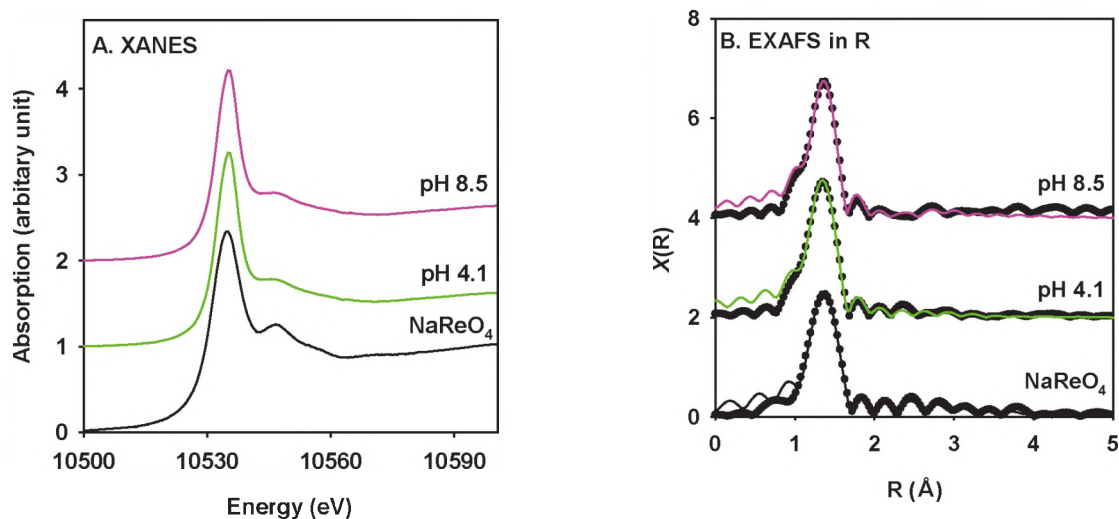


**Figure 4:** Re L<sub>3</sub>-edge X-ray absorption spectra of MIL-101-Cr-NO<sub>3</sub>-CTAB after exposure to  $5 \times 10^{-4}$  M ReO<sub>4</sub><sup>-</sup> in AGW at pH 4.1 (green) and 8.5 (pink), in comparison with the spectra of model compound NaReO<sub>4</sub> (black).

### 3. Ni-TIPA MOF for TcO<sub>4</sub><sup>-</sup> removal from the SRS tank waste

A Ni-TIPA MOF was acquired from collaborators at Soochow University. The crystal structure of Ni-TIPA is shown in Fig. 5A and 5B. It has a large pore size of 10.43×16.11 Å. Ni-TIPA was demonstrated to have high stability in aqueous media across a broad pH range, up to a pH value of 14, as well as high capacity and selectivity toward ReO<sub>4</sub><sup>-</sup> removal from aqueous media.

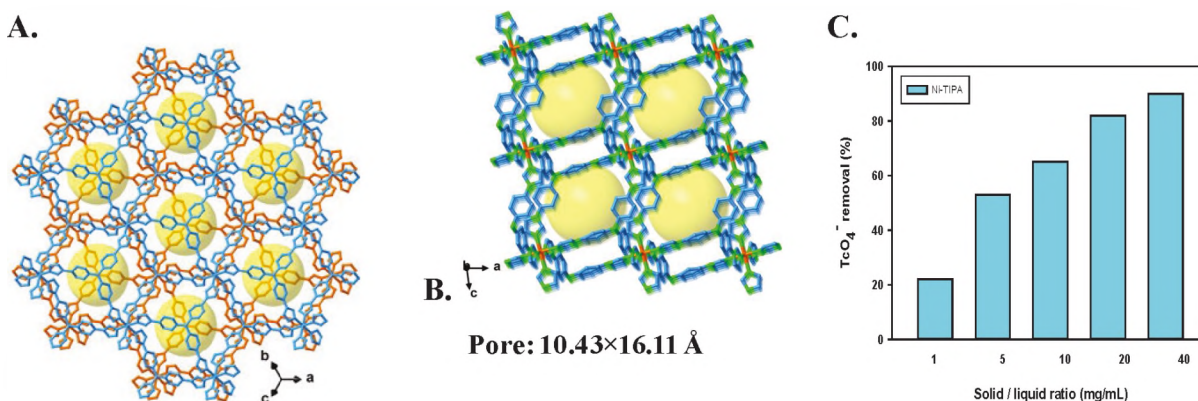


**Figure 5:** Crystal structure (A and B) of Ni-TIPA MOF and its performance for TcO<sub>4</sub><sup>-</sup> removal from the SRS tank waste stream (C).

A series of batch contact experiments to test this Ni-TIPA MOF were performed utilizing a sample of actual SRS tank waste.<sup>13</sup> The batch contact test results are shown Fig. 5C. The percent removal of <sup>99</sup>Tc increased as the phase ratio increased. At the highest phase ratio tested, 90% of the <sup>99</sup>Tc was removed from the SRS tank waste solution in 3 hours, in good agreement with experimental results performed using the simulated SRS tank waste. Pressure-induced vitrification technology was attempted to be developed for this Ni-TIPA MOF with loaded ReO<sub>4</sub><sup>-</sup>. The MOF glasses could be used as potential nuclear waste forms for Tc stabilization. However, these experiments were started but not completed yet due to Covid-19 lockdown.

## FY2020 Accomplishments

- Completed additional batch experiments on CTAB-functionalized MIL-101-Cr MOFs for  $\text{ReO}_4^-$  removal from AGW, including adsorption capacity, kinetics, effects of competing anions
- Completed additional data analysis on Re chemical speciation and molecular interaction with MIL-101-Cr through synchrotron X-ray absorption spectroscopy
- Completed and submitted two manuscripts to Journal of Environmental Radioactivity and Nature Communication. These manuscripts have been accepted for publication
- Prepared and shipped a sample for high pressure induced vitrification of Ni-TIPA MOF containing  $\text{ReO}_4^-$ . Completed and submitted a user proposal to APS for investigation of MOF vitrification behavior with pressure and Re structure in the MOF glass

## Future Directions

- Continue developing new MOFs for higher  $\text{TcO}_4^-$  removal capacity and improved stability and selectivity, especially under alkaline conditions
- Develop methods for vitrifying the MOFs as nuclear waste forms so that the entrapped contaminants are stabilized without leaching out
- Prepare proposals to DOE EM Soil & Groundwater Remediation Program, International Program, and DOE Nuclear Energy program

## FY 2020 Peer-reviewed/Non Peer-reviewed Publications

- Dien Li, Natalia B. Shustova, Corey R. Martin, Kathryn Taylor-Pashow, John C. Seaman, Daniel I. Kaplan, Jake W. Amoroso, Roman Chernikov, Anion-exchanged and quaternary ammonium functionalized MIL-101-Cr metal-organic framework (MOF) for  $\text{ReO}_4^-/\text{TcO}_4^-$  sequestration from groundwater, *Journal of Environmental Radioactivity*, **2020**, 222, 106372.
- Nannan Shen, Zaixing Yang, Shengtang Liu, Xing Dai, Chengliang Xiao, Kathryn Taylor-Pashow, **Dien Li**, Chuang Yang, Jie Li, Yugang Zhang, Mingxing Zhang, Ruhong Zhou, Zhifang Chai, Shuao Wang,  $^{99}\text{TcO}_4^-$  Removal from Legacy Defense Nuclear Waste by an Alkaline-Stable 2D Cationic Metal-Organic Framework, *Nature Communication*, **2020**, 11: 5571.

## References

1. Icenhower, J. P.; Qafoku, N. P.; Zachara, J. M.; Martin, W. J., The biogeochemistry of technetium: A review of the behavior of an artificial element in the natural environment. *American Journal of Science* **2010**, 310 (8), 721-752.
2. Liang, L. Y.; Gu, B. H.; Yin, X. P., Removal of technetium-99 from contaminated groundwater with sorbents and reductive materials. *Separations Technology* **1996**, 6 (2), 111-122.
3. Peretyazhko, T.; Zachara, J. M.; Heald, S. M.; Jeon, B. H.; Kukkadapu, R. K.; Liu, C.; Moore, D.; Resch, C. T., Heterogeneous reduction of Tc(VII) by Fe(II) at the solid-water interface. *Geochimica Et Cosmochimica Acta* **2008**, 72 (6), 1521-1539.
4. Plymale, A. E.; Fredrickson, J. K.; Zachara, J. M.; Dohnalkova, A. C.; Heald, S. M.; Moore, D. A.; Kennedy, D. W.; Marshall, M. J.; Wang, C. M.; Resch, C. T.; Nachimuthu, P., Competitive Reduction of Per technetate ( $\text{TcO}_4^-$ -Tc-99) by Dissimilatory Metal Reducing Bacteria and Biogenic Fe(II). *Environmental Science & Technology* **2011**, 45 (3), 951-957.

5. Li, D.; Kaplan, D. I., *Solubility of Technetium Dioxides ( $TcO_2-c$ ,  $TcO_2 \cdot 1.6H_2O$  and  $TcO_2 \cdot 2H_2O$ ) in Reducing Cementitious Material Leachates: A Thermodynamic Calculation*. Savannah River National Laboratory: Aiken, SC 20908, 2013.
6. Fredrickson, J. K.; Zachara, J. M.; Plymale, A. E.; Heald, S. M.; McKinley, J. P.; Kennedy, D. W.; Liu, C. X.; Nachimuthu, P., Oxidative dissolution potential of biogenic and abiogenic  $TcO_2$  in subsurface sediments. *Geochimica Et Cosmochimica Acta* **2009**, *73* (8), 2299-2313.
7. Liu, Y.; Terry, J.; Jurisson, S., Pertechetate immobilization in aqueous media with hydrogen sulfide under anaerobic and aerobic environments. *Radiochimica Acta* **2007**, *95* (12), 717-725.
8. Fan, D. M.; Anitori, R. P.; Tebo, B. M.; Tratnyek, P. G.; Pacheco, J. S. L.; Kukkadapu, R. K.; Engelhard, M. H.; Bowden, M. E.; Kovarik, L.; Arey, B. W., Reductive Sequestration of Pertechetate ( $(TcO_4^-)-Tc-99$ ) by Nano Zerovalent Iron (nZVI) Transformed by Abiotic Sulfide. *Environmental Science & Technology* **2013**, *47* (10), 5302-5310.
9. Um, W.; Chang, H. S.; Icenhower, J. P.; Lukens, W. W.; Serne, R. J.; Qafoku, N. P.; Westsik, J. H.; Buck, E. C.; Smith, S. C., Immobilization of 99-Technetium (VII) by Fe(II)-Goethite and Limited Reoxidation. *Environmental Science & Technology* **2011**, *45* (11), 4904-4913.
10. Zhao, T.; Jeremias, F.; Boldog, I.; Nguyen, B.; Henninger, S. K.; Janiak, C., High-yield, fluoride-free and large-scale synthesis of MIL-101(Cr). *Dalton Transactions* **2015**, *44* (38), 16791-16801.
11. Custelcean, R.; Moyer, B. A., Anion separation with metal-organic frameworks. *European Journal of Inorganic Chemistry* **2007**, (10), 1321-1340.
12. Darab, J. G.; Smith, P. A., Chemistry of technetium and rhenium species during low-level radioactive waste vitrification. *Chemistry of Materials* **1996**, *8* (5), 1004-1021.
13. Crawford, C. L., *Results for the First Quarter Calendar Year 2019 Tank 50 Salt Solution Sample, SRNL-STI-2019-00184, Rev. 0*. Savannah River National Laboratory: Aiken, SC 29808., 2019.

## Acronyms

AGW	Artificial groundwater
BET	Brunauer-Emmett-Teller
CTAB	Cetyltrimethylammonium bromide
DOE	Department of Energy
EDS	Energy dispersive X-ray spectroscopy
EXAFS	Extended X-ray absorption fine structure
FTIR	Fourier transform infrared spectroscopy
MIL	Materials Institute Lavoisier
MOF	Metal organic framework
SRS	Savannah River Site
TGA	Thermogravimetric analysis
TIPA	Tris(4-(1H-imidazol-1-yl)phenyl)amine
XANES	X-ray absorption near-edge structure
XRD	X-ray diffraction

## Student Researchers

Corey Martin, University of South Carolina

## Process Image Analysis Using Big Data, Machine Learning, and Computer Vision

**Project Team:** Bruce Hardy, Anna d'Entremont, Michael Martinez-Rodriguez, Brenda Garcia-Diaz, Lindsay Roy

**University of South Carolina**

**Collaborators:** Jason Bakos, Taylor Clingenpeel, Phil Moore, Ben Torkian, R. Doran

**Georgia Institute of Technology**

**Collaborators:** AJ Medford, Suvadip Das

**Project Start Date:** October 1, 2018

**Project End Date:** August 21, 2020

*The development of algorithms for machine learning and data analysis for the 3013 Materials Identification and Surveillance (MIS) corrosion surveillance program is a collaborative effort by SRNL, University of South Carolina and Georgia Institute of Technology. For corrosion detection, localized corrosion monitoring (LCM) image data is extracted from large binary files, with software written to convert the data to physical attributes (i.e. height, color and grayscale values; all as functions of a location in a plane projection). The user interface for the software permits selective downloading of binary data and interrogation of attributes. User input thresholds are used to flag attributes of interest. Machine learning*

*algorithms, developed for this application, are used to determine whether the features are the result of corrosion. To address the fundamental mechanisms of corrosion, machine learning algorithms are being developed to derive interatomic potential force-fields from ab-initio Density functional theory (DFT) calculations. The goal is to apply molecular modeling on a large enough scale to guide the design of resistant materials.*

### FY2020 Objectives

- Develop machine learning methods, based on computer vision, to analyze imaging data for corrosion
- Develop machine learning methods for molecular modeling of corrosion processes
- Identify 3013 data sets, and numerical methods, suitable for near-term development
- Determine preliminary set of attributes for training supervised machine learning (ML) algorithms
- Assemble training sets, train and test ML algorithms
- Classify features by size, quantity, density, and location
- Utilize computer vision to reduce amount of data needing manual analysis
- Identify additional data sets within SRNL that can be analyzed using the methodologies developed as part of this project
- Initiate development of ML methodology for obtaining adaptive force-fields from ab-initio molecular models (MM) for corrosion (added to originally approved scope)

### Introduction

Halides contained in Pu-bearing material have been found and produce corrosion in the Inner Can Closure Weld Region (ICWR) for the 3013-canister system used throughout the DOE complex. Inspections using a Laser Confocal Microscope (LCM) produce immense amounts of image data: approximately 6000 images per can, having 786,432 pixels per image, with 8 layers of data for each pixel. There is currently a 5-year backlog of images, with approximately 5 canisters/year, that must be evaluated. Simplistic computer-aided image analysis can flag parameters, such as pit depth and cracking to guide manual examinations for corrosion. However, while this approach greatly improves the efficiency of the examination process compared to unaided manual screening, it is still excessively time consuming. A more sophisticated approach is to assess the data using machine learning algorithms to identify corrosion without manual intervention. As a complement to corrosion detection, molecular level analyses can yield a fundamental

understanding of corrosion occurring in the ICCWR and guide the design of corrosion resistant materials, welding processes, and coatings. These two efforts comprise the research in this LDRD.

This two-year LDRD project had two concurrent objectives: The first was the development of machine learning algorithms to identify the presence of corrosion from a very large set of images generated by LCM scanning of 3013 canisters used to store Pu oxides. This portion of the LDRD constituted image analysis of a metal surface for the presence of corrosion. The image processing algorithms developed for this project are suitable basis for analysis of other types of corrosion data, which can be produced in vast quantities using modern analysis technology.

The second component of the LDRD consisted of the development of machine learning methodology used to develop molecular mechanics force-fields from *ab-initio* Density Functional Theory (DFT) calculations for corrosive attack by chlorides on 304L or 316L stainless steel. The long-term goal of this latter component was to understand corrosion on a fundamental level.

## Approach

### First Component – Image Analysis

Corrosion is strongly, but not exclusively, associated with surface pitting and cracking, coloration, along with shapes and patterns of surface features. Conversely, not all pits and surface lesions are the result of corrosion: some are artifacts of fabrication, impact, scoring or other non-corrosion events. Corrosion is identified via the combined properties of pit depth, area, edge contour, color and clustering. Software was developed to extract these features from large binary files generated by the LCM. The individual images, which collectively span the ICCWR were stitched together and corrected to eliminate the effect of curvature on measurement of the local height. Various methods were applied to the data to best relate it to presence of corrosion. Mathematical operations invoked for computer vision and image interpretation included, Deep Neural Networks (DNNs), gradient methods, statistical characterization, correlations and filters.<sup>12</sup>

The processed data would be input to ML algorithms; labeled data for training, and afterwards data for evaluation by the trained ML algorithm. The process is shown schematically in Figure 1.

### Second Component – ML based FF Derivation from DFT Calculations

The objective of the second part of the LDRD project is to advance the fundamental understanding of corrosion by developing novel methods to simulate the complex chemistry and physics through coupling quantum mechanical and empirical force field methods. In corrosion science, sophisticated multiscale models beginning at the *ab-initio* level provide mechanistic insight into metal-environment interactions resulting in general corrosion, intergranular corrosion, and pitting corrosion.<sup>3</sup> Specifically, this research focuses on designing machine-learning algorithms to develop and train adaptive force fields for the study and prediction of corrosion behavior, specifically the metal-environment interface.<sup>4</sup> Accurately calculating the parameters for a robust force field, however, is a much more complicated than a simple regression fit, requiring more sophisticated data analytics.<sup>5-7</sup> Further, the functional form of standard force fields is

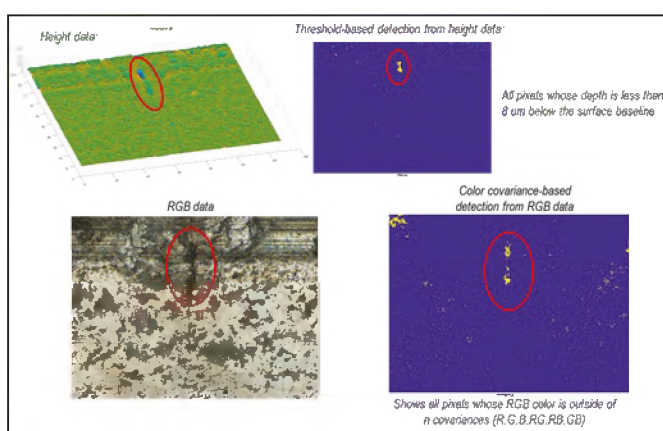


**Figure 1:** Crack and corrosion data from LCM images. Data channels include RGB, grayscale and height.

often insufficient to capture the complex physics of a reactive interface, especially in the case of the complex electronic structure of magnetic metal oxides. While atomistic modeling techniques are well suited to study the chemical reactions occurring at the interface between a material and its environment, modeling corrosion is computationally slow because the models must be constructed to resolve both relevant reaction mechanisms and mass transport processes. By developing machine learning methods to obtain quantitative structure-activity relationships considering both molecular and bulk boundary conditions, researchers will be able to significantly advance knowledge by exploring more combinatorial spaces and nonlinear processes which are difficult using traditional approaches.

## Results/Discussion

LCM image data taken for the MIS program was reviewed to obtain samples containing cracks, pits and other features characteristic of corrosion. The low incidence of corrosion and cracking in the actual ICCWR samples made it necessary to incorporate data augmentation schemes for proper training of the ML algorithms developed for this application. Images containing cracks were augmented by generating vertical and horizontal translations of the original labeled image. Capability for labeled image rotation was also developed. To provide an efficient means for handling large amounts of binary image data a GUI was developed to serve as an interface with the data files, manipulate and group images, label features for training the ML algorithm, group features with user defined thresholds, correct for sample tilt and curvature, stitch images, train ML algorithms, and apply the algorithms for crack and corrosion identification. Further, methods were developed to read binary WAMS data, which has recently been adopted for 3013 image interrogation. Studies conducted during FY 20 emphasized that larger views, represented by image tiles containing a larger number of pixels, improve the accuracy of crack detection by the ML algorithms.

After preprocessing, images obtained from LCM and WAMS data are partitioned into tiles (rectangular blocks of pixels). Image data used for training and testing ML algorithms is labeled. Cracks, pits and color patterns are all associated in various forms with corrosion. Pits can readily be detected using height data thresholds. Cracks, particularly “hairline” cracks do not always have a definitive height signature. Rather, crack identification is a combination of grayscale image intensity (pixel value) and height data. Initially, it was hoped that standard edge detection methods could be used with pixel values to extract crack edges. Methods considered included: erosion and dilation, blurring, Fourier and Gaussian filters, and gradient methods. Unfortunately, other surface features combined to create background noise that was similar in frequency to that associated with crack edges. To overcome this problem, DNN methods were developed as an attempt to identify cracks. Early in the development of this approach the training of the DNN algorithms suffered due to the small amount of crack data available. Training data was expanded by using augmented image data. Increasing the amount of labeled training data,

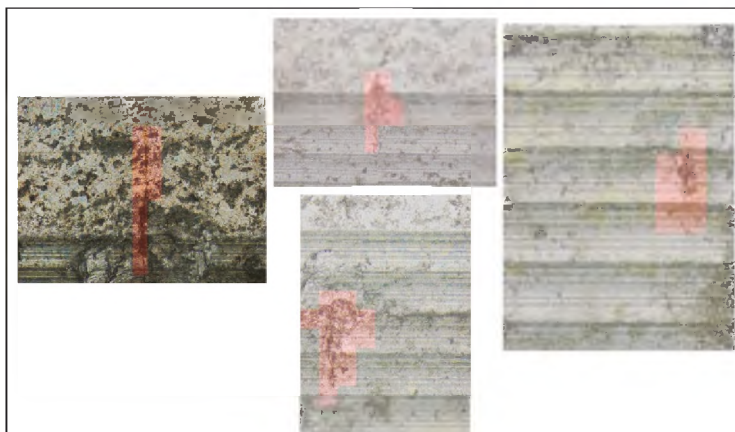


**Figure 2:** Examples of labeled data consisting of 112x112 pixel tiles (blocks). The training process used bootstrapped data samples that were augmented using horizontal and vertical translation. Highlighted regions are tiles that contain cracks.

adjusting the DNN algorithms, and increasing the image tile size from 64x64 to 112x112 pixels improved the precision and recall for crack identification. Examples of labeled training data for cracks, taken from LCM images are shown in Figure 2. It was found that the greatest accuracy was obtained by using a consensus drawn from an ensemble of randomly generated Convolutional Neural Network (CNN) algorithms, having the following characteristics:

- Two-channel input – grayscale contrast-adjusted peak intensity and smoothed height
- CNN depth of 1 to 5 layers, each layer consisting of a convolution layer using a RELU activation function and a maximum value pooling layer
  - Convolution layers have kernel sizes ranging from 1x1 to 3x3, with 1 to 128 feature maps
  - Pooling kernel size ranges from 1x1 to 3x3, with strides ranging from 1x1 to 3x3
- The final layer of the CNN consists of a fully connected layer of 1 to 128 neurons

The consensus is a vote on whether or not an image contains a crack. Results from this classification method are shown in Figure 3, which compares consensus accuracy with that of a single model and shows that the ensemble reached an accuracy greater than that of any individual algorithm within it. It was found that that accuracy was improved when training sets contain an approximately an equal number of tiles with and without cracks.

The second half of this project focused on establishing a pipeline for generating adaptive force fields that can be dynamically updated to match the results of quantum-mechanical calculations as closely as possible for corrosion on iron surfaces in water. There were two research routes established:

- Generating data with ReaxFF force field for iron/water
- Establishing a workflow for force field construction of iron oxide systems based on a set of diverse atomic environments and force data

The use of ReaxFF for generating initial sampling configurations provides an opportunity to sample a wide range of chemically relevant space by running molecular dynamics simulations at elevated temperatures or with enhanced sampling techniques such as metadynamics. In this work, a nearest-neighbor-based sampling technique is applied to identify a “maximum diversity” subset of simulations (Figure 4). The approach draws a uniform distribution from the high-dimensional fingerprint space, and the resulting subset can be used to improve the generality of neural-network models by ensuring that “rare” configurations from the tails of the distribution are included in training at all steps. Preliminary results

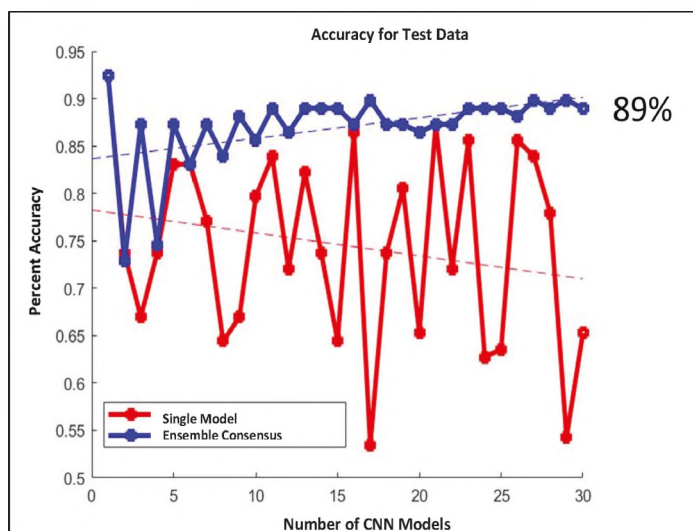


**Figure 3:** Comparison of the accuracy of crack identification from an ensemble consensus of CNN algorithms with the accuracy of a single model.

indicate that the number of atoms that must be simulated can be decreased by 2-3 orders of magnitude using sub-sampling.

The results of the initial ReaxFF Fe-O structures were then further analyzed to enable a wide range of training systems, including those that are explicitly similar to systems of interest. Since atomic forces are purely dependent upon the local environment, the construction of adaptive force fields is possible for any system where reliable quantum mechanical calculations can be performed. The first step requires that the reference data set for crystalline

materials be representative of a variety of chemical environments, or defects (e.g. defect-free bulk, surfaces, point defects; see Figure 5) in both equilibrium and non-equilibrium states. Calculation of the force component on each atom at equilibrium was then determined using DFT.

In a suitable representation for an atom and its environment, the force component must conform to any arbitrary direction and be invariant to basic atomic transformation operations (i.e., translation, rotation, permutation). One potential representation, or fingerprint, is:

$$V_i^u(\eta) = \sum_{i \neq j} \frac{r_{ij}^u}{r_{ij}} \cdot e^{-\left(\frac{r_{ij}}{\eta}\right)^2} \cdot f_d(r_{ij})$$

where  $r_{ij}$  is the distance between atoms  $i$  and  $j$ ,  $r_{ij}^u$  is a scalar projection of the distance along direction  $u$ ,  $\eta$  is the gaussian function width, and  $f_d$  is a damping function for atoms within a cutoff distance. This fingerprint was used to identify the atomic forces for >4600 unique environments. The results of ReaxFF and DFT data can then be combined using techniques from transfer learning to adaptively generate force fields that approach DFT accuracy while minimizing the required number of DFT simulations. Finally, the approaches will be combined with global optimization schemes to help automate the process of identifying the most accurate neural network architectures.

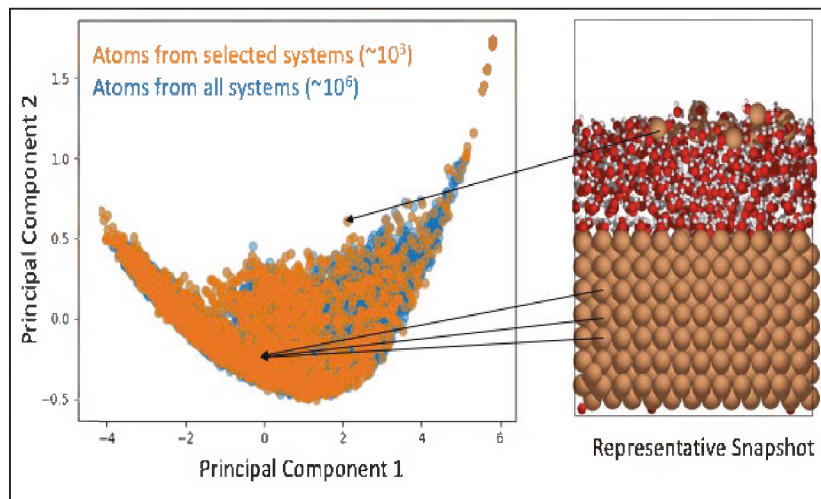


**Figure 4:** Illustration of sub-sampling algorithm applied to a collection of ReaxFF data for the iron/water interface. Individual atomic environments are displayed in PCA space (left) and representative atoms are qualitatively identified in a single snapshot of a molecular dynamics simulation (right).

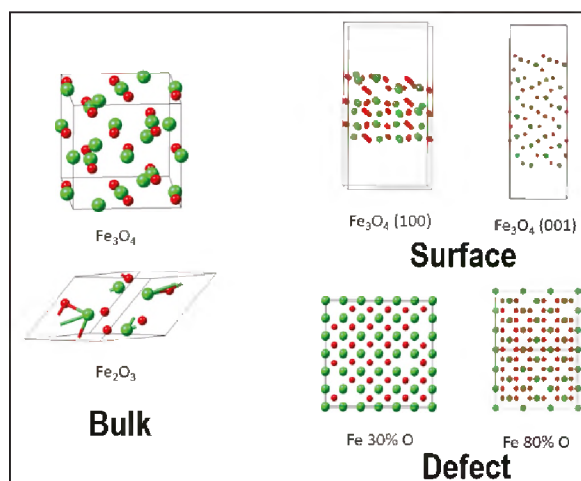


**Figure 5:** Reference configurations used to sample the Fe-O atomic environment for training and testing of force fields.

## FY2020 Accomplishments

- The functions developed for image analysis are now available through a user-friendly GUI that was developed specifically for this application. This includes
  - Data input
  - Data labeling, flagging of features of interest, and other diagnostics. Includes zoom capability
  - 3D surface imaging (including color and height data)
  - Convolutional Neural Network (CNN) Machine Learning (ML)
    - Training methods can be implemented through the GUI
  - ML algorithms are not yet in final form, but GUI access is modular so that updated algorithms can readily be imported, replacing the current ones
- ML algorithms are not yet in final form, but GUI access is modular so that updated algorithms can readily be imported, replacing the current ones
  - Tested different forms of ML algorithms
    - Algorithms tested included well regarded CNN's: such as ResNet 50, AlexNet, and custom CNN's which gave the best performance so far
  - Determined that overfitting (excessive response when applied to test data) and recall (a measure of the rate of false negative predictions) need to be improved in CNN algorithm development
  - Found that deeper neural networks don't necessarily result in better performance
  - Performed hyperparameter optimization, including genetic algorithm methods
  - Due to number of hyperparameters internal gradients (a custom method) will be used for optimization
  - The fine scale detail associated with cracks (in terms of grayscale and color intensity, along with height variation), complicates the process of distinguishing them from scratches, tooling marks, and sequences of pits protrusions on the surface
- Developed Convolutional Autoencoder (CAE) to obtain transfer learning for CNN's used for image analysis
  - The CAE supports transfer learning for accelerating the training of the CNN's, for the case of a relatively small amount of training data
- Developed software to enable rapid labeling of corrosion training data (Figures 1 and 2)
  - Labeled data is necessary for training the CNN's. A means for rapid labeling is necessary due to the volume of training data required
  - Completed software for mouse click labeling of corrosion training data for supervised learning (Figure 5)

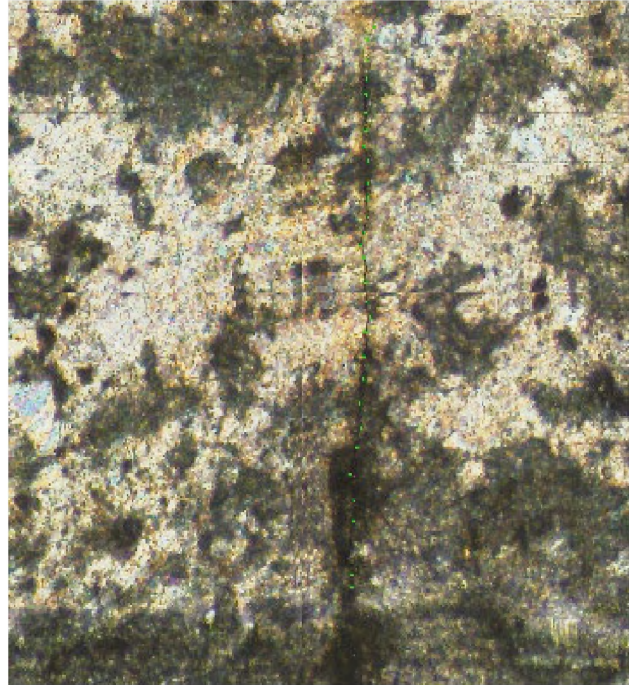
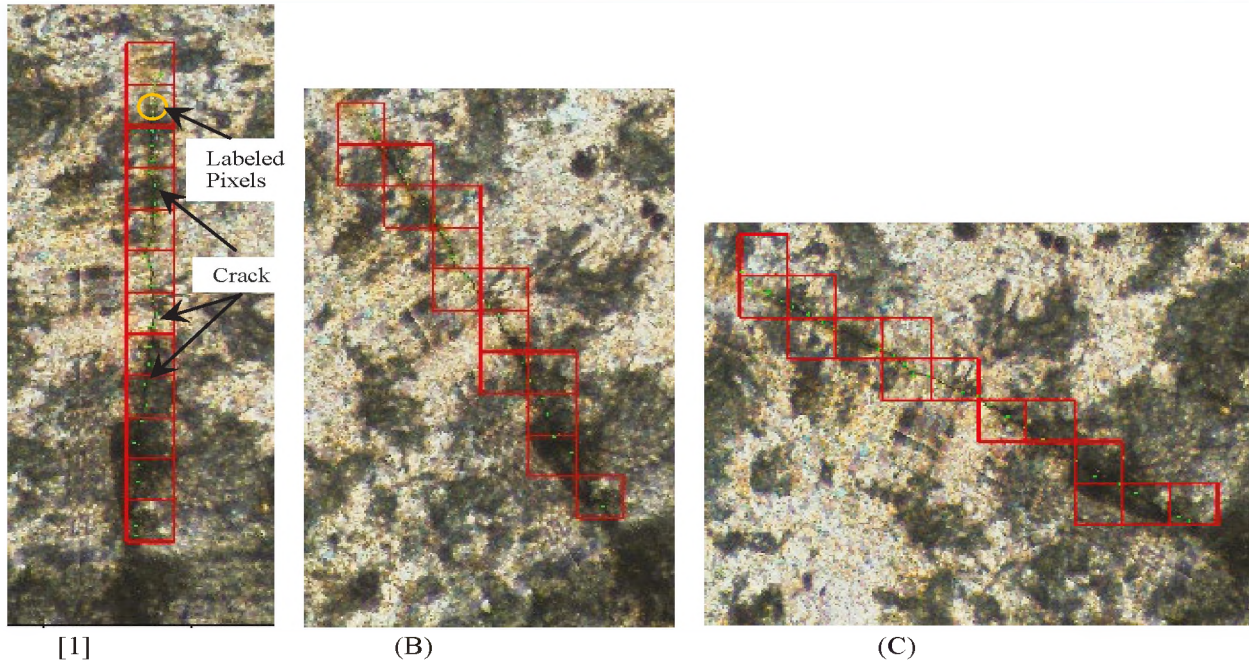
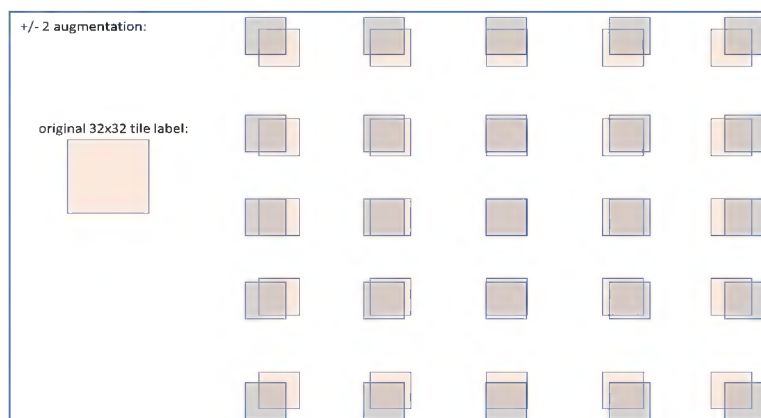


Figure 6: Pixels selected by mouse click are highlighted by green dots. The pixels are used to label the crack in rotational transformations that augment available data.



**Figure 7:** Data augmentation by rotation of crack image. The images are cropped show the highlighted region at a larger scale. Green dots (barely visible) along crack are pixels manually selected by the analyst by mouse click. The baseline orientation is shown in (A). When the image is divided into tiles, those containing a crack pixel are highlighted with a red boundary and labeled as a crack containing tile. Tiles that do not contain a crack pixel are defined and labeled as not containing a crack, but not highlighted. In (B) the image and crack pixels are rotated 30 degrees in the counterclockwise direction and the image is divided into tiles. Again, those tiles containing a crack pixel are highlighted with a red boundary and labeled as a crack containing tile. Tiles that do not contain crack pixels are defined and labeled as such, but unlabeled. Similarly, (C) shows a rotation 60 degrees in the counterclockwise direction.

- Labeled pixels are retained during geometric transformation for data augmentation (Figure 6)
- Developed baseline software for data augmentation via simulated geometric variations (Figures 7-8)
- Developed software that enables reading of WAMS binary data files
  - Will provide software to the LANL statistics group for their use
  - Will compare surface contour data from WAMS with that from the LCM files



**Figure 8:** Data augmentation by translation of image.

- Tests include proportionality between data sets for areas and heights of pits and protrusions
- Collaborating with the Los Alamos National Laboratory (LANL) statistics directorate
  - USC/SRNL will provide LANL with a method for extracting binary data from WAMS images (a newly applied technology for producing images used to screen for surface defects)

- Generated baseline Fe-O atomic force data for the FF training set
  - Calculated Fe/H<sub>2</sub>O interfaces using ReaxFF to illustrate the effectiveness of a weighted nearest-neighbor subsampling algorithm
  - Created reference data set of iron oxide environments from quantum mechanical calculations for >4600 chemical environments
  - Fingerprinted the atomic environment to enable mapping of atomic force components

## Future Directions

- L-basin corrosion analysis
- Extension of image analysis to inclusions in articles produced by additive manufacturing
- Application of AI methods to data analysis, particularly for corrosion and material degradation. This would also include analysis of analytical data (XPS, XRD, SEM, etc.)
- Apply ML to material synthesis based on empirical data with imposed physical constraints
- Applications to advanced process control, invoking reachability theory and fault tolerance. This aspect of AI, which takes advantage of the volume of data yielded by advanced sensor capability, would be particularly suitable for isotope separation, pit productions and waste processing
- Development of surrogate molecular models having reduced complexity but retaining a high degree of accuracy. This is related to material design at a fundamental level and is a compliment to data analysis that is used to identify material degradation
  - Submit proposals for more complete development of ML applications for FF derivation from DFT calculations, including experimental validation
  - Test FF algorithm with validation set
  - Incorporate iron/iron oxide defects with different water phases
  - Replace water with halides for corrosion and reactivity

## References

- 1 Ian Goodfellow, Yoshua Bengio, and Aaron Courville. *Deep Learning*. MIT Press, Cambridge MA (2016)
- 2 Aurélien Géron. *Hands-On Machine Learning with Scikit-Learn &Tensorflow*. O'Reilly, Sebastapol, CA (10/12/2018).
- 3 Gunasegaram, D. R.; *et al.*, *Int. Mater. Rev.* **2014**, *59*, 84.
- 4 Ghosh, S.; Suryanarayana, P. *Comput. Phys. Commun.* **2017**, *216*, 109.
- 5 Roy, L. E.; Jakubikova, E.; Guthrie, M. G.; Batista, E. R. *J. Phys. Chem. A* **2009**, *113*, 6745.
- 6 Joyce, J. J.; *et al.*, *Mater. Res. Soc. Symp. Proc.* **2010**, *1264*, Z09-04.
- 7 Li, W.; Ando, Y. *Physical Chemistry Chemical Physics* **2018**, *20*, 30006.

## Acronyms

AI	Artificial Intelligence
AIMD	Ab initio molecular dynamics
CAE	Convolutional autoencoder
CNN	Convolutional Neural Network
CS	Computer Science
DNN	Deep Neural Network
DOE	Department of Energy

DFT	Density Functional Theory
EAM	Embedded Atom Model – an interatomic potential that represents the energy between atoms
FF	Molecular mechanics Force-Field
GT	Georgia Institute of Technology, Atlanta, GA
GUI	Graphical User Interface
ICCWR	Inner Can Closure Weld Region
LCM	Laser Confocal Microscope
MD	Molecular Dynamics
MIS	Material Identification and Surveillance program
ML	Machine Learning
MM	Molecular Models
NN	Neural Network
TIP3P	Transferrable Intermolecular Potential with 3 Points – a 3 site rigid water model
USC	University of South Carolina, Columbia, SC
WAMS	Wide Angle Microscope System

## Post-Doctoral Researchers

One Post-doctoral researcher performed work at GT

## Student Researchers

- Two Undergraduate students performed work at USC
- One graduate student performed work at GT
- One MSIPP student performed work at SRNL

## Thermodynamics of Deuterium Oxide Separations in Aqueous Two-Phase Systems

**Project Team:** W.H. Woodham

**Project Start Date:** January 1, 2020

**Project End Date:** September 30, 2020

*The thermodynamic behavior of aqueous-organic-toluene ternary systems where aqueous components are water ( $H_2O$ ), deuterium oxide ( $D_2O$ ), and organic components including acetonitrile (MeCN), tetrahydrofuran (THF), and 1,4-dioxane (DIOX) have been recorded. Preliminary data has been taken for each ternary system to establish the concentration along the*

*spinodal line where Gibbs energy is minimized. In pursuit of this goal, simple laboratory techniques using common equipment was used to benchmark thermodynamic measurements against values reported in the literature. The impact of deuterium on aqueous two-phase separations was determined for each combination of solvents.*

### FY2020 Objectives

- Develop SRNL Hazard Assessment to allow work with organic solvents in non-radiological facilities
- Develop cost-effective analytical techniques to measure concentrations of multiphase mixtures in thermodynamic equilibrium
- Develop simple experimental protocols to facilitate thermodynamic measurements with commonly available laboratory tools
- Benchmark experimental protocols and analytical techniques against literature data to verify accuracy
- Determine the phase equilibria of  $H_2O$ -organic-toluene ternary systems
- Determine the phase equilibria of  $D_2O$ -organic-toluene ternary systems
- Quantify the impact of deuteration on phase separation in aqueous two-phase systems

### Introduction

One of the most important non-radiological compounds used in the nuclear industry and the nuclear research field is deuterium oxide ( $D_2O$ ), also known as “Heavy Water”.  $D_2O$  is produced around the world using a variety of inefficient separation techniques that employ dangerous chemicals, high energy expenditures, and large waste volumes. Among these production techniques, the most favored leverage slight differences in the chemical characteristics of O-H and O-D bonds to affect a marginal separation via thermodynamic equilibria. The challenges of hazardous chemicals, high cost of production, and inefficient separation make the large-scale production of  $D_2O$  a daunting task. Despite the availability of stockpiles of  $D_2O$ , the absence of an efficient domestic source of heavy water has often been critiqued by subject matter experts in the nuclear and national security arenas.<sup>1</sup>

The practice of using Organic Aqueous Tunable Solvents (OATS) as a vehicle for tunable separations is well documented and has been established as a robust solvent extraction process. The principle behind OATS is relatively simple: a water-miscible organic solvent (e.g. acetonitrile) is combined with water to form a single liquid phase. Upon necessity, an antisolvent (a compound exclusively soluble in one of the two solvents) is added such that a phase split is induced. In the case of OATS, this antisolvent is usually  $CO_2$ , which can be easily removed by depressurization to restore single-phase behavior. Once a second phase is formed.<sup>2</sup>

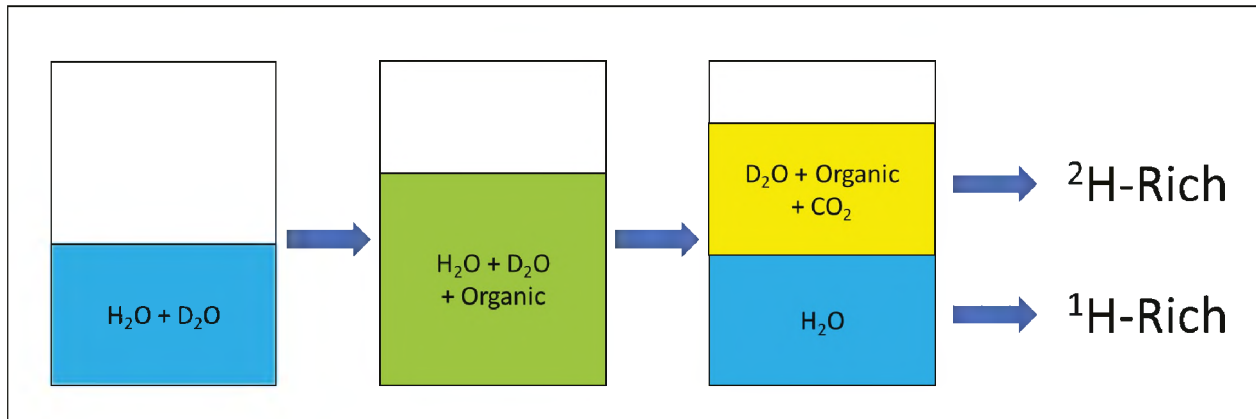


**Figure 1:** Simplified flowchart of OATS thermodynamics as applied to deuterium separation.

The objective of this program was to perform preliminary scoping studies to ascertain the applicability of OATS processing to the separation of  $D_2O$  from  $H_2O$ . In particular, the goal of this research was to measure the ternary phase behavior of aqueous-organic-toluene systems and determine the impact (if any) of deuteration on phase separation and critical solution compositions.

## Approach

The approach taken throughout this research program may be summarized in three objectives. The first objective was to develop testing protocols and analyses that would allow for low-cost, non-complex measurement of organic concentrations necessary to understand the ternary thermodynamic equilibria of OATS solvents and  $D_2O$ . The second objective was to perform measurements of concentrations along the spinodal line for aqueous-organic-toluene ternary systems in the presence and absence of deuterium (toluene was employed as an antisolvent for scoping purposes; use of pressurized  $CO_2$  would necessitate higher design and planning costs). The third objective was to quantify the differences in thermodynamic equilibria between systems containing  $H_2O$  and  $D_2O$  in order to ascertain the feasibility of OATS to serve as a separation tool for deuterium oxide processing.



**Figure 2:** Thermo Genesys 10S UV/Vis Spectrophotometer used in organic concentration measurement. Photo from Thermo Fischer.

## Results and Discussion

Using common laboratory glassware (i.e., 2- and 4-dram vials, beakers, disposable pipettes, etc.), a simple procedure for determining metastable ternary concentrations (defined as the region between the spinodal and binodal curves of a ternary mixture) was developed that allowed for a significant reduction in the time and financial cost of thermodynamic measurements. While the accuracy of this method is diminished compared to traditional tie-line measurements of biphasic systems, we were able to show that the data achieved using this technique is comparable to data reported in literature using conventional measurement techniques.<sup>3</sup>

In these ternary combinations, the number of components involved in any experiment is three (aqueous, organic, and antisolvent). However, the number of available phases is assumed to be two (two distinct liquid phases; the vaporization of organics and water was assumed to be negligible for the purposes of these scoping experiments). For this reason, temperature and pressure alone are not able to fully specify the properties of a mixture (the Gibbs phase rule indicates that the system is underspecified). Therefore, a measurement of at least one component's concentration is necessary to fully characterize each biphasic mixture. For this purpose, a benchtop UV/Vis spectrophotometer was used to measure the concentration of the antisolvent in each of the biphasic mixtures. This measurement necessitates only a small sample of the organic rich phase followed by large dilution into the organic solvent of choice before measurement. Throughout this work, the spectra of toluene between 200 and 300 nm was considered for quantification, with useful peaks occurring at 262 and 269 nm.

Once all the necessary data had been collected, comparisons were drawn between ternary systems containing H<sub>2</sub>O and ternary systems containing D<sub>2</sub>O. Generally speaking, differences in spinodal line concentrations are observable when H<sub>2</sub>O and D<sub>2</sub>O are interchanged. However, the differences at the conditions achievable at this scale are notably small, suggesting that further investigation should be made at different conditions (e.g., temperature).

## FY2020 Accomplishments

The following accomplishments were achieved as a result of this work:

- A Hazard Assessment was successfully developed that will allow future work with OATS materials and deuterium oxide with minimal modification
- A simple dilution protocol was developed for rapid determination of toluene in organic solvents using a benchtop UV/Vis spectrophotometer
- A quick, low-cost experiment was designed to allow rapid determination of ternary phase equilibria by observation of the cloud points at the metastable regions. This experimental technique was successfully benchmarked against conventional methods reported in literature and found to be capable of similar accuracy
- Phase equilibria of aqueous (H<sub>2</sub>O and D<sub>2</sub>O), organic (MeCN, THF, and DIOX), and toluene ternary phase behavior was measured
- Separability of deuterium via OATS was demonstrated on a small, unoptimized scale using toluene as a surrogate antisolvent

## Future Directions

Results from this research suggest that differences in H<sub>2</sub>O and D<sub>2</sub>O separation at room temperature, while quantifiable, are suboptimal compared to those achieved at lower temperatures (based on literature

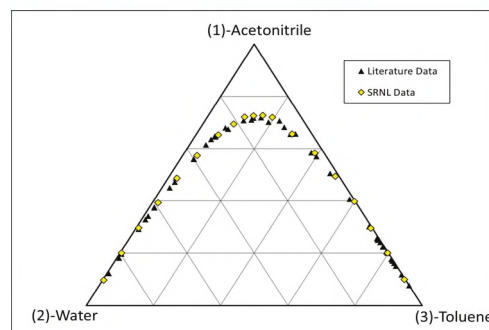


**Figure 3:** Ternary phase diagram of MeCN-H<sub>2</sub>O-Toluene equilibria.

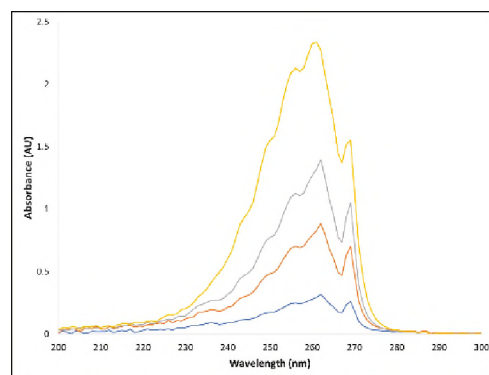


**Figure 4:** UV/Vis spectra of toluene in Tetrahydrofuran

studies with D<sub>2</sub>O and acetonitrile). While the direction of this optimality may not be universal (optimum temperatures in D<sub>2</sub>O-THF-CO<sub>2</sub> separations may occur at higher temperatures), it is clear that temperature variation studies are needed to fully refine and optimize OATS as a D<sub>2</sub>O separation process. Furthermore, it is desirable to transition from using the surrogate toluene to using an effective OATS antisolvent (such as CO<sub>2</sub> or propane). While this transition would include the development of testing equipment capable of handling high pressures, the use of a gaseous species greatly simplifies the measurement of phase equilibria concentrations (the degrees of freedom according to the Gibbs phase rule are decreased when a substantial vapor phase is introduced).

The following steps are recommended as a trajectory for future work:

- A pressure vessel capable of temperature control and optical measurements (e.g., compatible with a cathetometer) should be constructed to allow for non-destructive measurements of ternary phase equilibria across a wide range of temperatures and pressures
- Equipment for generating high pressures of CO<sub>2</sub> and propane should be procured to facilitate the use of antisolvent at pressures higher than those achievable from standard cylinders
- Non-destructive phase equilibria measurements should be performed for ternary systems of aqueous (H<sub>2</sub>O and D<sub>2</sub>O), organic (MeCN, THF, DIOX, and Isopropanol), and antisolvent (CO<sub>2</sub>) systems
- Optimized separation conditions should be used to design a cascade experiment to demonstrate the efficacy of OATS to separate D<sub>2</sub>O from H<sub>2</sub>O

## References

1. "Isotopes for the Nation's Future: A Long Range Plan"; NSAC Isotopes Subcommittee: 2009.
2. Pollet, P.; Hart, R. J.; Eckert, C. A.; Liotta, C. L., Organic Aqueous Tunable Solvents (OATS): A Vehicle for Coupling Reactions and Separations. *Acc. Chem. Res.* 2010, *43* (9), 1237-1245.
3. Cave, S. D.; Mazzarotta, B., Liquid-Liquid Equilibria for Ternary Systems Formed by Acetonitrile, Water, and Aromatic Hydrocarbons. *Journal of Chemical Engineering Data* 1991, *36*, 298-303.

## Acronyms

DIOX	1,4-Dioxane
MeCN	Acetonitrile
OATS	Organic Aqueous Tunable Solvents
THF	Tetrahydrofuran
UV	Ultraviolet

## Non-destructive Imaging of a Liquid Moving Through Porous Media Using a Computed Tomography Scanner

**Project Team:** Daniel I. Kaplan and Kenneth Gibbs

**Clemson University Collaborators:** Abdullah Al Mamun and Brian A. Powell

**Project Start Date:** February 1, 2019

**Project End Date:** April 30, 2020

*The most common approach used by modelers to describe movement of liquids through a porous solid, such as cement, sediment, or glass, is to assume a uniform flow rate, such as a Darcy Flux or a diffusion constant. However, this convenient simplification is problematic because in many cases it ignores the presence of fractures and macropores, which commonly dominate water flow and contaminant transport. For this reason, it is common that such modeling results do not reflect the multi-modal flow detected in laboratory and*

*field studies. The objective of this seedling study was to develop a new capability for SRNL to track liquid moving through macropores in soil using an X-ray Computed Topography (CT) Scanner. 4-dimensional anamated renditions were created that permitted quantifying traditional matrix flow and macropore flow. These animations were modelled using a public domain software, HYDRUS 1-D, describing one dimension, dual-porosity and dual-permeability processes. This new capability provides a proof of concept for reducing model uncertainty applicable to waste disposal risk calculations, environmental remediation, and waste form development when describing the movement of liquids as they pass through glass, cement, fractured rock, or soil.*

### FY2020 Objectives

- Develop a new capability for SRNL to study fluid mechanics by passing a non-radiological tracer through porous media within a CT scanner
- Conduct an experiment within the CT scanner of water moving through a dry core of SRS vadose zone sediment containing a wide range of pores, including micropores ( $\mu\text{m}$  diameter) and macropores (mm diameter)
- Use existing software to create animations from the >500 X-ray scans collected during the experiment.
- Model the results using a model that accounts for varying size pores

### Introduction

The most common approach used by modelers to describe movement of liquids through a porous solid, such as cement, sediment, or glass, is to assume a uniform flow rate, such as a Darcy Flux or a diffusion constant.<sup>1</sup> However, this convenient simplification is problematic because it ignores the presence of fractures and macropores, which, when present, can dominate water flow and contaminant transport. For this reason, modeling results commonly do not reflect the multi-modal flow detected in actual field studies. There have been several approaches for the *in-situ* detection of liquid movement through porous media, including Nuclear Magnetic Resonance,<sup>2</sup> CT scanning,<sup>3</sup> and synchrotron-based micro-CT scanning.<sup>4</sup> The objective of this project was to develop a new capability for SRNL to study fluid mechanics by passing a non-radiological tracer, sodium iodide, through porous media within a CT scanner. An important attribute of this scanner owned by the Imaging Robotics and Rad Systems group is its large size (60 x 60 cm), which is sufficiently large to capture large scale flow features, including fracture flow. Presently this CT scanner is set up to create 3-D renditions of solids. We established a capability that will permit setting up flow experiments within the scanner booth to capture 4-D renditions of the liquid as it passes through the porous media.

## Approach

An SRS vadose sediment was packed in a plexiglass core (25-cm L x 3-cm D). It was slowly saturated with water, then placed in a 60 °C oven to dry, creating micropores and macropores (e.g., cracks in the soil induced during drying). As such this is a disturbed sediment core in which the sediment structure was artificially created to insure a wide range of pore sizes for ease of detection. A peristaltic pump was used to introduce a 0.32 molar sodium iodide solution into the top of the sediment core drip at a rate of 0.149 mL/min (Fig. 1). The iodide in this influent solution acted as a tracer that was readily detectable by X-rays.

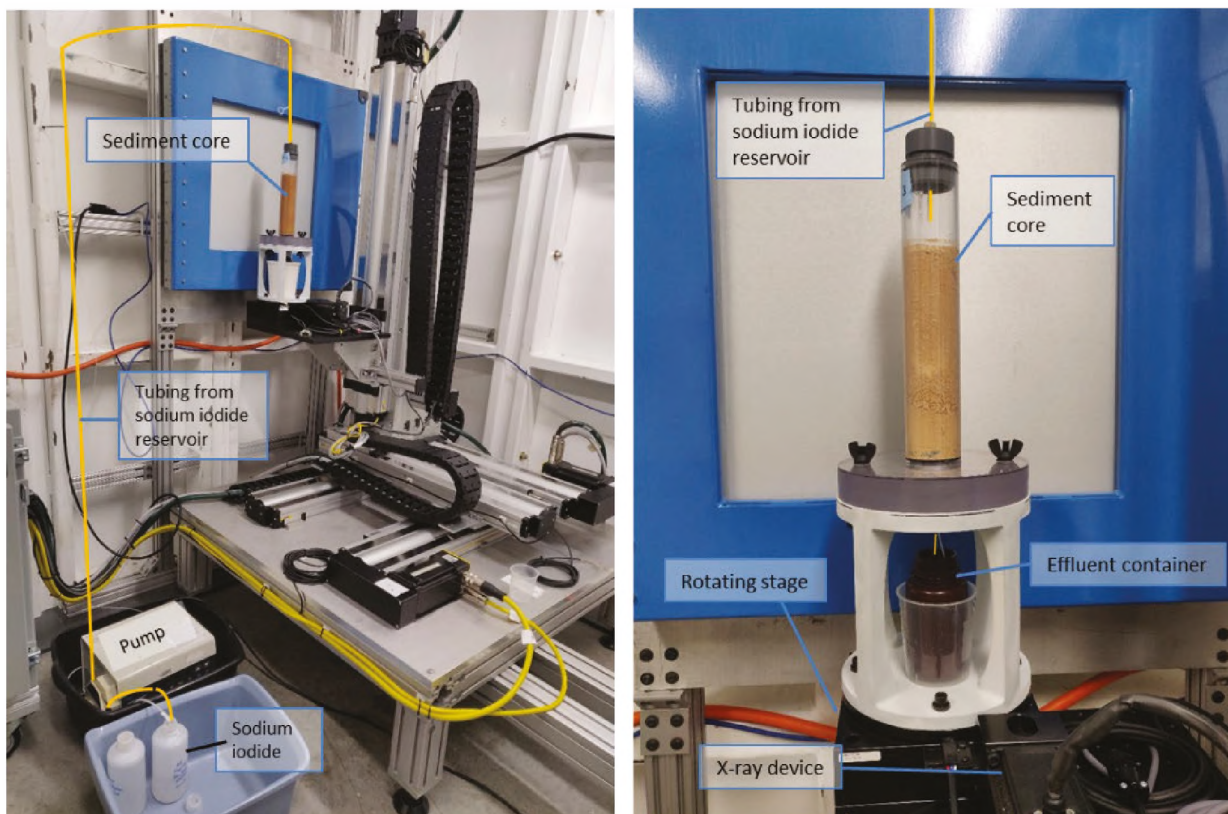


**Figure 1: (Left)** Set up within the CT scanner booth during the flow experiment of water (with sodium iodide added as X-ray tracer) slowly introduced into a dry sediment. **(Right)** Close up of the sediment core assembly on the rotating stage.

Prior to initiating the experiment, the CT scanner (781-A 420 kV X-ray Booth) was calibrated, which involved taking X-ray images of a moistened sediment core to measure the source to detector distance, the object to detector distance, the detector centerline row, the center of rotation, and effective pixel. Experiment continued until the entire core was saturated with water, resulting in a flow rate of 58.36 mL over 393 minutes or 0.149 mL/min. After the experiment, existing CT scanning software was used to compile various sets of scans into 4-D rendering of the water (more specifically the iodide) moving through size based. During the experiment, CT scan acquisitions were set for an exposure time of 0.45 sec, tube voltage of 400 kV and tube current of 8 mA while the sediment core rotated 360 degrees. The flow the sediment core. The voxel size of the CT reconstructions was 0.1mm x 0.1 mm x 0.1 mm. The data generated from these experiments were later modelled using a public domain software, HYDRUS-1D,<sup>5</sup> to describe one dimension, dual-porosity and dual-permeability processes.

## Results/Discussion

After completing the experiment, the data was compiled in a manner that permitted examining the core from any perspective, e.g., from top to bottom or longitudinally. Furthermore, animations were created that enhanced visualization of the data and accessing key time steps. Figure 2 provides an example of the resulting data, showing the dry sediment core at the start of the experiment (Figure 2, Left) and then a series of time steps during the experiment. After 7 minutes it is possible to see the moisture entering the core, as depicted by the light blue. By 27 minutes, close examination indicates the presence of some ponding on the soil surface, which was not intended to occur. By 45 minutes, the front progressed down the column in the shape of an upside down 'U,' suggesting that the plexiglass surface of the core was creating an experimental artifact, which is always carefully monitored during these types of experiments. It is not until 142 minutes, that the macropore on the left side of the core starts to fill up. It is important to note that the front of the matrix (micropores) advanced ahead of that of the macropores. This is consistent with well-established theory for these experimental conditions. The implications of this observation are that the presence of macropores in unsaturated sediment cores do not fill first, thereby by-passing the slower matrix flow. Once the macropores fill, they transmit greater fluxes of water than the matrix. At 252 minutes, the existence of the macropore at about 100 mm depth appears to be creating a type of capillary break, not permitting moisture to move left and below the macropore. Again, this is consistent with theory that predicts that finer pores fill first, and not until the water potential is sufficiently high, will it be able to enter the larger pore. By 309 minutes, the moisture front initially reaches the bottom of the column. By the end of the experiment, 398 minutes, the moisture front across the entire core cross-section had reached the bottom of the core. It is also note-worthy, that a similar height of ponding occurred throughout the study.

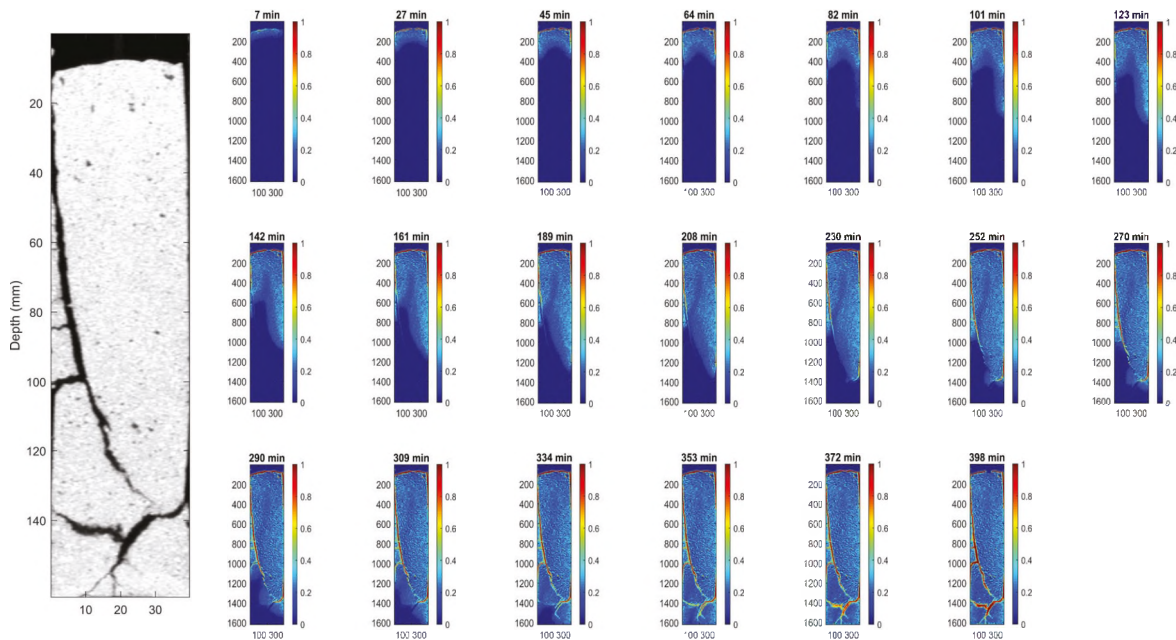


**Figure 2: (Left)** Dried soil core used at start of experiment with naturally occurring macropores. **(Right)** Progressive time-steps of fractional water content as water is introduced at the top of the column during 398 min experiment.

The averaged water contents of these profiles were estimated for the macropore (Figure 3A), the matrix/micropores (Figure 3b) and for the whole column (Figure 3C). Using HYDRUS-1D, we reproduced the water content profiles in the macropore and matrix domains (data not shown). However, we were unable to adequately reproduce the whole sediment column. This important finding brings into questions the accuracy of averaging flow in systems known to include both macropore and matrix flow. The problem stems from the inability to include geometry-explicit processes, pore-scale processes, in HYDRUS-1D. It is not possible to produce different macropore flow features, such as film flow or capillary bridging, because they are geometry-implicit processes. Also, HYDRUS-1D assumes capillary dominated Richards equation for the flow physics in macropore domain, which is not conceptually accurate. Thus, currently we are attempting to simulate the flow in macropores in a geometry-explicit 3D software, COMSOL Multiphysics, Ver. 5,<sup>6</sup> that will enable us to incorporate gravity-viscosity dominated Navier-Stokes equation to demonstrate different macropore flow mechanisms.<sup>1</sup>

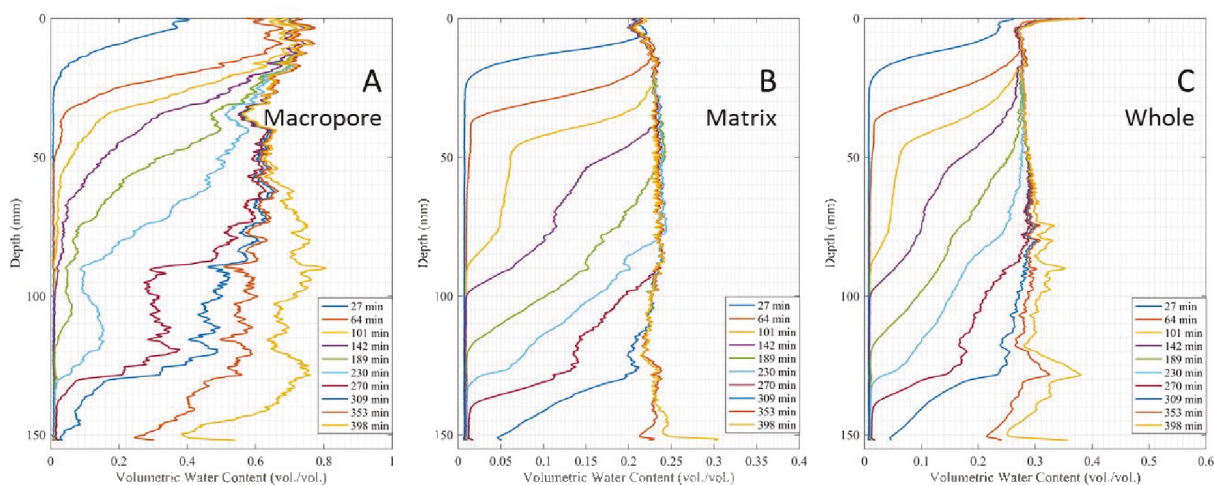


**Figure 3:** Averaged water contents of these profiles are provided for the macropore (A), the matrix/micropores (B), and for the whole sediment column (C).

## FY2020 Accomplishments

- **New Capability:** A new capability for SRNL was developed to study fluid mechanics by passing a nonradiological tracer through porous media within an X-ray CT Scanner
- **Business Development:** Can now write proposals (and manuscript) that include this new capability. This is especially useful in research related to environmental remediation, waste form development, and waste disposal risk calculations for describing the movement of liquids as they pass through glass, cement, fractured rock (e.g., Yucca Mountain) or soil

## Future Directions

- Continue modeling efforts using the geometry-explicit 3D COMSOL Multiphysics software
- Write manuscript describing these findings
- Using the information reported here as seed data, write a proposal to vary a series of sediment physics properties in a systematic manner to monitor changes in hydrological properties

## References

1. Hillel, D., *Introduction to environmental soil physics*. Elsevier: 2003.
2. Gummerson, R.; Hall, C.; Hoff, W.; Hawkes, R.; Holland, G.; Moore, W., Unsaturated water flow within porous materials observed by NMR imaging. *Nature* **1979**, *281* (5726), 56-57.
3. Anderson, S. H.; Wang, H.; Peyton, R. L.; Gantzer, C. J., Estimation of porosity and hydraulic conductivity from X-ray CT-measured solute breakthrough. *Geological Society, London, Special Publications* **2003**, *215* (1), 135-149.
4. Nakashima, Y.; Nakano, T.; Nakamura, K.; Uesugi, K.; Tsuchiyama, A.; Ikeda, S., Three-dimensional diffusion of non-sorbing species in porous sandstone: computer simulation based on X-ray microtomography using synchrotron radiation. *Journal of Contaminant Hydrology* **2004**, *74* (1-4), 253-264.
5. Simunek, J.; van Genuchten, M. T. Hydrus-1D, Version 4.17, Software Package for Simulating the Movement of Water, Heat, and Multiple Solutes in Variably Saturated Media. <https://www.pc-progress.com/en/Default.aspx?hydrus-1d> (accessed 5 April 2020).
6. COMSOL Multiphysics, Ver 5.0. <https://www.comsol.com/> (accessed 2 Feb. 2020).

## Acronyms

CT	Computed Tomography
SRNL	Savannah River National Laboratory
SRS	Savannah River Site

## Student Researchers

Abdullah Al Mamun, Ph.D. Candidate, Clemson University

## Development of Bio-Compatible Fluorescent Sensor

**Project Team:** Aaron L. Washington, II,  
John Bobbitt, III, LTC Jeremy Goodin

**Project Start Date:** February 20, 2020

**Project End Date:** August 10, 2020

*The development for biocompatible fluorescent sensors is used to understand the movement and tracking of wild boar at SRS. Current tracking methods for wild boar include physical tagging, camera monitoring, and foot tracks in the soil. None of these methods are highly effective in determining the path and habits of the animals as it depends on live imaging, soil consistency*

*(lack of rain), and potentially a global positioning system is tagged properly. This system allows tracking using an additive digested by the animal and released in the urine that will fluoresce when excited with a particular laser. This method helps determine the actual movements of the animals and even provide a potential prediction model based on their routine. We partnered with Ft. Gordon to utilize their animal testing expertise in determining the best material and pathway for these materials to be excreted.*

### FY2020 Objectives

- Identify material with fluorescence in the optimal region to avoid animal concern that is also safe for ingestion
- Procure reagent dyes at both Ft. Gordon and SRNL
- Determine imaging capabilities at SRNL for determining optical clarity
- Image samples in solutions of water and simulant urine to determine minimum detection limits
- Identify requirements needed in a biocompatible compound that include fluorescence intensity, optional wavelengths, and excitation sources for routine imaging capabilities and detector systems

### Introduction

Imagine the difficulty in tracking wildlife over 310 square miles of densely wooded forest. You can place cameras, add tracking devices for the animals you can catch, or try to monitor footprints for travel patterns. But there's a lot of difficulty in determining the natural movements, habits, and habitable areas for a particular animal on a nuclear site. Even if you tracked and tagged a few using cameras and GPS, you may not get a complete picture of their movements. This project has developed a fluorescent dye that's excretable through the animal's urine that can be tracked over a long distance and intended to be visible up 100 yards unimpeded.

Our focus in this task was to determine the best material that's capable of fluorescing in an optimal energy range that's outside of the normal visible range to avoid spooking the animals or causing them to disturb the trails that they or others left behind. We determined that near infrared dyes that functioned mostly in the 900-1400 nm range worked best in avoiding the animal visual acuity. There are only a few biocompatible dyes that function well in this region. Additionally, we had to acquire the equipment necessary to both excite these dyes and be able to image them in light and dark environments.

### Approach

Wild boar are currently tracked and monitored for the motion and habitats across the Savannah River Site. Current methods focus on traditional tracking systems that typically fail. The project focused on determining whether there was a COTS material available that could be excreted out of an animal through their urinary track. Developing and testing a material that was not only bio-compatible but also fluorescent in a non-visible region to avoid scaring or altering the pattern of the animal.

SRNL additionally approached the project looking to determine the most effective method of dye delivery to the animal. The most common methods for drug delivery include: oral, intravenously, and subcutaneously. Ft Gordon DDEAMC routinely deals with testing and evaluating animal responses to various drugs and treatments. SRNL partnered with Ft Gordon staff and researchers to find the best material and testing method.

## Results/Discussion

SRNL and DDEAMC have procured several fluorescent dyes that are bio-compatible and non-toxic at various dose levels. We evaluated them both visually with a black light illuminator and with a UV/Vis spectrometer/fluorimeter. The samples we suspended in both water and urine simulants for the visual and analytical analysis. The experiment has 3 different dyes (fluorescein, Evans Blue, and IR 1061) in serial dilution from concentrations of 0.077 mg/mL down to  $2.1 \times 10^{-11}$  mg/mL to show the limit of detection in both absorbance and fluorescence with concentration. The instrument, a BioTEK Synergy 2, was only able to analyze at certain wavelengths namely: 200, 352, 620, 790, 860, and 962 nm.

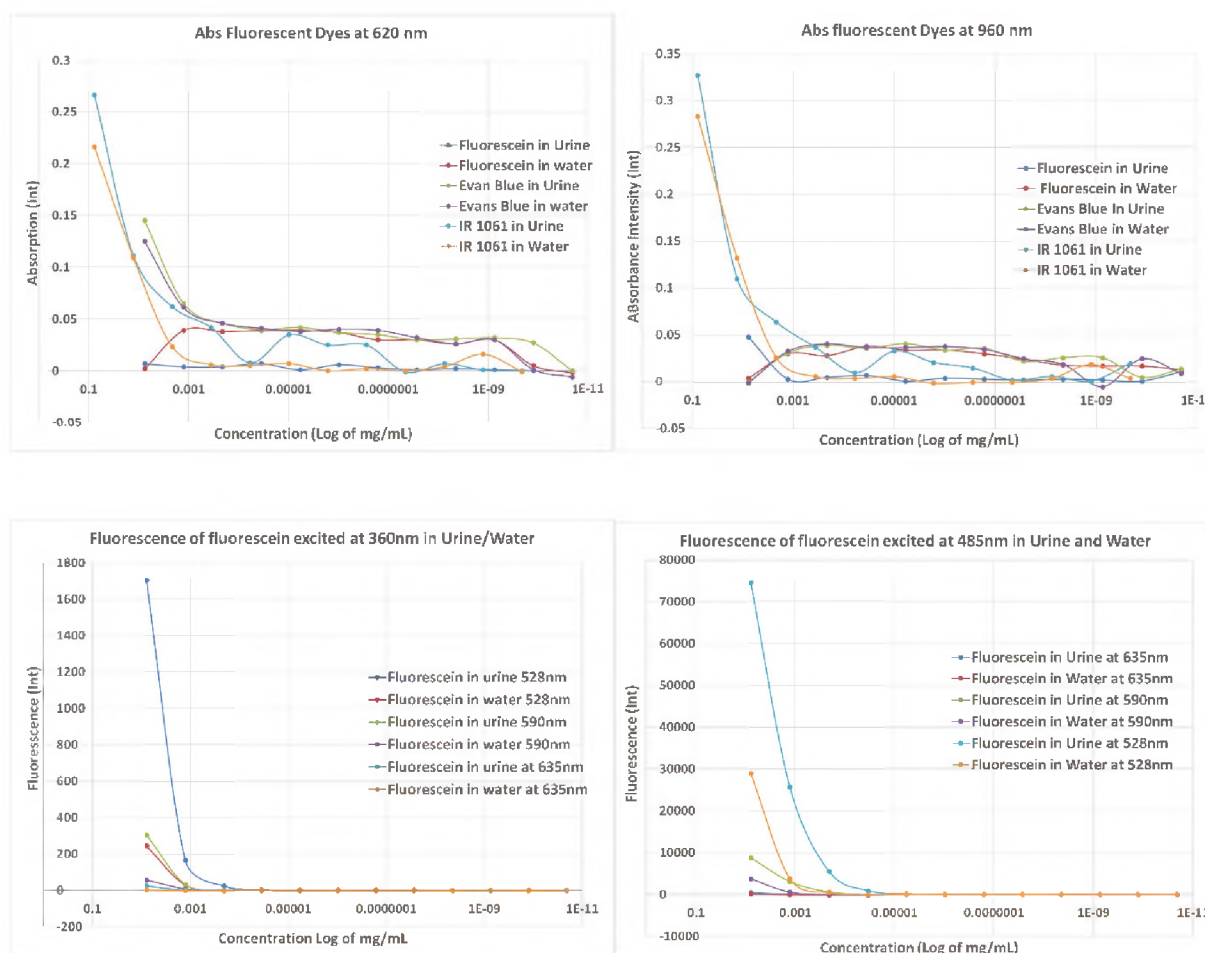


**Figure 1:** A) Absorption data of Fluorescein, Evans Blue, and IR 1061 suspended in simulated urine and water at various concentrations measured at 620 nm and B) 960 nm. C) Fluoresce of fluorescein in both water and urine excited at 360 and D) 485 nm with the filter set at either 528nm, 590nm, or 635nm.

There are some important takeaways from our experiment with these dyes in both a urine simulant and water. We now have confirmed both the complete solubility of the dyes in different solutions, optical detection limits for both absorption and fluorescence, and optical absorption range of the dyes. This information was all acquired with collaboration with FT Gordon DDEAMC team.

There were some interesting observations and conclusions made about the samples. First, the samples in the Urine have higher absorption and fluorescence intensities than the water. This is a very positive response. In that manner we know that the samples will all be brighter in our actual bio samples. So forward testing should allow us to use only water as a conservative measure and assume this to be a baseline. Additionally, there is no non-excited luminescence observed in this material.

## FY2020 Accomplishments

Brief descriptions of accomplishments to date in bullet form. Whenever possible, accomplishments should be stated quantitatively, as in the examples below, and indicate the contribution to meeting the objectives as well as the magnitude of the improvement over past work:

- Discovered that hydrogen storage capacities on HWCVD generated nano-crystalline graphite could be enhanced by the presence of iron nanoparticles. Preliminary measurements indicated an un-optimized capacity between 1 and 3 wt%
- Compressor design optimization has reduced maximum speed from 4800 rpm to 3200 rpm with no increase in volume

## Future Directions

There are several future directions for this project:

- Identify potential surface surfactants/encapsulation substrates to be evaluated for enhanced biological stability
- Investigate reaction mechanisms for in-vivo activation of fluorescent properties for suitable excretion and lifetime analysis.
- Develop animal protocol to test materials in vivo using multiple methods of delivery

## Acronyms

DDEAMC	Dwight D. Eisenhower Army Medical Center
NIR	Near Infrared
SRNL	Savannah River National Laboratory
SRS	Savannah River Site

## Intellectual Property

Patent Application Submitted

## External Collaborators (Universities, etc.)

Fort Gordon Dwight D. Eisenhower Army Medical Center

## Quantitative Determination of Total Cesium in SRS Tank Waste by Inductively Coupled Plasma Emission Spectroscopy

**Project Team:** Nathan Wyeth, Mark Jones, Thomas White, and Charles Coleman

**Project Start Date:** April 1, 2020

**Project End Date:** September 30, 2020

*The analysis of cesium (Cs) is fundamental for waste characterization and source identification of fission products in nuclear waste remediation and in non-radioactive simulant tests to support tank closure programs. Inductively Coupled Plasma Emission Spectroscopy (ICP-ES) has not been utilized for total Cs determinations in the past due to the inability for quantitative determination below sub-parts per million*

*(ppm) levels and spectroscopic interferences. Currently, Cs isotopic analysis for tank waste at SRS is performed by Inductively Coupled Mass Spectrometry (ICP-MS) to ppt concentrations. However, total Cs by ICPMS faces the problem of isobaric interferences of some Cs isotopes by barium ions when present in samples and leads to bias high quantitation. Utilization of the expanded wavelength detection range of the Leeman Prodigy ICP-ES in combination with an ionization buffer (IB) results in a significant increase in spectral intensity without the impact of potential Ba interference when present in sample. This technique increased the sensitivity of ICP-ES from low ppm concentrations to low ppb concentrations.*

### FY2020 Objectives

- Evaluate ICP-ES Cs emission signal at wavelength 894.347 nm
- Establish Calibration with a minimum  $R^2$  of 0.999
- Determine LOQ and evaluate methods to increase sensitivity
- Analysis of real SRS tank waste and simulant samples
- Data evaluation and direct comparison to ICP-MS
- Submission for publishing FY20

### Introduction

The quantitative determination of cesium (Cs) by Inductively Coupled Emission Spectroscopy (ICP-ES) was performed at the Savannah River National Laboratory (SRNL) on both a non-radiological and a contained radiological Leeman Prodigy ICP-ES. The analysis of Cs at the Savannah River Site (SRS) is fundamental for waste characterization and source identification of fission products in nuclear waste remediation. In addition, Cs measurements in non-radioactive simulant tests are also essential to support the development of tank closure programs. SRNL utilizes Inductively Coupled Plasma Mass Spectrometry (ICP-MS) for isotopic analysis of  $^{133}\text{Cs}$  (stable) and the  $^{134}\text{Cs}$  ( $t_{1/2} = 2$  y),  $^{135}\text{Cs}$  ( $t_{1/2} = 2.3 \times 10^6$  y) and  $^{137}\text{Cs}$  ( $t_{1/2} = 30$  y) radioisotopes. In samples containing barium ion daughter isotopes, Cs isotopic analysis is subject to isobaric interferences (e.g.,  $^{134}\text{Ba}$ ,  $^{135}\text{Ba}$  and  $^{137}\text{Ba}$ ).

ICP-ES is not a technique utilized due to the inability for quantitative determination below sub-parts per million (ppm) levels (e.g., Cs 455.531 nm) and spectroscopic interferences (e.g., Cs 852.120 nm)<sup>[1]</sup> on standard ICP-ES systems due to detector wavelength ( $\lambda$ ) range limitations (e.g., 165 nm to 785 nm).

Sensitivity issues stem from the low ionization potential of Cs at 3.893eV and spectroscopic interferences with Argon (Ar) creating complex challenges for elemental Cs by this method.<sup>1</sup>

The Leeman Prodigy ICP-ES was selected due to its wavelength detection range of 165 - 1100 nm.<sup>2</sup> The utilization of Cs emission line 894.347 nm in Axial mode provides a sensitive wavelength and a strong gaussian signal in comparison to line 455.531 nm (Figure 1). The line 894.347 nm is visible due to the instruments Large Format Programmable Array Detector (L-PAD).<sup>2</sup> Additionally, an ionization buffer (IB) solution composed of a Sodium Peroxide Fusion (NaPF) solution and Lithium Carbonate (Li<sub>2</sub>CO<sub>3</sub>) in 2% nitric acid (HNO<sub>3</sub>) is added to sample aliquots to increase line intensity. The goal is to lower the limit of quantitation (LOQ) from ppm concentrations to lower part-per billion (ppb) concentrations.

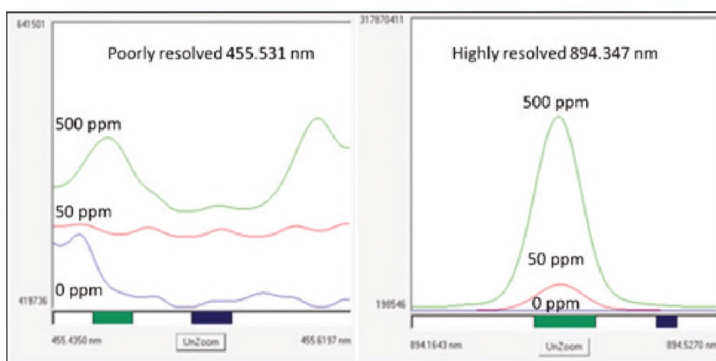


**Figure 1:** Spectral overlay of Cs at 500 ppm, 50 ppm and Blank in Axial Mode. Emission line 455.531 nm (Left); Emission line 894.347 nm (Right)

ICP-ES analysis of Cs was performed on real radiological Tank Closure Cesium Removal (TCCR) samples and Non radiological samples including a set of CsGa<sub>7</sub>O<sub>11</sub> leaching samples. All ICP-ES analytical testing results were directly compared to ICP-MS for method validation of total Cs. Utilizing the ICP-ES can provide an accurate quantitative value for total Cs while providing a complementary technique to the current ICP-MS analysis for all groups and organizations performing Cs analysis for the Department of Energy's (DOE) Nuclear Waste Mission.

## Approach

The approach of the project was to determine the sensitivity of Cesium in Axial mode at 894.347 nm with the primary goal of achieving an LOQ of 50 ppb or less and a method uncertainty of 30% 2-sigma at the LOQ. Following detection of a strong gaussian peak of total Cs, the project utilizes other easily ionizable elements (EIE) as ionization buffers by utilizing ionization interference to increase the signal of Cs.<sup>3</sup> Ionization interference is a phenomenon which shows a change in emission intensity, causing the ionization equilibrium to shift, when coexisting elements include an EIE, such as Na, K, and Cs.<sup>3</sup> The effect is expected to boost the emission intensity and lower the overall detection limit to low ppb concentrations for a total Cs determination.

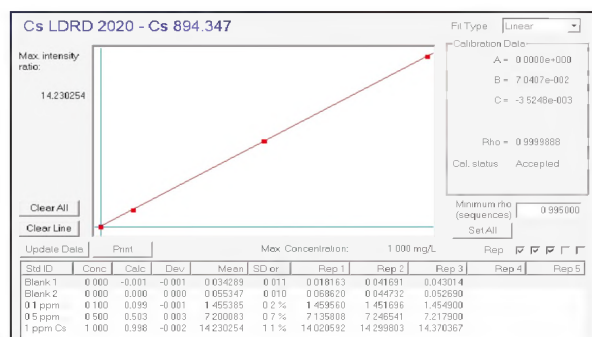


**Figure 2:** Four-point linear Cs 894.347 nm calibration with an R<sup>2</sup> 0.9999 from Blank, 100 ppb, 500 ppb and 1 ppm.

The final approach is to establish a minimum linear calibration of R<sup>2</sup> 0.999 (Figure 2) and perform Cs analysis on blanks, spiked samples at varying concentrations and real radiological/non-radiological samples from SRS nuclear waste mission. Only

samples previously analyzed by ICP-MS are measured for total Cs, and the data sets are directly compared for accuracy, precision and method validation.

## Results/Discussion

The IB for the method was chosen based on a measurement (n=3) of emission line 894.347 nm at 100 ppb of Cs in various matrices (Figure 3). The mixture of Li<sub>2</sub>CO<sub>3</sub> and NaPF (NaPFLiC) resulted in a 56% increase in spectral intensity compared to a 2% HNO<sub>3</sub> matrix at 100 ppb. The NaPFLiC mixture was selected for further method development and sample analysis to provide a lower detection limit.

A limit of quantitation (LOQ), or minimum reporting limit, for the elemental wavelength set up on the Leeman Prodigy ICP-ES method was measured. All standards and blanks were prepared in 2% v/v Nitric Acid with the addition of 200 uL of NaPF, 1 mL of 5000 ppm Li<sub>2</sub>CO<sub>3</sub>, 50 uL of 400 ppm Indium (Internal Standard) for a total of 10 mL. After analyzing ten blanks, the LOQ was determined using

$$LOQ = 10 \times \sigma$$

where  $\sigma$  is the standard deviation of the ten blank measurements.

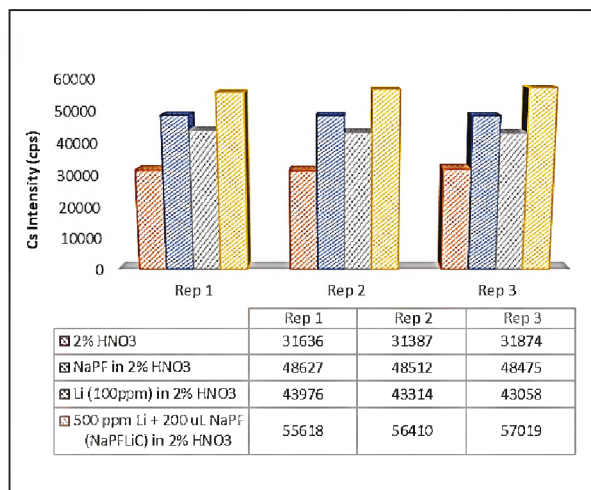


**Figure 3:** Effect of ionization buffer on 894.347 nm Cs spectral intensity at 100 ppb

**Table 1:** Leeman Prodigy Cs Limit of Quantitation

Element/Line	Leeman Prodigy LOQ(mg/L)
Cs 894.347 nm	0.005

The limit of quantitation was determined to be 0.005 mg/L for Cs 894.347 nm (Table 1). An LOQ in 2% HNO<sub>3</sub> with a NaPF IB solution was determined at 0.022 mg/L, 4.4 times higher than with the NaPFLiC IB solution. The LOQ for Cs demonstrates excellent sensitivity on the ICP-ES.

Method uncertainties for the Cs 894.347 nm were measured to evaluate method sensitivity and accuracy. 10 preparations of quality control standards were prepared in 2% HNO<sub>3</sub> with the NaPFLiC IB solution. 10 replicates were analyzed for Cs 894.347 nm at concentrations of 10 ppb. The uncertainty was calculated using

$$2\text{-sigma uncertainty} = [(\%RSD)^2 + (\%Bias)^2]^{1/2} \times 2$$

where the percent relative standard deviation (%RSD) is the standard deviation of the ten measurements divided by their mean times 100. The percent bias (%Bias) is the difference from the *true* value of the quality control standard, and the root sum of the squares (RSS) of the %RSD and %Bias was calculated and multiplied by 2 to obtain an uncertainty at 2-sigma. Table 2 lists the 2-sigma method uncertainty of Cs 894.347 nm at 10 ppb utilizing the NaPFLiC IB.

**Table 2:** Leeman Prodigy ICP-ES Uncertainty Determinations of Cs 894.347 nm utilizing NaPFLiC buffer.

Element/Line	10 ppb 2-Sigma % Uncertainty Leeman Prodigy ICP-ES
Cs 894.347 nm	10.7

A set of Non-Rad simulant TCCR samples from Crystalline Silicotitanate columns (CST), containing less than 5 ppm Na were analyzed at a 200x and 100x dilution utilizing the described method. <sup>4</sup> In addition, Table 3 shows a set of 16 samples from a CsGa<sub>7</sub>O<sub>11</sub> leaching study that were analyzed for total Cs and compared to ICP-MS. <sup>5</sup>

A set of various matrix SPK samples were also prepared and analyzed (Table 3) with a spike recovery within 10% of the expected value, further demonstrating method accuracy and precision. All results are less than 6% BIAS when compared to ICP-MS results except for the leaching study spike (SPK) data at less than 25% (Table 3).

Radiological TCCR samples from SRS Tank 10 Batch 3 were analyzed. <sup>6</sup> The samples contained ~1500ppm of Na, demonstrating the buffer impact to sensitivity when high level Na is present in the sample (Table 4).

The use of an IB on samples with high Na content resulted in elevated values. These values were ~ 1.5 times the expected value indicating an additional increase in intensity due to the high levels of sodium. When the same samples were analyzed without the IB and measured against calibration containing the IB; the results were less than 3.5% BIAS from the ICP-MS results (Table 4).

A set of radiological TCCR teabag samples from Batch 3 were also analyzed for comparison to ICPMS. <sup>6</sup> The samples contained ~35 ppm of Na and were analyzed at a 5x dilution and resulted in a higher %BIAS at 13%.

To conclude sample testing, a 2 g/L Cs standard was analyzed by ICP-ES with IB to demonstrate linearity and method accuracy beyond the calibration range. The ICP-ES detected 1970 mg/L of Cs at a 100x dilution. The result is 1.5% BIAS from the *true* value of 2000 mg/L and a 6.8% BIAS from the ICP-MS value of 2110 mg/L.

Total Cs method has established accuracy, precision and an exceptionally low LOQ on the Leeman Prodigy ICP-ES. The method can provide an accurate quantitative value for total Cs while providing a complementary technique to the current ICP-MS analysis in support of Total Cs analysis for the Department of Energy's (DOE) Nuclear Waste Mission.

# FY20 LDRD ANNUAL REPORT

**Table 3: Cs analysis of Non-Rad TCCR simulants and CaGa7O11 samples**  
via Leeman Prodigy ICP-ES utilizing NaPF<sub>6</sub>LiC buffer.

Sample/DF	Cs Matrix Spike mg/L	% Cs Spike Recovery	Cs ICP-ES (ug/g)	Cs ICP-MS (ug/g)	%BIAS
Column A CST 200x			6037	6103	-1.1
Column B CST Top 200x			5359	5302	1.1
Column B CST Bottom 200x			4059	3993	1.6
Column C CST 200x			7486	7289	2.7
Column A CST 100x			6092	6103	-0.2
Column B CST Top 100x			5487	5302	3.4
Column B CST Bottom 100x			4124	3993	3.2
Column C CST 100x			7666	7289	5.0
Column A CST 200x + Cs Spk	0.15	-102	*5928	6103	-2.9
Column B CST Top 200x + Cs Spk	0.25	-98	*5377	5302	1.4
Column B CST Bottom 200x + Cs Spk	0.20	-110	*4097	3993	2.6
Column C CST 200x + Cs Spk	0.50	-106	*7689	7289	5.3
CGO-pH2-A-48hr 8x			2384	2490	-4.3
CGO-pH2-B-48hr 8x			2430	2520	-3.6
CGO-pH2-A-168hr 8x			2729	2790	-2.2
CGO-pH2-B-168hr 8x			2807	2890	-2.9
CGO-pH7-A-48hr 8x			1411	1440	-2.0
CGO-pH7-B-48hr 8x			1366	1390	-1.7
CGO-pH7-A-168hr 8x			1367	1420	-3.8
CGO-pH7-B-168hr 8x			1331	1360	-2.2
CGO-pH7-A-48hr 8x + Cs Spk	0.20	-109	*1745	1440	-19.2
CGO-pH7-B-48hr 8x + Cs Spk	0.20	-109	*1746	1390	-22.7
CGO-pH7-A-168hr 8x + Cs Spk	0.20	-109	*1740	1420	-20.3
CGO-pH7-B-168hr 8x + Cs Spk	0.20	-105	*1684	1360	-21.3

\*denotes the SPK concentration minus total Cs value.

**Table 4:** Effect of IB on Cs in Rad Samples Containing High Levels of elemental Na.

Sample/DF	Cs ICP-ES (ug/L) Li <sub>2</sub> CO <sub>3</sub> Buffer	Cs ICP-ES (ug/L) NaPFLiC Buffer	Cs ICP-ES (ug/L) No Buffer	CS ICP-MS (ug/L)	%BIAS
Tk 10 Batch 3 A-2 20x	508	540	386	390	*-1.0
Tk 10 Batch 3 A-1 20x	494	558	378	390	*-3.1

\*denotes %BIAS compares no buffer ICP-ES to ICP-MS

**Table 5:** Cs Analysis of Radiological TCCR Teabag samples from Batch 3 utilizing NaPFLiC IB.

Sample/DF	ICP-ES (ug/g)	ICP-MS (ug/g)	%BIAS
Teabag A7 5x	1043	928	11.7
Teabag A8 5x	1038	911	13.0

## FY2020 Accomplishments

- Literature research and preliminary testing found that the Leeman Prodigy's extended wavelength range for detection could utilize wavelength 894.347 nm for a more sensitive Cs analysis which was not feasible with other ICP-ES systems due to detector limitations
- An increase in spectral intensity, at 894.347 nm, greater than 50%, when utilizing a NaPFLiC IB compared to no IB
- Calibration linearity was established at R<sup>2</sup> of 0.9999
  - LOQ was established at 5 ppb
  - Method uncertainty at 10 ppb is 10.7% 2-sigma
- Total Cs analysis results of radiological and non-radiological samples were directly compared to ICP-MS data with a less than 15% BIAS across data sets, with the majority of samples tested less than 6% BIAS

## Future Directions

Submission for publication

## References

1. Do V.K.; Yamamoto M.; Taguchi S.; Takamura Y.; Surugaya N.; Kuno T. *Quantitative determination of total cesium in highly active liquid waste by using liquid electrode plasma optical emission spectrometry. Talanta.* 2018;183:283-289.
2. Teledyne Leeman, *New Technical note describing the advantages of an ICP spectrometer with a wavelength range of 165 – 1100 nm*, [www.teledyneleemanlabs.com/companyinfo/Press-Releases/Pages/PR-Iodine.aspx](http://www.teledyneleemanlabs.com/companyinfo/Press-Releases/Pages/PR-Iodine.aspx), March 2006.
3. Morishige Y.; Kimura A., *Ionization Interference in Inductively Coupled Plasma-Optical Emission Spectroscopy*, SEI Technical Review Number 66, April 2008.

4. King W. D.; Nash C. A.; Taylor-Pashow K. M. L.; Hang T.; Hamm L.L.; Aleman S.E.; Fondeur F.F. *Cesium Removal Performance Comparisons of Crystalline Silicotitanate Media Batches with Savannah River Site Waste Simulant*. SRNL-STI-2019-00648, Rev 2, Savannah River National Laboratory (SRNL): Aiken, SC, 2020.
5. Juillerat C. A.; Kocevski V.; Klepov V. V.; Amoroso J. W.; Besmann T. M.; zur Loye H-C. *Structure and Stability of Alkali Gallates Structurally Reminiscent of Hollandite*. J Am Ceram Soc. 2020;00:1-12. <https://doi.org/10.1111/jace.17327>.
6. Taylor-Pashow K. M. L.; Nash C. A. *Summary of Expedited Results from Samples Supporting Tank Closure Cesium Removal (TCCR) Batch 3*. SRNL-STI-2020-00269, Rev 0, Savannah River National Laboratory (SRNL), Aiken, SC, 2020

## Acronyms

Ba	Barium
Cs	Cesium
CST	Crystalline Silicotitanate
DF	Dilution Factor
EIE	Easily Ionizable Elements
G/L	Gram/Liter
HNO <sub>3</sub>	Nitric Acid
IB	Ionization Buffer
ICP-ES	Inductively Coupled Plasma Emission Spectroscopy
ICP-MS	Inductively Coupled Plasma Mass Spectrometry
Li	Lithium
L-PAD	Large Format Programmable Array Detector
K	Potassium
LOQ	Limit of Quantitation
MG/L	Milligram per Liter
ML	Milliliter
Na	Sodium
NaPFLiC	Sodium Peroxide Fusion/Lithium Carbonate Buffer Solution
NM	Nanometers
NonRad	Non-Radiological
UG/G	Microgram per gram
PPB	Parts Per Billion
PPM	Parts Per Million
PF	Peroxide Fusion
RAD	Radiological
SRNL	Savannah River National Laboratory
SRS	Savannah River Site
TCCR	Tank Closure Cesium Removal
UL	Microliter

## Rapid, Inexpensive Analysis of Metal Contaminated Sediment Pore Water Using Combined Techniques

**Project Team:** Charles E. Turick, Anna S. Knox, Courtney E. Burckhalter

**Project Start Date:** April 1, 2020

**Project End Date:** August 25, 2020

*Sediments contaminated with heavy metals require frequent monitoring to quantify the bioavailable fraction of metals present. To understand the long-term effectiveness of a remedial action, sufficient pore water data are needed. Diffusive gradient thin film probes (DGT) selectively bind to bioavailable metals for in-situ monitoring. DGT probes are then returned to the lab for*

*acidification and metals extraction followed by ICP-MS analysis. Coupling DGT sampling with the electrochemical technique developed here could be used in the field to accelerate detection of bioavailable metal concentrations. Results will be known within minutes rather than days. In addition, this rapid field deployable analysis could reduce sampling costs. To achieve this goal, we used the electrochemical technique of stripping voltammetry to measure individual metals in solution as well as mixtures of metals. This technique measures specific metals based on oxidation potential thereby providing specificity and quantification of analytes, well suited for field applications.*

### FY2020 Objectives

- Electrode conditioning and analytical methods development
- Quantification of Cd, Pb, and Cu individually and mixed in solution
- Comparison of this method to existing techniques

### Introduction

Ongoing remedial actions of heavy metal contaminated sediments, as well as completed *in-situ* capping, both require monitoring to gauge the effectiveness of the remedies.<sup>1-4</sup> Dissolved metal concentrations in pore water is considered to most accurately reflect the bioavailable metal pool.<sup>2</sup> To understand with confidence the long-term effectiveness of a remedial action, sufficient pore water data are needed to establish a statistically defensible trend in contaminant behavior. While an abundance of quality data can be used to establish the confidence needed to draw reliable conclusions, the high cost of sample analysis most often necessitates minimalistic data acquisition and hence increased risk in decision making. The proposed electro-analytical techniques will combine existing methods to substantially decrease monitoring costs and improve risk management strategies relative to existing methods.

Conventional in-situ monitoring methods include surface water and pore water sampling and coring devices for sediment sampling, semi permeable membrane devices, and passive samplers like diffusive gradient thin film (DGT).<sup>1</sup> One of the promising techniques is DGT probes which include a collection gel-layer with a medium that selectively binds to the contaminant of interest and a diffusion gel-layer that selectively admits analyte molecules.<sup>5</sup> DGT tends to exclude non-bioavailable metals strongly bound to organic molecules and other ligands, thus providing a more accurate measure of potentially bioavailable metals compared to total or dissolved metal measurements. Metal contaminant concentrations are typically measured via ICP-MS from acid extracts of DGT probes and calculated as previously described.<sup>5</sup> In lieu of ICP-MS we used stripping voltammetry to measure individual metals and mixtures. Mixtures of metals were also evaluated to determine peak separation. Overall, this technique involves deposition of analytes onto the working electrode followed by a linear increase in oxidizing potential, which results in oxidation peaks of specific metals in proportion to concentration (Fig. 1). Since each metal responds

proportionally to its specific oxidation potential, specificity and quantification of analytes can be achieved faster and cheaper than ICP-MS.

The goal of this short term LDRD project was to combine existing technical approaches (DGT and electrochemical analyses) to accelerate the rate of analyses and significantly reduce analytical costs of bioavailable metal detection and measurement.

## Approach

Bioavailable metal concentrations are typically measured via ICP-MS from acid extracts of DGT probes and calculated as previously described<sup>5</sup> or directly from acidified pore water samples. In lieu of ICP-MS, we used stripping voltammetry to measure individual metals ranging from low ppm to high ppb. Mixtures of metals were also evaluated to determine peak separation, leading to metal identification from data. Overall, this technique involves deposition of analytes onto the working electrode followed by a linear increase in oxidizing potential, which results in oxidation peaks of specific metals in proportion to concentration (Fig. 1). Since each metal responds proportionally to its specific oxidation potential, specificity and quantification of analytes can be achieved faster and cheaper than ICP-MS. This has potential application in the field by analyzing the acidified samples from DGT probes.

The goal of this short term LDRD project was to accelerate the rate of analyses and significantly reduce analytical costs of metal detection for contaminated sediments. Our approach included square-wave stripping voltammetry, as previously described,<sup>6-8</sup> and incorporated carbon modified screen printed electrodes (PalmSens, NL). First, a method for conditioning the electrode was incorporated into our study. This is done electrochemically in order to sensitize the electrode to analytes to be measured. In this way, an electrode can be reused without compromising the data with a loss of sensitivity. Metals were then deposited onto the electrode poised at a reduction potential to assist in metal deposition. During this time, the solution was stirred. Metal analyses was conducted in a non-stirred solution using linear sweep square wave anodic stripping voltammetry. This removes metals previously deposited onto the electrode while quantifying concentrations based on the oxidizing current detected.

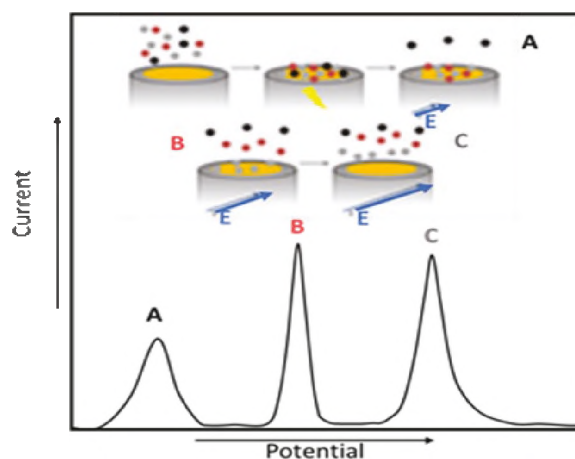


**Figure 1:** Metals in solution (depicted above as A, B, and C) are electrochemically deposited on an electrode. As the electrode is gradually oxidized, metals return to solution resulting in current increases proportional to concentrations. Metals are removed from the electrode based on their individual oxidation potential. This allows for separation of metals in solution for quantification of specific metals.

## Results/Discussion

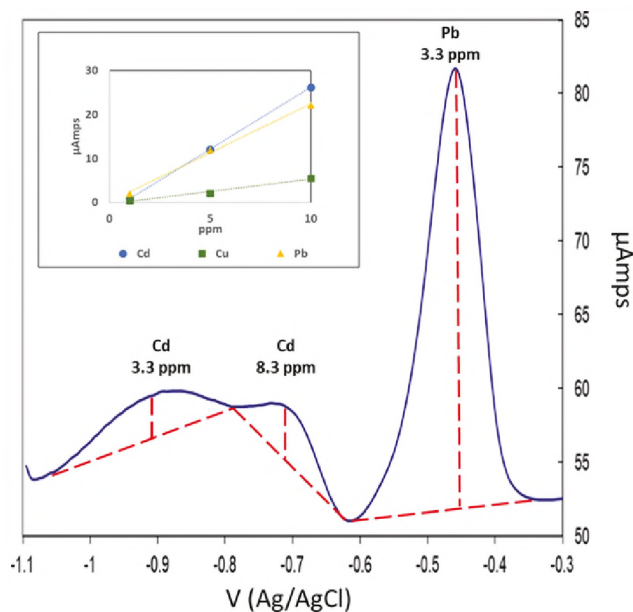


**Figure 2:** Cadmium, copper and lead were separated and quantified electrochemically using our methods. Analyte responses were linear up to at least 10 ppm (insert). Detection limits are in the ppb range.

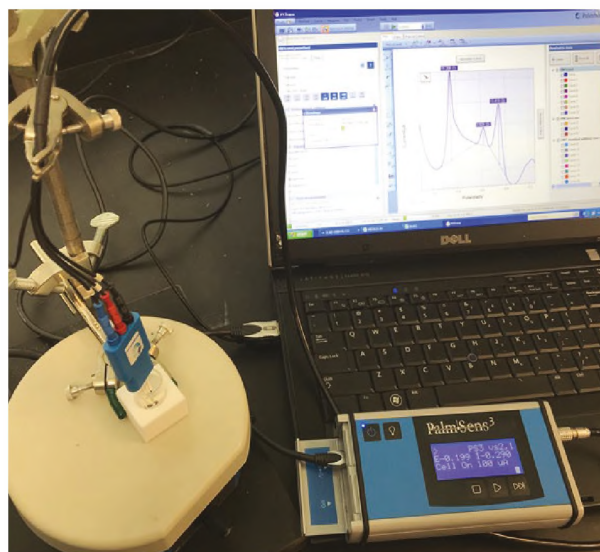


**Figure 3:** Field-ready analyses. Electrochemical methods are controlled by the potentiostat (foreground) and linked to a laptop computer. Miniature electrode and holder pictured on left.

Metal detection and quantification was accomplished with this technique. The capability of detecting metals in acidified samples will allow us to utilize this method for upcoming field deployments next fiscal year. Results depicted in Figure 2 are representative of this approach and were acquired within four minutes of analyses. The use of a small handheld potentiostat for electrochemical analyses and a laptop computer demonstrate the portability of this method and the potential for field deployment of this method (Fig. 3).

## FY2020 Accomplishments

- Implemented methods for electrode conditioning for metal analyses
- Demonstrated a linear response for Cd, Cu and Pb, in the low ppm ranges
- This method compares well to existing methods with advantages of
  - Lower cost
  - Rapid analyses
  - Field deployable

## Future Directions

- Field deployment
- Comparison of field results with ICP-MS

## References

1. *Contaminated Sediment Remediation Guidance for Hazardous Waste Sites*; EPA-540-R-05-012 Office of Solid Waste and Emergency Response; OSWER 9355.0-85; US EPA: Washington, DC, 2005; <http://www.epa.gov/superfund/resources/sediment/guidance.htm>
2. The Association of State and Territorial Solid Waste Management Officials. Sediments. In *Framework for Long-Term Monitoring of Hazardous Substances at Sediment Sites*. 2009; pp 13-16.
3. *R&D Needs for Long-Term Management of Contaminated Sediments*. SERDP and ESTCP Workshop; 2016. <https://www.serdp-estcp.org/Program-Areas>
4. Turick, C.E.; Knox, A.S.; Khune, W. Radioactive Elements/Issues in Soils. In *Soils and Human Health*. Brevik, E., Ed. Taylor and Francis Publishing: Boca Raton 2013 pp 148-150.
5. Knox, A.S.; Paller, M.H. Effect of bioturbation on contaminated sediment deposited over remediated sediment. *Sci. Tot. Environ.* **2020**, *713*, 136537
6. Ho, C.K.; Robinson, A; Miller, D.R.; Davis, M.J. Overview of sensors and needs for environmental monitoring. *Sensors*. **2005**, *5*, 4-37.
7. Palchetti, I; Laschi, S; Mascini, M. Miniaturised stripping-based carbon modified sensor for in field analysis of heavy metals. *Analyt. Chim. Acta* **2005**, *530*, 61-67.
8. Wang, J. Lu; Kirgöz, Ü. A.; Hocevar, S. B.; Ogorevc, B. Insights into the anodic stripping voltammetric behavior of bismuth film electrodes. *Analyt. Chim. Acta*. **2001**, *434*, 29–34.

## Acronyms

DGT	Diffusive Gradient Thin Film
ICP/MS	Inductively Coupled Plasma/Mass Spectrometry
ppm	Parts Per Million
ppb	Parts Per Billion

## Investigation of Optical, Physical and Corrosion Properties of Gamma-Irradiated International Simple Glass

**Project Team:** Charles Crawford, Robert Lascola, Devon McClane, Katie Hill

**Project Start Date:** January 1, 2020

**Project End Date:** August 21, 2020

*A simplified surrogate high-level waste glass from recent national and international testing was irradiated to a gamma dose of 100 Mrad. Properties of the irradiated glass were measured for comparison to the pristine unirradiated glass. Glass transition temperatures as well as Infrared and Raman spectroscopy measurements show no change in the irradiated glass. Short-term*

*aqueous corrosion tests on the glass powders also indicate no measurable differences. As expected from the observed radiation darkening of the glass, absorbance spectra of the irradiated glass with the pristine glass used as reference, indicates a broad absorbance over the range of 400 to 700 nm that is centered around 550-600 nm.*

### FY2020 Objectives

- Irradiate International Simple Glass with SRNL Gamma Irradiator to a nominal dose of 100 Mrad
- Compare measured properties of the unirradiated and irradiated glasses
- Measure optical properties like Raman Spectroscopy and UV-VIS absorption spectroscopy
- Measure the glass transition temperature
- Apply the ASTM static powder glass leach test to measure corrosion properties

### Introduction

Borosilicate glass has been adopted internationally for the treatment of nuclear waste with the object of long-term stabilization of the waste through vitrification.<sup>1,2</sup> Still, the effects of self-radiation through radioactive element decay over hundreds or even thousands of years on glass composition can only be modeled or simulated.<sup>3</sup> Accelerated tests considering worst-case scenarios are therefore useful for understanding glass behavior on the longer time scales in the interest of future generations.

Accordingly, the object of the proposed research is to gain understanding of the effects of gamma radiation resulting from radioactive element decay on the physical properties of borosilicate glass for use in the vitrification process. To this aim, the well characterized glass system referred to as International Simple Glass (ISG)<sup>4</sup> agreed upon by the international community as representative glass will be employed.

The ISG, a 6-component (Si, B, Na, Al, Ca, Zr) glass available at the Savannah River National Lab (SRNL), was subjected to a 100 Mrad dose via a Co-60 gamma irradiation. The effects of gamma rays on the ISG were then studied by spectroscopic analysis methods, differential scanning calorimetry and corrosion, in comparison with the unirradiated reference. The primary methods included optical absorption, Raman spectroscopy, glass transition temperature and short-term corrosion performance. The research is expected to provide insights into the long-term effects of gamma radiation emitted during radioactive waste decay.

## Approach

A 500 gram bar of the ISG was irradiated in the SRNL Co-60 gamma irradiator for a duration of 1,096 hr at a dose rate of  $\sim 9\text{E}+04$  rad/hr to obtain a cumulative gamma dose of  $\sim 100$  Mrad. **Figure 1** shows the modeled dose rate from the Co-60 source to the central bar of glass. The colors shown in the central rectangle indicate expected dose rates of  $\sim 9.15\text{E}+04$  rad/hr (yellow),  $9.45\text{E}+04$  rad/hr (blue) and  $9.75\text{E}+04$  rad/hr (purple). After irradiation exposure several 'slices' of the glass were cut/polished by the SRNL Glass Shop using a wet diamond cut blade and manual polishing aids including SiC, Cerium impregnated discs and 3-9 micron  $\text{Al}_2\text{O}_3$  grinding sheets. Photographs of the  $\sim 800$  grit and  $\sim 8,000$  grit (clear) cross section slides from the unirradiated glass are shown in **Figure 2**. The glass transition temperature of the glasses was measured using Differential Scanning Calorimetry (DSC) with 25 mg portions of (-)200 mesh glass powder (heated from room temperature to  $1200^\circ\text{C}$  in Pt-Rh crucibles under flowing nitrogen. The corrosion test used (-) 100 mesh to (+)200 mesh powder in deionized water at  $90^\circ\text{C}$  via the American Society for Testing Materials (ASTM C1285-14) procedure. Samples of pre- and post-irradiated glass were analyzed using Visible Reflectance spectroscopy, Attenuated Total Reflectance Fourier Transform infrared (ATR-FTIR) spectroscopy and Raman spectroscopy.

## Results/Discussion

The glass-liquid transition for glass is defined as the glass transition,  $T_g$ , and represents the gradual and reversible transition in amorphous materials from a hard and relatively brittle 'glassy' state into a viscous or rubbery state as the temperature is increased. **Figure 3** shows comparison of the pre- and post-irradiated glasses in which the  $T_g$  appears to be the same value of  $\sim 575^\circ\text{C}$  within the range expected for soda-lime glass ( $T_g$  of  $520\text{-}600^\circ\text{C}$ ).

Corrosion testing of the pre- and post-irradiated glass indicates no difference in the 7-day static leach test conducted in triplicate in pure water at  $90^\circ\text{C}$ . **Table 1** presents data from the glass leachate analyses showing that within experimental error of the triplicate tests, all average results for B, Na and Si are similar for the nonirradiated vs. the irradiated glass.

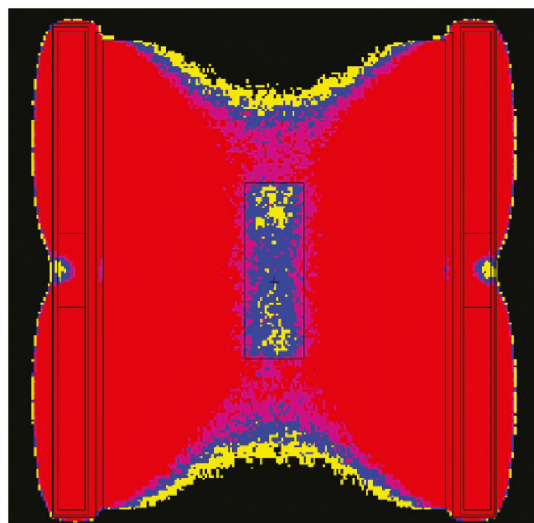


**Figure 1:** Modeled dose rate to the central /vertical glass bar.



**Figure 2:** Low (left) and high (right) polish unirradiated glass cross section specimens.

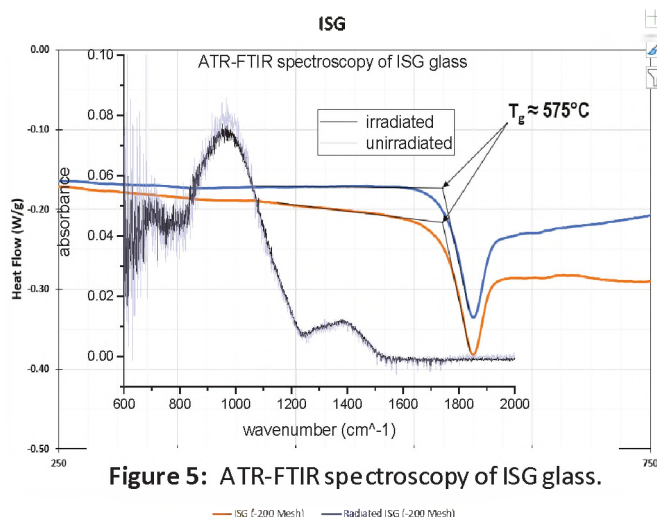


Figure 5: ATR-FTIR spectroscopy of ISG glass.

Figure 3:  $T_g$  determined at the onset by extrapolation.

and measured over the range 400-900 nm. The intensity spectrum of the unirradiated glass sample was used as a reference for calculation of the absorption spectrum of the irradiated glass. Both samples had similar surface finishes, and the specular reflection should be essentially identical. Figure 4 shows the resulting absorbance spectrum from the irradiated glass. The broad absorbance of green, yellow, and orange light, centered at 550-600 nm, is consistent with the lavender/purple appearance of the irradiated glass piece.

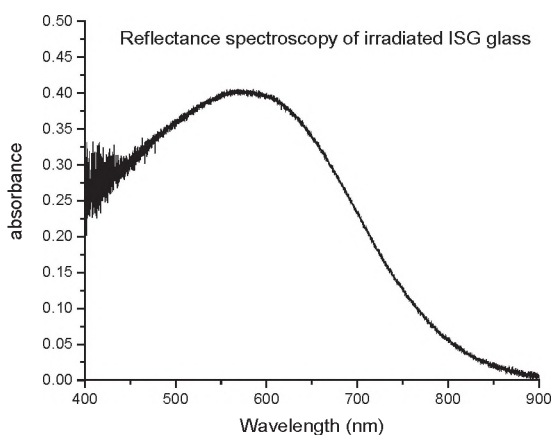


Figure 4: Reflectance spectroscopy of irradiated ISG glass.

changes in the molecular structure. There is a slight diminution of the peak near  $1000\text{ cm}^{-1}$  in the irradiated glass. This region of the spectrum is associated with vibrations of the  $\text{SiO}_4$  tetrahedra; specifically, tetrahedra with different numbers of bridging oxygens appear at different frequencies within the  $900\text{-}1200\text{ cm}^{-1}$  region. The “ $Q_2$ ” (2 bridging oxygens) feature appears near  $1000\text{ cm}^{-1}$ . However, there does not seem to be a corresponding increase in the  $Q_1$  ( $\sim 900\text{ cm}^{-1}$ ) or  $Q_3$  ( $\sim 1085\text{ cm}^{-1}$ ) bands. Additional spectra with improved signal quality would be required to determine if this change is significant.

For Reflectance spectroscopy, slices of the glass logs were positioned under a 6-around-1 optical fiber probe. The glass slices were positioned on top of a 98% absorbing reflectance standard, to reduce the collection of background light passing twice through the glass. The output of a tungsten-halogen source was directed into the center fiber, and the reflected light was collected into the surrounding fiber ring. The reflected light was directed into an Avantes spectrophotometer

Table 1: Corrosion Test Results

	B	Na	Si
NonIrrad. Avg., mg/L	0.130	0.214	0.121
St.Dev., mg/L	0.002	0.003	0.001
%RSD	1.7	1.3	0.8
Irrad. Avg., mg/L	0.129	0.208	0.121
St.Dev., mg/L	0.003	0.008	0.002
%RSD	2.5	3.7	1.6

The ATR-FTIR spectra were obtained on ground glass samples passed through a 200 mesh sieve. This was the finest powder provided and it yielded the best contact with the single-pass ATR crystal. A small pile of glass was placed on top of the crystal. A microscope slide was set on top of the glass, and was pressed down with a small clamp. This technique facilitated the best contact with the crystal and ensured good light absorption. Spectra of the pre- and post-irradiation glasses, between  $600\text{-}2000\text{ cm}^{-1}$ , are shown in Figure 5. The spectra have been scaled to negate any sampling differences.

The spectra of the two glasses shown in Figure 5 are largely the same, suggesting that irradiation has not caused any significant

Raman spectra presented in **Figure 6** for the unirradiated and irradiated glass were obtained on cleaved boule ends, with 100 mW excitation at 785 nm. We chose this excitation wavelength due to the reduced light absorbance in this spectral region compared to other excitation choices (532 nm or 640 nm). There is still some differential absorbance at 785 nm versus the longer wavelengths, which is evident in the obtained spectra (there is comparatively less signal at shorter Raman shifts, which correspond to shorter wavelengths). Spectra here are corrected for intensity throughput of the probe and spectrometer system using a commercially available white light source.

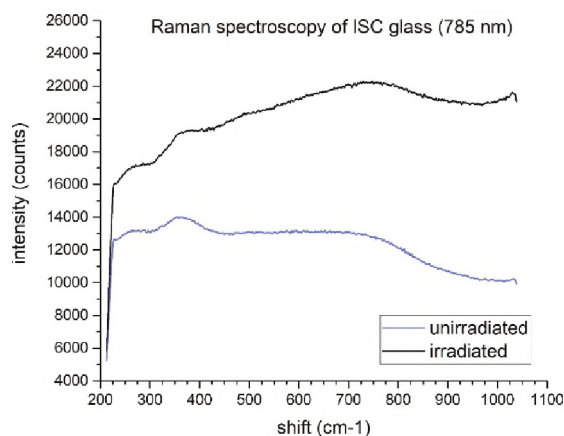


**Figure 6:** Raman spectroscopy of ISG glass.

Qualitatively, the underlying features of the spectra of the two glasses are similar, once varying backgrounds are taken into account. This result is consistent with the minimal change seen for the complementary ATR-FTIR spectra. A more quantitative analysis, based on fitting the features to underlying Gaussian-shaped peaks, will be undertaken when the project is resumed.

## FY2020 Accomplishments

- ISG specimen (500 g bar) was irradiated to a total gamma dose of 100 Mrad
- No potential influence from radiation damage was found relative to measurements pertaining to glass transition,  $T_g$ , aqueous corrosion leaching and optical spectroscopy (FT-IR and Raman)
- Reflectance spectroscopy measured a broad absorption spectrum centered in the range of 550-60 nm that supports the characteristic darkening of the irradiated glass and the lavender/purple appearance of the thin cut glass slides

## Future Directions

A follow-on FY21 Project seedling continuation has been preliminarily approved to extend this current work to acquire higher gamma doses on the existing ISG and to receive/irradiate a revised ISG sample glass that was recently fabricated for national/international study. Collaboration is planned through the Visiting Professor program at SRNL to utilize the expertise and laboratory research resources (photoluminescence spectroscopy) of Professor José A. Jiménez Lugo of Augusta University for the Summer of 2021.

## References

1. S. Gin, A. Abdelouas, L.J. Criscenti, W.L. Ebert, K. Ferrand, T. Geisler, M.T. Harrison, Y. Inagaki, S. Mitsui, K.T. Mueller, J.C. Marra, C.G. Pantano, E.M. Pierce, J.V. Ryan, J.M. Schofield, C.I. Steefel, J.D. Vienna, An international initiative on long-term behavior of high-level nuclear waste glass, *Mater. Today* 16 (2013) 243.
2. A. Goel, J.S. McCloy, R. Pokorny, A.A. Kruger, Challenges with vitrification of Hanford High-Level Waste (HLW) to borosilicate glass – An overview, *J. Non-Cryst. Solids* X 4 (2019) 100033.
3. W.J. Weber, Radiation and thermal ageing of nuclear waste glass, *Proc. Mater. Sci.* 7 (2014) 237.

4. T.C. Kaspar, J.V. Ryan, C.G. Pantano, J. Rice, C. Trivelpiece, N.C. Hyatt, C.L. Corkhill, C. Mann, R.J. Hand, M.A. Kirkham, C.L. Crawford, C.M. Jantzen, J. Du, X. Lu, M.T. Harrison, C. Cushman, M.R. Linford, N.J. Smith, Physical and optical properties of the International Simple Glass, *npj Mater. Degrad.* 3 (2019) 15.

## Acronyms

ISG	International Simple Glass
ASTM	American Society Testing Materials
SRNL	Savannah River National Laboratory
ATR-FTIR	Attenuated Total Reflectance Fourier Transform Infrared
UV-VIS	Ultraviolet-Visible

# NUCLEAR DETERRENT

---

## PROJECTS

Hyperspectral Raman Imaging using a Spatial Heterodyne Spectrometer (SHS)

Hydrogen Process Imaging Using Magnetic Fields

Deuterium Concentration Effects on Cell Cycle Progression

Extremely Durable Graphene Oxide Nanoribbon Reinforced Concrete

Identify Correct Feedbacks for Reinforced Learning in Robotics – Walk by  
Energy Conservation for a Small, Two-Servo Insect Robot

Assessment of Model Cloud Parameterizations for Improved Atmospheric Fate  
and Transport

Localized Electrorefining

## Hyperspectral Raman Imaging using a Spatial Heterodyne Spectrometer (SHS)

**Project Team:** Alicia Fessler, Willis Jones, Robert Lascola, Patrick O'Rourke

**University of South Carolina**

**Collaborator:** Michael Angel

**Project Start Date:** October 1, 2018

**Project End Date:** September 30, 2020

*Savannah River National Lab, and the larger community, has limited chemical-specific imaging (CHI) capabilities, which would be beneficial for remote detection of threat chemicals or use in inaccessible/harsh environments, as well as in-line process monitoring. CHI is underdeveloped due to issues of sensitivity, stable alignment and calibration, and ease of operation associated with most optical instruments. The project objective is to develop a novel, rugged, highly sensitive spectrometer to support real-time, CHI using hyperspectral Raman spectroscopy.*

*Raman spectroscopic analysis will provide chemical specificity and using a spatial heterodyne spectrometer (SHS) will increase the sensitivity due to the high light throughput design. The instrument will be assembled and initially applied to Raman gas detection of the Saltstone disposal unit headspace gas concentrations. Raman gas analysis is the most impacted by sensitivity issues and will be used to demonstrate the increased light collection capability of the SHS over a conventional dispersive spectrometer.*

### FY2020 Objectives

- Set up Holospec f/1.8 spectrometer and run comparison study using H<sub>2</sub> to determine the improved sensitivity for Raman measurements using the SHS
- Demonstrate hyperspectral imaging of relevant samples and develop data analysis/processing algorithms
- Laser stability testing on a UAV to improve understanding of capabilities for using rovers/UAVs for deploying spectroscopic instrumentation

### Introduction

The Spatial Heterodyne Spectrometer (SHS) is a recently developed technology for optical spectroscopy that promises enhanced sensitivity and new opportunities for process and field measurements compared to conventional spectrometers. Sensitivity gains of 10-100x are obtained through light collection over a wide field-of-view and measurement across a two-dimensional detector array. The SHS may provide a faster response time to facilitate process controls and reactions to emerging off-normal conditions, as might be used when monitoring dissolver headspaces for flammability concerns. With no moving parts, a SHS can support the use of typically delicate laboratory instrumentation in a field environment. More novel measurement applications take advantage of the 2D nature of the detection for obtaining images of the scene. One dimension can be used to provide spatial information at the sample, permitting chemically sensitive imaging that can provide real-time determination of chemical distributions. Examples where such information would be valuable include imaging chemical concentration gradients in a process vessel and rapid detection of "residues of interest" across a wide area. With sufficient development, temporal information may also be obtained, permitting tracking of rapidly evolving chemical reactions.

Saltstone disposal unit 6 (SDU6) requires controls to ensure the flammable gas concentration limit for a list of chemicals is not exceeded, left image in Figure 1. Calculated estimates of gas concentrations are very conservative and experimental measurements are needed to provide accurate gas concentrations to fill the tank with the appropriate amount of waste without exceeding the concentration limits. *In-situ* measurements are ideal to provide real-time analysis of the conditions within the tank. However, the current tests require pulling a sample through a sampling loop, right image in Figure 1, and the sampling loop does not work as intended.

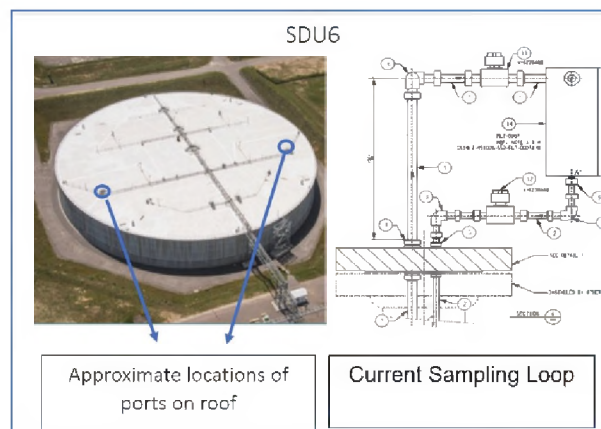


Figure 1: Saltstone Disposal Unit 6 and Sampling Loop.

## Approach

Raman spectroscopy is an optical scattering technique which provides a molecular “fingerprint” of compounds in the solid, liquid, or gas phase. Raman scattering is an inherently weak technique, as only 1 in  $10^8$  photons are Raman scattered. Increasing the irradiance of the laser, the number of molecules excited, or the collection efficiency are ways to improve signal strength. Of these methods, irradiance is often limited by sample photodegradation, and gases have the lowest molecular density of all sample phases which cannot be improved without pre-concentration. Therefore, increasing collection efficiency is the most viable option but has historically had several challenges. Conventional dispersive spectrometers typically obtain high spectral resolution at the cost of low collection efficiency due to the slit-based spectrometer design. Michelson interferometric spectrometers offer large collection efficiency, but wavelength separation is achieved via a moving mirror which must travel large distances (ultraviolet) or in an extremely stable environment (mid-infrared) for high resolution. Both conditions provide challenges for operation in a process or field environment.

A new type of interferometric spectrometer, the spatial heterodyne spectrometer (SHS), has recently been adapted for Raman spectroscopic analysis, Figure 2.<sup>1-6</sup> The instrument offers large collection efficiency and high resolution in a system with no moving parts. With no moving parts, the SHS design promises the ruggedness and stability required for instrumentation being placed in a facility or used in the field. The spectrometer design also allows for monolithic units to be engineered for specific wavelength ranges. As stated above, increasing the collection efficiency is an approach to improve the sensitivity of a Raman measurement technique, and the SHS is a spectrometer that offers large collection efficiencies without compromising resolution or instrument size and stability. We propose to investigate the collection efficiency improvements for gas samples in a backscattering ( $180^\circ$ ) or perpendicular ( $90^\circ$ ) sampling arrangement when using an SHS. Depending on the optical set up, we expect to achieve a collection efficiency 10-100

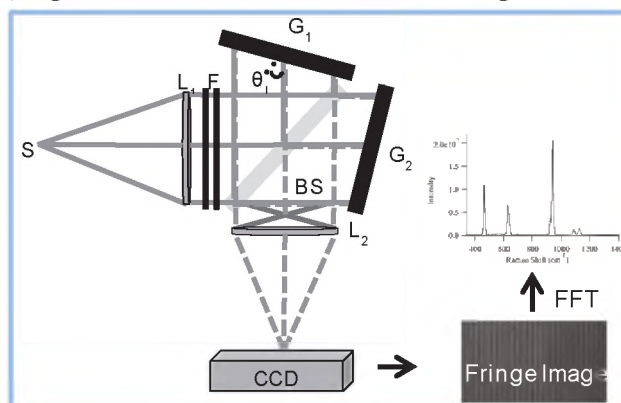
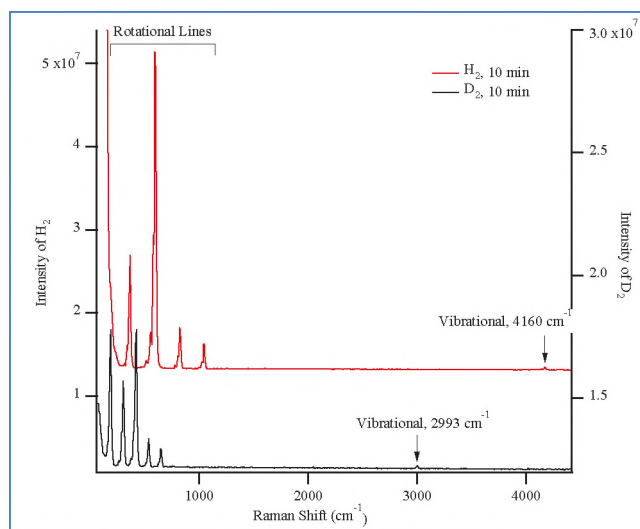


Figure 2: SHRS schematic; fringe image, and Raman spectrum from fast Fourier transform of fringe image.

times larger when using a SHS. The corresponding increases in sensitivity would make Raman spectroscopy a more attractive option for gas monitoring applications such as the SDU headspace analysis for flammable species. Sensitivity improvements could be used to lower detection limits, increase the speed of detection and response, or a combination of the two. The first year of the project focused on building an SHS and assembling a gas sample cell measurement scheme. The collection efficiency study, to compare the SHS to a conventional dispersive spectrometer, was delayed due to issues with measuring Raman spectra. Year two began with troubleshooting the instrument and Raman measurement set-up to determine and fix any issues preventing the collection of Raman spectra followed by optimization of instrument and collection parameters, as well as acquiring first Raman gas phase measurements with the SHS.

## Results/Discussion

The SHS specifications were designed for the Saltstone off-gassing detection of  $H_2$  and  $NH_3$ . The SHS was built to operate in the visible electro-magnetic spectrum using a commercially of the shelf (COTS) laser at 532 nm to take advantage of the increased Raman efficiency at shorter wavelengths. A spectral resolution of  $30\text{ cm}^{-1}$  is more than adequate for discriminating the Raman bands of  $H_2$  ( $540, 655, \text{ and } 4160\text{ cm}^{-1}$ ) and  $NH_3$  ( $934, 967, 3340, \text{ and } 3659\text{ cm}^{-1}$ ),<sup>7-9</sup> thus 50 gr/mm gratings were used to increase the spectral range to cover the entire Raman fingerprint region  $0 - 4200\text{ cm}^{-1}$ . With the new gratings, the rotational and vibrational lines of  $H_2$  and  $D_2$  were measured simultaneously without any spectrometer scanning mechanisms, Figure 3. The spectra in Figure 3 show  $H_2$  and  $D_2$  are easily discriminated, as well as the rotational lines of  $H_2$  and  $D_2$  are 110 and 45 times more intense, respectively, than the vibrational lines. Therefore,  $H_2$  analysis will use the rotational lines to determine the presence of  $H_2$  off-gassing. The SHS system was used to measure the Raman spectra other common gases ( $CO_2, N_2,$  and air) to demonstrate capability to discriminate various gases, Figure 4.



**Figure 3:** Raman spectra of  $H_2$  (red) and  $D_2$  (black) measured using 1.4 W, 532 nm laser for 10 min. Full spectral range with no moving parts in the spectrometer. Spectra offset for clarity.

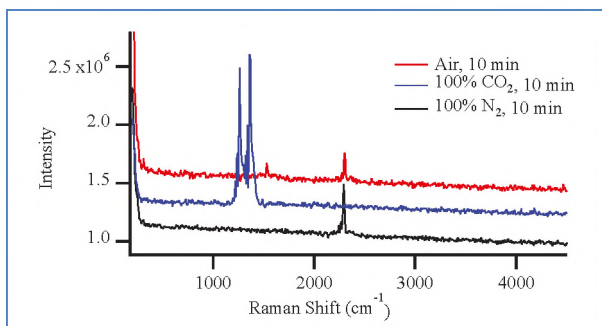


**Figure 4:** Representative Raman spectra of air (red), CO<sub>2</sub> (blue), and N<sub>2</sub> (black) measured using 1.4 W, 532 nm laser for 10 min. Spectra offset for clarity.

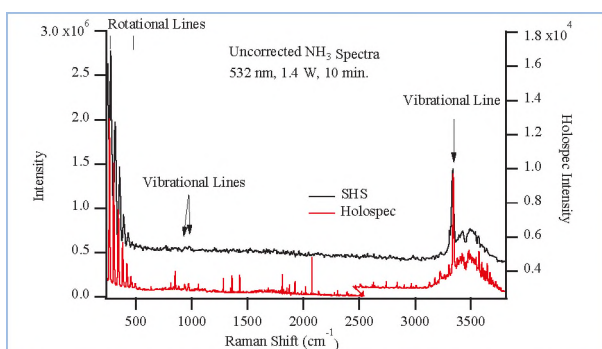


**Figure 5:** Raman spectra of NH<sub>3</sub> measured using the SHS (black) and Holospec (red) using 1.4 W, 532 nm laser for 10 min. Spectra offset for clarity.

Pure NH<sub>3</sub> and 1% H<sub>2</sub> were measured using the SHS and a Holospec f/1.8 commercial dispersive spectrometer to compare the performance. The uncorrected Raman spectra of NH<sub>3</sub> measured using each instrument are shown in Figure 5. The H<sub>2</sub> data is not shown here. The resolution for the Holospec at the 343 cm<sup>-1</sup> rotational band was ~6.4 cm<sup>-1</sup>, while the SHS resolution was 21 cm<sup>-1</sup>. The result is expected as the grating used in the Holospec is a higher groove density than the SHS gratings. Despite the lower resolution using the SHS, all the spectral features necessary for discrimination and detection are discernable. To make a fair comparison of signal collection, the Holospec NH<sub>3</sub> and H<sub>2</sub> data were corrected for differences in detector settings and quantum efficiencies. The SHS exhibited 7-8 times higher signal than the Holospec for each analyte. Due to differences in noise distribution, only an estimate of the signal-to-noise ratios (SNR) were calculated and showed the Holospec SNR was 3 times better than the SHS. However, the Holospec data was riddled with hot pixels and gamma rays as can be seen when comparing the flat areas of spectrum in the SHS data to Holospec data. The 1% H<sub>2</sub> Holospec spectrum was difficult to discern amid the hot pixels and gamma rays and required background correction to see the Raman peaks clearly.

The comparison between the two spectrometers shows the SHS collects more light at sufficient SNR in a compact system capable of easier field deployment.

To determine if the SHS could be used on an unmanned aerial vehicle (UAV) for field analysis such as plume detection, a laser was attached to a Typhoon UAV and the pointing stability was measured 9 m from a target, Figure 6. Laser pointing stability is important when using spectroscopic systems, because the illuminated sample signal must reach the spectrometer for analysis. Consequently, if the laser cannot be held in a defined area, then the signal will be lost. Given the large etendue of the SHS, the system can measure the signal over an approximately 480 mm diameter at 9 m. The laser pointing stability test demonstrated the Typhoon UAV could hold the laser within a 76 mm diameter, which is 6 times smaller than the SHS viewing limits. Recently a monolithic SHS was demonstrated for Raman spectroscopy by the Angel group at USC, and the SHS weighed 80 g.<sup>7</sup> A high-quality lens, low-noise spectroscopy camera, and other necessary parts for collecting the Raman-scattered light along with the SHS would weight ~3 kg. Commercial UAVs payloads range from 4 g to 220 kg.<sup>8</sup> Therefore, the SHS could be used with a commercial UAV with the proper weight payload capacity.

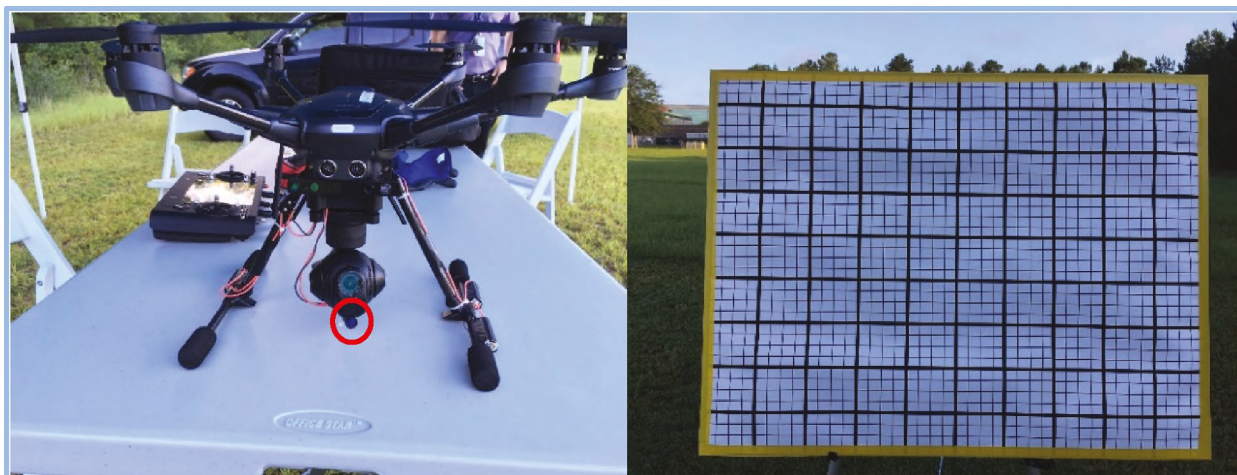


**Figure 6:** UAV laser pointing stability test drone (left) and target (right). The laser (circled in red) was attached to the drone camera, and the camera recorded the laser spot on the target.

## FY2020 Accomplishments

- SHS was demonstrated to measure down to 1% H<sub>2</sub> and should be able to measure 5 times less NH<sub>3</sub>. The flammability limit is 4%, so the SHS can detect the H<sub>2</sub> concentration before the limit is reached
- The SHS collected 7-8 times more light than a commercial dispersive system with an SNR 3 times lower
- A laser pointing stability test on a UAV was performed to determine if the UAV was stable enough to allow for aerial measurements using the SHS. The large etendue of the SHS provides a viewable diameter ~6 times that of the pointing stability of the laser. The lightweight payload of the spectroscopic system is compatible with the weight limits of commercial UAVs

## Future Directions

- Writing publication with collected data
- Exploring external funding sources

## FY 2020 Peer-reviewed/Non Peer-reviewed Publications

- Fessler, K. Alicia Strange; Waldron, Abigail; Colon, Arelis; Carter, Chance; Angel, Stanley. "A Demonstration of Spatial Heterodyne Spectrometers for Remote LIBS, Raman, Spectroscopy, and 1D Imaging." *Spectrochimica Acta B*. Invited paper. Submitted 09/14/2020.

## References

1. Gomer, N.R.; Gordon, C.M.; Lucey, P.; Sharma, S.K.; Carter, J.C.; Angel, S.M.; Raman Spectroscopy using a Spatial Heterodyne Spectrometer: Proof of Concept, *Appl. Spectrosc.* **2011**, *65*(8), 849-857.
2. Lamsal, N.; Angel, S.M.; Deep-Ultraviolet Raman Measurements using a Spatial Heterodyne Raman Spectrometer (SHS), *Appl. Spectrosc.*, **2015**, *69*(5), 525-534.
3. Barnett, P.D.; Angel, S.M.; Miniature Spatial Heterodyne Raman Spectrometer with a Cell Phone Camera Detector, *Appl. Spectrosc.*, **2017**, *71*(5); 988-995.

4. Barnett, P.D.; Strange, K.A.; Angel, S.M.; Improving Spectral Results through Row-by-Row Fourier Transform of Spatial Heterodyne Raman Spectrometer Interferogram, *Appl. Spectrosc.*, **2017**, *71*(6), 1380-1386.
5. Fessler, K. A.; Waldron, A.; Colon, A.; Carter, C.; Angel, S.; A Demonstration of Spatial Heterodyne Spectrometers for Remote LIBS, Raman, Spectroscopy, and 1D Imaging; *Spectrochimica Acta B*; Submitted 09/14/2020.
6. Strange, K.A.; Paul, K.C.; Angel, S.M.; Transmission Raman Measurements using a Spatial Heterodyne Raman Spectrometer; *Appl. Spectrosc.*, **2017**, *71*(2); 250-257.
7. Waldron, A.; Allen, A.; Colon, A.; Carter, J.C.; Angel, S.M.; A Monolithic Spatial Heterodyne Raman Spectrometer: Initial Tests; *Appl. Spectrosc.*; **2020**, Available Online.
8. Poljak, M.; How Much Weight can a Drone Carry. Drone Tech Planet.  
<https://www.dronetechplanet.com/how-much-weight-can-a-drone-carry/>

## Acronyms

CHI	Chemical-Specific Imaging
SDU	Saltstone Disposal Unit
SHS	Spatial Heterodyne Spectrometer
SNR	Signal-to-Noise Ratio
SRNL	Savannah River National Laboratory
UAV	Unmanned Aerial Vehicle
USC	University of South Carolina

## Intellectual Property

- SRS-19-008: *Static Electric Field Detection Using Raman Spectroscopy to Measure the Depolarization Ratio of Gas Molecules Influenced by Dielectrophoretic Forces*
- SRS-19-011: *Detector Mount of Plane Arrays in Optical Spectroscopic Measurement Systems*

## Hydrogen Process Imaging Using Magnetic Fields

**Project Team:** G. Larsen, K. Nguyen, K. Shanahan, Holly Ray, T. Guin

**University of Georgia Collaborators:**  
Hoang Luong, Minh Pham

**Project Start Date:** October 1, 2018

**Project End Date:** September 30, 2020

*The goal of this project is to develop a system that uses small magnetic fields to spatially and temporally determine the amount of hydrogen stored on a metal hydride bed within a processing facility environment. Such a capability does not currently exist – hydride beds are essentially “black boxes.” Therefore, a magnetic hydrogen measurement system would be a unique tool to assess and optimize the performance of these critical hydrogen processing components. Magnetic*

*characterization is also a promising technique for measuring hydrogen content in metal hydrides on the microscopic scale using magneto-optical techniques. The research will investigate these issues to develop a hydride imaging for both bulk and microscopic scale to improve hydrogen processing.*

### FY2020 Objectives

- Evaluate the effects of parameter variation on magnetic measurements of hydrides
- Incorporate knowledge gained to develop an imaging system using bulk measurements and magneto-optical effects
- Investigate hydrogen-induced modulation of novel phenomena, such as spin transport and plasmonic excitation, for the purpose of hydrogen detection and other applications

### Introduction

Metal containers safely enclose hazardous materials and energies, but their opacity and conductivity limit the types of signals that can be used for chemical process measurement, imaging, and optimization. Magnetic fields are among the few physical phenomena that can easily penetrate through both insulating materials and metallic materials, such as stainless steel, aluminum, and others. Therefore, magnetic fields could be used to probe the contents of chemical process vessels made from such materials. For example, researchers from the University College London and the Atomic Weapons Establishment (AWE) have recently shown that is possible to collect magnetic images of conductive objects, even when fully enclosed inside of two metallic ferromagnetic containers.<sup>1</sup>

The degree to which a magnetic field interacts with a system depends on several factors, including chemical and electronic states, and this can reveal underlying chemical processes. One example is when a metal absorbs hydrogen, an electron is transferred from the absorbed hydrogen to the metal lattice. Depending on the original electronic configuration of the metal, these donated electrons will cause the metal to respond less strongly (e.g., Pd, LANA.75) or more strongly (e.g., Pu, U) to an applied magnetic field, and the response will scale with total amount of hydrogen absorbed.<sup>2-5</sup> In this way, magnetic measurements can be used to detect hydrogen content of metals, even when they are enclosed inside of containers.

Magnetic characterization is a promising method for tracking and trending hydrogen adsorption on metal hydride beds, and unlike neutron imaging,<sup>6</sup> it could be straightforward to adapt the technique to applications outside of the laboratory. However, additional research is needed to demonstrate the use of magnetic measurements for assessing and imaging hydrides in process environments. Additionally, in-situ measurements of hydrogen loading on the microscopic scale are challenging, and the use of magneto-optical techniques could enable localized imaging of metal-hydrogen systems that have previously escaped visualization. The goal of this research project was to establish the practicality of these concepts.

## Approach

The main thrust of the project was to measure the magnetic and magneto-optical properties of metals in the presence of hydrogen. This was accomplished using AC susceptibility and a magneto-optical Kerr effect (MOKE) systems. These experimental geometries were adapted to Sieverts techniques during hydrogen sorption experiments. The effects of hydrogen process variations (e.g., isotope, temperature, aging) have on magnetic properties of metals and hydrides were investigated. These experiments informed the development of imaging systems that utilize changes in magnetic properties for visualization of hydrogen content (**Figure 1**). Finally, the knowledge gained from these experiments were extended to the develop novel technologies and sensors that used the hydrogen-induced changes in nanomaterials as signal transduction method.

## Results/Discussion

The objectives for this fiscal year have all been met. Process effects on hydride materials were examined. The magnetic susceptibility of LANA.75 follows a purely Curie-Weiss behavior for  $T \geq 150$  K, and changes on the order of 0.1%/K. However, significant changes were observed in the magnetic susceptibility of LANA.75 over several cycles, even though the isothermal behavior did not change. Magnetic-optical measurements of Pd showed no isotopic dependence for protium and deuterium. Thus, the effects of temperature were not significant impediments to implementation, but the variation due to aging will need to be overcome. Similar aging effects were not observed in palladium-based nanoparticles, and the changes to LANA.75 are likely attributed to morphological changes and dealloying.

Imaging of hydrogen absorption and desorption in real-time was accomplished via MOKE measurements. A bulk magnetic AC susceptibility imaging system was created and demonstrated the ability to characterize magnetic behavior of material stored inside of two metal containment vessels. These results demonstrate the project goals of imaging hydrides during operation. Finally, based on the concepts and materials investigated here, several advanced hydrogen sensor platforms were developed, with some

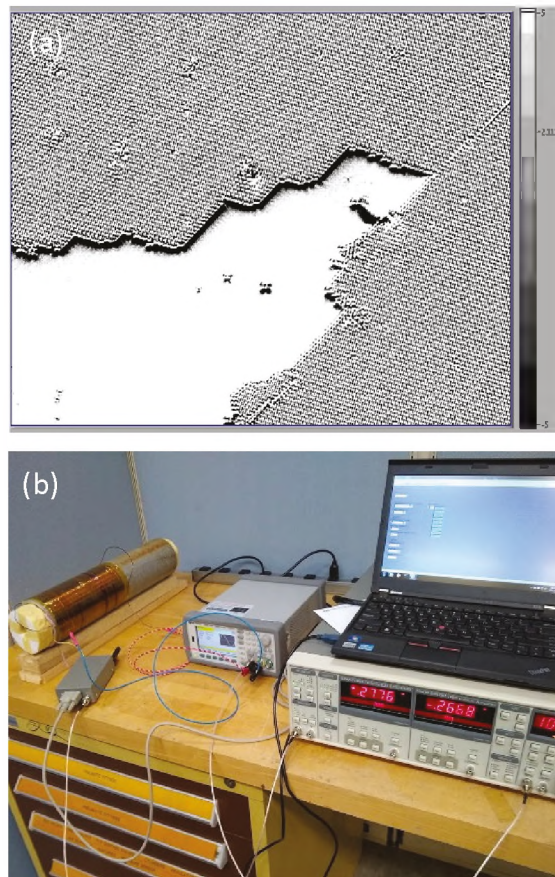


**Figure 1:** (a) Magneto-optical image of a PdCo nanoparticle array during hydrogen loading. (b) Magnetic susceptibility system designed to image through steel vessels.

achieving record-breaking response times and sensitivities. Further, these sensors were protected by encapsulation in a polymer layer, preventing negative effects due to surface poisons and making them relevant to real world applications.

## FY2020 Accomplishments

- Demonstrated microscopic imaging of hydrogen-metal interactions
- Demonstrated bulk one-dimensional magnetic imaging through two solid steel vessels
- Developed new ultrafast hydrogen sensors with a record response times with ppb and sub-ppb level detection capabilities

## Future Directions

Execution of this project revealed several promising directions for continued productive exploration. Development of these concepts and identification additional sponsors of this work will be pursued. A proposal that emerged from the concepts developed in this project has already been selected for funding in FY21.

## Publications

1. Pham, M. T.; Luong, H. M.; Pham, H. T.; Guin, T; Larsen, G. K.; Nguyen, T. D. Achieving ppb Detection Limit and Second Response Time in Highly Stable Hydrogen Electric Nanosensors (*submitted, Advanced Materials*).
2. Luong, H. M.; Pham, M. T.; Guin, T; Madhogaria, R. P.; Phan, M. H.; Larsen, G. K.; Nguyen, T. D. Optical Hydrogen Sensors with Sub-second Response and ppm Detection Limit Using Nano-patchy Particle Array (*under consideration, Nature Nanotechnology*).
3. Luong, H. M.; Pham, M. T.; Madhogaria, R. P.; Phan, M. H.; Larsen, G. K.; Nguyen, T. D. Bilayer plasmonic nano-lattices for tunable hydrogen sensing platform. *Nano Energy*, **2020**, *71*, 104558.
4. Pham, M. T.; Amerling, E.; Luong, H. M.; Pham, H. T.; Larsen, G. K.; Whittaker-Brooks, L.; Nguyen, T. D. Origin of Rashba Spin-Orbit Coupling in 2D and 3D Lead Iodide Perovskites. *Sci. Reports* **2020**, *10*(1), 1-10.

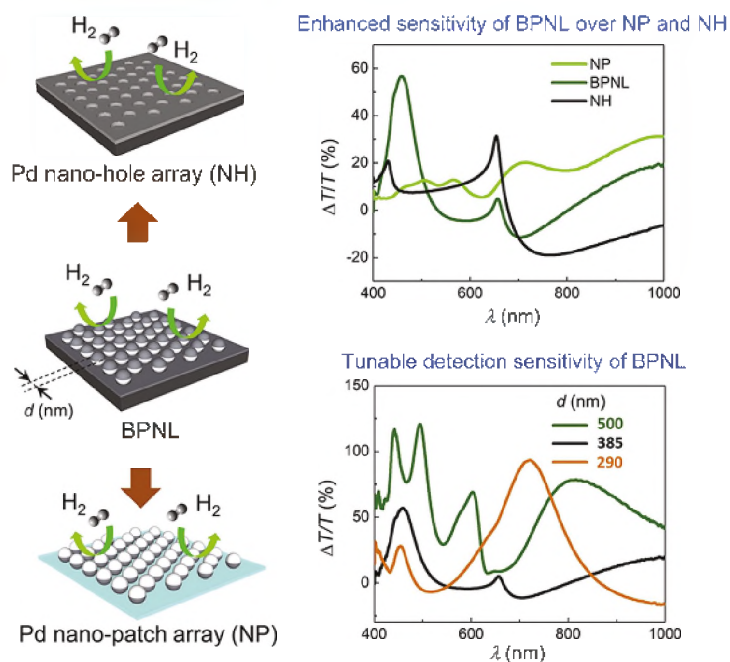


**Figure 2:** Graphical abstract illustrating the concept of one of the hydrogen sensing platforms developed during this project

## References

1. Darrer, B. J.; Watson, J. C.; Bartlett, P.; Renzoni, F., Magnetic Imaging: a New Tool for UK National Nuclear Security. *Scientific Reports* **2015**, *5*, 7944.
2. Termsuksawad, P.; Niyomsoan, S.; Goldfarb, R.; Kaydanov, V.; Olson, D.; Mishra, B.; Gavra, Z., Measurement of hydrogen in alloys by magnetic and electronic techniques. *J. Alloys Compd.* **2004**, *373* (1), 86-95.
3. Akamaru, S.; Hara, M.; Matsuyama, M., In situ measurement of alternating current magnetic susceptibility of Pd–hydrogen system for determination of hydrogen concentration in bulk. *Rev. Sci. Instrum.* **2012**, *83* (7), 075102.
4. Kim, J. W.; Mun, E.; Baiardo, J.; Smith, A.; Richmond, S.; Mitchell, J.; Schwartz, D.; Zapf, V.; Mielke, C., Detecting low concentrations of plutonium hydride with magnetization measurements. *J. Appl. Phys.* **2015**, *117* (5), 053905.
5. Gruen, D. M., Magnetic Properties of Uranium Hydride. *The Journal of Chemical Physics* **1955**, *23* (9), 1708-1710.
6. Jacobson, D. L.; Hussey, D. S.; Baltic, E.; Udovic, T. J.; Rush, J. J.; Bowman, R. C., Neutron imaging studies of metal-hydride storage beds. *Int. J. Hydrogen Energy* **2010**, *35* (23), 12837-12845.

## Acronyms

AWE	Atomic Weapons Establishment
LANA.75	lanthanum nickel aluminum alloy
MOKE	Magneto-optical Kerr effect

## Intellectual Property

Invention Disclosure: “Hydrogen Gas Sensors Using Magneto-Plasmonic Nanolattices”

## Deuterium Concentration Effects on Cell Cycle Progression

**Project Team:** Wendy Kuhne,  
Candace J. Langan, Lucas Angelette

**Augusta University Collaborator:**  
Lesleyann Hawthorne

**Project Start Date:** October 1, 2019  
**Project End Date:** August 21, 2020

*Deuterium (D), which is found in natural water at ~ 150 ppm, seems to play an important role in biology. For example, D concentrations above 150 ppm are known to produce toxic effects in many organisms. There is also evidence to suggest D levels significantly less than 150 ppm can cause delays in progression through the normal mitotic cell cycle. Some have even theorized that the D:H ratio in cells may impact an organism's radiation resistance. Therefore, evaluating the role of D and the D:H ratio in eukaryotic and prokaryotic cells should lead to a better understanding of cell cycle progression and radiation resistance in these organisms.*

*Research in this field has likely been stalled by the limited availability of D<sub>2</sub>O with varying D concentrations needed to accurately study the deuterium effects. However, SRNL can currently manufacture D<sub>2</sub>O in varying concentrations, and we have assembled a unique team of radiation biologists, microbiologists, radiochemists, and health physics to form an interdisciplinary research group to study the cell cycle as a function of D concentration in order to address several fundamental science questions. Proposed work in FY20 was a collaborative effort with Augusta University to utilize BSL-2 mammalian cell lines. Lab work was halted due to the COVID-19 pandemic. An intensive literature review was performed and identified pertinent knowledge gaps that could be filled in future research efforts.*

### FY2020 Objectives

- Generation of deuterium depleted water (D<sub>2</sub>O) for cell culture studies in concentrations of 50, 75, 100, 124 and 140 ppm). Additional D<sub>2</sub>O above 150 ppm was also generated
- Perform initial cell culture survival studies and measure effects to cell cycle progression
- During cell culture survival studies, measure D<sub>2</sub>O concentrations to ensure levels are maintained throughout the study using the PICARRO and measure changes to the cell culture media via ICP- MS

### Introduction

Investigation into the effect of deuterium depleted water (DDW) on biological systems began less than 20 years ago.<sup>1</sup> Much of the published literature has focused on the effect of DDW on the phenotypic growth of normal/stem cells, tumor transplantation models, and tumor cell systems, with little emphasis on molecular mechanisms involved.<sup>2</sup> The few studies that attempt to investigate the effect of DDW on normal eukaryotic cells are either under hypoxic conditions, are poorly controlled and are ultimately largely uninformative.<sup>3</sup> The lack of information in this regard creates an opportunity to investigate and understand the mechanisms associated with why cell cycle is delayed under DDW conditions in a controlled manner.

The role of D in biology is thought to be a missing piece in understanding cancer and cancer epidemics in western populations. Little has been revealed on the time-dependent effects of DDW on normal/cancer human cells or how the reduction of cell growth/proliferation is associated with cell cycle regulation/consequence on gene expression. Many different genes are involved in cell cycle regulation and activation of specific genes dictates response to cell proliferation (Figure 1).

The purpose of the project is to unravel the novel mechanisms involved with the effect of DDW, in differing



## FY2020 Accomplishments

- Intensive literature review was completed and it was determined that significant knowledge gap exists and future work should focus on 1) the time-dependent effects of DDW on normal/cancer human cells and 2) investigate if a reduction of cell growth/proliferation is associated with cell cycle regulation/consequence on gene expression
- Bio Safety Level 2 laboratory space has been identified and is under review by SRS Bio Safety Committee for FY21

## Future Directions

- Obtain cell cultures from approved vendors (example; ATCC)
- Experimental approaches described in FY20 will be completed in FY21 at SRNL

## References

1. Hohlefelder, L. S.; Heavy water reduces GFP expression in prokaryotic cell-free assay at the translation level while stimulating its transcription *BioMed Research International* **2013**, 1-9.
2. Basov, A., L. F., Baryshev, M.; Dzhimak, S.; Deuterium-Depleted Water Influence on the Isotope 2H/1H Regulation in Body and Individual Adaptation. *Nutrients* **2019**, 11 (8), 1903.
3. Zlatska, O.V.; D. Z., Vasyliiev, R.; Syroeshkin, A.; Zlatskiy, I.; Deuterium Effect on Proliferation and Clonogenic Potential of Human Dermal Fibroblasts In Vitro. *Problems of Cryobiology and Cryomedicine* **2018**.
4. Bild, W.; Haulica, I.; Lupușoru, C.; Titeșcu, G.; Iliescu, R.; Nastasa, V.; Research Concerning the Radioprotective and Immunostimulating Effects of Deuterium-Depleted Water. *Romanian journal of physiology: physiological sciences* **1999**, 36 (3-4), 205-218.

## Acronyms

D	Deuterium
D2O	Deuterium Oxide
DDW	Deuterium Depleted Water
L	Liter
μg	Microgram (one millionth of a gram)
mg	Milligram (one thousandth of a gram)
ppb	Parts per billion (μg/L)
ppm	Parts per million (mg/L)

## Extremely Durable Graphene Oxide Nanoribbon Reinforced Concrete

**Project Team:** Christine Langton, Jay Gaillard, J. Meany, E. Hansen, M. Elvington

**University of South Carolina**  
**Collaborator:** Fabio Matta

**Project Start Date:** October 1, 2019  
**Project End Date:** September 30,

*Reinforced concrete makes up a very large component of the US Departments of Energy, Transportation, and Defense infrastructure. Improving concrete durability and mechanical properties are universally recognized needs for concrete produced by conventional methods and 3D printed robotic construction/fabrication methods. This research evaluated the potential for the addition of partially unzipped multiwall carbon tubes and graphene oxide ribbons to enhance durability of conventionally placed concrete. Improved performance results from: (1) arresting microcrack*

*propagation and bridging cracks that transport moisture and corrosive chemicals, (2) reducing surface loss/damage due to abrasion, and (3) reducing cracks due to loading by strengthening the matrix. Enhancements will reduce life cycle cost (less maintenance, longer service life) and reduce resource consumption and embedded energy. Multi-scale, carbon-based reinforcement of cementitious composites, including cast concrete and printed concrete, can be commercialized in the near-term (2-10 years) with successful demonstration of: performance, implementation of first-generation solutions, and minimal modification of existing codes and standards.*

### FY2020 Objectives

The technical objectives of the proposed research were to:

- Develop a new class of multi-functional concrete component admixtures, based on a physically stable GONR-aqueous suspension, that imparts enhanced matrix nano-reinforcement, microcrack sealing, reduction in permeability, and surface abrasion resistance to concrete
- Demonstrate scalable synthesis of the GONRs and scale-up of the aqueous suspension
- Demonstrate the effectiveness of this new class of admixtures in average and high-performance cement paste, grout, and concrete, and advanced mix designs for 3D printed paste and concrete

### Introduction

Concrete is the most widely used construction material in the world. Strength, workability, and durability govern design specifications. Multiwall carbon nanotube (MWCNT) addition to concrete to improve these properties has been recently commercialized. In comparison to MWCTs, partially unzipped carbon nanotubes (PUCNTs) and graphene oxide nanoribbons (GONRs) have superior mechanical, physical and chemical compatibility properties. Although PUCNTs and GONRs currently are more expensive to produce than graphene and CNTs, PUCNTs and GONRs are expected to be more effective at lower concentrations due their high surface areas and aspect ratios. Therefore, they are expected to have a greater impact on concrete durability per unit mass compared to other carbon-based additives. PUCNT and GONR amended concretes have the potential to be a transformational technology and lead to a new generation of commercially viable concrete nano-reinforcement technologies.

This project adds to SRNL's technical leadership in concrete durability and will promote SRNL in the field of inorganic GONR-composite materials. An invention disclosure has been prepared for a GONR concrete component product, a GONR-aqueous suspension that is expected to be beneficial to both high performance and conventional concrete. Future funding opportunities beyond durable concrete are expected for exploring potential applications of GONR for its thermal and electrical conductivity properties to produce unique composite cement-based materials. Printed concrete is a rapidly developing technology and offers funding opportunities and collaboration with universities to design, print, and evaluate these new multi-level reinforced materials. See Figure 1.

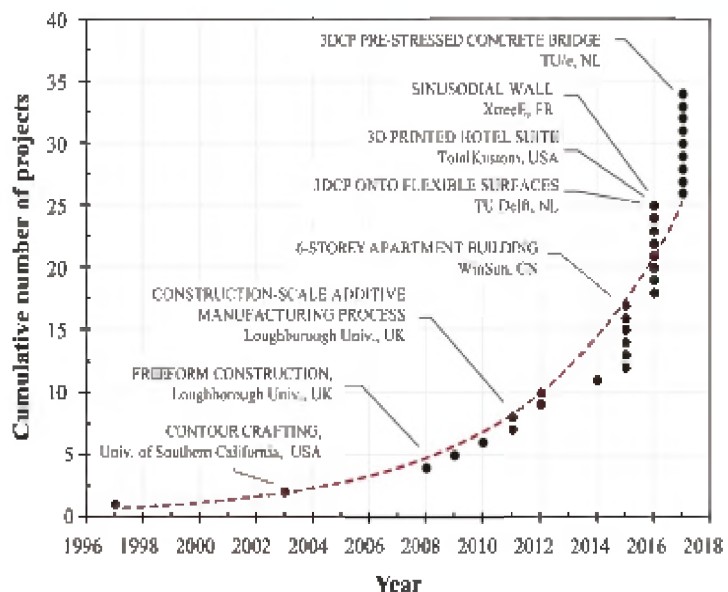


Figure 1: Printed concrete projects vs time.

## Approach

The technical approach consisted of:

- Developing a method for synthesizing PUCNTs and GONRs from MWCTs using a modified Hummer's method
- Scaling the method to produce enough material for detailed characterization, cement-composite sample preparation and mechanical and hydraulic property testing
- Designing and testing a cement-water paste control mix
- Evaluating carbon nanoparticle dispersibility in water and cement paste
- Optimizing nanoparticle loading on mechanical and hydraulic properties of cast specimens both of which affect durability
- Evaluating the effect of nanoparticle morphology and aspect ratio on mechanical and hydraulic properties of cast specimens
- Developing mix designs with and without nanoparticles for printed cement paste
- Procuring mixing and printing equipment to print mortar and concrete test specimens
- Documenting results

A multi-disciplinary, multi-institutional team was assembled to design and carry out this research program. Capabilities, equipment, expertise was leveraged to produce results and 3 to 5 manuscripts over two years. The approach was modified to account for 2020 COVID-related restrictions which limited access to laboratory facilities at both SRNL and USC.

## Results/Discussion

PUCNT with oxygen contents of at least 30 percent were synthesized for this project and were shown to be very stable in aqueous suspensions which makes them an excellent candidate for incorporation in concrete admixture products, Figure 2.<sup>1</sup> Dynamic light scattering results for the PUCNT suspensions are shown in Figure 3.

Compressive strength and elastic stiffness (resistance of matrix when force is exerted) results for Portland cement paste control samples and composite samples containing three PUCNT loadings cured for 7, 14, and 28 days are shown in Figure 4.<sup>2-6</sup> **A 29 % increase in average compressive strength and a 25 % increase in elastic stiffness were measured for samples containing the 0.05 wt. % PUCNT loading compared to control samples with no PUCNTs.** See Figure 4. The improvement in mechanical properties of the cement paste composites containing 0.005 wt. % PUCNTs was attributed to the superior dispersibility of the oxygen functionalized PUCNTs in water at this concentration compared that in the 0.05 wt.% suspension in which agglomeration was detected.<sup>7</sup> Figure 5 illustrates the morphology and relative size of the PUCNTs in the Portland cement matrix cured for 28 days.

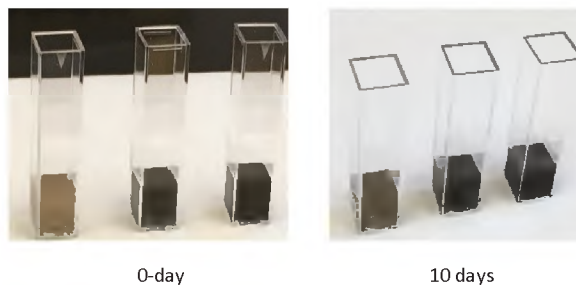


**Figure 2:** PUCNT-aqueous suspensions after sonication:

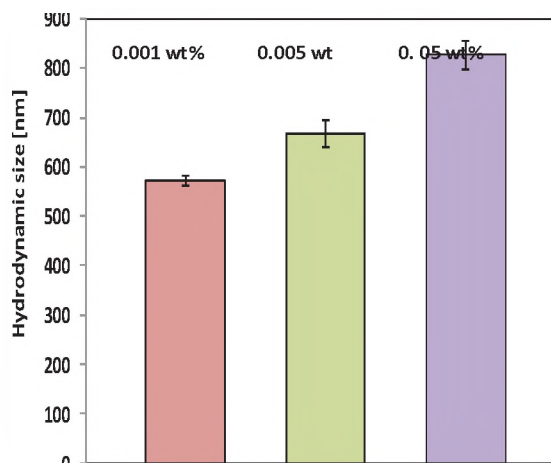


**Figure 3:** PUCNT Hydrodynamic Particle Size by Dynamic Light Scattering as a function of GNR concentration in aqueous suspensions.

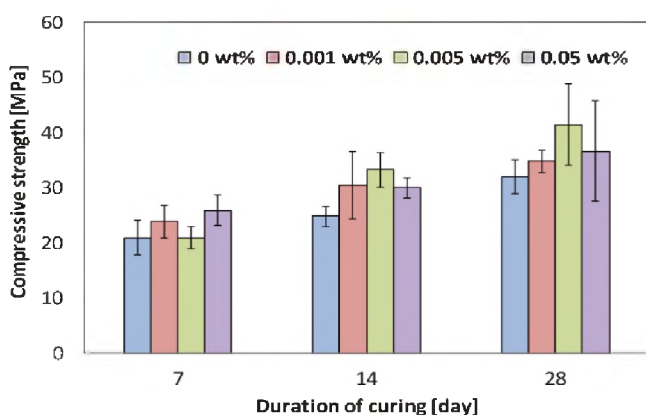


**Figure 4:** Compressive strength of control and PUCNT composite Portland cement pastes as a function of time and PUCNT content.

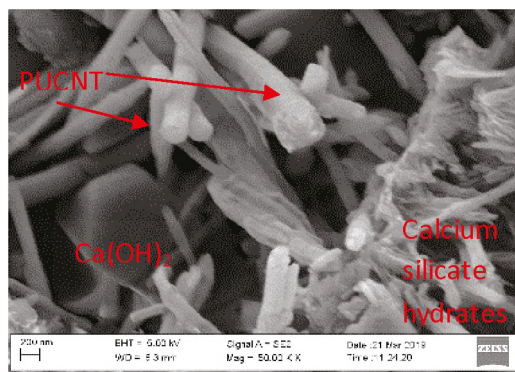


**Figure 5:** SEM image of fractured surface illustrating PUCNTs in Portland cement matrix cured for 28 days.

In addition to synthesizing oxygen functionalized PUCNTs, considerable effort was spent to synthesize GONRs with high oxygen functionality and high aspect ratios from MWCNTs. The unique morphologies of

GONRs prepared in three trial batches are illustrated in Figure 6. All three of these GONRs were synthesized by slightly different modifications of the Hummers method and form very stable aqueous suspensions. Consequently, they can be included in a wide range of commercial concrete and mortar admixtures as matrix reinforcement components which greatly simplifies addition under large scale batching conditions. Based on PUNCT-paste composites, they are expected to be easily dispersed in cement pastes, mortars and concretes with normal and low water to cement ratios (0.5 to 0.35).

Based on morphology, particle size and dispersibility (oxygen functionalization of 32 to 38 atomic % oxygen), they are also expected to be dispersible and very compatible in printed paste, mortar and concrete formulations which have unique fresh property/rheological requirements. Based on morphology and expected dispersibility, they are also expected to provide superior matrix reinforcement, crack bridging, and surface wear resistance for printed cementitious composites. These new GONRs fill a gap in reinforcement of multi-scale reinforcement materials used for cementitious composites. They have superior mechanical strength, morphologies, and hydrophilic properties compared to other reinforcement materials currently in use. These GONRs have not been fully characterized or evaluated in cement paste-GONR composites to date.



**Figure 6:** Examples of GONRs synthesized by three different syntheses based on the Hummer's method. These GONRs have 32 to 38 % oxygen functionality, form stable aqueous suspensions and are expected to provide better cement paste reinforcement than PUCNTs based on morphology and high aspect ratio.

## FY2020 Accomplishments

The accomplishments to date are listed below:

- PUCNTs with oxygen functionalities of 30 to 50 % oxygen for stable suspensions which makes them good candidates for further development of commercial concrete admixtures for matrix strengthening, crack bridging, and reducing surface wear abrasion
- PUCNT suspensions have excellent dispersibility in water and cement paste
- PUCNT-Portland cement composite samples resulted in an average compressive strength increase of 29 % and average elastic stiffness increase of 25 % compared to Portland cement-only control samples. The PUCNT loadings that resulted in these mechanical property improvements were 10X lower than loadings typically reported for graphene (0.005 vs 0.05 wt.% of the cement). The lower loadings may offset the additional PUCNT/GONR production cost
- The new class of GONRs were synthesized from high aspect ratio MWCNTs which form very stable aqueous suspensions and are expected to improve the mechanical properties and reinforce the matrix of composite cement paste and concrete based on morphology, aspect ratio, and oxygen functionality
- Attachments needed to print cement paste on the HYREL printer (SRNL user facility) were purchased and cement paste formulations were printed using this printer
- Equipment for 3-D printing mortar and concrete, a pug mill mixer and SCARA printer, were purchased and are partially set up

## Future Directions

Funding opportunities will be sought to continue work on GONR-cement composites and to utilize the results to design, test, and evaluate durability and life-cycle extension for GONR-mortars and -concretes.

Funding opportunities will also be sought to continue mix designs for 3-D printed mortars and concrete. The 3-D printing equipment acquired for this project, university and industry contacts made as the result of this task will be leveraged to develop scope for the SRNL Additive Manufacturing Initiative.

## Publications

- Manuscript Submitted to *Cement, Concrete Composites*, Impact Score 6.257: “Effect of Adding Low Concentrations of Partially Unzipped Carbon Nanotubes on Nano-Micro-Structural and Mechanical Properties of Cement Past” S. Iffat,<sup>1</sup> M. Skder,<sup>1</sup> M. Baalousha,<sup>1</sup> M. Elvington,<sup>2</sup> P. Tinkey,<sup>2</sup> J. Gaillard,<sup>2</sup> F. Matta,<sup>1</sup> (<sup>1</sup>USC, <sup>2</sup>SRNL). SRNL is corresponding author.
- Manuscript being Drafted for Publication: “Effect of Oxygen Functionalized - Carboxyl Modified - Partially Unzipped Carbon Nanotubes on Properties of Cement Paste”, F. Matta,<sup>1</sup> S. Iffat,<sup>1</sup> C. Langton,<sup>2</sup> J. Meany,<sup>2</sup> M. Elvington,<sup>2</sup> J. Gaillard.<sup>2</sup> (<sup>1</sup>USC, <sup>2</sup>SRNL). SRNL is corresponding author.

## Presentations

- S. Iffat<sup>1</sup> “Effect of Low Concentrations of Partially Unzipped Carbon Nanotubes on Nano-Micro-Structural and Mechanical Properties of Cement Paste” American Concrete Institute, March 28 – April 1, 2021, Baltimore MD.

## References

1. Du, H.; Pang, S.D. Dispersion and stability of graphene nanoplatelet in water and its influence on cement composites. *Constr. Build. Mater.* **2018**, *167*, 403–413.
2. Gong, K.; Pan, Z.; Korayem, A.H.; Qiu, L.; Li, D., Collins, F.; Wang, C.M.; Duan, W.H. Reinforcing effects of graphene oxide on Portland cement paste. *J. Mater. Civ. Eng.* **2015**, *27*, A4014010.
3. Krystek, M.; Pakulski, D. Patroniak, V., Gorski, M.; Szojda, L.; Ciesielski, A.; Samori, P. High-performance graphene-based cementitious composites. *Adv. Sci.* **2019**, 1801195.
4. Wang, B.; Pang, B.; Mechanical property and toughening mechanism of water reducing agents modified graphene nanoplatelets reinforced cement composites. *Constr. Build. Mater.* **2019**, *226*, 699–711.
5. Xu, S.; Liu, J.; Li, Q. Mechanical properties and microstructure of multi-walled carbon nanotube-amended cement paste. *Constr. Build. Mater.* **2015**, *76*, 16–23.
6. Luo, J.; Chen, S.; Li Q, Liu, C.; Gao, S.; Zhang, J.; Guo, J. Influence of graphene oxide on the mechanical properties, fracture toughness, and microhardness of recycled concrete. *Nanomaterials* **2019**, *9*: 325.
7. An, J.; Nam B. H.; Alharbi Y.; Cho B. H.; Khawaji M. Edge-oxidized graphene oxide (EOGO) in cement composites: Cement hydration and microstructure. *Composites Part B* **2019**, *173*, 106795.

## Acronyms

GO	Graphene oxide
GONR	Graphene oxide nanoribbon
MWCNT	Multiwalled carbon nanotube
PUCNT	Partially unzipped carbon nanotube
SEM	Scanning electron microscope (microscopy)
SRNL	Savannah River National Laboratory
SRNS	Savannah River Nuclear Solutions
USC	University of South Carolina

## Post-Doctoral Researchers

- Joseph E. Meany, Post-Doctoral Research Fellow, SRNL
- Mithun Skder, Post-Doctoral Research Fellow, Smith College

## Student Researchers

- Shohana Iffat, Graduate Research Assistant, University of South Carolina
- S. James Ramsey, Junior, Civil Engineering, Clemson University

## External Collaborators

- Fabio Matta, Associate Professor, Dept. of Civil and Environmental Engineering, Columbia, SC 29280 (off-site research, SRNL contract with USC)
- Mohammed Baalousha, Associate Professor Center of Environmental Nanoscience and Risk, Arnold School of Public Health, University of South Carolina, Columbia, SC 29208 (off-site research, USC SRNL contract with USC)
- Professor J. Biernacke, Tennessee Technical University, Department of Civil and Material Engineering, Cookeville, TN (off-site consultation)
- Professor F. Sanchez, Vanderbilt University, Department of Civil and Environmental University, Nashville, TN (off-site consultation)
- Nathan Tregger, Grace Construction Products chemist, W.R. Grace, MD (off-site consultation)
- Jason Wimberly, Grace Construction Products, Technical Services, FL (off-site consultation)
- Scott Z. Jones, National Institute of Standards and Testing, Gaithersburg, MD (off-site consultation)

## Identify Correct Feedbacks for Reinforced Learning in Robotics – Walk by Energy Conservation for a Small, Two-Servo Insect Robot

**Project Team:** X. Steve Xiao, Holly B. Ray, Henry (Tommy) Sessions

**Project Start Date:** January 31, 2020

**Project End Date:** August 21, 2020

*Machine learning (ML) and artificial intelligence (AI) programs are studied with a small, simple insect robot made of two servo motors and an Arduino Nano microprocessor in order to identify the correct feedback for ML. The report summarizes 7-weeks intense investigation with fruitful outcomes, currently at peak productivity. The team picked up speed sharply,*

*constructed a prototype insect robot with demonstrated functionality of 'walking', power consumption (current) measurement, distance sensor, wireless communication, and EEPROM data storage. This allowed ML and AI development to identify the correct feedbacks as minimum energy consumption per distance instead of maximum distance per step. First attempt ML and AI were demonstrated successfully. The knowledge gained in machine learning and robotics would benefit unmanned remote operation in nuclear and radiological environment, surveillance, as well as industrial automation.*

### FY2020 Objectives

- Learn Arduino and Processing language for microprocessor programming
- Build prototype insect robot that walks
- Incorporate working current sensor, ultrasonic sensor, and radio frequency transceiver into the robot;
- Implement initial Machine Learning and Artificial Intelligence program

### Introduction

While machine learning (ML) algorithm is more mature nowadays and widely used, the training dataset (including data collection) is a major bottleneck in machine learning. However, robotic onboard sensors provide unlimited signals with time and location stamps. We studied ML with an insect robot then exploit the feedbacks (or the policy) to optimize the robot's (agent's) actions. A quadrupedal insect robot was preliminarily fine-tuned for a set of learning parameters adaptive to its body weight, momentum, foot friction, etc. but the moving pattern became "long-jump" with the feedback of optimized distant per step. In the meantime, the battery power was drained noticeably quicker. We currently theorized that a robot's correct feedback for learning on how to walk properly should be minimizing energy consumption for a fixed payload.

A small, two-servo insect robot was constructed with a current sensor for power consumption measurement and ultrasonic sensor for distance. The servo motors making up the robot are controlled and programmed by an Arduino microprocessor. The microprocessor is also used to collect the analog data from the current sensor and digital input from the ultrasonic sensor. A radio frequency transceiver wired to the microprocessor communicates information from the robot back to the computer, allowing for data observation (for surprised learning).

An Artificial Neural Network code utilizes known inputs (servo motor inputs) cases and the measured (current and distance) output values to train the microprocessor.<sup>1</sup> The ANN essentially refines parameters in two hidden layers to represent the "learned" insect robot system, and stores this into the Electrically Erasable Programmable Read-Only Data (EEPROM). The goal is for the insect robot to self-learn how to walk properly – optimized between the servo parameters and the measured current, distance, and time.

When the insect robot walks and simultaneously demonstrates low energy consumption then the robot's 'walk pattern' will be compared with animals in the nature to determine the next step "learning feedbacks".

## Approach

The first objective was to procure the hardware for the robot and assemble it into the prototype insect robot with all parts operating as expected. This required that each piece of hardware be personally vetted through experiments to understand component operation. For example, the Arduino Nano analog input pin converts the signal from current sensor into low resolution 10-bit data (0 – 1023). This required that the current sensor be calibrated against resistors to determine how the current sensor output responded. Furthermore, the ultrasonic sensor and servo motors, the main chassis of the robot, were vetted by having the insect robot move forward toward an object, using arbitrary input values.

Once the robot was assembled, which was an essential objective, the ML and AI aspect of training the robot to 'walk' could be explored. This goal was motivated by the Biological Neural Network of an animal or insect such as a cat or ant.<sup>2</sup> The animal's or insect's BNN ensures that the creature walks in an efficient manner, so the ANN would essentially mimic this BNN.<sup>3</sup> Although the insect robot is a simplified version of an animal or insect, meaning it has no joints, the basic principal of energy conservation can be explored. If the insect robot can be optimized to 'walk' and consume minimal energy per distance traversed, then ML and AI learning was a success and could be explored in further applications.

## Results/Discussion

A successful build of the Prototype Insect Robot was demonstrated by 'walking' the two servos with initial input values. The Prototype also has the capability to measure current and distance with sensors. The radiofrequency communication was demonstrated between the robot (for current and distance data) and computer. First attempt ML and AI were implemented on the insect robot. The board and robot have successfully been trained, but further optimization of the algorithm variables (learning rate, momentum, max weight), inputs, and outputs need to be explored in future experiments.

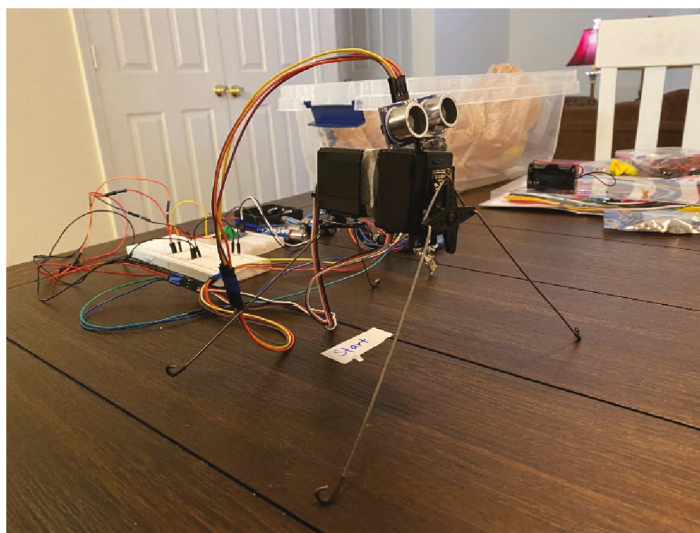


**Figure 1:** Insect Robot made of two servo motors and steel wire. The Ultrasonic Sensor is mounted atop the front servo for distance measurements.

## FY2020 Accomplishments

- A postdoctoral research associate was hired, who joined SRNL on June 1, 2020
- A successful build of the Prototype Insect Robot was demonstrated by 'walking' the two servos using initial input values
- Demonstrated capabilities was added to the prototype: power consumption (current) measurement, distance sensor, wireless communication, EEPROM data storage
- ML and AI algorithm was created in the inset robot. First attempt ML and AI were demonstrated successful

## Future Directions

The board and robot have been successfully trained, but further optimization of the algorithm variables (learning rate, momentum, max weight), inputs, and outputs need to be explored in future experiments. The optimized insect robot will need to be evaluated for the 'walk pattern' comparing to animals in the nature to determine if the learning "feedback" is appropriate.

## References

1. Heymsfeld, R.; A Neural Network for Arduino. <http://robotics.hobbizine.com/arduinoann.html>. (accessed Aug 4, 2020).
2. 3Blue1Brown.; But What is a Neural Networks? <https://www.youtube.com/watch?v=aircArvnKk>. (accessed Aug 5, 2020).
3. Hodgins, S.; Arduino Neural Network Robot. <https://hackaday.io/project/27938-arduino-neural-network-robot>. (accessed Aug 5, 2020).

## Acronyms

Artificial Intelligence (AI)  
Artificial Neural Network (ANN)  
Biological Neural Network (BNN)  
Electrically Erasable Programmable Read-Only Data (EEPROM)  
Machine Learning (ML)

## Post-Doctoral Researchers

Holly B. Ray

## Assessment of Model Cloud Parameterizations for Improved Atmospheric Fate and Transport

**Project Team:** Stephen Noble and Brian Viner

**Project Start Date:** February 3, 2020

**Project End Date:** August 21, 2020

*Clouds interact with pollutants released into the atmosphere. This interaction makes them important to the fate and transport of pollutants. This research assesses the ability of mesoscale models used by SRNL to forecast clouds that could affect dispersion at the Savannah River Site. We found that one model better predicted the cloud base altitude during the day, and*

*another predicted it better at night. Both models underpredicted the cloud fractions (amount of cloud) that were observed and poorly predicted low clouds that are most important for dispersion. Future adjustments to model parameterizations that may improve model performance were identified.*

### FY2020 Objectives

- Assess current ATG mesoscale model parameterizations and configurations in ability to forecast macrophysical cloud properties
- Review the DOE E3SM model capabilities and develop an understanding of E3SM to improve SRNL competency
- Assess E3SM capabilities in development of macrophysical cloud properties

### Introduction

ATG's national security and emergency response missions focus largely on fate and transport modeling of atmospheric releases. Solutions are dependent on the accuracy of meteorological models for predicting winds, turbulence, and other atmospheric properties that affect the release. Current model analyses focus primarily on dispersion and deposition but are limited in their ability to predict constituent transformations during downwind transport, including effects through interactions with clouds. Clouds interact with atmospheric particle and trace gas emissions through scavenging and processing of particles and gases<sup>1</sup> or changes in atmospheric photochemistry due to modified actinic flux<sup>2</sup>. Thus, the presence of clouds alter dispersion and transform atmospheric constituents.

Accurately predicting the interaction of a release with clouds depends on accurate modeling of the location, size and amount of clouds. Because clouds are highly variable across spatial scales many aspects must be parameterized in models. This research aimed to assess the skill of current ATG high resolution model configurations at forecasting cloud macrophysical properties and review capabilities of the state-of-the-art DOE Energy Exascale Earth System Model (E3SM),<sup>3</sup> which is at the forefront of model parameterization of aerosol-cloud interactions, in modeling cloud properties. This work will increase SRNL fate and transport capabilities and competitiveness.

### Approach

Forecasted values of cloud base altitude (CBA) and cloud fraction (CF) were calculated from two high resolution mesoscale models, RAMS<sup>4</sup> and WRF<sup>5</sup>. These models are run operationally, providing forecasts for the Savannah River Site (SRS). Observations of CBA and CF from a ceilometer located at SRS were used to assess the capabilities of these models to accurately forecast CBA and CF. We developed an averaging technique in order to reduce spatial and temporal differences between the models and observations in an effort to provide a better comparison. RAMS was evaluated for one year of available stored forecasts

in a combined effort from other work scope. But, WRF forecasts are overwritten and thus extraction and collection of cloud properties began in April, limiting inter-model comparisons.

A review of E3SM was undertaken of the extensive literature on model development, updates and capabilities. Model code was downloaded, and a review of the extensive model data library was undertaken. Model data was downloaded for review of possible comparisons with cloud metrics but due to limitations in LDRD timing and data set size, this effort was suspended. While not undertaken as part of this LDRD, SRNL E3SM efforts are buoyed by the addition of personnel with a stronger background in large scale models.

## Results/Discussion

We completed assessments and comparisons of springtime forecasts from RAMS and WRF. Results from forecast scoring and average comparisons indicate that WRF better forecasted CBA during the daytime with bias towards lower CBA at night (Figure 1). RAMS better forecasted nighttime CBA and was biased towards higher CBA during the daytime. Neither model forecasted cloud amount particularly well. Nearly 50% of the time (50% for RAMS and 54% for WRF) the both models failed to predict clouds when they were detected by the ceilometer. This likely led to model CF that was generally lower than observed CF. Much of this was attributed to the models consistently struggling with resolving low clouds. Better cloud parameterizations, such as double moment microphysics in WRF and convective parameterizations for the low-resolution grid in RAMS, could improve these forecasts. A hybrid scheme using RAMS at night and WRF during the day might provide the best optimization for dispersion modeling. The best configuration for a hybrid scheme, including methods to blend the models during transition periods at dawn and dusk, would need to be determined in future work.

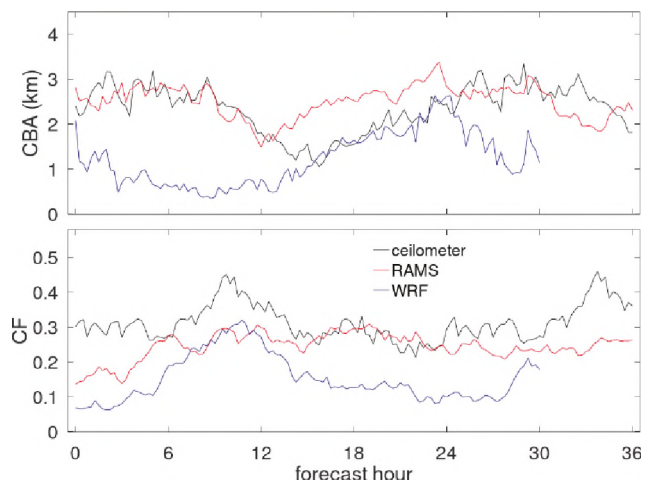


**Figure 1:** Springtime averaged CBA and CF for RAMS (red), WRF (blue) and observations (black). Time period beginning at 00:00 UTC (8:00 pm local).

We also evaluated RAMS CBA and CF by month based on one year of forecasts. RAMS predicted CBA best in mild months of October, November, February, April and to a lesser extent May. RAMS CBA in warmer months (June, July, August, and September) was overall too high. In colder months (December and January), RAMS predicted lower CBA at night and higher CBA during the day. In July and August, RAMS predicted greater CF than the observations while in most other months RAMS predicted CF lower than observed CF. Overall, RAMS predicted the best CBA in February and best CF in April. Some errors in prediction are due to poorly timed events and could likely be improved by high quality data assimilation. Errors from occasional failed forecasts (5% of the time) were found to be from the domain edge being too close to mountainous terrain. Future runs will solve this by increasing the outer domain to separate the model boundary from the complex terrain. Identifying this failure now will prevent this issue in future implementation of this RAMS version operationally. The errors in summer months indicate that the RAMS model is not correctly simulating convective cloud development. A similar issue was observed in WRF for the late May and June period. It is known that convective clouds can exhibit great variability in space and

time, making them difficult to predict. However, it is also a key area for future improvement for applications where spatial and temporal characteristics of cloud development are important.

E3SM is a global model including complex interactions between land, ocean, atmosphere and biosphere and is currently under development by DOE.<sup>6</sup> These interactions, 72 vertical layers and global coverage (low resolution - 1° and high resolution - 0.25°) make E3SM computationally expensive and limited temporally. It is, thus, not feasible to be utilized for dispersion forecasting but could be useful for historical dispersion studies. E3SM implements a state-of-the-art convective scheme<sup>6</sup> and a three moment microphysical scheme<sup>7</sup> that improves model prediction of cloud properties<sup>8</sup>. Application of these parameterizations could possibly be included in future operational mesoscale models to improve forecasts of cloud properties. Time limitation from early LDRD termination restricted our ability to assess the ability of E3SM to model cloud properties in the southeastern US at SRS.

## FY2020 Accomplishments

- Identified limitation in domain configuration near complex terrain of RAMS forecasts that led to 5% model failure rate
- Developed analysis method for comparing model cloud spatial information with single point ceilometer temporal observations
- Assessed the model skill of forecasting cloud properties of ATG mesoscale models
- Identified the diurnal cloud property differences between ATG mesoscale models for future use in dispersion modeling
- Identified possible improvements to ATG mesoscale model configurations to better forecast cloud properties

## Future Directions

- Increase data assimilation capabilities for RAMS
- Assess precipitation forecasts that could affect dispersion
- Implement new RAMS domain configuration to eliminate the 5% failure rate from domain errors
- Increase SRNL capabilities with E3SM

## Publications

- Noble, S.; Viner, B.; Buckley, R.; Chiswell, S., Assessing the skill of forecasting springtime macrophysical cloud properties in the southeastern US. *Atmosphere*. 2020. Submitted August 2020 by Stephen Noble of SRNL.
- Noble, S.; Buckley, R., RAMS model assessment of cloud and meteorological properties for improved atmospheric fate and transport. Technical report in progress to be completed September 2020 in combination with additional work at SRNL.

## Presentations

- Noble, S.; Viner, B.; Buckley, R. Assessment of springtime cloud forecasts from two mesoscale models – American Geophysical Union Fall Meeting, December 2020.

## References

1. Hudson, J. G.; Noble, S.; Tabor, S., Cloud supersaturations from CCN spectra Hoppel minima. *Journal of Geophysical Research: Atmospheres* **2015**, *120* (8), 3436-3452.
2. Los, A.; van Weele, M.; Duynkerke, P. G., Actinic fluxes in broken cloud fields. *Journal of Geophysical Research: Atmospheres* **1997**, *102* (D4), 4257-4266.
3. Golaz, J.-C.; Caldwell, P. M.; Van Roekel, L. P.; Petersen, M. R.; Tang, Q.; Wolfe, J. D.; Abeshu, G.; Anantharaj, V.; Asay-Davis, X. S.; Bader, D. C.; Baldwin, S. A.; Bisht, G.; Bogenschutz, P. A.; Branstetter, M.; Brunke, M. A.; Brus, S. R.; Burrows, S. M.; Cameron-Smith, P. J.; Donahue, A. S.; Deakin, M.; Easter, R. C.; Evans, K. J.; Feng, Y.; Flanner, M.; Foucar, J. G.; Fyke, J. G.; Griffin, B. M.; Hannay, C.; Harrop, B. E.; Hoffman, M. J.; Hunke, E. C.; Jacob, R. L.; Jacobsen, D. W.; Jeffery, N.; Jones, P. W.; Keen, N. D.; Klein, S. A.; Larson, V. E.; Leung, L. R.; Li, H.-Y.; Lin, W.; Lipscomb, W. H.; Ma, P.-L.; Mahajan, S.; Maltrud, M. E.; Mamatjanov, A.; McClean, J. L.; McCoy, R. B.; Neale, R. B.; Price, S. F.; Qian, Y.; Rasch, P. J.; Reeves Eyre, J. E. J.; Riley, W. J.; Ringler, T. D.; Roberts, A. F.; Roesler, E. L.; Salinger, A. G.; Shaheen, Z.; Shi, X.; Singh, B.; Tang, J.; Taylor, M. A.; Thornton, P. E.; Turner, A. K.; Veneziani, M.; Wan, H.; Wang, H.; Wang, S.; Williams, D. N.; Wolfram, P. J.; Worley, P. H.; Xie, S.; Yang, Y.; Yoon, J.-H.; Zelinka, M. D.; Zender, C. S.; Zeng, X.; Zhang, C.; Zhang, K.; Zhang, Y.; Zheng, X.; Zhou, T.; Zhu, Q., The DOE E3SM Coupled Model Version 1: Overview and Evaluation at Standard Resolution. *Journal of Advances in Modeling Earth Systems* **2019**, *11* (7), 2089-2129.
4. Pielke, R. A.; Cotton, W. R.; Walko, R. L.; Tremback, C. J.; Lyons, W. A.; Grasso, L. D.; Nicholls, M. E.; Moran, M. D.; Wesley, D. A.; Lee, T. J.; Copeland, J. H., A comprehensive meteorological modeling system—RAMS. *Meteorology and Atmospheric Physics* **1992**, *49* (1), 69-91.
5. Powers, J. G.; Klemp, J. B.; Skamarock, W. C.; Davis, C. A.; Dudhia, J.; Gill, D. O.; Coen, J. L.; Gochis, D. J.; Ahmadov, R.; Peckham, S. E.; Grell, G. A.; Michalakes, J.; Trahan, S.; Benjamin, S. G.; Alexander, C. R.; Dimego, G. J.; Wang, W.; Schwartz, C. S.; Romine, G. S.; Liu, Z.; Snyder, C.; Chen, F.; Barlage, M. J.; Yu, W.; Duda, M. G., The Weather Research and Forecasting Model: Overview, System Efforts, and Future Directions. *Bulletin of the American Meteorological Society* **2017**, *98* (8), 1717-1737.
6. Rasch, P. J.; Xie, S.; Ma, P.-L.; Lin, W.; Wang, H.; Tang, Q.; Burrows, S. M.; Caldwell, P.; Zhang, K.; Easter, R. C.; Cameron-Smith, P.; Singh, B.; Wan, H.; Golaz, J.-C.; Harrop, B. E.; Roesler, E.; Bacmeister, J.; Larson, V. E.; Evans, K. J.; Qian, Y.; Taylor, M.; Leung, L. R.; Zhang, Y.; Brent, L.; Branstetter, M.; Hannay, C.; Mahajan, S.; Mamatjanov, A.; Neale, R.; Richter, J. H.; Yoon, J.-H.; Zender, C. S.; Bader, D.; Flanner, M.; Foucar, J. G.; Jacob, R.; Keen, N.; Klein, S. A.; Liu, X.; Salinger, A. G.; Shrivastava, M.; Yang, Y., An Overview of the Atmospheric Component of the Energy Exascale Earth System Model. *Journal of Advances in Modeling Earth Systems* **2019**, *11* (8), 2377-2411.
7. Paukert, M.; Fan, J.; Rasch, P. J.; Morrison, H.; Milbrandt, J. A.; Shpund, J.; Khain, A., Three-Moment Representation of Rain in a Bulk Microphysics Model. *Journal of Advances in Modeling Earth Systems* **2019**, *11* (1), 257-277.
8. Xie, S.; Lin, W.; Rasch, P. J.; Ma, P.-L.; Neale, R.; Larson, V. E.; Qian, Y.; Bogenschutz, P. A.; Caldwell, P.; Cameron-Smith, P.; Golaz, J.-C.; Mahajan, S.; Singh, B.; Tang, Q.; Wang, H.; Yoon, J.-H.; Zhang, K.; Zhang, Y., Understanding Cloud and Convective Characteristics in Version 1 of the E3SM Atmosphere Model. *Journal of Advances in Modeling Earth Systems* **2018**, *10* (10), 2618-2644.

## Acronyms

ATG	Atmospheric Technology Group
CBA	Cloud base altitude
CF	Cloud fraction
DOE	Department of Energy
E3SM	Energy Exascale Earth System Model
LDRD	Laboratory Directed Research and Development
RAMS	Regional Atmospheric Modeling System
SRNL	Savannah River National Laboratory
WRF	Weather Research and Forecasting model

## Localized Electrorefining

**Project Team:** Brenda L. Garcia-Diaz, Dale Hitchcock, Prabhu Ganesan, Hector Colon-Mercado

**Clemson University Collaborators:** Kyle Brinkman and Chris Dandeneau

**Project Start Date:** April 1, 2020

**Project End Date:** September 30, 2020

*Savannah River National Lab (SRNL) has demonstrated electrorefining of noble corrosion-resistant alloys such as stainless steels and zirconium alloys in molten salt electrolytes to remove these materials when they are used as barriers such as cladding material. Electrorefining is an electrolytic reaction that oxidizes the components of an alloy at the anode and reduces those same components at the cathode, thus transferring the materials between the electrodes. However, there are times where it would be useful to perform electrorefining on a localized portion of an alloy. SRNL has developed a concept for self-heating,*

*localized electrorefining based on fundamental principles of electrochemistry that could be utilized in different applications.*

## FY2020 Objectives

- Develop concept for system
- Identify chemistries of interest
- Test self-heating initiation reactions

## Introduction

SRNL is developing concept electrode systems for performing localized electrorefining that can easily be transported. The system will be self-heating using reactants such as thermites and the salt composition could be tailored for the alloys to be electrorefined. The adiabatic heat of reaction will be used to understand the heat that can be produced from the initiation reaction for melting the salt and raising the system temperature. Initiation of the reaction will be investigated to identify potential methods for starting the process. These initial experiments will lead to a more detailed model and cell design that can be used for the process.

## Approach

The project will start with thermodynamic modeling and comparison with literature data for the heat of reaction for self-heating of the cell. Thermodynamic values will be utilized to develop heat transfer models. The initial experimental part of the research focuses on the initiation reaction that will be used for heating along with the design of a cell for the reaction. Initial testing of the initiation reaction will be carried out ex-situ and different methods of initiation are investigated.

## Results/Discussion

The self-heating reaction needs to heat the molten salt for electrorefining to a temperature well above its melting point. The current molten salt that is being tested is  $\text{MgCl}_2\text{-KCl-NaCl}$  and the melting point of commercial salts in a typical composition range are around 400 °C. The adiabatic heats of reaction for various thermite pairings were calculated based on thermodynamic properties along with a comparison to literature data for the different reactions.

The adiabatic heats of reaction that were calculated were within 10% of the literature values. This provided confidence that the adiabatic heats of reaction from thermodynamic properties can be used as a valid estimate of the heat released by the reaction for modeling heat transfer in the applications.

Initial tests were conducted with Al and Fe<sub>2</sub>O<sub>3</sub> because it is the most traditional thermite composition. The initiation of the reaction was tested using a potassium permanganate and glycerin reaction as well as a Mg ribbon. The ignition using a Mg ribbon was very reliable and quickly ignited the mixture without problems. The potassium permanganate and glycerin reaction was much more dependent on getting the configuration of the chemicals correct in the cell and would have more variation in how well it worked. However, with experience the initiation became easier.

**Table 1:** Comparison of Theoretical and Actual Adiabatic Reaction Temperatures for Various Thermite Reactions Considered for the Process

Reactants	$T_{ad}$ (K)	$T_{ad}$ (K)	$T_{ad}$ (K): S.H. Fischer <i>et al.</i>	Percent Difference (%)
	Metal Product: Liquid Oxide Product: Liquid	Metal Product: Liquid-Gas Oxide Product: Liquid	Metal Product: Liquid-Gas Oxide Product: Liquid	
2Al-3CuO	4555	2924	2843	2.8
2Al-3NiO	3081	3045	3187	4.6
2Al-3CoO	3390	3246	3201	1.4
2Al-3AgO	5882	3239	3253	0.4
2Al-Fe <sub>2</sub> O <sub>3</sub>	3405	3047	3135	2.8
8Al-3Fe <sub>3</sub> O <sub>4</sub>	3239	3095	3135	1.3
4Al-3SnO <sub>2</sub>	3799	2764	2876	4.0
10Al-3Nb <sub>2</sub> O <sub>5</sub>	2876*	2876*	2705*	6.1

\*Nb<sub>2</sub>O<sub>5</sub> remains in solid state

## FY2020 Accomplishments

- Identified potential thermite reactions that can generate the heat needed to melt molten salts for electrorefining and calculated adiabatic heats of reaction as a foundation for heat transfer modeling
- Tested initiation reactions to understand kinetics as well as configuration effects on reactant mixtures for cell design. Mg was a more reliable initiation reaction, but potassium permanganate and glycerin worked with even distribution and dosing of reactants

## Future Directions

- Developing cell designs based on initial reaction tests to meet configurational needs
- Developing heat transfer models that can predict the amount of reactants needed for heating of the electrorefining cell

# NUCLEAR MATERIALS THREAT REDUCTION

## PROJECTS

Development of Direct Injection/Ionization Mass Spectrometry Methods for Whole Molecule Characterization

HEMP Transformer Defense Through Power Electronics

Time Domain Thermoreflectance and Photodeflection Signatures of He Bubbles in Metals

Collaboration with USACyS for Signals Manipulation

Fundamental  $^{235}\text{U}$  Uranium Nuclear Resonance Spectroscopy

Comprehensive Chemical Fingerprinting by Multidimensional GC and Supervised Machine Learning

Portable Industrial Control Systems Simulator

Effect of GPS Manipulation to Traditional and Next Generation Relay Protection

High Resolution Actinide Speciation Using Tensioned Metastable Fluid Detector (TMFD)

Develop Water Detritiation Models Based on Bench Scale and H/D Pilot Plant Performance

High-Sensitivity Electric Field Detection Based on Gas Polarization

Laser-Based Means for Accelerating Nuclear Decay Rate

Photon Entanglement Spectroscopy and Imaging in Actinide Research

Development of FRET Clusters for CBRN Detection

Novel Perovskite Semiconductors for the Detection of Special Nuclear

High Performance 3D Printable X ray Scintillators for Remote Radiation Sensing Applications Material

Crystal Growth and Material Development of CZTS for Radiation Detector Applications

Electric Field Imaging Small Scale Testing

## Development of Direct Injection/Ionization Mass Spectrometry Methods for Whole Molecule Characterization

**Project Team:** W. Kuhne, K. Lawrence, A. Swindle, D. Mannion, R. Smith, J. Mannion, C. Shick, M. Wellons

**Collaborator:** C. Cody (JEOL USA Inc.)

**Project Start Date:** October 1, 2019

**Project End Date:** September 30, 2020

*Soft ionization methods for mass spectrometry allow the detection of partial or whole molecular species to enable rapid, unambiguous identification of species relevant to environmental remediation and nuclear safeguards challenges. In this project, the trace detection of whole molecule uranyl complexes, including uranyl acetate, uranyl nitrate, uranyl chloride, and uranyl oxalate were successfully demonstrated using matrix-assisted ionization mass spectrometry (MAI-MS). Detection and characterization of uranium analytes using 3-*

*nitrobenzlnitrile (3-NBN) as the ion generating matrix is the first demonstration of uranium complex analysis using MAI techniques. Paper spray ionization mass spectrometry (PSI-MS) and Electrospray ionization mass spectrometry (ESI-MS) of strontium and cerium species led to ppm limits of detection (LOD) with fast (<1 min) measurement times and no sample preparation. Additionally, the detection and characterization of explosive compounds were carried out using standards for RDX and TNT to develop and optimize methods for concentrating samples swiped from surfaces. This work has demonstrated a new characterization modality for convenient and rapid analysis with minimal sample preparation.*

### FY2020 Objectives

- Development of matrix-assisted ionization techniques for uranium complexes
- Optimization and quantification of Sr and Ce species detection using ESI-MS and PSI-MS
- Development of AMS methods for explosive material detection and characterization

### Introduction

The rapid characterization of trace inorganic molecules and complexes is important for a litany of applications, including forensic analysis, nuclear safeguards monitoring,<sup>1-2</sup> environmental monitoring,<sup>3,4</sup> and geochronical measurements.<sup>5</sup> For nuclear safeguards applications, the quantification of inorganic isotopes from environmental samples typically involves extensive chemical and physical processing prior to analysis. Harsh sample preparation results in the loss of the original chemical speciation (i.e. what the metal was bonded to/with when found in the environment) as well as the mixing of anthropogenic uranium with background material contained within the collection media (e.g. a swipe or soil). To overcome these challenges, soft ionization techniques using ambient mass spectrometry (AMS) techniques, including paper spray ionization (PSI), matrix assisted ionization (MAI), and electrospray ionization (ESI) were employed for the rapid analysis of intact uranium complexes, strontium and cerium analytes, and explosives compounds for national security applications (Figure 1).

Matrix assisted ionization (MAI) uses a chemical matrix that spontaneously produces analyte ions when exposed to the vacuum of a mass spectrometer. Unlike the other AMS techniques, MAI does not require the use of photons, electron beams, high voltage or added heat to initiate ionization to produce a mass spectrum. Instead, it is dependent on the choice of matrix and vacuum conditions.<sup>6</sup> The actual mechanism by which MAI produces analyte ions is unknown, and this technique is often referred to as “magic ionization.” MAI is typically carried out by introducing solid matrix crystals directly into vacuum; however the introduction of liquid solutions containing saturated 3-NBN concentrations has yielded rapid results for inorganic species.<sup>7</sup> Though detection limits comparable to ESI-MS have been demonstrated for a variety of organic analytes using MAI-MS,<sup>8-11</sup> no reports exist in the literature of utilizing MAI for inorganic analysis. This method was employed for uranium complexes, including uranyl nitrate, uranyl chloride, uranyl acetate, and uranyl oxalate with ng LODs for most species and analysis times of <5 seconds.

FY20 data built upon initial studies from FY19 and focused on the quantification of other inorganic species as well as explosives compounds.

## Approach

The goal of this work was to develop analytical techniques for the identification and quantification of inorganic and explosives compounds. Initial studies began in late FY19 for the detection and quantification of uranyl complexes, RDX and TNT and extended into FY20 with an additional \$50K to continue LOD optimization and to leverage against a planned field exercise. All samples were analyzed with an AccuTOF™ DART® 4G mass spectrometer from JEOL (Boston, MA, USA).

### MAI analysis for inorganic elements and complexes with uranium ions

In FY20, MAI analysis was carried out using a common ionization matrix material, 3 nitrobenzonitrile (3-NBN), to investigate the direct ionization method for uranyl hydrate complexes of nitrate, chloride, acetate, or oxalate speciation. Samples were analyzed in negative ion mode, as no spectra corresponding to uranyl was detected in positive ion mode. Stock solutions of uranyl chloride, uranyl acetate, and uranyl oxalate salts composed of natural uranium (International Bio-Analytical Industries, Boca Raton, FL, USA) were used to make solutions of 1, 10, 50, 100, 250, and 500 µg/mL of each uranyl salt in ASTM Type II water.

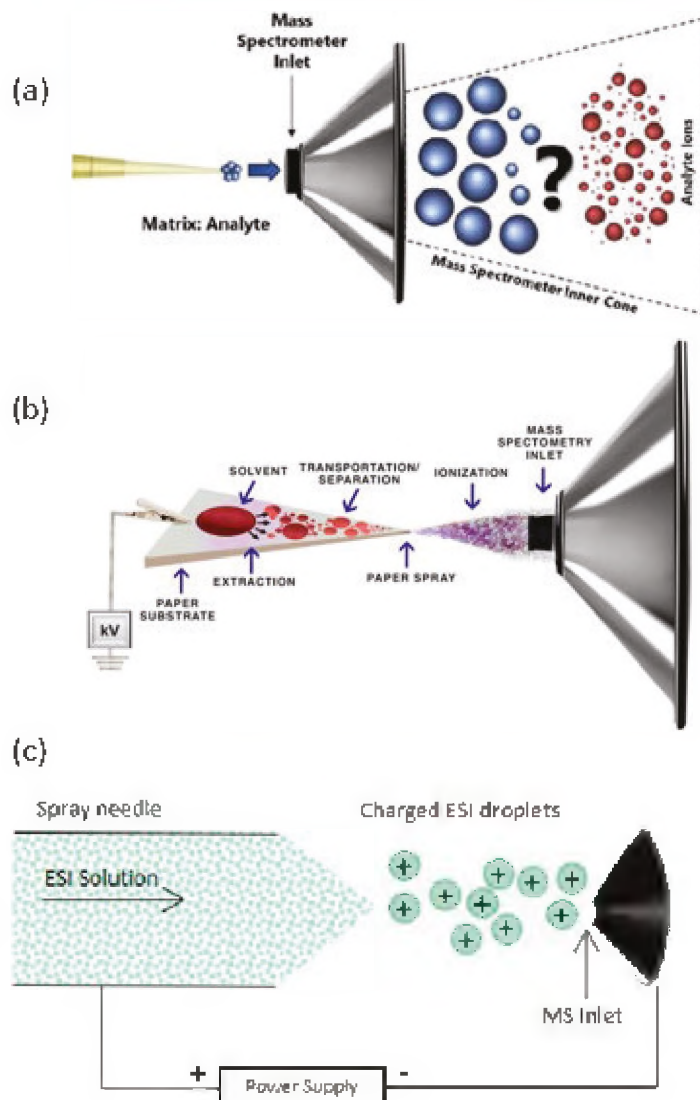


**Figure 1:** Overview of the different ionization modes that were used: (a) MAI-MS; (b) PSI-MS; (c) ESI-MS.

A stock solution of depleted uranium certified reference material U005 (New Brunswick Laboratory, Argonne, IL) was used to make solutions of 0.1, 0.5, 1, 10, 50, and 100  $\mu\text{g}/\text{mL}$  uranyl nitrate in 2% nitric acid. Samples were prepared for MAI analysis by mixing each sample with methanol (ACS Reagent Grade, Sigma-Aldrich, St. Louis, MI, USA) to create 50:50 sample/methanol mixtures.

## PSI-MS and ESI-MS for inorganic species of Ce and Sr

All samples were analyzed in positive ion mode. The radiofrequency quadrupole ion guide was set to an amplitude of 50–1000 V for cerium analysis and 250–500 V for strontium analysis, the cone (“orifice 1”) voltage was set to 180 V, the needle voltage was set to +3.0 kV and the detector voltage was set to 2.5 kV. For PSI-MS, the spectrometer was equipped with a JEOL paper spray ion source, which consists of a copper clamp, safety interlock and manual positioning system. The paper spray source was held at +3.0 kV for positive-ion mode. JEOL version 4 was used in msAxel software for data acquisition, mass calibration, and to export spectrum data from regions of interest in the extracted ion current chromatogram (EICC). Peak deconvolution was carried out in OriginPro 2016 using second order derivatives to obtain peak locations and intensities. For the calibration curves, the intensities were extracted from raw data using RStudio with MALDIquant and MALDIquantForeign packages.

## RDX and TNT Explosives Detection

Calibration curves were created using explosive standards in acetonitrile and methanol in negative ion mode using DART. Analytes were measured by introducing the sample into the gas stream using a capillary tube and  $\sim 5 \mu\text{l}$  of sample.

## Results/Discussion

### MAI-MS analysis of inorganic uranyl complexes ions

Ionized forms of the four uranyl species investigated were putatively identified. The calculated LODs were found to be 5 ng of uranyl nitrate, 10 ng of uranyl oxalate, 100 ng of uranyl acetate, and 200 ng of uranyl chloride. Additionally, six anion peaks were observed in all mass spectra containing 3-NBN. Subsequent analysis of the matrix by GC/Q-TOF suggest these ions are created from the matrix during the ionization process and are not matrix contaminants. Two of these matrix derived anions were found to form detectable ion complexes with the uranyl analyte.

The uranyl ligands analyzed were detected in negative ion mode and when aspirating liquid sample saturated with suspended 3-NBN crystals. The four uranyl ligand species examined were all detected as negative ion complexes composed of one uranyl cation in conjugation with anions totaling three negative charge equivalents. For example,

uranyl nitrate was primarily observed as uranyl complexed with three nitrates, though other ion complexes were observed that were the result of oxide, hydroxide, and matrix-derived adducts (Figure 2).

### PSI-MS and ESI-MS for inorganic species of Ce and Sr

The detection of inorganic species, strontium nitrate and cerium nitrate, using internal standards was successfully carried out in both ESI-MS and PSI-MS with relatively low error and detection limits observed

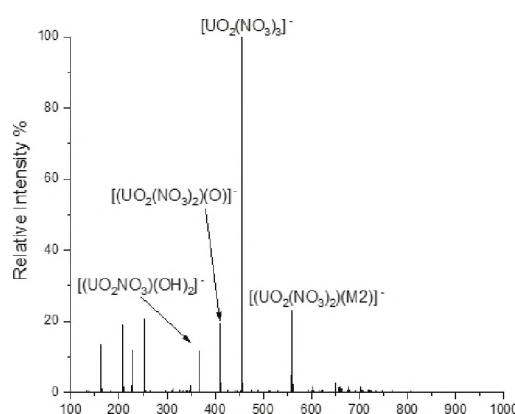


**Figure 2:** Negative ion MAI mass spectra of uranyl nitrate.

in the ppm range in FY19. Adducts produced via these ionization modes, to include adducts from the original nitrate molecules, have been observed. For cerium adducts, the PSI-MS had lower LOD at 100 and 250 V but had higher LOD at the higher voltages. LOD for Sr was higher with PSI-MS than ESI-MS. Isotopic abundancies were measured with less than 10% error for Sr using ESI-MS and less than 25% error for PSI-MS at the lowest abundant isotope (0.56% abundance for <sup>84</sup>Sr). The measured abundancies for Ce isotopes were around 1% or lower for ESI-MS but up to 25% on PSI-MS. The higher percent error for PSI-MS compared to ESI-MS is attributed to a generally lower signal. In FY20, a more thorough comparison of ESI-MS and PSI-MS for the detection of Sr and Ce species was performed to investigate associated error within the measurements. A drinking water standard was also analyzed to validate the calibration curve. As shown in Table 1, the concentration of Ce in a drinking water standard containing other metal analytes was determined to have the lowest calculated percent error when measured with 100 V. With the appropriate selection of internal standards, PSI-MS is a viable method for the rapid detection and quantification of inorganic species, Sr and Ce, with isotopic discrimination requiring minimal sample preparation efforts.

**Table 1:** Measured concentration and percent error for a standard sample containing Ce from the obtained calibration curve

CP-MS-TS-21 Standard Containing Ce (Internal Standard Gd) using PSI-MS Expected Value: 0.26 ppm		
Voltage (V)	Calculated [CeO <sup>+</sup> ] (ppm)	% error
100	0.23	9.97
250	0.22	14.8
500	0.29	11.6
1000	0.21	19.0

## **RDX and TNT Explosives Detection**

Measurement of TNT and RDX were carried out using ESI-MS. Contaminants associated with the solvents methanol and acetonitrile, including palmitic acid-H at  $m/z$  255.24, steric acid-H at  $m/z$  283.48, and myristic acid-H at  $m/z$  227.38 were identified. Initial findings showed that [TNT-H]<sup>-</sup> ( $m/z$  = 226.01) and [RDX-H]<sup>-</sup> ( $m/z$  = 221.12) do not mutually ionize at the same instance, however there does seem to be a relationship between their ionization and that of palmitic acid, indicating there is a matrix effect as a result of solvent impurities. A stronger relationship seemed to be present for TNT compared to RDX. Additional work was required to fully understand this relationship.

## **FY2020 Accomplishments**

FY20 accomplishments were primarily focused on:

- Method development using ESI-MS and PSI-MS were developed for the direct analysis of inorganic Strontium and Cerium with ppm to ppb LODs
- Successful analysis of uranyl complexes using MAI providing <5 second analysis times with the identification of potentially novel matrix-derived anions

Over three years, this project has employed four junior SRNL scientific staff and supported two DOE SULI interns with statistical/data analysis experience, thus building the technical expertise of the next generation. Work products from the efforts in FY20 include a manuscript submitted to a peer-reviewed journal on uranyl complex analysis using MAI-MS, and a manuscript in preparation for a peer-reviewed journal on Sr and Ce detection using PSI-MS.

## Future Directions

- A Discovery Science LDRD was granted for FY21 to build upon the experiments conducted on MAI uranium analysis to investigate the fundamentals of the inorganic ionization mechanism. A full proposal was requested and submitted to the NNSA Defense Nuclear Nonproliferation Research and Development program for the FY21 call for proposals entitled “FY21-SR-PD1Ac- P39: Triboluminescent Matrices for Rapid Trace Detection and Characterization of Actinides”
- A full proposal was requested and submitted on topics related to PSI-MS method development to an external USG Research, Development, and Integration (RDI) Fund for a FY21 call for proposals in collaboration with an external USG partner

## FY20 Publications/Presentations

- Mannion, Danielle R.; Mannion, Joseph M.; Kuhne, Wendy W.; and Wellons, Matthew S. (2020). Matrix Assisted Ionization of Molecular Uranium Species. *Journal of the American Society for Mass Spectrometry*. Submitted
- Coopersmith, Kaitlin; Swindle, Ashlee; Dunbar, Joshua; Kuhne, Wendy W.; and Wellons, Matthew S. (2020). Rapid Detection of Inorganic Strontium and Cerium Molecular Species by Ambient Mass Spectrometry Techniques. *Journal of the American Society for Mass Spectrometry*. (In Preparation)

## References

1. Lamouroux, C.; Moulin, C.; Tabet, J. C.; Jankowski, C. K. Characterization of zirconium complexes of interest in spent nuclear fuel reprocessing by electrospray ionization mass spectrometry. *Rapid Commun. Mass Spectrom.* **2000**, *14* (19), 1869-1877.
2. Zheng, J.; Tagami, K.; Watanabe, Y.; Uchida, S.; Aono, T.; Ishii, N.; Yoshida, S.; Kubota, Y.; Fuma, S.; Ihara, S. Isotopic evidence of plutonium release into the environment from the Fukushima DNPP accident. *Sci. Rep.* **2012**, *2* (304), 1-8.
3. Liu, W.; Dai, X.; Bai, Z.; Wang, Y.; Yang, Z.; Zhang, L.; Xu, L.; Chen, L.; Li, Y.; Gui, D.; Diwu, J.; Wang, J.; Zhou, R.; Chai, Z.; Wang, S. Highly Sensitive and Selective Uranium Detection in Natural Water Systems Using a Luminescent Mesoporous Metal–Organic Framework Equipped with Abundant Lewis Basic Sites: A Combined Batch, X-ray Absorption Spectroscopy, and First Principles Simulation Investigation. *Environmental Science & Technology* **2017**, *51* (7), 3911-3921.
4. Xiao, S. J.; Zuo, J.; Zhu, Z. Q.; Ouyang, Y. Z.; Zhang, X. L.; Chen, H. W.; Zhang, L. Highly sensitive DNAzyme sensor for selective detection of trace uranium in ore and natural water samples. *Sens. Actuators B* **2015**, *210*, 656-660.
5. Spano, T. L.; Simonetti, A.; Balboni, E.; Dorais, C.; Burns, P. C. Trace element and U isotope analysis of uraninite and ore concentrate: Applications for nuclear forensic investigations. *Appl. Geochem.* **2017**, *84*, 277-285.
6. Lee, C.; Inutan, E. D.; Chen, J. L.; Mukeku, M. M.; Weidner, S. M.; Trimpin, S.; Ni, C.-K. Toward understanding the ionization mechanism of matrix-assisted ionization using mass spectrometry experiment and theory. *Rapid Commun. Mass Spectrom.* **2019** 0(0).

7. Cody, R. B. Ambient Profiling of Phenolic Content in Tea Infusions by Matrix-Assisted Ionization in Vacuum. *J. Am. Soc. Mass Spectrom.* **2018**, *29* (8), 1594-1600.
8. Inutan, E. D.; Trimpin, S., Matrix assisted ionization vacuum (MAIV), a new ionization method for biological materials analysis using mass spectrometry. *Mol. Cell. Proteomics* **2013**, *12* (3), 792-796.
9. Trimpin, S.; Inutan, E. D. Matrix assisted ionization in vacuum, a sensitive and widely applicable ionization method for mass spectrometry. *Journal of The American Society for Mass Spectrometry* **2013**, *24* (5), 722-732.
10. Trimpin, S.; Inutan, E. D. New ionization method for analysis on atmospheric pressure ionization mass spectrometers requiring only vacuum and matrix assistance. *Anal. Chem.* **2013**, *85* (4), 2005-2009.
11. Wang, B.; Dearing, C. L.; Wager-Miller, J.; Mackie, K.; Trimpin, S. Drug detection and quantification directly from tissue using novel ionization methods for mass spectrometry. *Eur. J. Mass Spectrom.* **2015**, *21* (3), 201-210.

## Acronyms

AMS	Ambient Mass Spectrometry
DART	Direct analysis in real time
EICC	Extracted ion current chromatogram
ESI-MS	Electrospray Ionization Mass Spectrometry
LOD	Limit of detection
MAI	Matrix Assisted Ionization
MS	Mass Spectrometry
<i>m/z</i>	mass to charge ratio
RDX	1,3,5-Trinitroperhydro-1,3,5-triazine
3-NBN	3-Nitrobenzotrile
PSI-MS	Paper Spray Ionization Mass Spectrometry
S/N	Signal to noise ratio
TBP	Tributylphosphate
TNT	Trinitrotoluene

## HEMP Transformer Defense Through Power Electronics

**Project Team:** Klaehn Burkes and Vincent Cyssens

**Clemson University Collaborator:** Johan Enslin

**Project Start Date:** October 1, 2018

**Project End Date:** September 30, 2020

*High-altitude electromagnetic pulses and geo-magnetic disturbances have the potential to severely impact the electric power grid by damaging large power transformers and causing severe power quality issues. This impact comes as a result of a quasi-static bias induced on transmission lines by geomagnetically induced currents, which saturate magnetic components in the electric power system. This paper introduces the concept of utilizing a h-bridge inverter on the neutral of a LPT to inject a DC bias equivalent voltage onto the neutral*

*side of the transformer windings. This biasing floats the transformer windings, eliminating the effect of the DC current and keeping the transformer from saturating. Schematic diagrams will be presented, along with simulation model data using Typhoon and PLECS, and finally test results from a benchtop hardware test.*

### FY2020 Objectives

- Perform controller hardware in the loop testing of GIC compensation and validate with simulations from last fiscal year
- Build benchtop prototype of the GIC protection device
- Test benchtop prototype and validate with controller hardware in the loop testing
- Clemson develop grid support functions for improving business case for implementation

### Introduction

High altitude electromagnetic pulses (HEMPs) and geo-magnetic disturbances (GMDs) are grave concerns for the electric power grid. These two events, through different means, both produce geomagnetically induced currents (GICs) on long transmission lines.<sup>1</sup> These GICs are quasi-DC in nature in that they do not change fast with respect to the 60Hz power system. Therefore, these quasi-DC currents pose a serious threat to large power transformers (LPT) because the amplitude of GICs from HEMP and GMDs are large enough to saturate the core of the LPT, resulting in potentially fatal damage and large amounts of reactive current consumption.<sup>2</sup> This large amount of reactive power consumption takes the form of heat and due to the temperature increase can cause damage to the insulation and windings of the transformer.<sup>3</sup>

GICs flow through the power system through long transmission lines and back to ground via grounded neutrals on the transformers. If these ground paths are removed, GICs will not flow within the transmission system. The electric field magnitudes from E3 can be on the amplitude of up to 35 V/km<sup>4</sup> which can affect shorter length transmission and distribution. However, GMD is typically in the range from 1–6 V/km;<sup>5</sup> therefore, high voltage potential difference can only be built up on longer lines, and for power systems, these will primarily be extra high voltage (EHV) transmission lines. This is because of the longer line lengths and lower average resistance. Therefore, EHV transmission lines typically have more induced DC current and transformers in the EHV system will experience higher levels and longer times of saturation. This can impact the electric power grid significantly because the EHV system is critical backbone for routing large amounts of power over long distances from large generation to large loads in the bulk power system.<sup>6</sup>

Several different techniques have been proposed to solve or mitigate this problem,<sup>2a7,8</sup> but in this paper we put forward an alternative solution. Here, it is proposed to add a device to the neutral of the high voltage winding of LPTs which would inject a DC bias, equal to the quasi static DC bias from GICs, theoretically to float the transformer windings by the few volts removing the voltage differential in the power lines from HEMP or GMD. This research is a proof of concept from simulation to a low voltage benchtop system for testing. This design was tested in Typhoon and PLECS modeling software. Design schematics and model simulation results are presented and compared. Then, a low voltage single phase hardware benchtop system was designed, fabricated, and tested. The test setup is described, and the data gathered from this test is presented. Finally, comparison to high voltage simulation results and low voltage experimental results are presented to show the theoretical functionality of the proposed protection method.

## Approach

The GIC protection device (GPD) is comprised of a h-bridge inverter with a capacitor, resistor and DC voltage source on the DC side, and a LC filter on the h-bridge output in parallel with a resistor. The GPD is attached on the neutral of the high voltage winding of LPTs, which would inject a DC bias, equal to the quasi static DC bias from GICs, see Figure 1. Theoretically, this floats the transformer windings by the amount of DC GIC volts, removing the voltage differential in the power line from HEMP. This research was proof of concept from simulation to a low voltage benchtop system for testing. Final comparison of the high voltage simulation results and low voltage experimental results show the theoretical functionality of the proposed method works.

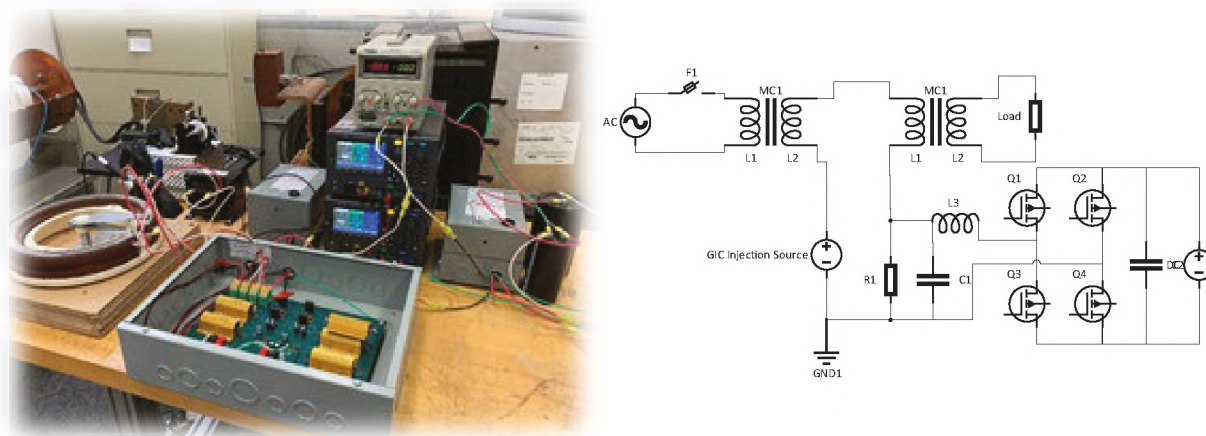


Figure 1: GPD Experimental Setup and Schematic Diagram.

## Results/Discussion

With most of the simulations done during the previous FY, the goal of the hardware benchtop test was to demonstrate that the results seen in the simulations are achievable in the real world. Often, simulations do not, or cannot, capture the complexities of real circuits. First, as a baseline, data was collected with the system set at 70% of its max input, with the GPD disconnected from the system, the transformer neutral

connected directly into the power supply negative terminal, and no GIC. The 70% input allows for the operation of the benchtop system without getting close to its operating limits, and thus avoiding any saturation that may happen at those operating limits. The results can be seen in Figure 2. This waveform is free from saturation and provides a clean signal that can be utilized to compare future waveforms.

Next, it is important to understand how the system will respond without the GPD but under GIC. 8.7 VDC was used for the GIC voltage input from the power supply. This was chosen as it is large enough to elicit a large amount of half-cycle saturation, allowing the GPD to better demonstrate its protection capabilities. The input current to the system under test with 8.7 VDC GIC can be seen in Figure 3. The waveform can be seen with half-cycle saturation on both the positive and negative cycles of the current waveform. In the current testing topology, there are two transformers present. The DC is also in different polarities across the two transformers. This causes one transformer to saturate in the negative region and the other to saturate in the positive region. Therefore, the source must supply both saturation currents and sees two half cycle saturation waveforms superimposed on top of the 60 Hz load current. Without the GPD connected and running, the peak-to-peak current has more than doubled. The base waveform was not affected by saturation and has remained unchanged.

Now that the system's baseline and GIC current responses have been demonstrated, the GPD was added to the circuit, and the system's current waveform with 8.7 VDC GIC and the GPD set at 80% duty cycle (for a 9.0 VDC output). The GPD was set at 9 V, slightly above the 8.7 V GIC, because of the losses inside the GPD. The waveform can be seen in Figure 4.

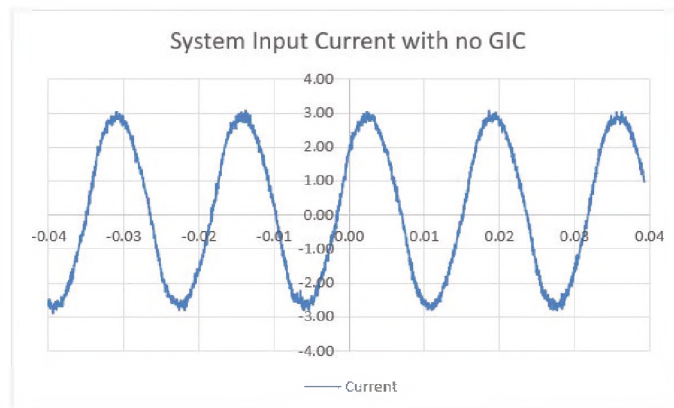


Figure 2: Input current as measured by the CT with no GIC.

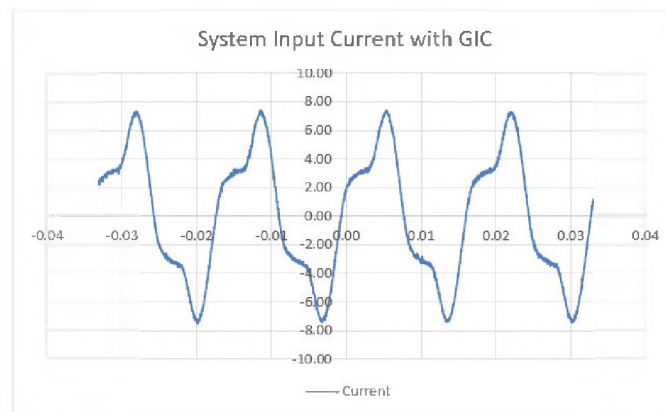


Figure 3: Current Absorbed by the Test System with 8.7VDC GIC Input.

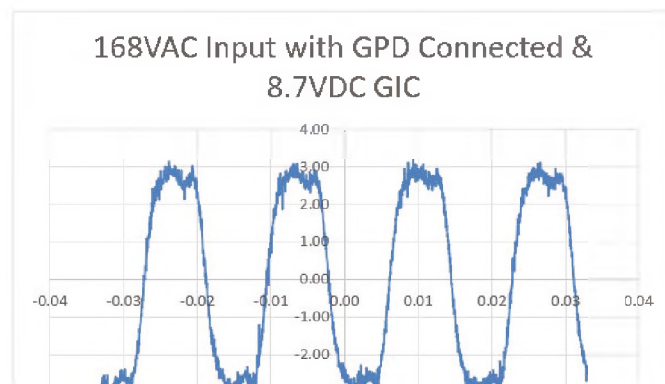
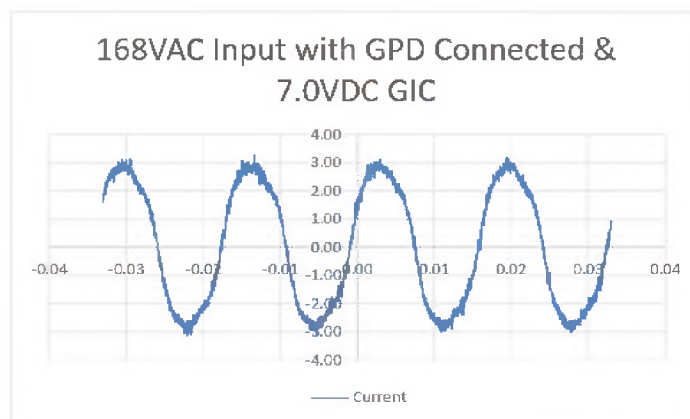


Figure 4: Current Waveform with GPD connected with 8.7VDC GIC.

The half-cycle saturation humps have been drastically reduced, though not completely removed, and the peaks and troughs of the graph are noisier than before. Overall, a comparison between Figure 3 and Figure 4 demonstrates the GPD's ability to bias the transformers voltage differential from GICs and reduce the saturation effect. However, the remaining presence of saturation as evidenced by the slight half-cycle current humps indicates that the expected losses were greater than calculated. It turns out that the small accommodation made for losses was not nearly enough. To account for these losses, the GIC voltage was adjusted down to 7 VDC with the GPD output held constant at 80% duty cycle. This imitates a situation where the total losses have been calculated, and the output has been biased up to account for them. The current waveform with the GIC adjusted to 7.0 VDC can be seen in Figure 5. From these results it is clear the GPD benchtop system is capable of compensating for the electric potential differential across transmission lines from HEMP or GMD thus causing GIC to not flow through the transformer coils.



**Figure 5:** Current Waveform with 7VDC and GPD Connected with 80% Duty Cycle.

## FY2020 Accomplishments

- One provisional patent submitted and will be finalized this fiscal year
- Five peer reviewed journals and two conference submissions
- Working with Clemson professor, and PhD student, developed code to perform grid support functionality
- Coded control algorithms on microcontroller and successfully testing using Typhoon CHIL
- Designed and Built prototype device and motherboard to allow for bench testing
- Built Bench Test System to check device operation
- Successfully removed half-cycle saturation current that was 200% of rated amplitude

## Future Directions

SRNL will integrate this GPD into the Distribution Substation Testing Facility that SRNL is building. From there it will be tested on distribution transformers and those and these results will be presented to DOE AMO and TRAC offices for funding for technology transition and further testing.

## FY 2020 Peer-reviewed/Non Peer-reviewed Publications

- M. Nazir, K. Burkes and J. Enslin, "Converter-based Power System Protection against DC currents in Transmission and Distribution Networks," in *IEEE Transactions on Power Electronics*, vol. 35, no. 7, Dec. 2019.
- M. Nazir, K. Burkes, M. Babakmehr, F. Harirchi and J. H. Enslin, "Transformerless Converter-based GMD Protection for Utility Transformers," *2020 IEEE 35th Applied Power Electronics Conference (APEC)*, NewOrleans, LA, USA, 2020.

- M. Nazir, J. H. Enslin and K. Burkes, "Enhanced Grid Stability through GIC elimination and Grid Support," *2020 IEEE 11th Conference on Innovative Smart Grid Technologies (ISGT)*, Washington, DC, USA, 2020.
- M. Nazir, J. H. Enslin and K. Burkes, "Solar Farm Harmonic Analysis and Operation under DC currents," *2020 IEEE 11th International Symposium on Power Electronics for Distributed Generation Systems (PEDG)*, Dubrovnik, Croatia, 2020, In press.
- M. Nazir, K. Burkes, and J. H. Enslin, "Converter-Based Solutions: Opening New Avenues of Power System Protection Against Solar and HEMP MHD-E3 GIC," Accepted to IEEE Transactions on Power Delivery
- M. Nazir, K. Burkes, and J. H. Enslin, "Electrical Safety Considerations of Neutral Blocker Placements for Mitigating DC Currents," Submitted to IEEE Transactions on Industry Applications.
- M. Nazir, K. Burkes, and J. H. Enslin, "Transformation of Traditional Grid Transformers into Hybrid Smart Transformers," Submitted to IEEE Transactions on Power Electronics.
- V. Ceyskens, K. Burkes, "Simulation and Testing of a GIC Protection Device on Transformer," Submitted to IEEE Transactions on Power Electronics.

## References

1. Albertson, V. D.; Bozoki, B.; Feero, W. E.; Kappenman, J. G. Larsen, E. V.; Nordell, D. E. Ponder, J.; Prabjakara, F. S.; Thompson, K.; Walling, R. Geomagnetic Disturbance Effects on Power Systems. *IEEE Transactions on Power Delivery* **1993**, *8* (2), 1206 - 1216.
2. Glibert, J.; Kappenman, J. Radasky, W.; Savage, E. *The Late-Time (e3) High-Altitude Electromagnetic Pulse (HEMP) and Its Impact on the U.S. Power Grid*. Oak Ridge: Federal Energy Regulatory Commission, 1-3.; 2010 [https://www.ferc.gov/industries/electric/industry/reliability/cybersecurity/ferc\\_meta-r-321.pdf](https://www.ferc.gov/industries/electric/industry/reliability/cybersecurity/ferc_meta-r-321.pdf). (Accessed December 2019).
3. Horton, R. "Perspective on Protecting the Electric Grid from an Electromagnetic Pulse or Geomagnetic Disturbance." Washington D.C.: Hearing of the U.S. Senate Homeland Security and Governmental Affairs Committee. February 27, 2019.
4. Kappenman, J. *Geomagnetic Storms and Their Impacts on the U.S. Power Grid*. Goleta, CA: Metatech Corporation. January 2010.
5. Kappenman, J. *Low-Frequency Protection Concepts for the Electric Power Grid: Geomagnetically Induced Current (GIC) and E3 HEMP Mitigation*. Oak Ridge: Federal Energy Regulatory Commission. [https://www.ferc.gov/industries/electric/industry-act/reliability/cybersecurity/ferc\\_meta-r-322.pdf](https://www.ferc.gov/industries/electric/industry-act/reliability/cybersecurity/ferc_meta-r-322.pdf). 2010.
6. Molinski, T. S. Why Utilities Respect Geomagnetically Induced Currents. *J. Atmos. Solar-Terrestrial Phys.* **2002**, *64*, 1765-1778.
7. Nazir, M.; Enslin, J. H. Babakmehr, M.. Power System Protection Response Under Geomagnetically Induced Currents. 2020 Clemson University Power Systems Conference, Clemson, SC. 2020.
8. NERC. "Geo-Magnetic Disturbances (GMD): Monitoring, Mitigation, and Next Steps." *April 2011 NERC GMD Workshop*. 2011.
9. NERC. "Geo-Magnetic Disturbances (GMD): Monitoring, Mitigation, and Next Steps." Atlanta GA. 2011.

10. Phillips, T. *Solar Shield--Protecting the North American Power Grid*. NASA. October 26, 2010.. [https://science.nasa.gov/science-news/science-at-nasa/2010/26oct\\_solarshield](https://science.nasa.gov/science-news/science-at-nasa/2010/26oct_solarshield) (Accessed December 17, 2019).
11. Rajapakse, A. D.; et al. Power Grid Stability Protection Against GIC Using a Capacitive Grounding Circuit. *PES T&D 2012*. Orlando. 2012.
12. Nobuo, T.; Oshu, T.; Miyawaki, F.; Saito, S.; Fujiwara, Y. An Experimental Analysis of DC Excitation of Transformers by Geomagnetically Induced Currents. *IEEE Trans. Power Deliv.* **1994**, *9* (2), 1173-1182.

## Acronyms

LPT	Large Power Transformer
HEMP	High-altitude Electro-magnetic Pulse
GMD	Geo-Magnetic Disturbance
GIC	Geo-magnetically Induced Current
GPD	GIC Protection Device

## Intellectual Property

- K. Burkes, V. Ceysens, J. Enslin, M. Nazir, "E3 EMP/GMD Compensation for Large Power Transformers through Neutral Current DC Injection," SRS Invention Disclosure SRS-20-004.
- K. Burkes, V. Ceysens, J. Enslin, M. Nazir, "DC Compensation for Power Transformer Through Neutral DC Injections," Provisional Patent Number 62/989,004

## Post-Doctoral Researchers

- Mohammad Babakmehr: off-site at Clemson
- Farnaz Harirchi: off-site at Clemson

## Student Researchers

- Septimus Boshoff: off-site Clemson Master Student
- Moazzam Nazir: off-site Clemson PhD Student

## Time Domain Thermoreflectance and Photodeflection Signatures of He Bubbles in Metals

**Project Team:** Eliel Villa-Aleman, Amanda L. Houk, Don D. Dick, Dale A. Hitchcock, Don D. DeWayne, Paul S. Korinko

**Project Start Date:** October 1, 2018

**Project End Date:** August 21, 2020

*The mechanical properties of the steel and weldments for different components are affected by the formation of helium bubbles as a result of tritium decay. Therefore, periodic analyses of metals exposed to tritium gas are conducted to determine structural defects and temporal damage from tritium gas decay and He precipitation. Transmission electron microscopy (TEM) and autoradiography are the current analytical methods for the evaluation of metal damage. These methods are functional after several years of damage to the crystal lattice where  $^3\text{He}$  bubble formation damage can be seen with TEM. New analytical methods that can assess the*

*damage to the crystal lattice early during the exposure to tritium are highly sought to ascertain the effects of material processing and tritium interactions. Further, simple sample preparation, compared to TEM, at a significantly reduced cost is highly desirable. A pump-probe laser technique using a femtosecond laser has been demonstrated to measure the thermal diffusivity of different materials. The time domain thermoreflectance (TDTR) laser setup can provide thermal diffusivity and phonon lifetime, which can be correlated with lattice damage. This advanced nonlinear optical technique will enable measurements of nanostructure damage in the metal before and after tritium exposure within a year. This report discusses current efforts in the design and development of the technique and the application to material characterization.*

### FY2020 Objectives

- Demonstrate the concept of pump-probe laser setup for thermal characterization and phonon time domain to measure lattice damage
- Demonstrate that a pump-probe laser experiment with a high repetition rate femtosecond laser can be used to characterize crystal lattice
- Complete design and build experimental breadboard for time domain thermoreflectance (TDTR) and Transient Incoherent anti-Stokes Raman spectroscopy (TRIARS)
- Acquire tritiated samples and test materials with known damage in a clean laboratory

### Introduction

Periodic analyses of reservoirs filled with tritium are conducted at the Tritium Facility to determine the effects of tritium to the stainless steel and the temporal damage from helium (He) precipitation (Figure 1a). The mechanical properties of the walls and pinch weld of the tritium vessels are affected by the tritium decay resulting in the formation of He bubbles (Figure 1b). Transmission electron microscopy (TEM) and autoradiography are the current analytical methods for the evaluation of the reservoir metal. These methods are functional after several years of damage to the crystal lattice where  $^3\text{He}$  bubble formation damage can be seen with TEM (Figure 1c and d). New analytical methods that can assess the damage to the crystal lattice early during the exposure are highly sought to ascertain the effects of material processing and tritium interactions. Further, simple sample preparation, compared to TEM, can be done at a significantly reduced cost. An ultrafast pump-probe laser technique is a potential innovative approach to this problem, where only 20  $\mu\text{m}$  of material is required for analysis.

The time domain thermoreflectance (TDTR) technique will enable measurements of nanostructure damage in the metal before and after tritium exposure within a year. If this work is successful will result in significant savings to the program (short turnaround analysis) and could help provide new directions for research on new materials, effects of processing, metal coatings and new designs for tritium storage systems. This work is also applicable to other tritium production and storage products, such as tritium producing burnable absorber rods (TPBARS). This new technology will enhance SRNL's reputation as the leader for tritium storage research through years to come, which can result in significant funding from NNSA Weapons Programs. This report discusses current efforts in the design and development of the TDTR technique and the application to material characterization.

## Approach

Paddock *et al.*<sup>1</sup> in 1986 demonstrated for the first-time thermal diffusivity measurements from thin metal films using picosecond transient thermoreflectance to measure the thermal properties of metal films as thin as 100 nm. The thermal conductivity of the material is based on an ultrafast heating pulse inducing a change in the index of refraction of the material, and therefore a change in the optical properties. The ultrafast pump-probe technique is a two-laser beam technique that depends on one laser for heating the surface (pump), while another laser probes the heating effect on the material via reflection (Figure 1). Technology has evolved using a femtosecond laser instead of a picosecond laser, different colors for the pump and probe (better discrimination) and the optical modulation of the laser beam to enhance the signal-to-noise ratio. Additional improvements have been added with the interference of two optical beams reflected from the front surface and scattering depth. These improvements have resulted in the understanding of thermal properties of nanoparticles with dimensions less than 10 nm. Other variants include the ultrafast demagnetization of a sample while probing its recovery, such as the magneto-optical Kerr effect.

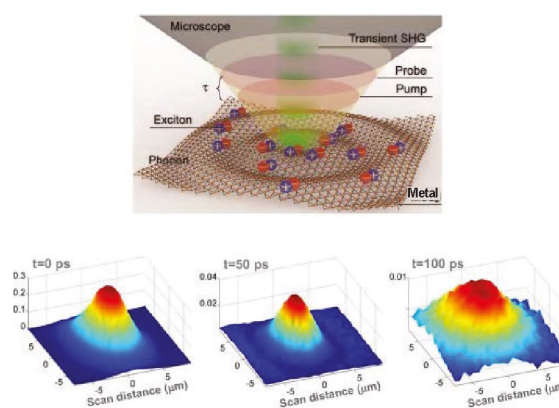


**Figure 1:** The pump-probe temporal surface dynamics.

The advances in pump-probe laser technologies can be used to demonstrate the detection and quantification of damage in materials. The beta decay of tritium results in the formation of <sup>3</sup>He, which precipitate in bubbles. The <sup>3</sup>He precipitates damage the metal crystal lattice producing phonon scattering points. Phonons (collective excitation in a periodic, elastic arrangement of atoms or molecules in condensed matter) produced during the laser heating pulse travels through the crystal lattice until thermalization. The presence of defects in the lattice shortens the phonon lifetime. This effect will be valuable to determine the crystal lattice damage by the beta decay and precipitation of He bubbles.

Since metals do not show Raman bands, the best option is to measure the phonon lifetime based on thermal conductivity. Previous work by Weisensee *et al.*<sup>2</sup> measured the effect of ion irradiation on the thermal conductivity of UO<sub>2</sub>, and U<sub>3</sub>O<sub>8</sub> using TDTR. Thermal conductivity measurements via TDTR were also used to characterize radiation-induced damage of ZIRLO<sup>3</sup>, a low oxidation Zircaloy, and in silicon. Lattice impurities have been shown to affect the thermal conductivity of materials. For instance, oxygen impurities changed the thermal conductivity of beta-Si<sub>3</sub>N<sub>4</sub> from 120 W/m-K to 88 W/m-K.<sup>4</sup> The same techniques can be used to study acoustic and optical phonons in a material.

## Results/Discussion

A TDTR setup was assembled on a laser table adjacent to the Astrella laser to take advantage of the Vitara oscillator laser (80 MHz, 35 fs) embedded within the Astrella laser system. Our TDTR setup was developed as a two-tint pump-probe technique, meaning the pump and probe wavelengths are split into two beams from a single broadband beam and the wavelengths of the two beams are only separated by  $\sim 10 \text{ nm}^5$ . In addition, to the assembly and alignment of the TDTR setup, programming to control the delay stage, lock-in amplifier and spectrograph is underway. Thermal code is also being written to extract thermal conductivity and capacitance information from the collected TDTR data. Figure 2a shows the schematic of our TDTR setup and Figure 2b shows a photo of our actual laboratory setup.

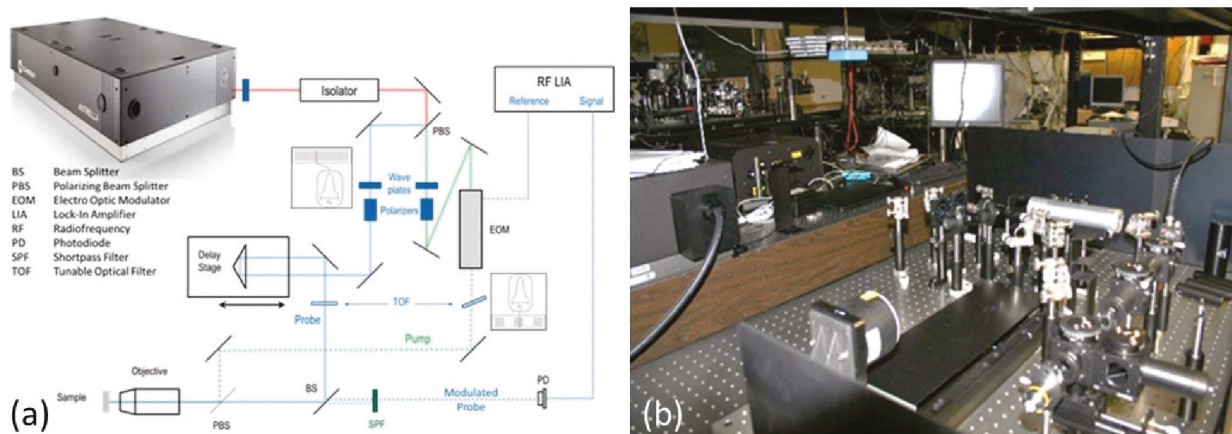


**Figure 2:** (a) Pump-probe experimental setup (TDTR) under development and (b) actual pump-probe TDTR experimental setup under development.

A sample cell tested by the SRNL/Defense Programs to transport tritiated materials in an inert, argon atmosphere was selected as a sample holder for this program. A plan for the transfer of tritium-loaded samples to a clean laboratory was discussed with Radiological Protection and was approved. A sample from PNNL containing tritium was also received for this program.

## FY2020 Accomplishments

- Covid-19, technical problems with the laser, and early termination of the LDRD project affected significantly the outcome and results of this project
- Different TDRD and TRIARS setups were designed for this project
- A system based on a single broadband wavelength laser with two filters (two-tint) was chosen for this project
- Components for TDRD breadboard were procured and assembled
- The TDRD setup was assembled next to the Astrella laser to take advantage of the embedded 80 MHz, 35 fs oscillator laser
- Initial laser beam alignment through the TDRD system was complete
- Programming to control stage, lock-in amplifier and spectrograph is underway
- A tritiated sample in argon atmosphere was brought for analysis
- Discussions with the Tritium Facility resulted in the preparation of samples with tritium for delivery to SRNL
- Modulation of the laser beams and observation of the modulation was measured with a lock-in amplifier
- A coherent anti-Stokes Raman spectrometer setup was modified for TRIARS measurements

## Future Directions

- The thermal conductivity and capacitance will be measured for several materials to ensure the instrument is properly calibrated
- After the repair of the Vitara laser, the equipment will be used for NA22 funded project
- Samples with known dosage and time exposed to tritium will be investigated

## References

1. Paddock, C. A.; Eesley, G. L. Transient Thermoreflectance From Thin Metal Films. *J. Appl. Phys.* **1986**, *60* (1), 285-290.
2. Weisensee, P. B. Feser, J. P. Cahill, D. G. Effect of Ion Irradiation on the Thermal Conductivity of UO<sub>2</sub> and U<sub>3</sub>O<sub>8</sub> Epitaxial Layers. *J. Nucl. Mater.* **2013**, *443*, 212-217.
3. Cheaito, R.; Gorham, C. S.; Misra, A.; Hattar, K.; Hopkins, P.E. Thermal Conductivity Measurements Via Time-Domain Thermoreflectance for the Characterization of Radiation Induced Damage. *J. Mater. Res.* **2015**, (09), 1403-1412.
4. Yokota, H.; Ibukiyama, M. Effect of LATTICE IMPURITIES on the THERMAL CONDUCTIVITY of  $\beta$ -Si<sub>3</sub>N<sub>4</sub>. *J. Eur. Ceram. Soc.* **2003**, *23* (1), 55-60.
5. Kang, K.; Koh, Y. K. Chiritescu, C.; Zheng, X. Cahill, D. G. Two-Tint Pump-Probe Measurements Using a Femtosecond Laser Oscillator and Sharp-Edged Optical Filters. *Rev. Sci. Instrum.* **2008**, *79*, 114901.

## Acronyms

ASL	Advanced Spectroscopy Laboratory
He	Helium
TDTR	Time Domain Thermoreflectance
TEM	Transmission Electron Microscopy
TPBARS	Tritium-Producing Burnable Absorber Rods

## Post-Doctoral Researchers

Don D. Dick, on site at SRNL

## Collaboration with USACyS for Signals Manipulation

**Project Team:** Mackenzie Morris Klaehn  
Burkes, Jon Dollan

**Project Start Date:** October 1, 2018  
**Project End Date:** September 30, 2020

*Savannah River National Laboratory has been investing into cybersecurity capabilities since 2019. Cybersecurity has been a rapidly growing area for the CSRA in general and has included the consolidation of Cyber and Electronic Warfare units at Fort Gordon. This consolidation has been driven by the convergence of cyberwarfare and electronic warfare as the technologies*

*underpinning Army Cyber Command's vision of Information Warfare. This convergence, investment by SRNL into cybersecurity for critical infrastructure, and the desire for collaboration between the Army and SRNL has resulted in an opportunity for SRNL to develop R&D capabilities in electronic warfare that will complement SRNL's cybersecurity efforts. Discussions between SRNL and the U.S. Army Cyber School (USACyS) has identified a general gap in ICS training lab capability in which both entities could contribute to solve. It is proposed to design and architecture that meets this need.*

### FY2020 Objectives

- Develop virtual ICS architecture that allows soldiers the ability to train with minimal hardware
- Establish encrypted GNSS capability into SRNL Critical Infrastructure, ICS and Cybersecurity (S-CIIC) lab
- Establish a Strategic Partnership Projects (SPP) Agreement with Cyber Center of Excellence

### Introduction

The Central Savannah River Area, or CSRA, has seen a significant increase in investment into Cybersecurity over the last few years. Fort Gordon has been designated as the location that will consolidate the Army Cyber School, Army Cyber Command Headquarters, Information Warfare Operational Commands, and Electronic Warfare Units. SRNL is in the process of investing into developing capabilities and personnel who can tackle high level R&D projects in cybersecurity. The lab's focus has been industrial control system (ICS) security, which more broadly is part of critical infrastructure. This area is of interest to the Army, as critical infrastructure is important for national defense, but also because electronic warfare techniques are becoming increasingly applicable to cyber-attacks on ICS as these systems become more dependent on advanced electronics and communication systems. The proximity of SRNL and Fort Gordon, and mutual interests in national security, inevitably resulted in dialogue between the two entities.

In these discussions, the Army has expressed that they are seeking to advance their training laboratory capability in ICS security. They would like to work with SRNL Cyber Security Programs, which has experience in ICS equipment and laboratory implementation, to scope and execute a proof of concept for a novel method emulating an ICS environment with minimal hardware components that allow for cyber students to train. Development of this system will set SRNL apart since this capability is still being sought by the Army. The Army's contribution to the collaboration will include rotating personnel to SRNL to work directly with engineers during all stages of this project.

With the completion of a successfully developed architecture, it is expected that fully implementing the architecture will be initiated via a SPP on the part of the Army. This initial investment will allow SRNL to build that trust and relationship as well as the capability and personnel to continue to engage in this area of research. Success in this area will define a new area of expertise for the lab and allow us to pursue funding opportunities in advanced signaling and communications.

## Approach

SRNL and the USACyS identified that in order to do research into hardening systems from electronic warfare, training ranges with the equipment and capabilities of operational systems must be established. Therefore, SRNL identified and developed an architecture using equipment already owned by SRNL to create 8 interactive training ranges that cover multiple different ICS components. 6 of these ranges consist of factory floor ICS equipment, 1 range represents the electric grid feeding power to these factories, and finally a full virtualized SCADA system provides access into all the previous developed ranges. This along with an encrypted GNSS simulator allows for SRNL to emulate many different environments the army is currently active.

## Results/Discussion

Through this project SRNL built a working relationship with the USACyS and also established new capability within the S-CIIC for encrypted GNSS simulation, PLC programming, and virtual SCADA architecture design. These were all gaps in SRNL's capabilities before this LDRD. It was identified by the USACyS that GNSS simulation is very important for a controlled lab environment but to collaborate fully SRNL needed encrypted communication capability. This led to SRNL research and demonstrating several GNSS simulators' capabilities before identifying the BroadSim GNSS simulator as the most flexible and cost effective. BroadSim uses software defined radios to allow for the same radio to perform multiple GNSS constellation communication capabilities. This was the only system that did not use custom radios for each GNSS constellation and thus reducing the cost by a factor of 10. The BroadSim platform is an advanced jamming and spoofing Navigation Warfare (NAVWAR) system that can perform high dynamics, jamming, spoofing, and encrypted military codes. The system is capable of simulating multiple constellations through the software defined radios such as GPS, GLONASS, Galileo, BeiDou, and QZSS. This system is critical for any Army NAVWAR collaboration.

Another achievement of this project was identifying a cost savings of \$1.7M and executing the recovery of this equipment. Through the monitoring of the excess system at SRNS and with the closure of several projects and a mission at the SRS, a selection of equipment was identified that contained enough PLC and accessory components to build about 15 full ICS environment with redundant PLCs and over 1000 I/O modules.

Through this recovery SRNL built the capability to program PLCs and emulate the factory floor utilizing a simulation platform called FactoryIO. With this gained expertise SRNL was then capable of executing the foundational objective of this project which was to develop the architecture for a training system for USACyS. Through one strategic hire and internal personnel developing new skill sets from the recovered equipment, SRNL designed a training platform that would consist of minimal hardware, 6 PLCs and 6 Relays with just two platforms used to simulate the SCADA system and the power grid. The architecture, which is emulating real world capability and functionality, resulted in overwhelming support from USACyS and also the desired replication by the Army Cyber Protection Brigade. USACyS executed a SPP with SRNL to build the designed architecture and thus accomplishing the main objective of this project, thus establishing SRNL as the USACyS's location for ICS cybersecurity hands-on training.



Figure 1: BroadSim NAVWAR GNSS simulator.

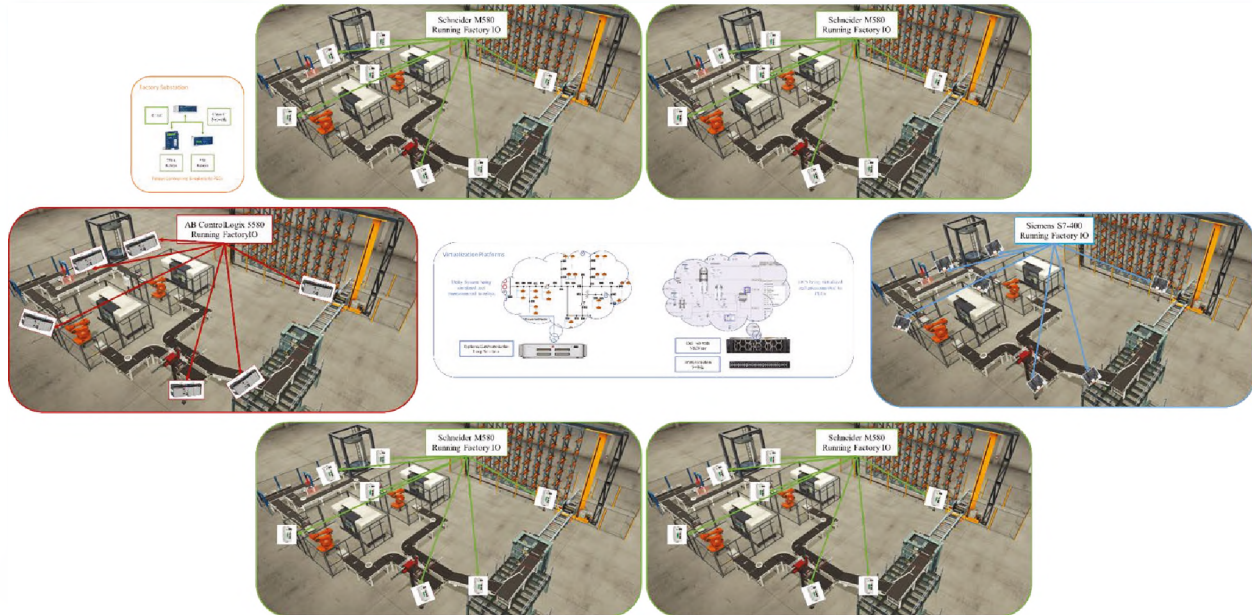


Figure 2: Proposed Architecture for USACyS Training System.

## FY2020 Accomplishments

- SRNL and USACyS have entered a strategic partnership project (SPP) agreement in which SRNL builds an ICS training platform integrated with the S-CIIC. This establishes SRNL as the location for USACyS's hands-on training mission
- Received \$300k follow-on funding for building the architecture developed in the project
- Cost savings of \$1.7M is Schneider PLC equipment recovery from excess
- One strategic PLC programmer hire

## Future Directions

SRNL will execute J-SOW-A-00031 to build the architecture developed and get the system operational for the Army Cyber Center of Excellence.

## Acronyms

GNSS	Global Navigation Satellite System
NAVWAR	Navigation Warfare
PLC	Programmable Logical Controller
S-CIIC – SRNL	Critical Infrastructure, ICS, and Cybersecurity
SPP	Strategic Partnership Project
USACyS	US Army Cyber School

## Fundamental $^{235}\text{U}$ Uranium Nuclear Resonance Spectroscopy

**Project Team:** A. Taylor Baldwin,  
Jonathan Christian, Thomas Shehee,  
Michael Bronikowski, Bryan Foley

**Naval Research Laboratory Collaborators:**  
Christopher Klug, Joel Miller

**Project Start Date:** October 1, 2019  
**Project End Date:** September 30, 2022

*Uranium-235 is ubiquitous in the nuclear industry however, detailed characterization by magnetic resonance spectroscopy has remained largely elusive to-date. Conventional nuclear magnetic resonance techniques are ill-suited for characterizing  $^{235}\text{U}$  due to the small gyromagnetic ratio and extremely large quadrupole moment of this spin  $7/2$  isotope. Thus, we propose to develop a nuclear quadrupole resonance instrument and method for measuring the quadrupole resonance of this important isotope. A successful nuclear quadrupole resonance measurement of  $^{235}\text{U}$  would be a significant accomplishment and could yield valuable*

*physical parameters such as chemical shifts, local electric field gradients, and through-bond and through-space internuclear couplings all of which are directly related to local structure. These terms can be used to improve computational modeling of uranium compounds for which accurate reference data is lacking.*

### FY2020 Objectives

- Develop work plan and safety controls
- Set up subcontract with Naval Research Lab (NRL)
- Equip radiological laboratory space for chemical synthesis
- Procure and set up new instrumentation (high-frequency nuclear quadrupole resonance (NQR) at NRL;  $^{19}\text{F}$  NMR probe at SRNL)
- SRNL staff training on NQR at NRL
- Procure depleted and highly enriched uranium certified reference materials
- Generate single-crystal NQR and nuclear magnetic resonance (NMR) samples (recrystallization/synthesis)
- Initial characterization of samples (microscopy, X-ray diffraction [XRD])
- NQR measurements on tantalum reference materials
- $^{19}\text{F}$  NMR measurements of uranium fluoride
- Method development for NQR experiments on uranium

### Introduction

Because of its non-zero spin,  $^{235}\text{U}$  is potentially accessible via magnetic resonance spectroscopy (MRS). However, the gyromagnetic ratio of  $^{235}\text{U}$  is estimated at 0.78 MHz/T, meaning the nuclear magnetic resonance (NMR) frequency,  $\nu$ , of  $^{235}\text{U}$  due to Zeeman splitting in a magnetic field of 11.7 Tesla is 9.13 MHz, compared to 500 MHz for  $^1\text{H}$ . Therefore, conventional NMR spectrometers are inapt at measuring this rare isotope. Furthermore, since signal-to-noise generally scales as  $\nu^{5/2}$ , detection of  $^{235}\text{U}$  NMR at very low frequencies is challenging. The significance of these obstacles is evidenced by the scarcity of magnetic resonance literature pertaining to  $^{235}\text{U}$ . The only published  $^{235}\text{U}$  NMR reference is a two-and-a-half-page letter from 1983 involving 93.5% enriched liquid uranium hexafluoride heated to 380 K. The linewidth at 11.747 T was said to be 20 KHz, but no other relaxation information was given. This work has been rarely cited and most of those papers are theoretical.

Although the predicted NMR frequency of  $^{235}\text{U}$  is extremely low and there appears to be numerous barriers in measuring and analyzing an NMR signal from this isotope, the nuclear quadrupole resonance (NQR) of  $^{235}\text{U}$  is predicted to be near 1 GHz. This is over two orders of magnitude larger than the conventional NMR frequency, meaning that the quadrupole term is likely the dominant energy term in the  $^{235}\text{U}$  nuclear spin Hamiltonian. Therefore, direct measurement of this term would be a significant scientific achievement and should give further insight into the magnetic properties of this important isotope.

In this project, SRNL has combined its unique expertise in the preparation of high-purity, highly-enriched nuclear materials with the U. S. Naval Research Laboratory's (NRL) extensive experience in the application of MRS, including NQR, to attempt measurement of the nuclear quadrupole resonance spectrum of  $^{235}\text{U}$ . In fiscal year 2020 (FY20), SRNL developed robust methods for producing high quality single crystals of two different uranium compounds –  $\text{UO}_2(\text{NO}_3)_2 \cdot 6\text{H}_2\text{O}$  (with  $^{15}\text{N}$  enrichment) and  $\text{U}_3\text{F}_{12}$ . SRNL and NRL also designed and procured components for a homebuilt NQR spectrometer capable of measuring MRS up to 3 GHz without the need to heterodyne the resonance excitation source. Preliminary functional tests of this instrument will be performed using tantalum-halide reference materials in late FY20, early FY21.

## Approach

Uranium-containing single crystals were produced using modified published methods, including recrystallization and hydrothermal synthesis. These crystals are amenable to both NQR and  $^{15}\text{N}$  and  $^{19}\text{F}$  NMR measurements, which will be conducted in FY21.

A homebuilt NQR spectrometer was designed and all components were procured in FY20 to allow assembly of a new high frequency NQR spectrometer in early FY21. Our homebuilt system includes a Pasternack 48 dB gain and 50 W high power GaN amplifier, multiples heat sinks, a Pasternack 51 dB gain and 100 W high power LDMOS amplifier, a Pasternack frequency synthesizer module with phase locked loop with 35 MHz – 4.4 GHz output, multiple Aim-TTi PowerFlex DC power supplies, and a compact, modular, NMR / MRI / NQR Tecmag Redstone console configurable with multiple transmitters, receivers, and gradient channels. With its numerous options, the Redstone can be configured for any magnetic resonance application in the frequency range from 2 kHz to 3.5 GHz and does not require manual heterodyning of excitation signals.

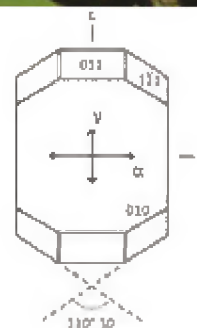
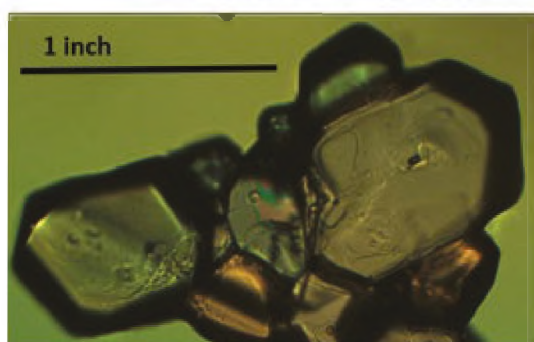
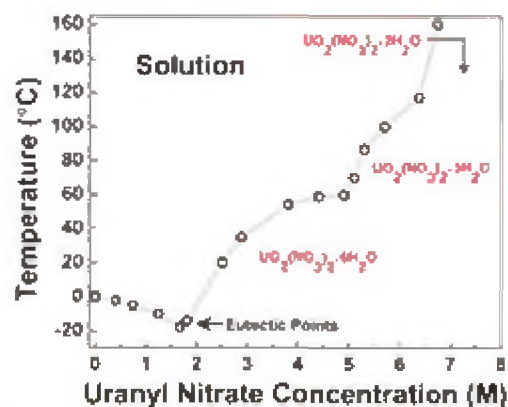


**Figure 1:** Top: The phase diagram of uranyl nitrate was used to develop a robust method for producing high quality single crystals of  $\text{UO}_2(\text{NO}_3)_2 \cdot 6\text{H}_2\text{O}$ . Middle: Micrograph of multiple single crystals of  $\text{UO}_2(\text{NO}_3)_2 \cdot 6\text{H}_2\text{O}$ . Bottom: Illustration of the crystallographic shape and axes for  $\text{UO}_2(\text{NO}_3)_2 \cdot 6\text{H}_2\text{O}$  crystals.

## Results/Discussion

Due to the radiological nature of the materials synthesized and analyzed in this project, numerous logistical steps were required prior to commencement of experimental work. A few of these steps included, acquisition of 50 g depleted  $\text{UO}_2$ , acquisition of enriched uranium certified reference materials, removal of legacy waste ( $^{76}\text{Kr}$ , SS with trace Be,  $^{137}\text{Cs}$ ) to create space for experiments, and activation of two new radiological gloveboxes in a newly remodeled lab module for highly-enriched uranium experiments. The latter step was a large undertaking that required installation of safety significant components to new gloveboxes followed by facility approval and activation of the lab space. Utilization of this remodeled lab module provides benefits to both safety and scientific quality for the future aspects of this and other projects within SRNL.

Synthesis of  $\text{UO}_2(\text{NO}_3)_2 \cdot 6\text{H}_2\text{O}$  (UNH) with  $^{15}\text{N}$  enrichment occurred via slow dissolution of depleted  $\text{UO}_2$  in an excess (4:1 molar ratio) of  $^{15}\text{N}$ -enriched nitric acid at  $55^\circ\text{C}$ . During this dissolution, the hazy black  $\text{UO}_2$  mixture became clear and yellow indicating formation of UNH. If allowed to slowly cool, single crystals of UNH typically precipitate from this solution within a week. Due to the hygroscopic nature of UNH, it is imperative to target a solution concentration close to a eutectic point in the UNH phase diagram (Figure 1 top).

$\text{U}_3\text{F}_{12}(\text{H}_2\text{O})$  was synthesized via a mild hydrothermal route using depleted  $\text{UO}_2(\text{CH}_3\text{CO}_2)_2 \cdot 2\text{H}_2\text{O}$ ,  $\text{Cu}(\text{CH}_3\text{CO}_2)_2 \cdot 2\text{H}_2\text{O}$ , and dilute HF.<sup>1</sup> First,  $\text{UO}_2(\text{CH}_3\text{CO}_2)_2 \cdot 2\text{H}_2\text{O}$  was synthesized by dissolving  $\text{UO}_3$  in a small amount of nitric and acetic acid in a hot water bath at  $100^\circ\text{C}$  for over 24 hours. Crystalline solids of  $\text{UO}_2(\text{CH}_3\text{CO}_2)_2 \cdot 2\text{H}_2\text{O}$  were then filtered and utilized in subsequent hydrothermal reactions. For hydrothermal reactions, the mixture of reactants was placed into a 23 mL Teflon-lined autoclave that was sealed, heated to  $200^\circ\text{C}$ , held for 24 h at this temperature, and cooled to room temperature at approximately  $6^\circ\text{C}/\text{hour}$ . Needle crystals were obtained, and remaining copper was selectively removed by dissolving in concentrated nitric acid. For both UNH and  $\text{U}_3\text{F}_{12}$ , preparation and planning for use of these techniques with enriched uranium was completed and enriched uranium experiments are expected to commence in early FY21.

## FY2020 Accomplishments

- Completed HAS and all associated safety documentation
- Completed 3yr subcontract with NRL
- Procured crystal synthesis equipment
- Cleaned out radiological hoods in 735-A and set up synthesis equipment (Figure 2)
- Oversaw and promoted the activation of new radiological gloveboxes in 773-A (Figure 3)
- Submitted monthly update reports
  - Quarterly reports were delivered to the LDRD committee and senior laboratory management.
  - Synthesized large ( $\text{cm}^3$ ) depleted uranyl nitrate hexahydrate crystals using saturated solutions while optimizing growth conditions for single crystals
  - Synthesized  $\text{U}_3\text{F}_{12}(\text{H}_2\text{O})$  via a mild hydrothermal route using depleted  $\text{UO}_2(\text{CH}_3\text{CO}_2)_2 \cdot 2\text{H}_2\text{O}$ ,  $\text{Cu}(\text{CH}_3\text{CO}_2)_2 \cdot 2\text{H}_2\text{O}$ , and dilute HF.
- Designed a novel high frequency NQR spectrometer



**Figure 2:** SRNL researchers evaluate newly formed uranium compounds in a radiological laboratory.

- Procured equipment, including a Redstone TECMAG spectrometer for performance of high frequency NQR experiments
- Refurbished SRNL NMR probe for  $^{19}\text{F}$  measurements
- Developed testing plan for samples submitted to NRL
- NRL prepared equipment and cryostat for initial sample testing using surrogate compounds.
- During telework, drafted two publications on uranium chemistry using existing  $^{19}\text{F}$  NMR data obtained jointly between SRNL and NRL.
- Acquired depleted and highly enriched (>90%) uranium materials for crystal synthesis
- Directly on-boarded one postdoctoral researcher to work on project, brought another post-doc on board to assist with publications.
- Planned tentative shipment schedule to NRL for sample characterization and initial NMR.



Figure 3: SRNL researchers experiment inside a newly activated radiological glovebox in 773-A.

## Future Directions

- NQR instrumentation will be shipped to NRL for assembly and preliminary testing using tantalum-halide compounds
- SRNL researchers will travel to NRL to oversee development of the NQR instrument and to learn experimental techniques
  - Video networking will be utilized if travel restrictions are in place
- Depleted uranium crystals will be analyzed via powder X-ray diffraction
- Depleted uranium crystals will be packaged and shipped to NRL for baseline characterization via  $^{19}\text{F}$  and  $^{15}\text{N}$  NMR
  - If travel is allowed, SRNL PI's will go to NRL to oversee handling of the depleted uranium samples.
- SRNL will commence production of enriched uranium crystals inside one of the new radiological gloveboxes in 773-A C135/139
- SRNL will utilize single crystal X-ray diffraction measurements to study the structural effects of radiological degradation on enriched uranium crystals.
  - If results are fruitful, a publication on this topic is planned.
- Enriched uranium crystals will be packaged and shipped to NRL for baseline characterization via NMR and NQR
  - A publication on baseline NMR measurements is planned.
- Detailed NQR measurements will be performed using the most promising samples from baseline characterizations

## FY 2020 Peer-reviewed/Non Peer-reviewed Publications

Christian, J.; Groden, N.; DeVore II, M.; Baldwin A. T.; Klug, C.; Villa-Aleman, E.; Wellons, M., **Characterizing the Hydrolysis Product  $\text{UF}_4(\text{H}_2\text{O})_{2.5}$  Generated from Neat Water Reactions with  $\text{UF}_4$  at Room Temperature.** Revision submitted to *Dalton Trans.* Sept. 2020.

## Presentations

A poster presentation describing this project was made to representatives from the DOE Office of Science on October 2019.

## References

1. Yeon, J.; Smith, M. D.; Sefat, A. S.; Tran, T. T.; Halasyamani, P. S.; zur Loye, H.-C., U3F12(H2O), a Noncentrosymmetric Uranium(IV) Fluoride Prepared via a Convenient In Situ Route That Creates U<sup>4+</sup> under Mild Hydrothermal Conditions. *Inorg. Chem.* **2013**, 52 (15), 8303-8305.

## Acronyms

FY	Fiscal Year
NMR	Nuclear Magnetic Resonance
NRL	Naval Research Laboratory
NQR	Nuclear Quadrupole Resonance
SRNL	Savannah River National Laboratory
UNH	Uranyl Nitrate Hexahydrate

## Post-Doctoral Researchers

Two post-doctoral researchers performed research on site at SRNL:

- Bryan Foley (Ph.D. Inorganic Chemistry, Texas A&M, 2019)
- Nicholas Groden (Ph.D. Micro/Nanosystems Engineer, Louisiana Tech, 2018)

## Comprehensive Chemical Fingerprinting by Multidimensional GC and Supervised Machine Learning

**Project Team:** Joseph Mannion, Heather Brant, Jiexin Shi

**Clemson University Collaborator:** Sapna Sarupria

**Project Start Date:** October 1, 2019

**Project End Date:** September 30, 2021

*This project leverages advances in machine learning based data analysis techniques and untargeted organic analytical methods to progress nuclear nonproliferation technologies beyond current capabilities. The developed approaches can be used to identify and detect complex chemical fingerprints of facilities of interest. These techniques have been developed for fields such as metabolomics and genomics but have not been applied to nuclear nonproliferation applications. Adaptation of these techniques for volatile organic compound analysis*

*has far reaching application within the scientific community including environmental chemistry, atmospheric physics, and climate sciences.*

### FY2020 Objectives

- Analytical method development for multidimensional gas chromatography analysis of volatile organic compounds
- Training data set collection utilizing multidimensional gas chromatography
- Machine learning based data analysis development utilizing open source data

### Introduction

Volatile organic compound (VOC) collection and analysis techniques have been under development at SRNL for more than two decades for national security applications. Traditionally these approaches have attempted to identify one to two “signature” species that are indicative of a given activity. The shortcoming of these efforts has been the fundamental limitations of a silver bullet approach with regards to organic signatures. VOC production and emissions are complex, highly dynamic, and subject to complicating matters such as holdup, chemical transformations, and complex backgrounds (up to 10,000 unique chemical species have been identified in a single air sample). Despite these challenges, VOC signatures are attractive as their inherent complexity is in part due to their sensitivity to process conditions within a facility; therefore, VOC signatures carry complex process information that can be used to deeply characterize operations.

The major goal of this project is to utilize machine learning based data analysis approaches to develop multi-species chemical signature “fingerprints” of processes relevant to nonproliferation interests. This untargeted approach will assess organic emissions as a comprehensive collection, rather than a “silver bullet” approach, to create more robust and informative chemical fingerprints of activities. The objective is to collect, analyze, and identify patterns present in measured volatile organic emissions from facilities of interest. The product of this work is data collection modalities, machine learning based data analysis algorithms, and a fingerprint database allowing for identification and assessment of activities (ex. process upsets, efficiencies, etc.).

A multipronged approach was taken for project efforts in FY20. The focus at SRNL was analytical method development for comprehensive VOC analysis utilizing the multidimensional gas chromatograph procured in FY19. This system is one of the most powerful commercially available instruments for VOC analysis and

was found to afford ~4 orders of magnitude improved sensitivity (and 1–2 orders of magnitude peak capacity) over traditional GC/MS systems at SRNL. The focus at Clemson University was the development of machine learning based data analysis approaches utilizing the open source EPA Speciate database. This database contains more than 3000 pollution profiles from industrial, commercial, and residential emission sources. Traditional chemometric techniques were compared to the machine learning based approaches with the intent of publishing the results in FY21. Additionally, a variety of machine learning approaches for plume detection were developed at SRNL utilizing historic single-dimensional GC data sets acquired in previous efforts. Efforts in FY21 will focus on merging the newly developed analytical capabilities at SRNL with data analysis methods developed at Clemson University with the goal of demonstrating these techniques in future SRNL sampling campaigns.

## Approach

Multidimensional gas chromatography (MDGC) is an established technique for the analysis of highly complex samples (Figure 1).<sup>1</sup> It is uniquely suited to applications involving complex matrices and hundreds to thousands of analyte species. Thousands of volatile organic compounds have been identified in the atmosphere that arise from both biogenic and anthropogenic sources.<sup>2,3</sup> When MDGC is applied to complex samples and coupled with multichannel detectors, such as mass spectrometers, enormous amounts of data are generated (on the order of gigabytes for a single run). Traditional data analysis methods are not practical with such large data sets; therefore, modern data analysis techniques must be applied that take advantage of the higher order dimensionality of the data sets. These methods convert chemical data into information using algorithms. Machine learning based clustering and pattern recognition is utilized for this work.

The number of applications utilizing machine learning has vastly expanded in recent years; however, limitations, pitfalls, and hurdles exist in the implementation of machine learning techniques to some applications. Analysis of complex VOC emissions is an example of the curse of dimensionality.<sup>4</sup> In essence, when the dimensionality of a problem increases (i.e. the number of chemicals present in a sample) the volume (i.e. data space) grows so quickly that the data becomes sparse. As the number of features (i.e. chemicals) increases, the data (i.e. number of samples) must grow exponentially to maintain accurate representation; for example, a system with 15 features may require millions of samples to accurately classify the system. Application of machine learning techniques for complex systems such as atmospheric VOC analysis containing thousands of features therefore requires implementation of approaches such as dimensionality reduction and feature engineering to overcome this curse of dimensionality.<sup>5</sup> These techniques and various clustering approaches are explored in this work utilizing an adequately complex data set that represents real world data.

## Results/Discussion

The EPA Speciate database was used for data analysis algorithm development. This database contains pollution profiles from more than 3000 industrial, commercial, and residential emission sources (i.e. samples) and over 20,000 unique chemicals (i.e. features). This database represents a high dimensionality

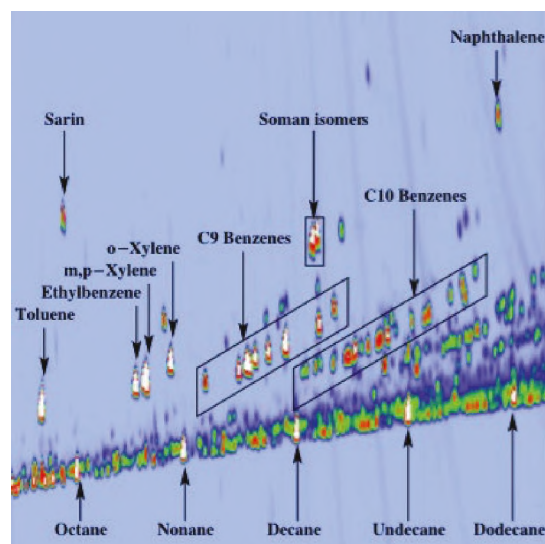


**Figure 1:** Separation of chemical warfare agents from a complex matrix via multidimensional GC.

data set with more features than observations. This situation will likely be encountered in any atmospheric VOC analysis application due to the abundance and variety of VOCs in the atmosphere and the limited analytical throughput of instrumentation (typically 25–60 samples/day for a GC system). The database was first curated to remove spurious and incomplete entries then feature engineered to reduce dimensionality based on chemical features. This was achieved by grouping chemicals with similar chemical functionality using Python and the CAS or SMILES index of a given chemical. This resulted in the reduction of >20,000 features to 54 features representing chemical classifications such as alkanes, alcohols, carboxylic acids, etc. and greatly reduced the sparsity of the data set. The reduced dataset was then subjected to various linear and non-linear data reduction methods including principle component analysis (PCA), t-distributed stochastic neighbor embedding (t-SNE), locally linear embedding (LLE), uniform manifold approximation and projection (UMAP), and autoencoders (AE). Simple features scaling such as the standard scalar method were investigated. Various clustering algorithms were then used to assess the quality of data reduction and scaling based on the silhouette coefficient including density-based spatial clustering of applications with noise (DBSCAN) and k-nearest neighbor (KNN) clustering. Non-linear machine learning dimensionality reduction methods such as t-SNE were found to greatly outperform classic chemometric approaches such as PCA (Figure 2).

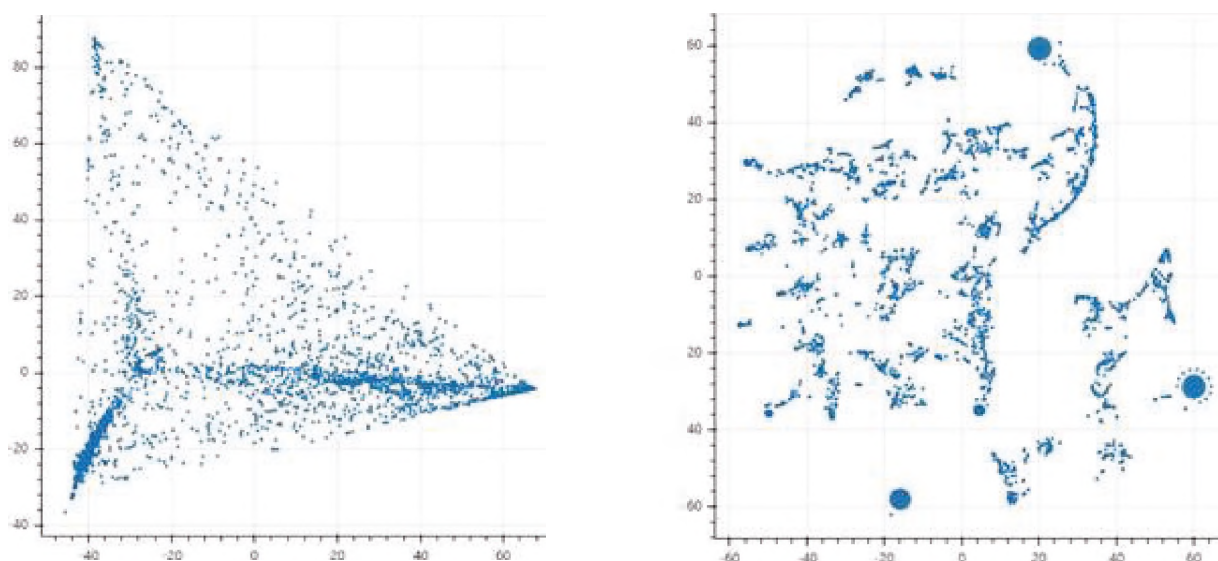


**Figure 2:** Data visualization of the EPA Speciate database after processing; each point represents a pollution profile contained in the database. (Left) 2-component 11 feature PCA data reduction representing classic chemometric approaches and (right) t-SNE non-linear machine learning based dimensionality reduction represented visually in 2 components.

Analytical methods for comprehensive organic analysis were developed utilizing an Agilent 7250 GC quadrupole time-of-flight high resolution mass spectrometry (Q-TOF) equipped with a Zoex ZX2 thermal modulator for multidimensional analysis. Methods were developed for a variety of potential sample types of interest for future training data set development. Parameter optimization included standard GC method development such as inlet type/temperature and oven ramp programs as well as multidimensional parameters such as modulation period and primary/secondary column selection. The viability of various training data set collections was assessed including on-site environmental sampling at SRS. The multidimensional GC/Q-TOF was found to be several orders of magnitude more sensitive than traditional GC/MS systems, with sub-picogram detection limits. This is in part due to the high-resolution mass spectrometer, which allows for the separation of isobars and the isolation of target ions. This is illustrated in Figure 3; six ions are identifiable at a nominal mass-to-charge ( $m/z$ ) ratio of 96. Traditional

unit mass resolution mass spectrometers would display a single summed peak of all ions near  $m/z$  96. The high-resolution Q-TOF allows for the extraction of trace target ions from interfering species, greatly improving detection limits.

In addition to sensitivity improvements derived from the use of a high-resolution mass spectrometer, the use of a thermal modulator to create multidimensional GC chromatograms further improves the sensitivity of analyses by approximately 1.5 orders of magnitude (Figure 4). This is due to a chromatographic focusing effect which improve the signal to noise ratio of the chromatographic peak. These combined improvements result in

a MS based system that is more sensitive for known target compounds than the traditional electron-capture-detectors (ECD). Although ECD detectors are highly sensitive, species identification is ambiguous due to solely relying upon a retention time. Traditionally, GC/MS systems have not been sensitive enough for end-use applications which necessitated the use of more sensitive but ambiguous ECD systems. Developing MS based analytical methods capable of out-performing ECD systems is a major milestone in operationalization of SRNL developed technologies. Additionally, the use of MS based systems allows for identification of a broad range of chemical species, enabling development of multi-species chemical fingerprints of activities of interest.

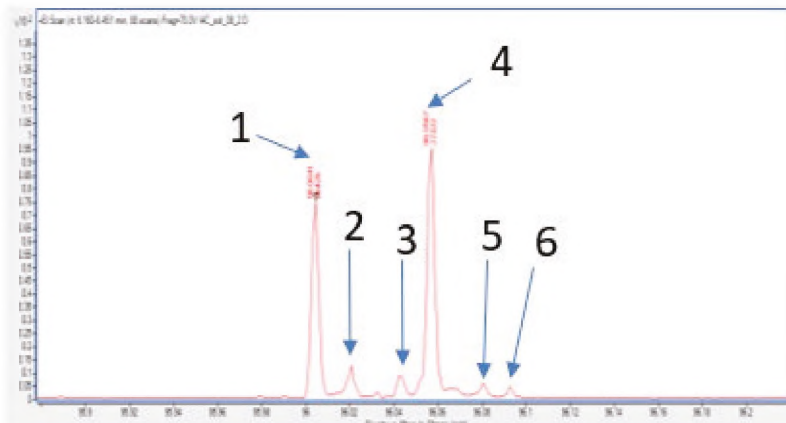


**Figure 3:** High resolution Q-TOF allows for the separation of isobaric interferences greatly improving the sensitivity for target trace ions.

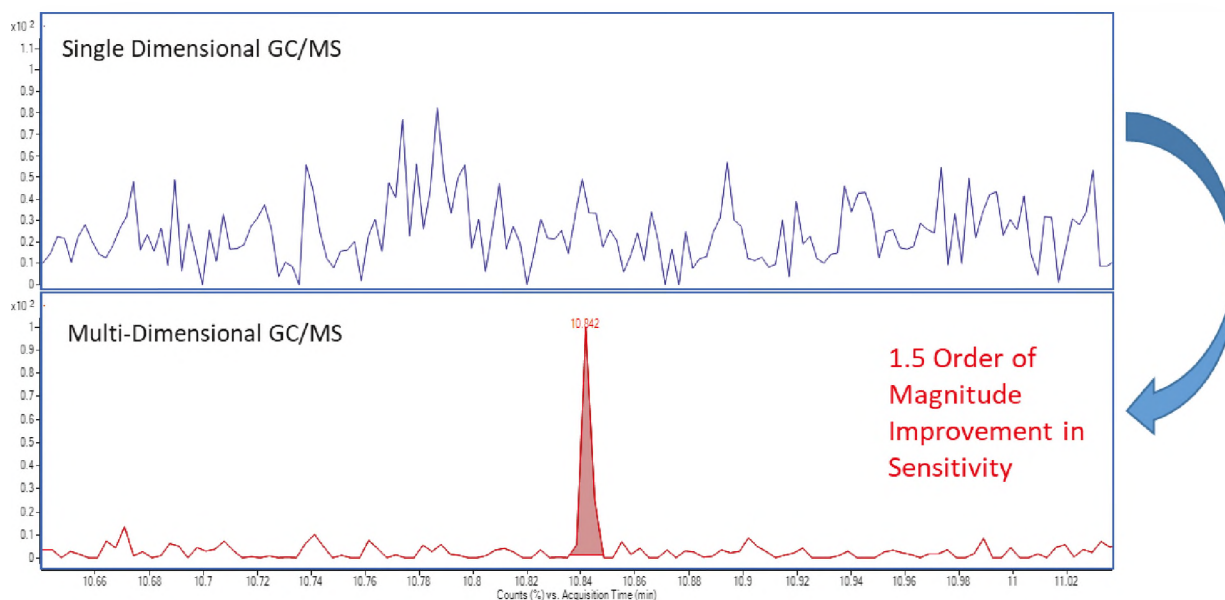


**Figure 4:** Comparison of sensitivity of the GC/Q-TOF in single-dimensional operation vs. multi-dimensional thermal modulation. The improvement in sensitivity is due to chromatographic focusing of the sample.

## FY2020 Accomplishments

- Sixty-page literature review on machine learning applications in GC/MS data analysis provided by Clemson University
- Developed machine learning based approaches for organic fingerprint detection utilizing the open source EPA SPECIATE database
- Analytical methods developed on new instrumentation improve sensitivity by 4 orders of magnitude over traditional GC/MS systems for species of interest and 1 order of magnitude over GC/ECD systems representing an order of magnitude increased detection range
- Developed multiple machine learning algorithms capable of detecting plume “hits” using historic single dimensional data sets (SRNL)
- SRNL PI taught himself Python and R for data processing and algorithm development
- LDRD research presented to 5 NNSA program managers
- New skill-set development for SRNL researcher
- Completion of instrument installation including facility modifications
- Establishment of a University subcontract and collaborative relationship with new external researchers and graduate students

## Future Directions

- Continued development of machine learning based data analysis approaches utilizing the open source data including the further development of auto encoder and uniform manifold approximation and projection dimensionality reduction methods
- Merge SRNL analytical methods and data collections with data analysis algorithms developed at Clemson University
- Continued collection of training data sets utilizing SRNL analytical methods
- Development of adversarial controls to test the accuracy of machine learning based classifications

## FY 2020 Peer-reviewed/Non-peer reviewed Publications

Publication of algorithm development activities is expected in early-mid 2021.

## Presentations

- Two Presentations to NNSA headquarters program managers
- One Presentation to SPP end user

Planned: 19th Conference on Artificial Intelligence for Environmental Science

Planned: ISCC & GCxGC 2021

## References

1. Prebihalo, S. E.; Berrier, K. L.; Freye, C. E.; Bahaghighat, H. D.; Moore, N. R.; Pinkerton, D. K.; Synovec, R. E. Multidimensional Gas Chromatography: Advances in Instrumentation, Chemometrics, and Applications. *Anal. Chem.* **2017**, *90* (1), 505-532.
2. Arsene, C.; Vione, D.; Grinberg, N.; Olariu, R. I. GCxGC-MS Hyphenated Techniques for the Analysis of Volatile Organic Compounds in Air. *J. Liq. Chromatogr. Relat. Technol.* **2011**, *34* (13), 1077-1111.

3. Hamilton, J.; Webb, P.; Lewis, A.; Hopkins, J.; Smith, S.; Davy, P. Partially Oxidized Organic Components in Urban Aerosol Using GCXGC-TOF/MS. *Atmos. Chem. Phys.* **2004**, *4* (5), 1279-1290.
4. Verleysen, M.; François, D. The Curse of Dimensionality in Data Mining and Time Series Prediction. In *International Work-Conference on Artificial Neural Networks*, Springer, **2005**, 758-770.
5. Newell, E. W.; Cheng, Y. Mass Cytometry: Blessed with the Curse of Dimensionality. *Nat. Immunol.* **2016**, *17* (8), 890-895.

## Acronyms

AE	Autoencoders
DBSCAN	Density-based Spatial Clustering of Applications with Noise
ECD	Electron Capture Detector
EPA	Environmental Protection Agency
GC	Gas Chromatograph(y)
KNN	k-nearest Neighbor
LLE	Locally Linear Embedding
m/z	Mass-to-charge Ratio
MS	Mass Spectrometer
NNSA	National Nuclear Security Administration
PCA	Principle Component Analysis
Q-TOF	Quadrupole Time-of-flight
SRNL	Savannah River National Laboratory
t-SNE	t-distributed Stochastic Neighbor Embedding
UMAP	Uniform Manifold Approximation and Projection
VOC	Volatile Organic Compound

## Student Researchers

Clemson University, PhD Student, Jiexin Shi

## Portable Industrial Control Systems Simulator

**Project Team:** Mackenzie Morris and  
Klaehn Burkes

**Project Start Date:** October 1, 2019  
**Project End Date:** September 30, 2021

*Operational technology (OT) and industrial control systems are some of the most difficult systems to use for research and development. They are either committed to operations or widely expensive to set up in a life like environment. Virtualization and simulation will allow these otherwise accessible systems to be a test bed for*

*the training, development, and research of customers to SRNL or engineers and scientists at SRNL. This will allow the testbed to fit into a small form factor and interact with a simulator with minimum hardware components for easy transports and replication effort within the environment.*

### FY2020 Objectives

- Develop a specific ICS virtualized environment
- Develop the capability to efficiently sniff and scan a complex ICS network to replicate
- Build a virtualization stack to host the environment

### Introduction

Industrial Control Systems (ICS) and Operational Technology (OT) merging as a unified system has become a target of foreign adversaries and a rapidly growing vulnerability for the United States. Our critical infrastructure, from chemical manufacturing to city streetlights, are controlled by these technologies. Commercial entities have been racing to add intelligence to these systems to provide efficiency, better control, and better data acquisition from these networks. This race has historically left cybersecurity concerns absent or as an afterthought from rigorous integration. This has led the US to a situation where our critical infrastructure technology has become smarter but significant security omissions have exposed our national infrastructure to malicious hacking and a viable target to U.S. adversaries. Security awareness is improving among both the users and developers of these technologies, but we are living in a landscape of dubiously secure devices, and completely insecure legacy devices. The nature of these systems creates major hurdles for addressing their security issues.

This project will give SRNL a tool to rapidly map these ICS/OT networks to then perform vulnerability assessments without impacting the operational system. However, the current methods for mapping these networks are crude and harmful to the operation of the functioning production facility. SRNL will perform research to advance these methods to develop a product that is less intrusive on the functioning network but still capable of fully mapping the system. This will require advancing the traditional sniffing techniques placing SRNL in a leading position in ICS/OT network analysis. The results of which will allow SRNL to deploy environments for education and future research for the cyber protection of ICS environments.

### Approach

To accomplish this goal SRNL will collaborate with UNCC and USACyS to identify existing methods for mapping ICS/OT environments, and identify gaps where methods are needed. The project will then proceed two ways; (1) SRNL will work with UNCC to expand the capability of their portable ICS System Simulator to gather data for a broad range of ICS/OT devices (presently they are limited to machine shop technologies), while (2) also working with the USACyS to identify or develop advanced techniques that can also be utilized for ICS environments. Successful completion of these two will give SRNL a tool to rapidly map ICS/OT networks to then perform vulnerability assessments without impacting the operational system. Three existing techniques will be the primary focus for fingerprinting: passive collection of packet traffic that can be parsed for device information (packet sniffing with backend

parsing), semi-passive which identifies protocol structure to ascertain the device maker and device type and then attempts to communicate with the device directly in a controlled manner, and lastly any safe active methods that can be deployed. Network mapping will further evaluate packet data to determine depth of devices from the collection point and the types of interfaces between the collection point and network edges (i.e. the identification of firewalls or aggregators between the point of collection and a PLC controlling a mixer).

These techniques will be implemented onto a prototype portable ICS System Simulator (server and computer procurements required) running the adapted version of the software tools suite developed by UNCC to use them. This prototype will deploy to a pilot network (the pilot to be identified during collaboration) to map and fingerprint the network. This information will be used by the simulator to develop a virtual model of the network. SRNL will host this model network on our Security and Cyber Technologies lab, and an operator for the network will be invited to verify this environment behaves as their real environment.

## Results/Discussion

The promises of the capabilities of UNCC's sniffing and scanning tool were embellished. Upon further collaboration and discussion, it became apparent that it was not going to be effective in the sniffing and deployment of ICS networks from passive data capture. A new method using a master server swap has been selected due to its applicability to ICS systems at SRS. Rather than listening on a network, backing up the tag database of a master server will allow an engineer to "restore" that backup into the virtual system effectively creating an identical master server. At this point the virtual environment will need to auto deploy enough endpoints to match that tag database.

Virtualization is still key to this project, a VM cloud foundation hypervisor has been deployed onto a cluster of servers to serve as the backbone for deployment of hosts and the ICS network. DeltaV has been selected as an appropriate DCS system due to its prevalence on site, the broader DOE complex, and external customers. A PLC has been successfully integrated with a virtual I/O using a simulation software FactoryIO. This simulation has been developed of a manufacturing floor and successfully controlled from a PLC, which is the bottom half of the ICS environment. This is by far the more difficult part of the project as the tag list needs to be converted from the PLC to the DCS. This is the first step for a stagnant environment, after which a more dynamic solution of interchangeable parts will be implemented allowing users to utilize different PLCs or simulated environments.

## FY2020 Accomplishments

- Established VMware Cloud foundation loaded on servers in the SRNL-Critical Infrastructure, ICS, and Cybersecurity lab
- Identified DeltaV as appropriate DCS system for USACyS, SRTE, and SRPPF
- Integrated Schneider Modicon PLCs into the S-CIIC
- Emulated the factory floor with FactoryIO
- Programmed PLCs to control FactoryIO simulations

## Future Directions

- Every component will be virtualized except for the PLC
- This will be accomplished through utilization of one server running VMWare
- This will then create virtual servers for DeltaV ProPlus, Bexec, Historian, Agent, MIMIC, SIEM/NSM
- Another Virtual PC will be running FactoryIO

- A single software defined network switch will be utilized to define different access points within the network
- A Schneider Modicon PLC will control FactoryIO through Modbus communication
- Integrated into a portable rugged container that utilizes less that 10U rack space

## Acronyms

DCS	Distributed Control System
ICS	Industrial Control System
OT	Operational Technology
PLC	Programable Logic Controller
S-CIIC	SRNL – Critical Infrastructure, ICS, and Cybersecurity
USACyS	US Army Cyber School
UNCC	University of North Carolina Charlotte

## Effect of GPS Manipulation to Traditional and Next Generation Relay Protection

**Project Team:** Klaehn Burkes, Ian Webb

**Project Start Date:** October 1, 2019

**Project End Date:** September 30, 2021

*This project's objective is to test the effect of GPS timing variations on relay protection algorithms to determine vulnerabilities and the associated hazards to the electric grid. This will focus on differential protection which utilizes peer to peer communication between substations to determine if the current is not equivalent. This requires the use of GPS to sync the two substations and can be*

*vulnerable to GPS manipulation. However, the effects of GPS manipulation are not a commonly known risk. Therefore, this LDRD will address the risks of GPS manipulation for such a widely implemented technology. For differential protection a GPS resilient architecture was implemented and tested for differential protective relays through a direct serial fiber connection between the two relays. This allows for one relay to be the master and provide synchronization outside of timestamp for differential protection.*

### FY2020 Objectives

- Set up SEL-411L differential protection relay within the SRNL-Critical Infrastructure, ICS and Cybersecurity (S-CIIC) lab
- Program protective relays to perform differential protection through controller hardware in the loop platform Typhoon
- Develop IRIG-B code generation and implement in Typhoon platform
- Time shift IRIG-B to perform time manipulation and then conduct faulting sequences

### Introduction

The electric power system is upgrading the supervisory control and data acquisition (SCADA) and protective relaying equipment from electromechanical relays to microprocessor-based relays. This has allowed for more advance control through distributed and real time methods, requiring more communication between intelligent electronic devices (IEDs) and remote terminal units (RTUs). These devices are inherently programmable logic controllers (PLCs) that resemble the communication protocols of industrial control systems (ICS).<sup>1</sup> However, the protocols and communication methods specific to the electric power system (traditionally Distribution Network Protocol (DNP3)) are being replaced with International Electrotechnical Commission (IEC) 61850. DNP3 has no timestamped data in its messaging protocol, meaning relay protection algorithms are not affected by GPS time stamps or data.<sup>2</sup> However, IEC 61850 uses many different protocols that are based on fast fiber connections that utilize timing as a key part of the data transfer. These protocols such as Manufacturing Message Specification (MMS), Generic Object-Oriented Substation Event (GOOSE), and Sample Measured Values (SMV) all run over Transmission Control Protocol/Internet Protocol (TCP/IP) networks utilizing high speed switching ethernet to obtain the necessary response times for millisecond protective relaying controls.<sup>3</sup> Now the future of protective relaying is relying on accurate and synchronized timing to improve the electric power system reliability and stability.

An example of a protection scheme that utilizes high-speed communication is line differential protection Figure 1, which requires peer to peer communication between substations. This protection scheme compares the current leaving a substation on one end of a transmission line and the current entering another substation at the other end of the transmission line and compares the values recorded to detect abnormalities that occur in a fault scenario. This requires two substations to be synchronized on an accurate clocking signal, typically a GPS receiver. This project's objective is to research into the effects of GPS signal

manipulation between two substations. This will be performed by slowly walking off one substations GPS signal and monitoring how the protection algorithms are affected to determine the failure mechanisms of these millisecond protective relaying functions. SRNL has already proven in previous work that the GPS receivers cannot detect small steps of GPS signal deviations implying that the receiver does not revert to the backup timing source. This project will allow for SRNL to become a leader in the field of GPS timing manipulation with previous knowledge of GPS receiver operation and the knowledge gained through determining the failure mechanisms of the millisecond protective relay functions of differential and time domain protection.

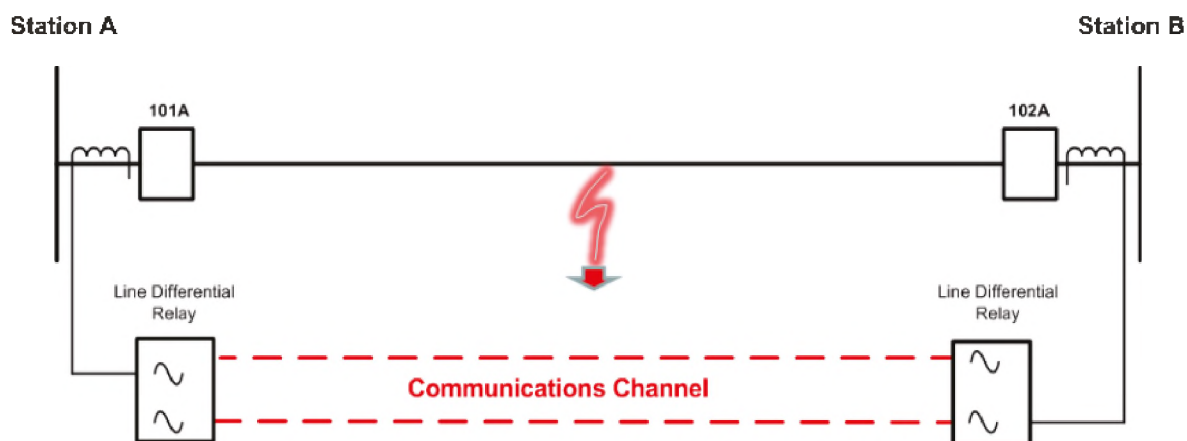


Figure 1: Differential Protection Concept.

## Approach

The approach for implementing and testing this is through setting up a controller hardware in the loop (CHIL) test bed for the protective relays. CHIL testing allows for controllable and repeatable testing of different protective relays. This allows for running many different scenarios to get precise controlled results. To implement GPS spoofing on protective relays the Typhoon platform was used to emulate the electric power grid, output waveforms of voltage and current to the protective relays, calculate and output IRIG-B timing signals to the relays, and finally take contactor inputs to control breakers in the simulation. Through this method every input and output to the protective relays were controlled through the Typhoon platform and allowed for testing the protective relay as if they were deployed in the field. This all allowed for implementing and testing multiple differential protection architectures and examining their vulnerabilities to GPS time walk off. Specifically, directly related to the different IRIG-B inputs for the relays. Figure 2 represents the test network established in the S-CIIC.

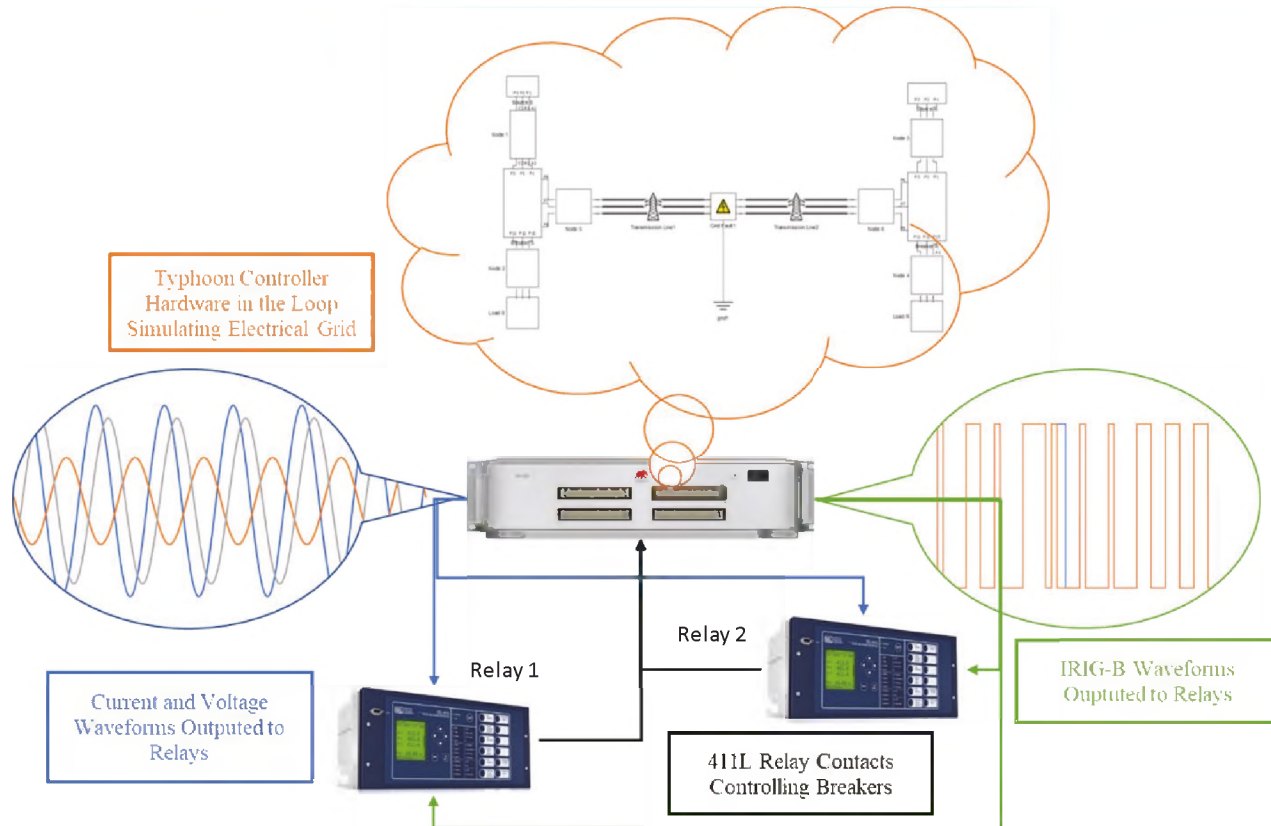


Figure 2: Controller Hardware in the Loop Testing Network.

## Results/Discussion

The goal of the CHIL testing was to determine what the vulnerabilities differential protection algorithms had in regard to GPStiming manipulation. The two relays were setup and programed to perform only 87L line differential protection and not trip for any other relaying scheme. In Typhoon a simple power system network was established with two sources, two loads and a transmission line between. The voltages and currents were fed into the low voltage testing inputs to the relay. A high accuracy IRIG-B output from Typhoon

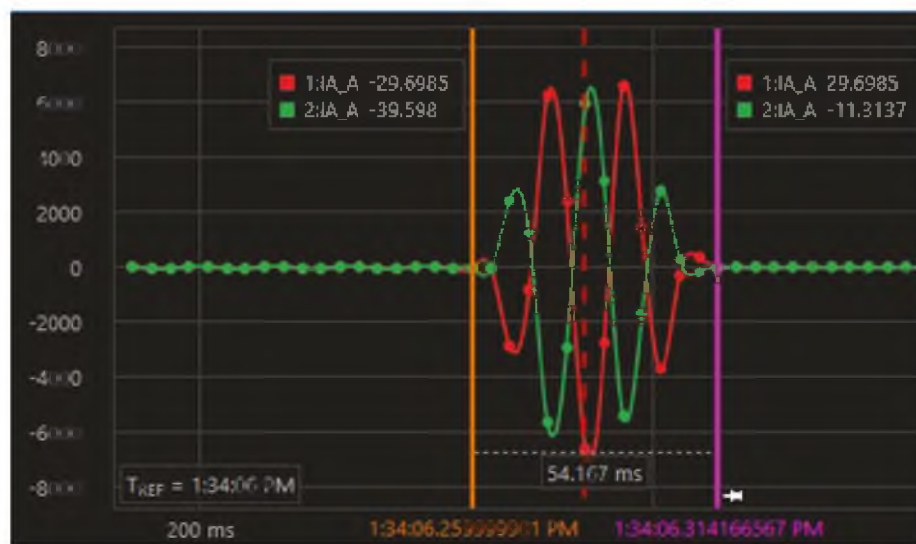


Figure 3: Relay 1 & 2 Current for Phase A to Ground Fault without 1ms Time Spoof.

was established in both relays and then a series of faults were performed and detected by the relay only results from a phase A to ground fault are shown in Figure 3. This allows for a better look at the fault current as there is only one phase. The two currents are equivalent and opposite in polarity as the fault is located in the middle of the line

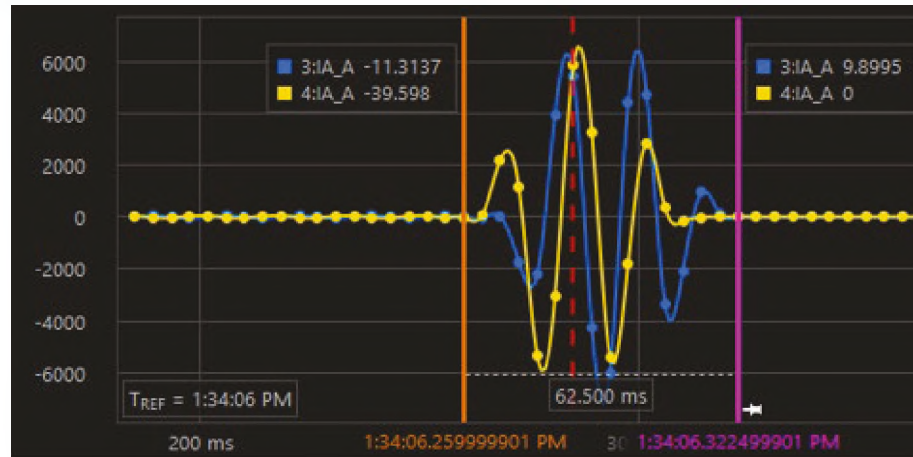


Figure 4: Relay 1 & 2 Currents for Phase A to Ground Fault without 1ms Time Spoof.

and the impedance is equivalent. The red wave form in Relay 1 The time to clear the fault is 54 ms about 3.3 cycles, and the time to detect the fault was 25 ms about 1.5 cycles. This verifies that the differential protection algorithm is working and functioning properly.

Then a 1ms delay is placed on relay 1's IRIG-B signal. The timing maintained a high quality IRIG-B suitable for PMU timing. Then a series of faults were performed on the CHIL testbed. The following will present the phase A to ground fault to show a comparison to the baseline presented with no time shift. Figure 4 shows the fault current for both Relay 1 (blue) and Relay 2 (yellow). The waveforms no longer are inverse images of each other, and Relay 1 current is shifted from Relay 2s. However, the relays still operate and perform their required tripping functions. It just takes longer for the relays to clear the fault.



Figure 5: Differential Current Trip Signal.

The reason why the differential relay algorithm still operated with the mismatched currents is because the Relay 1 was configured to be a slave to Relay 2 in reference to timing. Therefore, the relay still recorded all data with its time stamp but the logic to trip required a second communication or ping pong between Relay 1 and Relay 2 before Relay one could make the trip decision. Therefore, there was a delay in tripping for Relay 1 by 8  $\mu$ s. This can be seen in Figure 5 where the differential trip bits are shown for the relays: red is Relay 1 with no time change, green is Relay 2 with no time change, blue is relay 1 with 1 ms time change, and yellow is Relay 2 with 1 ms time change. Anything greater than 1 ms would cause the relay to fall back onto its internal clock and disregard the time source as legitimate. This results in the differential protection function being resilient to GPS and timing manipulation when utilizing a direct fiber connection and configured properly to perform a ping pong verification of the timestamp with one relay as a slave and other as the master.

## FY2020 Accomplishments

- Implemented and tested a GPS resilient architecture for differential protective relays through a direct serial fiber connection between the two relays.
- Received \$350k for implementing a PTP timing signal with the protective relays from Office of Electricity
- Established a relay experimental test bed to function test relays with controllable voltage and current outputs, timing signals, and breaker inputs
- Developing Journal Publication on Results

## Future Directions

SRNL will next be testing the latest type of relay produced the time domain protection relay. This system makes claims of being able to locate the fault to the tower and detect a fault within 1 microsecond. About 30 times faster than line differential protection relays could.

## References

1. Ward, S.; O'Brien, J.; Beresh, B.; Benmouyal, G.; Holstein, D.; Tengdin, J.; Fodero, K.; Simon, M.; Carden, M.; Yalla, M.; Tibbals, T.; Skendzic, V.; Mix, S.; Young, R.; Sidhu, T.; Klein, S.; Weiss, J. Cyber Security Issues for Protective Relays. From *C1 Working Group Members of Power System Relaying Committee, GE Grid Solutions, 2007.*
2. East, S.; Butts, J.; Pap, M.; Sheno, S. A Taxonomy of Attacks on the DNP3 Protocol. In *International Federation for Information Processing, 2009.*
3. Gadelha da Silveira, M.; Henrique Franco, P. IEC 61850 Network Cybersecurity: Mitigating GOOSE Message Vulnerabilities. Presented at *6th Annual PAC World Americas Conference, Raleigh, North Carolina, 2019.*

## Acronyms

CHIL	Controller Hardware in the Loop
DNP3	Distribution Network Protocol 3
GOOSE	Generic Object-Oriented Substation Event
GPS	Global Positioning System
ICS	Industrial Control System
IEC	International Electrotechnical Commission
IED	Intelligent Electronic Device
IRIG-B	Inter-range Instrumentation Group-B
MMS	Manufacturing Message Specification
RTU	Remote Terminal Units
SCADA	Supervisory Control and Data Acquisition
SCIIC	SRNL Critical Infrastructure, ICS, and Cybersecurity
SMV	Sample Measured Value
TCP/IP	Transmission Control Protocol/Internet Protocol

## High Resolution Actinide Speciation Using Tensioned Metastable Fluid Detector (TMFD)

**Project Team:** David DiPrete, Kalee Fenker, Tad Whiteside, Rusi Taleyarkhan

**Purdue University Collaborator:** Rusi Taleyarkhan

**Project Start Date:** October 1, 2019

**Project End Date:** September 30, 2020

*Currently, no laboratory or field-deployable alpha spectrometer exists that is capable of resolving low activity levels of Pu-239 and Pu-240 to determine whether a plutonium sample is weapons-grade or higher burn-up. No such device is available to distinguish U-235 from U-236 to determine whether a uranium sample has been exposed to neutrons. No such device exists to measure U-233 in the presence of U-234 to determine if material is from the thorium fuel cycle. The goal of this project is to establish whether a device based on Tensioned Metastable Fluid Detector (TMFD) technology*

*developed by Purdue can solve problems such as these. Additionally, the device has the potential to measure low levels of actinides with detection limits superior to those of solid-state alpha spectrometry. Those detection limits combined with the potential high-resolution capabilities could allow this device to assay numerous alpha-emitting isotopes to levels lower than that achievable by mass spectrometry.*

### FY2020 Objectives

- Establish contract for collaborative research between SRNL and Purdue University
- Provide research isotopes of interest to Purdue for study in their radiological TMFD facility
- Establish TMFD capabilities at SRNL for parallel evaluations to those conducted at Purdue University
- Research superior actinide extractive solvents compatible with TMFD technology to those available at Purdue

### Introduction

Numerous alpha-emitting isotopes emit alpha particles with energies not resolvable (<20 keV) with solid-state alpha spectrometers. Radiochemical separations followed by alpha spectrometry can be used to resolve isotopes with overlapping alpha energies such as Pu-238&Am-241, Np-237&U-234 and Cm-242 & Cf-252. Mass spectrometry is required to resolve elements with isotopes with overlapping energies such as U-235&U-236, U-233&U-234, Pu-239&Pu-240, and Cm-243&Cm-244. No field deployable systems exist capable of resolving any of these pairs with unresolvable energies. In the nuclear forensics' world, there is value in having the capability in the field of measuring any of these pairs. In the non-proliferation world, having the capability of measuring Pu-239 to Pu-240 ratios allows for the determination of whether the plutonium sample being analyzed is of a weapons grade or a reactor grade material origin. Being able to discriminate between U-235 and U-236 allows for the determination of whether a uranium sample has been exposed to a neutron flux. Being able to discriminate U-233 from U-234 allows for the determination of whether a uranium sample is from the thorium fuel cycle or the uranium fuel cycle. Tensioned Metastable Fluid Detector (TMFD) technology has been explored and refined by R. Taleyarkhan's Purdue University research team<sup>1,2,3,4</sup> through funded/internal grants for the purposes of special nuclear material

detection via neutron detection (Figure 1). TMFD spectroscopy is based on the general theory of nucleation and how vapor bubbles form in “stressed” liquids. When a liquid is spun, it is placed under negative pressure. As work is done on this system (through higher rates of spin or energy deposited by radiation) the fluid fractures and a bubble forms. From the rate of fracture (by measuring the bubbles) and a library of known energies, the TMFD can measure fission products, neutrons, or alpha-containing compounds. The Purdue team continued to study the capabilities of the device built to support the DOE scope to detect fissile material in contact with the device’s fluid by fission track detection and more recently by detection of alpha emissions by measuring alpha-emission induced isotope recoil. Initial experiments conducted by the team indicated energy resolution of 1.4 keV may be achievable, capable of resolving Pu-238 from Am-241 (Figure 2).



**Figure 1:** TMFD Conceptual(left) and Prototype (Right) Device.

TMFD detectors also have a sensitivity benefit by having essentially zero response to gamma-beta-background radiation. When assaying an alpha/fission emitter that has been mixed with the devices fluids, it is measuring the analyte with a theoretical 100% ( $4\pi$ ) counting efficiency. For comparison, a liquid scintillation counter also measures with a counting efficiency approaching 100%, but sensitivity suffers from higher backgrounds and quenching. A solid-state alpha spectrometer measures with at best 50% counting efficiency, with steadily increasing background levels from the initial zero background. The Purdue research group have claimed to have measured low alpha activity levels ( $<0.1$  dpm/aliquot) using the prototype TMFD for 1-hour analysis periods, which would be superior to competing counting methods, and superior to mass spectrometry for numerous alpha-emitting isotopes. Alpha spectrometry by TMFD is currently in its infancy. SRNL has considerable nuclear measurement and radiochemistry expertise as well as nuclear materials on hand. The SRNL collaboration with the Purdue research group is explore the potential of this technology for extending the nuclear measurement of actinides capabilities of this technology. SRNL is providing research isotopes to Purdue for their evaluation with this technology. Purdue is providing expertise to SRNL for SRNL to develop TMFD testing capabilities in the laboratory. SRNL is studying various extractant/solvent combinations that are superior for extracting large suites of actinides and are compatible with TMFD technology.

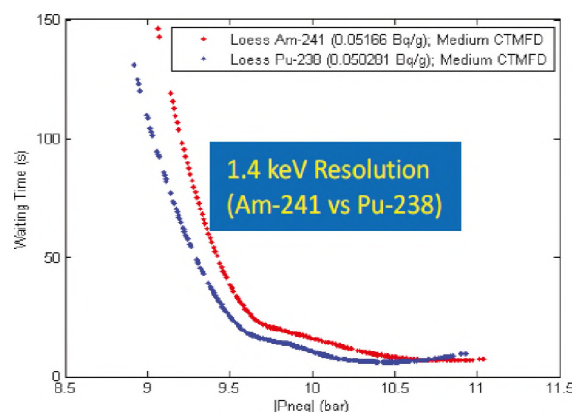


**Figure 2:** TMFD Resolution between Am-241 and Pu-238.

## Approach

Initially a contract was established between SRNL and Purdue for this collaboration to move forward. The contract was successfully executed two months into the project. An SRNL team traveled to Purdue to review the TMFD technology that has been established with the Taleyarkhan Group. The Taleyarkhan

Group subsequently traveled to SRNL to for a tour of Nuclear Measurement's laboratories and to deliver a TMFD prototype for testing.

SRNL worked to generate TMFD Cells for evaluating various scenarios. The SRNL glass shop produced various designs of glassware based on the Purdue prototype design. Couplers between the glassware and the motors were first 3-D printed, then later machined from polyethylene. Aluminum sleeves were also fabricated to provide additional structural support to the polyethylene couplers (Figure 3). A variable drill press was purchased to be used to test the various designs, to avoid stressing the Purdue supplied prototype (Figure 4). Initially, glassware designs were tested with decafluoropentane (DFP), the solvent used primarily by Purdue. Fluids were tensioned using the drill press system. The tensioned fluids were exposed to an americium-lithium (AmLi) neutron source until cavitation was observed. Conditions were repeated in the absence of neutrons to establish the fact that the cavitations were truly induced by incident neutrons. In addition to glassware developed at SRNL based on the Purdue TMFD designs, additional designs were produced by the SRNL glass shop (Figure 5) and tested.

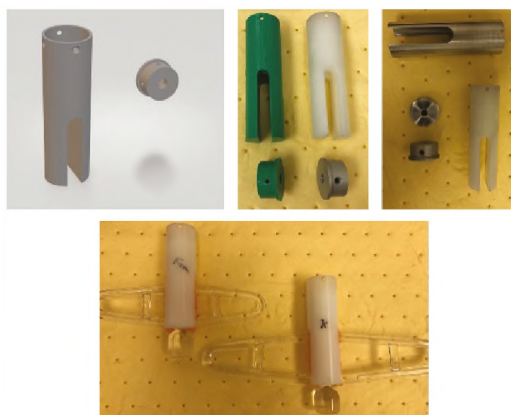


Figure 3: SRNL Fabricated glassware and couplers.

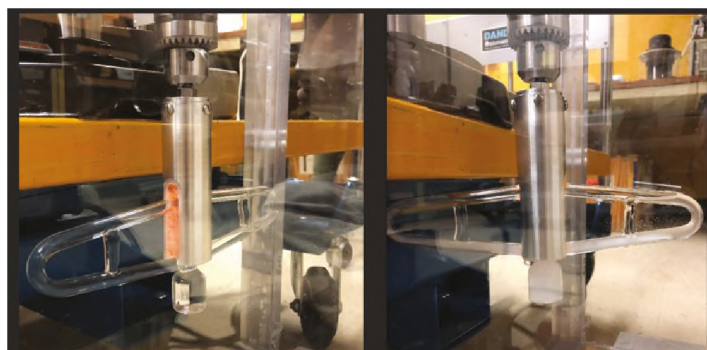


Figure 4: SRNL Developed Glassware and Coupler coupled to a Drill Motor Test Bed.

In parallel to the SRNL efforts to establish TMFDs in-house, Purdue carried out efforts to test the TMFD alpha resolution for various isotopes using their existing systems to support this LDRD project. Purdue procured a plutonium-239 and plutonium-242 standard for testing. SRNL provided low levels of isotopically pure plutonium-240 standard which had previously been extracted from SRS curium-244. Plutonium-240 is the radiological daughter of curium-244. In addition to the Pu-240 sample, SRNL provided low levels of high burn-up SRS HEU, which contained U-234, U-235, U-236, and U-238. SRNL also provided low levels of an SRS 94:6 mass ratio Pu-239 to Pu-240 sample for testing at Purdue.

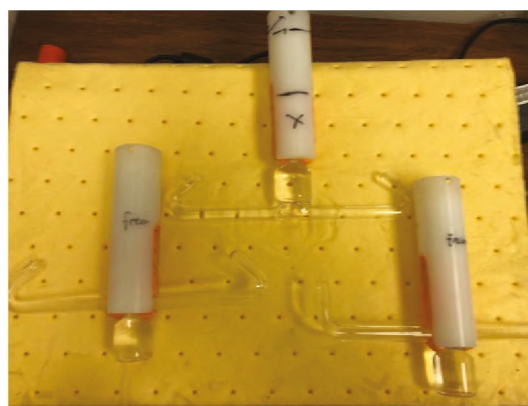


Figure 5: Various SRNL Designs of TMFD Glassware.

Once SRNL had developed working prototypes of TMFD glassware prototypes, the prototypes were benchmarked against the Purdue supplied TMFD glassware filled with DFP in the Purdue TMFD device. A controlled testing environment was set up for incremental exposures to a neutron flux from AmLi standards. The TMFD was shielded to an extent from ambient background neutron radiation with polyethylene shielding (Figure 6).



**Figure 6:** SRNL TMFD neutron irradiation set-up.

SRNL then embarked on a study to find actinide extracting solvent systems both suitable for TMFD and superior to the current extractants used by Purdue. Purdue was currently working with tributyl phosphate. That extractant is excellent at extracting tetravalent actinides such as plutonium, and hexavalent actinides such as uranium. However, that extractant has no affinity for trivalent actinides, such as americium, curium or californium, or actinides such as plutonium that was in its reduced trivalent state.

SRNL studied HDEHP (Di-(2-ethylhexyl)phosphoric acid). This extractant is suitable for extracting hexa, tetra and trivalent actinides, so could be used for quantitative actinide extractions. TMFD suitability studies were then undertaken to establish whether solvents that HDEHP were miscible in would also cavitate when exposed to radiation. The neutron interrogation set-up that was previously described was used to test various extractant-solvent systems until a candidate was identified that would cavitate when exposed to a neutron flux but would not cavitate in the absence of that neutron flux.

Once a suitable candidate for TMFD was identified, solvent-solvent extraction studies were conducted to establish that this HDEHP solvent system could be used to extract various actinides. Tests were conducted to evaluate the retention of a trivalent isotope (Am-241) and a tetravalent actinide (Pu-238)

## Results/Discussion

SRNL successfully produced glassware/coupling combinations capable of conducting TMFD experiments at SRNL. Figure 7 depicts the  $\text{Log}_{10}(\text{WaitTime})$  vs counts vs distance for measurement of DFP contained in SRNL produced glassware and couplers on the Purdue TMFD system. As expected, count rate rose as distance decreased. Wait times for cavitations held constant at far distances but began to

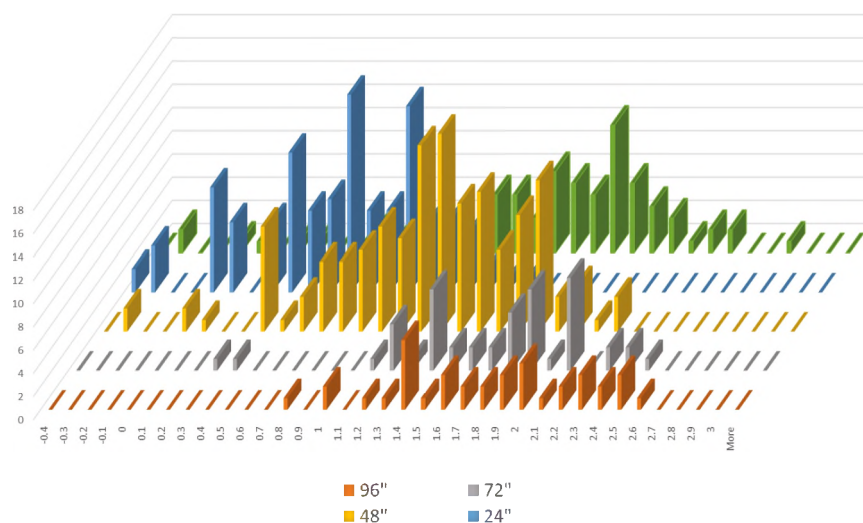


**Figure 7:**  $\text{Log}_{10}(\text{WaitTime})$  vs counts vs distance for Decafluoropentane (DFP) using SRNL glassware and couplers on Purdue TMFD System.

drop as the neutron flux increased until neutron pile-up became too high for the instrument to measure incident neutron flux.

Initial evaluations of HDEHP were used with its conventional dodecane solvent (in kerosene form). Unfortunately, efforts to get dodecane to cavitate in the presence of a neutron field at tensions generated using the testing system's maximum spin rates failed. HDEHP was then introduced into the Purdue solvent system of choice (DFP). However, HDEHP was found to be immiscible in DFP. A second solvent system for HDEHP was then explored using an oil extraction solvent made by HORIBA Advanced Techno with the product name S-316. S-316 is a chlorofluoro-hydrocarbon which also goes by the trade name of Flon. Flon did cavitate in the presence of a neutron fields. Unfortunately, Flon also cavitated at similar tensions when no neutrons were present at tensions used to cavitate DFP. It was discovered that Flon did work as an emulsifier between HDEHP and DFP, and this extraction system of HDEHP, Flon and DFP continued to cavitate under conditions similar to the conditions used to cavitate pure DFP.

A 1 M HDEHP solution diluted in FLON was tested for extraction efficiency for Am-241 and Pu-238. A 20 second contact of a 5:2 aqueous (0.1 M nitric) to organic system was evaluated and found to quantitatively extract the actinides (Figure 8)

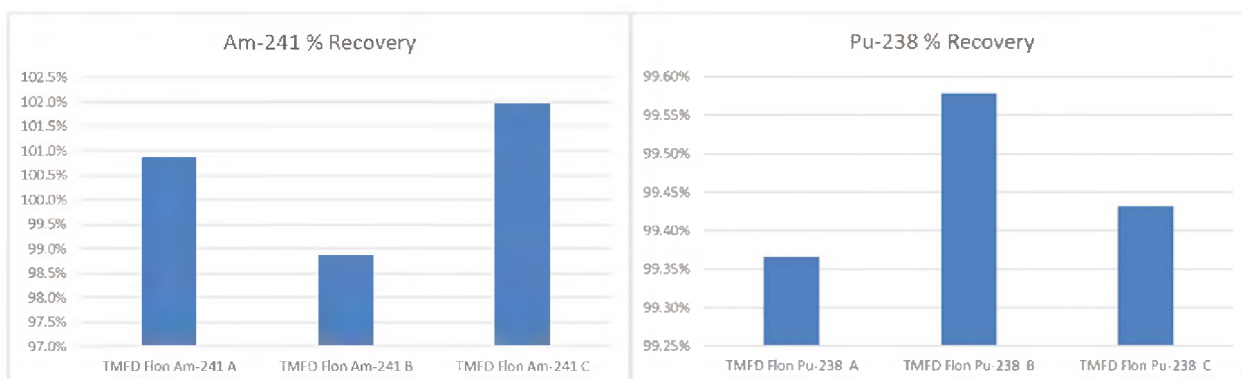


Figure 8: 1M HDEHP diluted in FLON Am-241 and Pu-238 Extraction Efficiencies.

Purdue evaluated the resolution of their TMFD systems using radioisotopes commercially procured as well as radioisotopes provided by SRNL. Initially Purdue demonstrated they could resolve plutonium-239 (5.15 MeV alpha energy) and Pu-242 (4.90 MeV alpha energy) using TFMD (Figure 9). These isotopes are also resolvable using conventional, commercially available alpha spectrometers.

Using Pu-240 received from SRNL Purdue next demonstrated using TMFD they could discriminate between Pu-239 (5.15 MeV alpha energy) and Pu-240 (5.17 MeV alpha

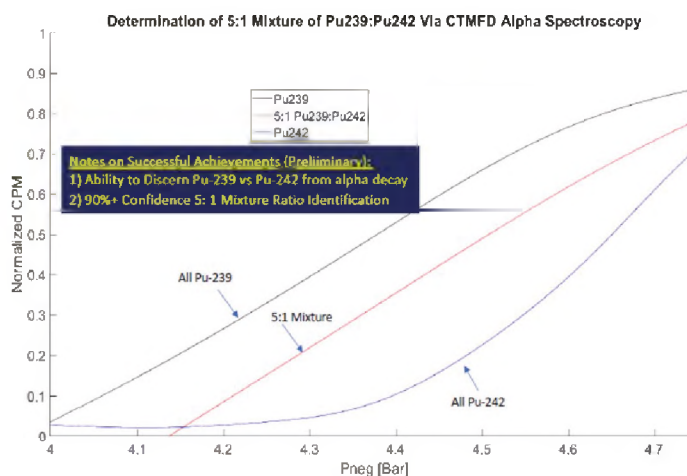


Figure 9: TMFD Measurements of Pu-239 and Pu-242.

energy) (Figure 10). These isotopes cannot be measured independent of one another using conventional, commercially available alpha spectrometers.

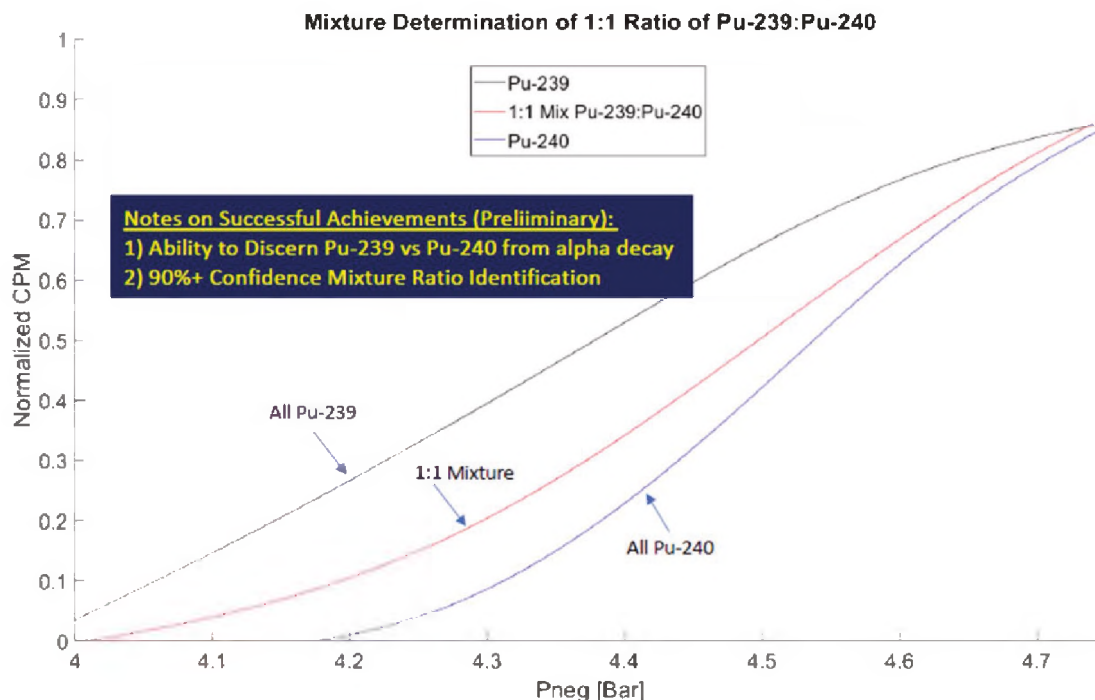


Figure 10: TMFD Discrimination between Pu-239 and Pu-240.

## FY2020 Accomplishments

- Project demonstrated TMFD technology can be used to measure alpha emitters at a higher resolution than commercially available alpha spectrometers
- Project identified superior actinide extractants that are compatible with TMFD technology
- Project established a working relationship between the Purdue University Taleyarkhan group and SRNL
- Project established a TMFD capability at SRNL
- Joint proposal to continue alpha spectrometry research using TMFD and well as studying TMFD applications for neutron dosimetry and fission product measurements was funded by NNSA NSRD for \$1.2M for three years.

## Future Directions

Collaborative effect between SRNL and Purdue continues with a funded 3-year project from NNSA NSRD to continue to study the potential of Tensioned Metastable Fluid Detectors for alpha spectrometry, neutron dosimetry and fission measurement applications.

## Publications

One paper from the collaboration between SRNL and Purdue University, *Actinide in Air (Rn-Progeny Rejected) Alpha Spectrometry with Tensioned Metastable Fluid Detectors*, has been accepted for publication in the Journal of Nuclear Engineering and Radiation Science.

## References

1. Grimes, T.; Taleyarkhan, R. P. Fast Neutron Spectroscopy with Tensioned Metastable Fluid Detectors. *Nucl. Instr. Methods Phys. Res., Sect. A.* **2016**, *830*, 355-365.
2. Webster, J. A.; Hagen, A.; Archambault, B.; Hume, N.; Taleyarkhan, R. P. High-Efficiency Gamma-Beta Blind Alpha Spectrometry for Nuclear Energy Applications. *J. Nuc. Eng. Rad. Sci.*, **2015**, *1* (3), 031006.
3. Archambault, B. A.; Webster, J.; Grimes, T.; Fischer, K.; Hagen, A.; Taleyarkhan, R. P. Advancements in the Development of a Directional-Position Sensing Fast Neutron Detector Using Acoustically Tensioned Metastable Fluids. *Nucl. Instr. Methods Phys. Res., Sect. A.* **2015**, *784*, 176-183.
4. Taleyarkhan, R. P.; Lapinskas, J.; Archambault, B.; Webster, J. A.; Grimes, T. F.; Hagen, A.; Fischer, K.; McDevitt, S.; Charlton, W. Realtime Monitoring of Actinides in Chemical Nuclear Fuel Reprocessing Plants. Special Issue – *Chem. Engr. Res. Dev.* **2013**, *91*, 688-702.
5. Horwitz, E. P.; Bloomquist, C. A. A. Chemical Separations for Super-Heavy Element Searches in Irradiated Uranium Targets. *J. Inorg. Nucl. Chem.* **1975**, *37*, 425-434.

## Acronyms

DFP   Decafluoropentane  
HDEHP Di-(2-ethylhexyl)phosphoric acid  
TMFD   Tensioned Metastable Fluid Detector

## Student Researchers

Three Purdue student researchers supported the project at Purdue University: Nathan Boyle, Catalin Harabagiu, and Stepan Ozerov.

## Develop Water Detritiation Models Based on Bench Scale and H/D Pilot Plant Performance

**Project Team:** Lucas Angelette, Paul Beaumont, Matt Kesterson, Raymond Belliveau

**Project Start Date:** October 1, 2019

**Project End Date:** September 30, 2020

*The progress of the development of the SRNL water detritiation process has been encouraging, supported by convincing tritium removal data, successful column regeneration by hydrogen, and construction of a H/D pilot plant. It is strongly desirable to integrate these pieces of positive experimental data into simulation models. Two models have been constructed: one for water isotope separation and another for catalytic*

*isotope exchange during column regeneration. Model tuning, scientific understanding, and pilot plant validation was performed. A stage height model for hydrogen gas isotope separation was used for water isotope separation with feedback from experimental data, adapted from the TCAP (thermal cycling absorption process) team.*

### FY2020 Objectives

- To greatly extend our understanding and improve the SRNL water detritiation process
- Develop a model for the Water Isotope Separation / Detritiation process
- Develop a model for the catalytic Isotope Exchange / Regeneration process

### Introduction

Water detritiation is very important for tritium production and reduction of environmental releases. Over the past four decades no breakthrough technologies have been developed to process tritium-contaminated water efficiently and economically despite continuing interest and efforts.<sup>1-5</sup> Combined Electrolysis Catalytic Exchange (CECE), water distillation (WD), and Girdler-Sulfide (G-S) processes are still among the leading processes to separate water molecules with different hydrogen isotopes. Both CECE and WD are very energy intensive and G-S uses the toxic and corrosive chemical  $H_2S$ , which is problematic when combined with radioactive hazards. The potential for an energy efficient direct isotope separation of water molecules is of considerable interest.

SRNL has been developing a novel 3-step process to separate and remove tritium from water. Water isotopologues (e.g., HDO, HTO,  $H_2O$ ) are separated directly via a water isotope exchange (WIE) column. When the column reaches breakthrough, it is regenerated by catalytic isotope exchange (CIE) with hydrogen. The effluent HT in  $H_2$  stream is then separated in TCAP, leaving no secondary waste stream. The approach leverages the SRNL expertise in hydrogen isotope separation, in which we are the world's technological leader. The SRNL water detritiation development is encouraging, supported by convincing tritium removal data, successful column regeneration by hydrogen, and construction of a H/D pilot plant. It is strongly desirable to integrate these pieces of positive experimental data into simulation models.

### Approach

Two models were developed with COMSOL Multiphysics using a combination of computational fluid dynamics (CFD) coupled with chemical reactions to enhance our understanding and improve the SRNL water detritiation process. The first model focused on the initial water isotope separation process and the second model focused on the catalytic isotope exchange during column regeneration. The packed bed system allows the user to specify column length and diameter as well as feed flowrates and composition. Based on the packing density of the column and input flow properties, the model predicts an average flow

profile and pressure drop across the column. The inclusion of the chemical reaction engineering module allows for chemical species tracking as well as adsorption/desorption kinetic terms. Model tuning, scientific understanding, and pilot plant validation was also performed to further support findings.

Validation of each model was performed using the previously constructed 18 ft pilot plant, through the comparison of the experimental data against each model, ultimately validating the developed models. Having the 18 ft pilot plant on hand enabled the opportunity for model optimization and verification procedures to validate accuracy. Changes made were based on observations to improve precision of the models, when appropriate. The pilot plant is expected to have much better isotope separation performance than the 1 ft bench scale column due to having 18 times more separation stages. The sizable scale also provided better material balance as well as opportunities to study mass and heat transfer, pressure drop and reaction kinetics. For example, anticipated decontamination factor (DF) and expected  $H_2/H_2O$  molar ratio in the overall WIE/CIE cycle can be derived from the pilot plant data and the modeling activities. The data can be used to design a production column as to determine the column height and throughput

## Results/Discussion

A COMSOL Multiphysics model has been developed to simulate the adsorption and desorption of deuterium in a column exchange process. For the adsorption process, the model uses system inlet flow rates and compositions to determine outlet pressure and concentration of DHO in the effluent stream. The model parameters (bed porosity, permeability, adsorption kinetics) have been adjusted based on experimental data. The same model was run in a reverse flow direction for the desorption of deuterium and regeneration of the column.

Results of the COMSOL modeling had demonstrated that the isotope front moved through the column in a smear-like pattern, rather than the preferred plug-flow as one may expect for this system. As a result, several variables were investigated to improve front flow through the column including, water and carrier gas flow rates, flow direction, and pressure drop restrictions. Efforts were then made to test the predictive nature of the modeling and adjust the operating parameters of the pilot plant to mirror the results of the models. This brought several areas of improvement to light, allowing for further enhancement of the pilot plant and increased reliability coupled with additional calculations supporting the changes.

To further verify the COMSOL modeling, models were compared to experimental data of the 1 ft bench top scale column, found to be in good agreement with each other. Additionally, an Inverse-Gaussian model of the chromatographic deuterium breakthrough was developed (Figure 1) allowing for the identification of the point of diminishing returns and the calculation of the number of theoretical plates in the column. This information was used to determine the optimal time period for column regeneration.

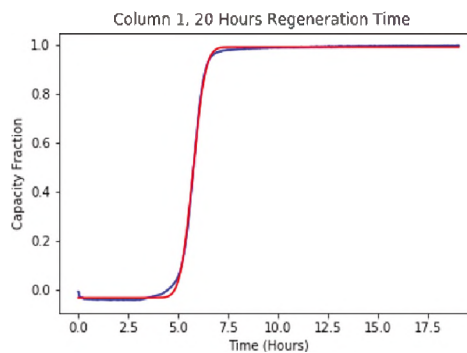


**Figure 1:** H/D breakthrough curve with inverse-Gaussian model of chromatographic breakthrough.

## FY2020 Accomplishments

- A COMSOL Multiphysics model has been developed to simulate the adsorption and desorption of deuterium in a column exchange process. The model parameters (bed porosity, permeability, adsorption kinetics) have been adjusted based on experimental data
- For the adsorption (WIE) process, the model uses system inlet flow rates and compositions to determine outlet pressure and concentration of DHO in the effluent stream
- For the desorption (CIE) process, the same model can be run in a reverse flow direction for the desorption of deuterium and regeneration of the column
- Models verified on smaller scale benchtop column
- Several improvements were made to the pilot plant based on derived models and calculations, illustrating areas of potential improvement

## Future Directions

Further improvements to the models and calculations would be made to enhance the core SRNL competencies of isotope separation, collection, and recovery. This information will be used to further develop the predictive nature of the models and calculations, to be used in designing and optimizing future isotope separation systems.

## References

1. Lin, K. H. *Tritium Enrichment by Isotope Separation Technique*; ORNL-TM-3976, Oak Ridge National Laboratory, 1972.
2. Rae, H. K. Selecting Heavy Water Processes. In *Separation of Hydrogen Isotopes*; ACS Symposium Series 68, Washington D.C., 1978.
3. King, C. M.; Brunt, V. V.; King, R. B.; Garber, A. R. *Concepts for Detritiation of Waste Liquids*; WSRC-MS-91-027, Savannah River Site, 1991.
4. Fulbright, H. H.; Schwirian-Spann, A. L.; Looney, B. B.; Jerome, K. M.; Van Brunt, V. *Status and Practicality of Detritiation and Tritium Production Strategies for Environmental Remediation*; WSRC-RP-96-0075, Savannah River Site, 1996.
5. Geniesse, D. J.; Stegen, G. E. *2009 Evaluation of Tritium Removal and Mitigation Technologies for Wastewater Treatment*; DOE/RL-2009-18, Hanford Site, 2009.

## Acronyms

CECE	Combined Electrolysis Catalytic Exchange
CIE	Catalytic Isotope Exchange
DF	Decontamination Factor
GS	Girdler-Sulfide Process
SRNL	Savannah River National Laboratory
TCAP	Thermal Cycling Adsorption Process
WD	Water Distillation
WIE	Water Isotope Exchange

## Intellectual Property

Method for Water Isotope Separation

## High-Sensitivity Electric Field Detection Based on Gas Polarization

**Project Team:** Alicia Fessler, Willis Jones, Anna d'Entremont, Dale Hitchcock, Jay Gaillard

**Clemson University Collaborator:** Steve Serkiz

**Project Start Date:** October 1, 2019  
**Project End Date:** September 30, 2020

*The Emergency Response community would greatly benefit from a diagnostic tool capable of determining the charge state of a high-voltage object. The proposed work investigates the detection of gas polarization from dielectrophoretic (DEP) forces as a highly sensitive, static, direct current electric field detector. The polarization, and subsequent alignment of molecules, in the gas phase will have minimal gravity and drag forces, therefore the DEP polarization process is expected to be extremely sensitive at a greater distance from the source and at lower field strengths than existing electric field probes. The DEP*

*assembly and polarization of the gas can be measured using spectroscopic techniques.*

### FY2020 Objectives

- Develop a spectroscopy system for measuring gas polarization
- Conduct proof-of-concept of gas polarization in DC fields

### Introduction

The project scope is to investigate the detection of gas polarization from dielectrophoretic (DEP) forces as a high-sensitivity, non-invasive static direct current (DC) electric field detector with target sensitivity significantly higher than commercial devices and high/low voltage differentiation. Particles, molecules, and atoms within a non-uniform DC electrical field gradient are polarized by DEP forces. While DEP forces are relatively small, recent work funded by the Render Safe Technology Integration Program and reported in the open literature, have shown that these forces are sufficient to overcome kinetic (thermal), Brownian, gravity (mass), and drag forces to cause an alignment (i.e., self-assembly) of large molecules (such as carbon nanotubes) at room temperature and at distances of about ten inches with potentials as low as 100 V<sup>1</sup>. Additionally, unlike most other field detection approaches, this approach does not require a change in, or perturbation of, the electric field to produce a signal.

Because gas molecules are much lighter than carbon nanotubes, the gas molecules should have greatly reduced gravity and drag forces. Therefore, the gas molecules should be much more sensitive to the polarization and alignment from the DEP forces. The increased influence of the DEP forces on the gas molecules should allow for polarization to be detected at a greater distance from the source and at lower field strengths than with the carbon nanotubes. The overall process is illustrated for a single component gas in Figure 1 with: a) random orientation of gas molecules, b) polarization and

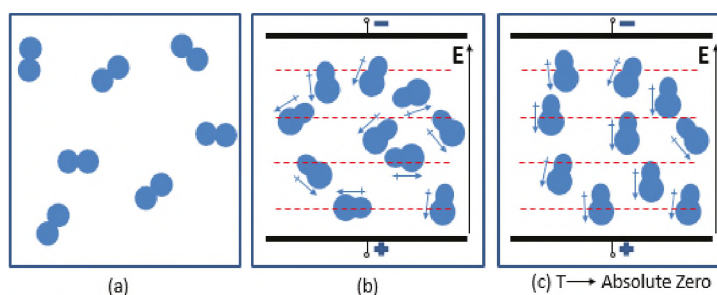


**Figure 1:** Gas molecules in a gas cell under ambient conditions without (a) and with (b) an applied static electric field; red dashed lines are equipotential lines. As temperature approaches absolute zero, thermal effects are reduced and the gas molecules more uniformly align to the applied electric field (c).

reorientation of gas molecules at ambient temperatures under a DC field, and c) greater alignment at lower temperatures under a DC field.

The research will develop a new type of detection method for DC electric fields and set the groundwork for development of a handheld tool which could be used by emergency response workers to detect the charge state of a suspicious object. Several direct and passive methods to determine charge state have been investigated, but without close proximity (several millimeters) to the high-voltage electrical components, the methods lack the sensitivity to unequivocally determine charge state. The DEP forces are expected to have effect on gaseous molecules about 10 inches or more from the electric field source based on measurements of carbon nanotubes.<sup>1</sup> The research will also improve our understanding of the effects of dielectrophoretic forces on gas molecules, as well as quantify the effects (i.e., field strength, source distance, and field geometry) related to the phenomenon being used as a detection method for DC electric fields.

## Approach

The proposed work investigates using a spectroscopic technique to measure gas phase constituents under the influence of an external electric field and develop a diagnostic tool to measure polarization changes. A deployable tool would consist of a handheld electric-field detector and a diode laser/detector package to measure gas polarization. In operation, the probe would be moved toward the exterior of an unshielded package of interest, or the interior with a shielded package, and the degree of gas polarization would indicate the charge state of the static DC field.

## Results/Discussion

To estimate the strength of the electric field as a function of distance, a 2D axisymmetric model was used with two 1 mm spherical electrodes spaced with the centers 2 mm apart in air and a 1 kV voltage between them. Figure 2 is a plot of the electric field magnitude along the axis of the two-dot pair starting from the outer edge of one of the electrodes. The electric field drops off quickly with only 5% of the value at the electrode surface still present within 5 mm and 10 V/m (from  $>10^6$  V/m) at  $\sim 5$  cm from the source. The maximum electric field strength in the simulation at the electrode surface between the dots was  $\sim 1.7e6$  V/m. The dielectric strength of air is  $\sim 3e6$  V/m, so there is limited scope for increasing the voltage in order to expand the region for large electric fields at a distance from the source. Therefore, the developed sensor would need to be able to detect 10 V/m or less to increase the distance from the source required for detection.

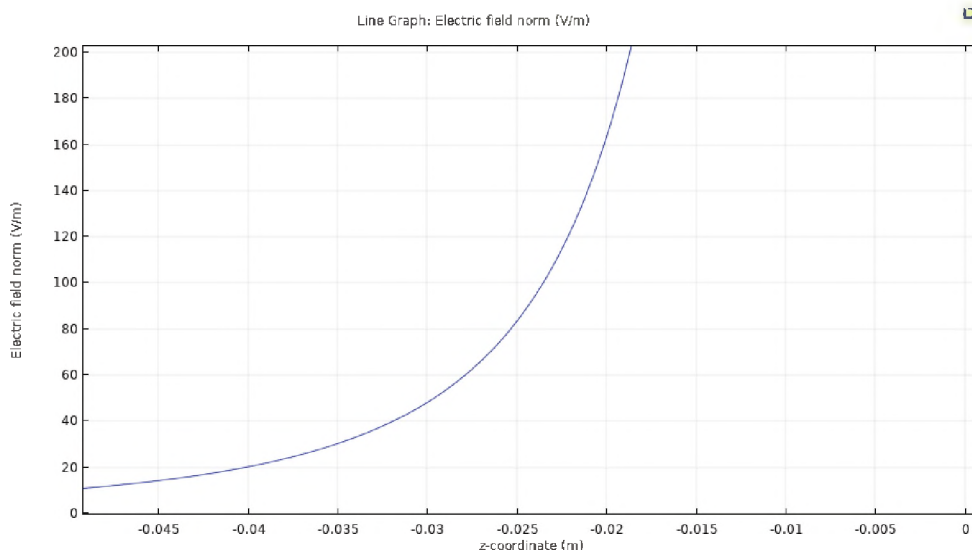


**Figure 2:** Plot of the electric field strength (V/m) as a function of distance from the source.

The spectroscopic measurement system consists of a Laser Quantum Gem 532 nm laser and a Kaiser f/1.8 Holospec spectrometer. An optically compatible quartz glass cell filled halfway with liquid cyclohexane was allowed to reach equilibrium within the cell to obtain gaseous cyclohexane in the upper half of the cell. Note: the cell was not pumped down prior to adding the liquid, so some air remained in the cell, as seen in the Figure 3 gas phase spectrum. The gas cell was placed between two copper plates which were connected to a voltage power supply. Initial testing has only employed a polarized laser for the spectroscopic polarization measurements. Figure 3 shows spectra of liquid and gaseous cyclohexane. The spectrum shows the expected cyclohexane peaks along with some peaks from air constituents. In Figure 4, the parallel and perpendicularly polarized spectra of liquid cyclohexane are shown to demonstrate the capability of measuring polarized gas molecules with the designed setup. Laser polarized gaseous cyclohexane is shown in Figure 5, and the change in intensity between the two polarizations does not seem identical to the liquid phase. However, literature shows there should be no difference in the degree of polarization between liquid and gas samples, and the observation is likely due to a light collection discrepancy.

## FY2020 Accomplishments

- Designed electric field apparatus to fit gas cell inside field plates
- Modeling performed to estimate field strength/distance shows the electric field strength falls to 10 V/m at ~5 cm from the high voltage source
- Laser polarized measurements of liquid cyclohexane demonstrates the system is capable of measuring the two polarization states
- Spectra of liquid and gaseous cyclohexane demonstrates system is aligned and ready to measure electric field effects on the spectra

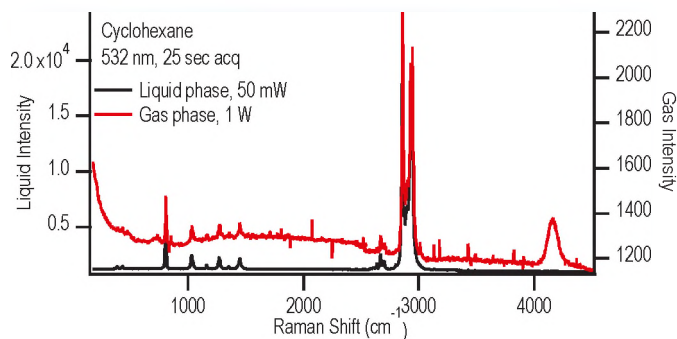


**Figure 3:** Spectra of liquid (black) and gaseous (red) cyclohexane.

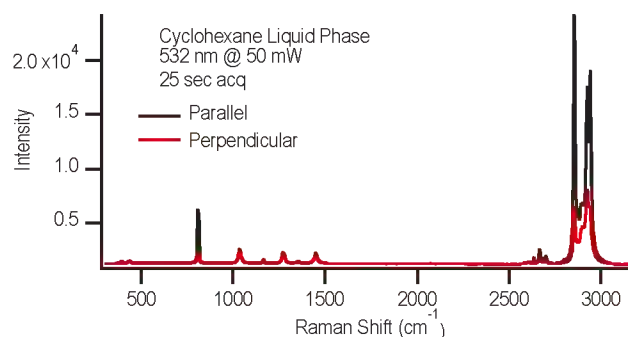


**Figure 4:** Spectra of parallel (black) and perpendicular (red) laser polarized liquid cyclohexane.

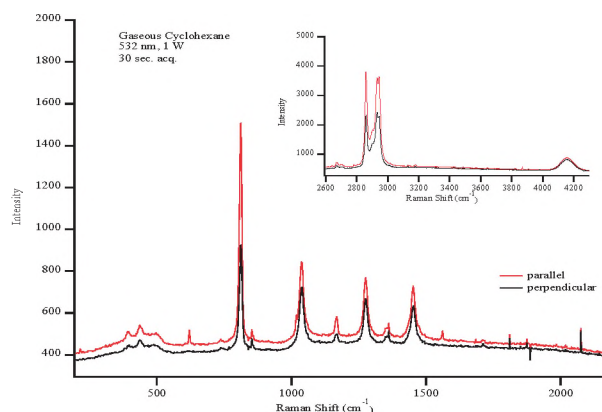


**Figure 5:** Spectra of parallel (black) and perpendicular (red) laser polarized gaseous cyclohexane.

## Future Directions

- Use pulsed electric field at higher voltages and a femtosecond laser to study polarization effects of electric field
- Cool the gas cell using a thermoelectric cooler to reduce thermal effects
- Evaluate CO<sub>2</sub> spectrum change under electric field influence
- Add insulating gas to evaluate reduction of electric field induced break down limit

## References

1. Oliveira, L.; Saini, D.; Gaillard, J.; Podila, R.; Rao, A. M.; Serkiz, S. M. Directed-assembly of carbon structures in a nonpolar dielectric liquid under the influence of DC-generated electric fields. *Carbon* **2014**, *93*, 32-38.

## Acronyms

DC	Direct Current
DEP	Dielectrophoretic

## Intellectual Property

Invention Disclosure: SRS-19-008.

## Post-Doctoral Researchers

Willis Jones is an SRNL post-doctoral researcher who contributed to this work in FY20 by performing work on site.

## Laser-Based Means for Accelerating Nuclear Decay Rate

**Project Team:** Robert Lascola, Michael Thomas (postdoc), Simona Murph, David DiPrete, Kalee Fenker

**Project Start Date:** October 1, 2019

**Project End Date:** September 30, 2021

*This project aims to replicate and build upon a reported series of results whereby nuclear decay of unstable species has been accelerated under laser irradiation in the presence of resonantly excited plasmonic nanoparticles. We are currently utilizing a laser system similar to that used within these reports as well as optimizing nanoparticle solution environments in an attempt to replicate reported results or provide*

*alternative pathways that may explain some perceived discrepancies. The current work is being performed with equipment and techniques currently available at SRNL, including nanoparticle synthesis and pulsed lasers for plasmon excitation. The results of these experiments could provide quantitative data that can be used to resolve the discrepancies in the calculations and better estimate the ultimate utility of the process. If verified, this would represent a pathway for using readily available and scalable technology to reduce the long-term radiological storage requirements of certain forms of nuclear waste.*

### FY2020 Objectives

- Overall objective: investigate the accelerated  $\alpha$  and  $\beta$  decay of radionuclides through exposure to the intense electric fields associated with laser-irradiated nanoparticles and nanopatterned surfaces
- Reproduce observations reported in the literature
- If observations are reproduced, establish quantitative relationships between experimental parameters and changes in the decay rates
- If observations are not reproduced, propose and investigate alternative explanations for the reported results

### Introduction

This project aims to replicate and build upon a reported series of results whereby nuclear ( $\alpha$  or  $\beta$ ) decay of unstable species has been accelerated under laser irradiation in the presence of resonantly excited plasmonic nanoparticles.<sup>1-2</sup> Calculations support the possibility that a non-resonant interaction of an atom with an intense external electric field can alter nuclear processes, but disagree on the magnitude of the effect that can be expected.<sup>3-7</sup> Resonant excitation of plasmonic nanoparticles can lead to increases of electric field strength on the order of  $10^5$ - $10^6$  near the nanoparticle surfaces. Laser pulses from commercially available, benchtop sources (such as a Nd:YAG laser) can thus be enhanced to  $10^{18}$ - $10^{19}$  W/cm<sup>2</sup>, which is sufficient to excite relativistic energies in electrons.<sup>8</sup> In the reported work, fs, ps, and ns pulses directed into a solution of colloidal gold nanoparticles and dissolved UO<sub>2</sub>Cl<sub>2</sub> altered the <sup>238</sup>U decay pathway, as detected by changes in the concentrations of daughter products <sup>234</sup>Th and <sup>234m</sup>Pa.

The significance of these results is that the equipment and materials used to generate changes in nuclear decay rates are much more readily accessible than synchrotron sources or free-electron lasers which would access nuclear transitions directly.<sup>9</sup> The ability to accelerate decay rates would permit transformation of nuclear waste from a radiological and chemical problem at geologic time scales to a shorter-term chemical problem. Although significant engineering challenges would remain, not least of which being the determination of the form and materials for nanoparticles which can be used in massive quantities, the confirmation of these results would justify continued development in this field. Additionally, as implied in the above discussion, there is substantial disagreement between various calculations with respect to the magnitude of the effects that are possible. A more quantitative approach

to irradiation parameters and the kinetics of decay and regrowth will inform and help to refine the calculations.

Work in FY20 followed two parallel paths. The main direction of work was towards setting up an experiment where highly energetic laser pulses could be safely focused into a radiological solution. This work was slowed by necessary repairs of the Nd:YAG laser that was procured for this purpose. We were able to design and test a reaction cell and focusing optics that allow us to maintain a large beam diameter at the window faces (preventing cell damage) and a tight focus inside the solution (maximizing power density). This arrangement should be ready for radiological testing in early FY21. The second path was an initial investigation of the chemical effects of laser-induced plasmas inside the solution on both the nanoparticles and dissolved materials. A possible alternate explanation for the disappearance of radionuclides is their incorporation into agglomerated precipitates, which were observed in the original experiments. It is likely that in the previous work, the agglomerated particles were not included in the radiological characterization. We have demonstrated the ability to make gold agglomerates from dissolved gold salts and will rapidly expand this work to determine if co-dissolved materials also are removed from solution.

## Approach

Achieving the goals of the project brings together SRNL capabilities in nanoparticle synthesis and evaluation, lasers, radiochemical solution handling, and analytical measurements (rad and non-rad). Replication of the reported results will be accomplished by laser irradiation of uranyl chloride solutions with natural abundance  $^{235}\text{U}$ . Solutions will be characterized before and after irradiation by gamma spectroscopy and mass spectrometry. If the equilibrium of the decay products is found to be altered, then variations in experimental parameters (laser characteristics, exposure time, types of nanoparticles) will be explored to try to improve yields and enhance mechanistic understanding. Not observing the same results would lead to an investigation of the chemistry of irradiated solutions, to try to find an alternative explanation for the reported observation.

## Results/Discussion

Initial evaluation of the procured Nd:YAG nanosecond (ns) laser found repairs necessary for proper function at high output power (>2W). As of the end of FY20, all parts needed to fully refurbish the laser have been procured. A similar laser was used in experiments up to this point (Nd:YAG ns laser using the second harmonic at 1.5W output power with a 10 Hz pulse repetition interval). After constructing an optical pathway post-laser output (Figure 1), we found that standard cell configurations led to issues in both heat production and cell damage. Thus, we designed a new cell, which was made by the SRNL Glass Shop (see Figure 2). The cell was able to keep temperatures of irradiated solution around room temperature and was not damaged during experiments, which lasted up to six hours. During some experiments, where a transparent solution was used, the focus of the laser could be seen (Figure 3) and the laser-nanoparticle interaction could also be witnessed, as seen in Figure 4.



**Figure 1:** Optical setup. Pathway: laser tuner, turning mirrors, Galilean beam expander, beam focuser, sample cell, beam dump.

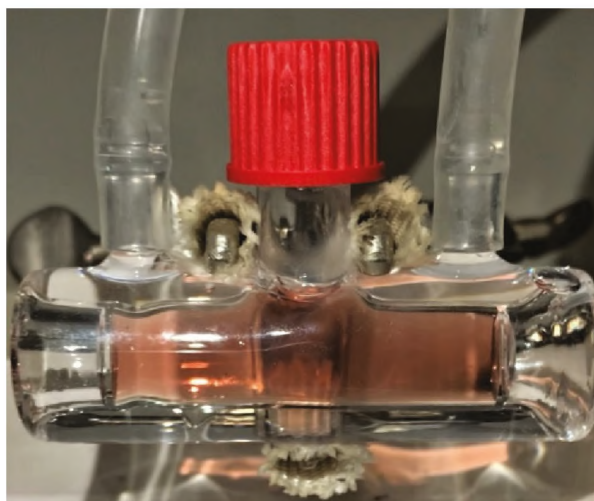


**Figure 2:** Designed cell containing a solution of gold nanoparticles with water flowing through the water jacket.

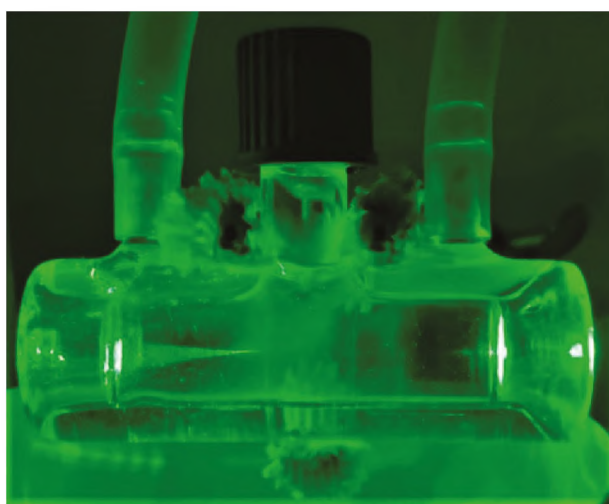


**Figure 3:** Focused laser light is witnessed in a gold nanoparticle solution demonstrating proper optical setup for both beam expander and focus lens.

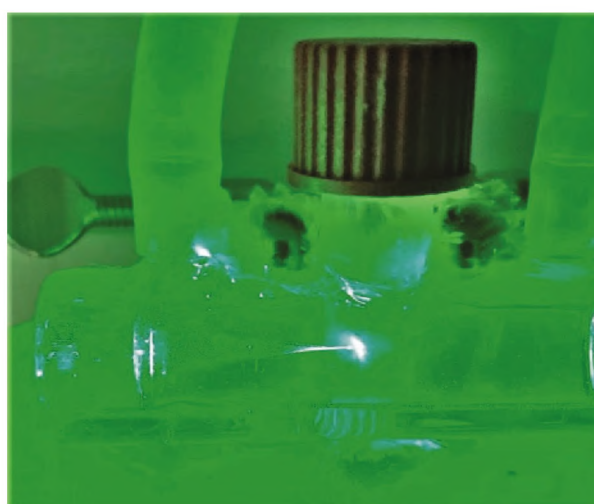


**Figure 4:** Focused beam interaction with gold nanoparticles creating a resonant plasmonic effect is witnessed. Note the bright flash and large area of effect where interaction occurs.

With a properly functioning cell in hand, baseline studies were conducted to ensure proper setup of optical system. A solution of gold tetrachloride ( $\text{HAuCl}_4$ ) was irradiated by a Nd:YAG ns laser using the second harmonic (532 nm) at a power output of 1.5W for 2.5 hours. The characteristic plasmon absorbance peak for gold nanoparticles appeared, leveling off over time, indicating the formation of gold nanoparticles from the solution (Figure 5). Visually, there was a color change of the solution, a further indication that a product or mixture of products was produced. Other particulates that fell out of the solution when irradiated have yet to be characterized.

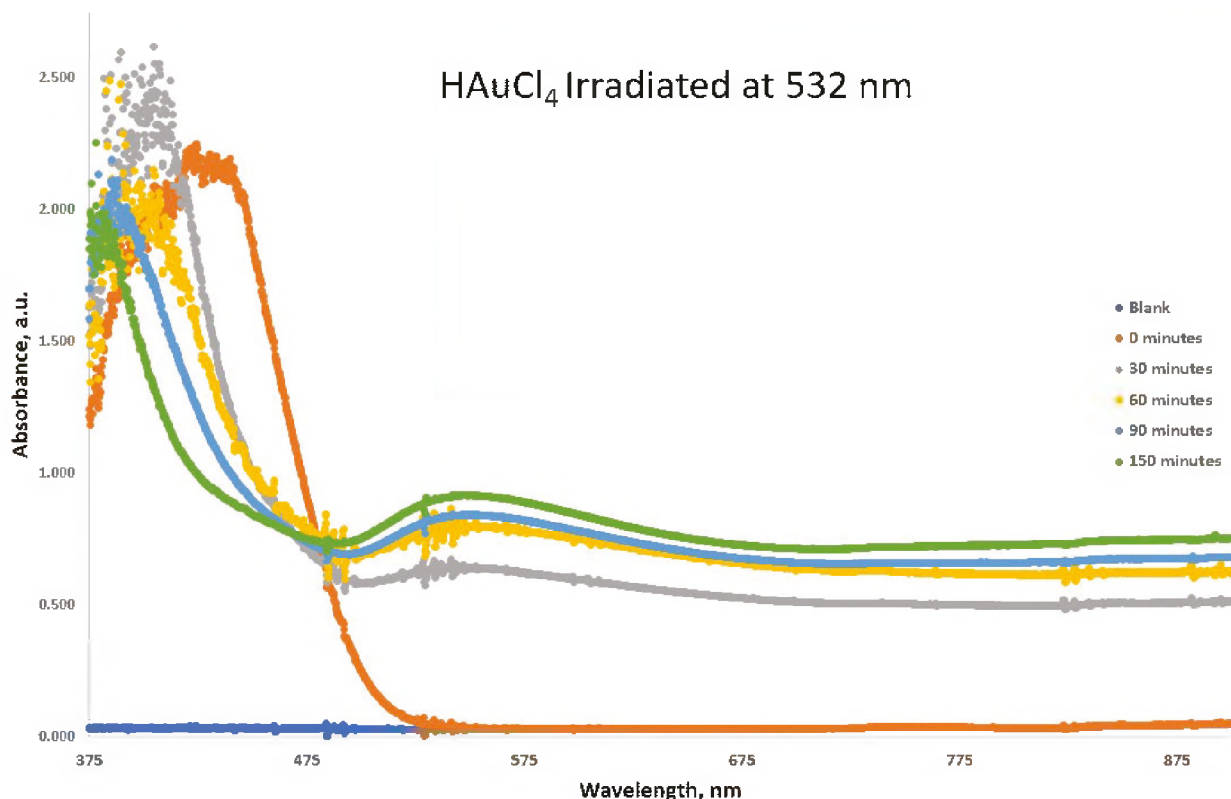


**Figure 5:** Absorbance plot of HAuCl<sub>4</sub> solution irradiated at 532 nm at 1.5W with a pulse repetition rate of 10 Hz for 2.5 hours. Note the growth and blue shift of the peak around 530-550 nm, characteristic of gold nanoparticles.

We believe this crashing out mechanism may be one of the pathways that led to discrepancies in the reported literature. Other metals and mixtures of metals are being tested to determine their ability to create nanoparticles, metal amalgams, or other types of mixtures that will crash out of solution.

### FY2020 Accomplishments

- Refurbished Nd:YAG laser to optimize pulse power
- Designed and tested optical and sampling handling setup. Developed new sample cell to withstand laser fluence and dissipate heat associated with sample absorbance
- Conducted preliminary experiments to demonstrate that co-agglomeration is a potential pathway for removal of co-dissolved species from solution

### Future Directions

This project has been continued for FY21. Primary research efforts will include:

- Pursuing the original objective of replicating the reported observations and claims of accelerated nuclear decay. More rigorous chemical and radiological characterization of all products of the process will provide evidence for the fate of the radionuclides
- A continued examination of the types of nanoparticles and agglomerates formed from solution under pulsed laser irradiation will not only help explain the original results, but also suggest a way to make new materials with interesting plasmonic properties

- We will also pursue the modification of nanoparticles with actinide-sorbent shells<sup>10</sup>. The shells will be based on materials that have been shown to be selectively sorbent to uranyl nitrate in acidic conditions. By increasing the concentration of actinides near the nanoparticle surface, it is thought that plasmon-mediated effects can be introduced more efficiently than if relying on random proximity within a solution

## References

1. Simakin, A.V.; Shafeev, G.A. *Quantum Electron.* **2011**, *41*, 614-618.
2. Barmina, E.V.; Simakin, A.V.; Shafeev, G.A. *Quantum Electron.* **2014**, *44*, 791-792.
3. Gamov, G. Z. *Phys.* **1928**, *51*, 204-212.
4. Qi, J. *et al. Phys. Rev. C* **2019**, *99*, 044610.
5. Apostol, M. *Open Acc J. Math Theor. Phy.* **2018**, *1*, 155-159.
6. Delion, D.S.; Ghinescu, S.A. *Phys. Rev. Lett.* **2017**, *119*, 202501.
7. Matinyan, S. *Physics Reports* **1998**, *298*, 199-249.
8. DiPiazza, A. *et al. Rev. Mod. Phys.* **2012**, *84*, 1177-1228.
9. Ledingham, K.W.D., *et al. Science* **2003**, *300*, 1107-1111.
10. Yuan, D., *et al. J. Mat. Chem. A* **2017**, *5*, 22735-22742.

## Acronyms

Nd:YAG – Neodymium: yttrium-aluminum-garnet

## Post-Doctoral Researchers

Michael Thomas started work at SRNL in June 2020.

## Photon Entanglement Spectroscopy and Imaging in Actinide Research

**Project Team:** Eliel Villa-Aleman, Patrick Ward, DeWayne Dick

**Project Start Date:** November 1, 2019

**Project End Date:** September 30, 2021

*Quantumly entangled particles are capable of transmitting information to their entangled counterpart instantaneously once one particle has changed. Herein, quantumly entangled photons are generated by spontaneous parametric down conversion through a temperature controlled non-linear optic. This process generates two photons of lower energy of which the sum of energy equals the energy of the pump photons. These*

*entangled photons can be separated and provide imaging capabilities by using one set of photons for imaging and the other set of photons for detection.*

### FY2020 Objectives

- Acquire single longitudinal mode laser and optics necessary to construct an imaging system by entangled photons
- Demonstrate spontaneous parametric down conversion and define conditions for photon wavelength matching between two non-linear optics
- Construct breadboard system for entangled photon imaging

### Introduction

Second order non-classical interference has been demonstrated previously with indistinguishable photon pairs.<sup>1,2</sup> The generation of photon pairs from a non-linear optic (signal and idler) by spontaneous parametric down conversion provides entangled photons which can be separated based on their wavelength by dichroic mirrors. When idler photons are perfectly aligned with another set of idler photons generated in a second non-linear optic, the photons are now indistinguishable and therefore satisfy the requirement necessary for quantum interference. This allows for interference to be observed in the signal photons generated from the first non-linear optic and therefore imaging of an object from photons which have never actually physically interacted with that object. This methodology opens a multitude of possibilities for imaging solutions since the photons interacting with the object of interest do not need to be detected directly. Instead, their entangled photons can be observed to provide the image of the interest.

Inspired by the recently illustrations of this ability to image using undetected photons,<sup>3,4</sup> we have set out to develop our own breadboard quantum imaging system and advance the technique to provide application in practice.

### Approach

A 532 nm signal longitudinal mode (SLM) laser is used to generate quantum entangled photon pairs by spontaneous parametric down conversion in a pair of periodically poled potassium titanyl phosphate (ppKTP) crystals. A SLM laser and bandpass filters for the signal photons are used to significantly reduce the bandwidth of the beams and therefore increase the coherence length. A breadboard system was constructed to focus idler photons from the first non-linear optic onto the beam profile of idler photons generated from a second non-linear optic. The wavelengths

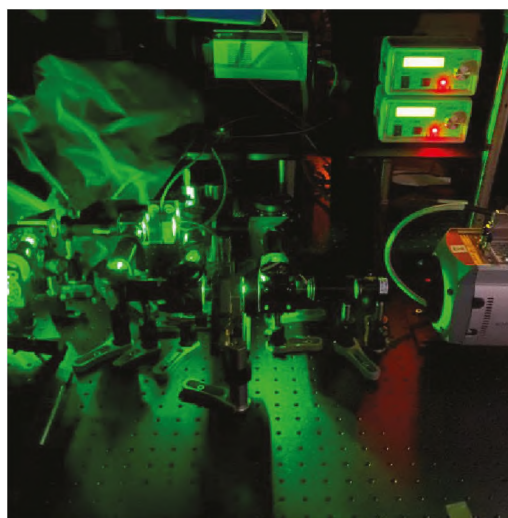


**Figure 1:** Image of breadboard system during operation.

generated from each non-linear optic were measured in a spectrometer and the temperature of the ppKTP (non-linear optic) adjusted to provide identical wavelengths for photon pairs generated from each non-linear optic. The idler photons from non-linear optic 1 were aligned to pass through an object of interest and the signal photons aligned with the signal photons from the second non-linear optic. The signal photons were then split in a 50:50 beam splitter and half of the beam sent to a CCD detector for imaging and the other half dumped.

## Results/Discussion

In order to develop the breadboard system for quantum entangled photon imaging certain conditions must first be satisfied. First, the photons must be indistinguishable to allow for quantum interference to occur. Therefore, a single 532 nm laser was passed through a polarizing beam splitter and then a half wave plate on one side to produce a pump laser which was equivalent in power and polarity for two independent ppKTP crystals. Furthermore, the wavelengths generated by spontaneous parametric down conversion from each non-linear optic must be identical to allow for indistinguishability. The wavelength of the signal and idler photons was controlled in each non-linear optic by precisely controlling the crystal temperature during laser illumination. The

generated photons were measured using a spectrometer as shown for the signal photons in Figure 2. The idler photons wavelengths (1550 nm) were also verified and aligned using an IR detector. Idler photons from the first non-linear optic were passed through the second non-linear optic and aligned to provide the condition of indistinguishability. The signal photons from both non-linear optics were aligned and mixed in a 50:50 beam splitter and sent to the Si detector CCD camera. A series of lenses were used to focus the beam onto the camera and an 810 nm bandpass filter used to prevent any other wavelengths from reaching the detector.

Now that the system has been constructed, fine tuning of the beam for image quality and assurance of coherence length matching will be carried out to provide initial images and provide guidance for the next series of experiments related to imaging through fiber optics and imaging a sample which changes over time.

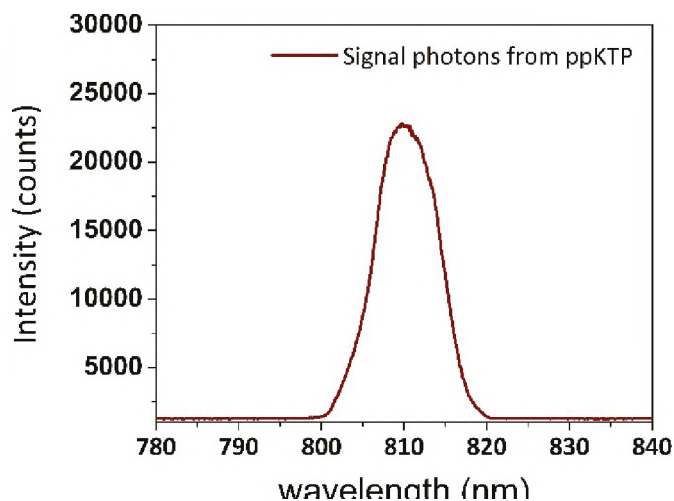


Figure 2: Spectrum of signal photons generated from ppKTP crystal #1 at 54.0 °C

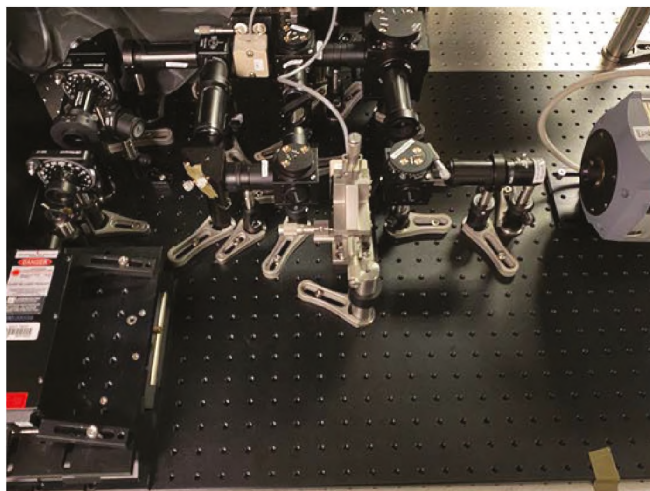


Figure 3: Picture of breadboard entangled photon imaging system.

## FY2020 Accomplishments

- Breadboard quantum imaging system constructed using continuous wave 532 nm SLM laser
- Wavelengths of photon pairs generated by spontaneous parametric down conversion measured and temperature profiles necessary for photon pair matching defined
- Idler and signal photons from 2 separate ppKTP crystals were wavelength matched and aligned to satisfy the quantum interference condition of indistinguishability
- Polarity and power matching were accomplished for pump photons going to both non-linear optics

## Future Directions

- Generate samples for imaging using constructed breadboard system
- Demonstrate use of fiber optics to transport light over greater distances and therefore provide higher application fidelity for advanced imaging techniques
- Demonstrate imaging of a sample which is undergoing change and image that change as it occurs

## References

1. Zou, X. Y.; Wang, L. J.; Mandel, L. Induced Coherence and Indistinguishability in Optical Interference. *Phys. Rev. Lett.*, **1991**, *67* (3), 318-321.
2. Wang, L. J.; Zou, X. Y.; Mandel, L. Induced Coherence without Induced Emission. *Phys. Rev. A* **1991**, *44* (7), 4614-4622.
3. Lahiri, M.; Lapkiewicz, R.; Lemos, G. B.; Zeilinger, A. Theory of Quantum Imaging with Undetected Photons. *Phys. Rev. A* **2015**, *92*, 013832-1 - 1013832-8.
4. Lemos, G. B.; Borish, V.; Cole, G. D.; Ramelow, S.; Lapkiewicz, R.; Zeilinger, A. Quantum Imaging with Undetected Photons. *Nature* **2014**, *512*, 409-412.

## Acronyms

CCD Charge coupled device

ppKTP Periodically Poled Potassium Titanyl Phosphate

SLM Single Longitudinal Mode

## Post-Doctoral Researchers

Don DeWayne Dick (SRNL)

## Development of FRET Clusters for CBRN Detection

**Project Team:** Kaitlin Lawrence, Wendy Kuhne and Ashlee Swindle

**Project Start Date:** November 15, 2019

**Project End Date:** August 21, 2020

*Advanced sensor capabilities for the simultaneous on-site detection of specific chemical, biological, and radiological/nuclear (CBRN) threats are important to significantly limit the risk of exposure to personnel and allow the rapid collection of essential scientific data and critical evidence. Commercially available sensor capabilities are generally complex, and/or require highly*

*specific and ultra-sensitive methods that are often power demanding or require offsite post-analysis for positive detection, leaving personnel vulnerable. The goal of this project is to develop a portable sensor capable of simultaneously detecting CBRN signatures using a multiplexed Förster Resonance Energy Transfer (FRET) based sensor. FRET sensors are tailorable, specific, and highly dependent on the donor-acceptor distance. In this project, nanoparticles were functionalized with aptamers that were designed for the detection of methylphosphonate, a sarin metabolite. FRET was measured between quantum dot donors and dye and metal nanoparticle acceptors using optical spectroscopy.*

### FY2020 Objectives

- Functionalize metal and semiconductor nanoparticles with targeting ligands: Chemically functionalized aptamers and antibodies to target biological warfare agents, chemical warfare surrogate targets, and nuclide resin materials are commercially available and will be coupled to the nanoparticle surfaces through ligand exchange and coupling chemistries
- Develop individual FRET clusters: A FRET cluster will be developed to target a chemical threat for proof of concept validation. FRET parameters will be measured using optical spectroscopy to determine energy transfer efficiency in the absence and presence of the targeted threat.

### Introduction

Development of a multifunctional portable fluorescent sensor with high selectivity for the simultaneous detection of specific chemical, biological, and nuclear threats (CBRN) is extremely valuable for various entities and situations, including emergency responders, forensics, and environmental sampling. Current detection techniques for CBRN are generally complex and require highly specific and ultra-sensitive methods. For example, biological threats, such as anthrax or ricin, are routinely analyzed off-site through the laboratory response network, where samples of interest are first sent to a sentinel lab, followed by a reference laboratory, and then, if the biological threats are not ruled out at the first two laboratories, the samples are sent to a national laboratory. This network uses fixed laboratory equipment with mass spectroscopy (MS) techniques which are highly sensitive (ricin reported detection limits of 0.64 ng/mL)<sup>1</sup>; however, they require complex data analysis, especially for biological samples, which have numerous MS fragments and potential matrix effects that can interfere with the determination of the analyte. Alternatively, fluorescence based Förster Resonance Energy Transfer (FRET) sensors for ricin also have reported detection limits below the median lethal dose ( $LD_{50} = 5\text{--}10$  ng/mL detection limits)<sup>2</sup> with much faster, real-time response time and a simpler signal readout. FRET sensors are ideal for in field detection due to the low detection limits, miniature size and low power requirements.

In FRET, an excited donor (D) molecule transfers energy to an acceptor (A) through nonradiative dipole-dipole interactions.<sup>3</sup> For successful FRET, the donor and acceptor should have appropriate spectral overlap, where the emission of the donor overlaps with the absorbance of the acceptor (overlap integral,  $J$ ) and the donor and acceptor must be in close proximity (20-60 Å

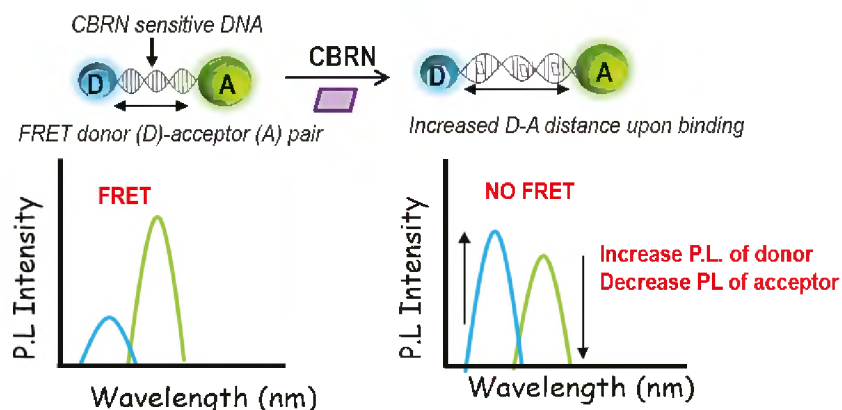


**Figure 1:** Demonstration of the change in FRET between a donor (D) and acceptor (A) upon analyte binding.

separation), which can be accomplished by covalently linking the donor and acceptor. The transfer efficiency between a donor and acceptor is very sensitive and is proportional to  $1/r^6$  ( $r = D-A$  distance) for FRET or  $1/r^4$  for nanometal surface energy transfer (NSET) which occurs when a metal nanoparticle is the acceptor. Upon analyte binding (biological, chemical, radionuclide specificity), a decrease in transfer efficiency occurs due to a change in the distance between the covalently bound donor and acceptor (Figure 1).

The change in the D/A ratio of fluorescence emission can be used to quantitatively measure the presence of the analytes upon binding, which changes the distance between the donor and acceptor. Similar to absorbance, fluorescence emission follows Beer's Law ( $A = \epsilon bc$ , where  $A$  is absorbance,  $\epsilon$  is molar absorptivity,  $b$  is cell path length,  $c$  is concentration) for quantitative measurements, but fluorescence emission is more sensitive.<sup>3i</sup> Most FRET sensors use organic dyes as the fluorescent donors; however, organic dyes are susceptible to photobleaching, have lower quantum yields (QY), and have pH dependent fluorescence. Inorganic fluorophores such as quantum dots (qdots) and quantum rods (qrods) have higher photostability, higher absorption coefficients, narrow emission peaks, and have higher quantum yields compared to organic dyes, therefore they are more robust for deployment applications. Qdot and qrod fluorescence emissions are tailored based on size from around 400-1300 nm and the ligands can be tailored to change solubility and surface functionalization. The narrow emission wavelengths allow for the measurement of multiple qdots simultaneously on one channel with spectral separation that is required for FRET detection.<sup>4</sup> Qdots have a large surface area, so multiple types of ligands to be bound to the surface at the same time. Self-assembled and FRET based devices also have applications beyond sensors, including the development of molecular devices,<sup>5</sup> quantum computing,<sup>6</sup> and imaging.<sup>7</sup> **The goal of this project is to develop a FRET sensor for the detection of specific CBRN threats with high selectivity, high confidence, and reduced false positives.** For proof-of-concept validation, a FRET cluster for the detection of a sarin metabolite, methylphosphonic acid, was created. Future work will focus on the creation of multiplexed FRET sensors to detect multiple hazards simultaneously. FRET based sensors can not only provide fast detection capabilities, on the order of minutes rather than hours to weeks for polymerase chain reaction (PCR) and mass spectrometry (MS) techniques, but for some targeted analytes, it can provide detection limits well below what is currently commercially available and with high confidence.<sup>8</sup>

## Approach

This seedling focused on the proof of concept validation of inorganic based FRET clusters for chemical warfare detection. For this work, FRET pairs were designed using DNA based aptamers that were designed for the detection of a sarin metabolite, methylphosphonic acid (MePA).<sup>9</sup> These aptamers were chosen against other similar molecules, leading to high selectivity. Qdots were first phase transferred into aqueous solutions using standard ligand exchange techniques and then coupled to the aptamers to create qdot-aptamer conjugates. The energy transfer between qdots and different acceptors, including AuNPs, which which quench fluorescence based on NSET, qdots and dye quenchers, was measured to determine the best acceptor for analyte quantification. FRET was measured using UV-Vis and photoluminescence (PL) spectroscopy.

## Results/Discussion

### Nanoparticle Functionalization

To create the FRET pairs, qdots and AuNPs were functionalized with DNA aptamers. Qdots with different sizes and emission wavelengths (Figure 2) underwent ligand exchange and dispersed in aqueous buffers where they were then coupled to the aptamers through standard coupling chemistry. After phase transferring, the QY of the qdots were relatively stable, with QY up to 25% after phase transferring. QY preservation is important for the FRET process, as the QY of the donor plays a role in FRET efficiency.<sup>3i</sup> AuNPs were functionalized with DNA through ligand exchange with thiol functionalized aptamers. As shown in Figure 3, AuNP-DNA conjugates have an additional absorption peak for the DNA, demonstrating successful functionalization. The AuNP-DNA conjugates that were created with MePA aptamers were calculated to have an average of 113 DNA per AuNP. This high density of targeting ligands is a result of the large surface area, which can lead to more sensitive detection.

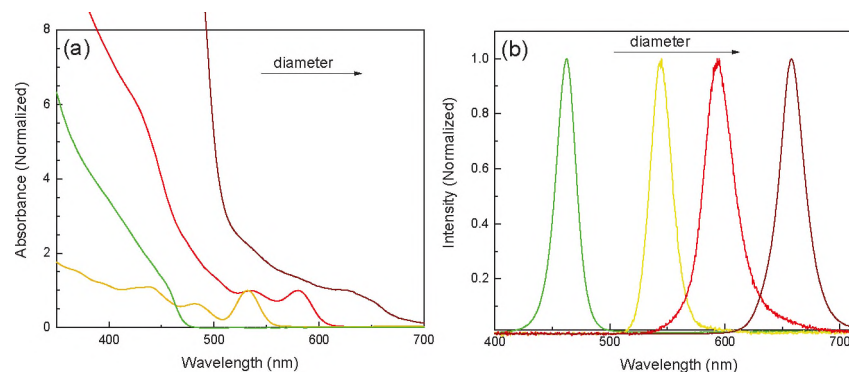


Figure 2: (a) UV-vis of and (b) PL of different sized qdots.

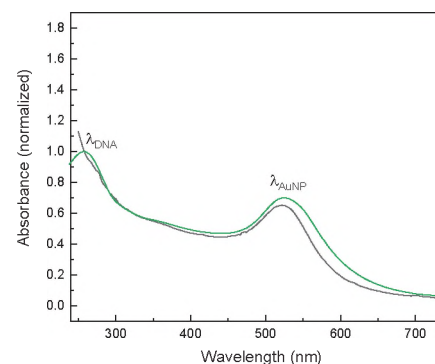


Figure 3: UV-Vis of AuNP-DNA.

### Qdot donors with quenching acceptors

A quencher was linked to the qdot surface through dsDNA hybridization to study the FRET between the qdot donor and the quenching acceptor. As shown in Figure 4a, there is a high degree of spectral overlap between the donor and acceptor. After the addition of the complementary strand to the qdot-ssDNA conjugate, the PL of the qdot decreased as a result of FRET.

## Qdot donors with AuNP acceptors

The energy transfer between qdot donors and AuNP acceptors was measured via PL. As shown in Figure 5a, there is spectral overlap between the UV-vis of the AuNP acceptor and the PL of the qdot, which is required for energy transfer to occur. After addition of AuNPs to the qdots, there was a decrease in PL as a result of energy transfer, as depicted in Figure 5b. This successful demonstration of energy transfer between the qdot and AuNP can be used to measure the concentration of MePA in solution.

## Qdot donors with qdot acceptors

Qdots have the ability to be both FRET donors and acceptors because of their broad absorption spectra and narrow emission peaks. As shown in Figure 6, there is a high degree of spectral overlap between a qdot with emission at 540 nm (qdot540) and a qdot with emission at 600 nm (qdot600). One challenge to qdot-qdot FRET pairs is spectral cross talk, which results from the broad qdot absorption profiles. Three dimensional fluorescence excitation emission matrix (EEM) spectroscopy was measured for the qdot pair in the absence of FRET (Figure 7). For this FRET pair, there is good spectral separation at all the measured wavelengths. At the higher wavelengths, the acceptor is selectively excited as expected based on the absorbance spectra (Figure 6). EEM spectroscopy allows the measurement of the FRET processes on non-FRET channels, which is above 560 nm for this FRET pair. When the FRET pairs become more complex, such as in three color FRET conjugates, EEM is a powerful technique for quantifying FRET processes. This technique will be applied in higher order FRET pairs for FRET quantification.

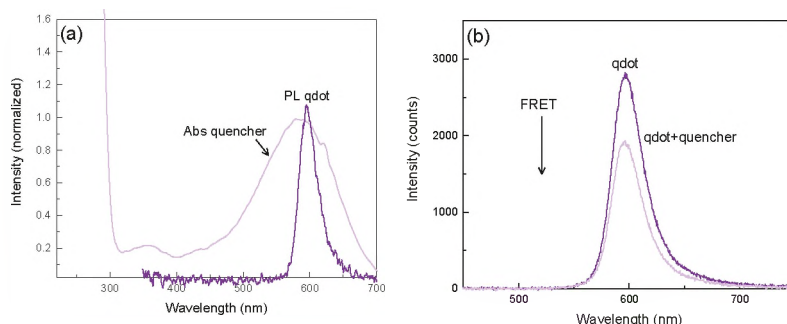


**Figure 4:** (a) Spectral overlap for the qdot donor and acceptor quencher and (b) decrease in qdot PL after quencher binding.

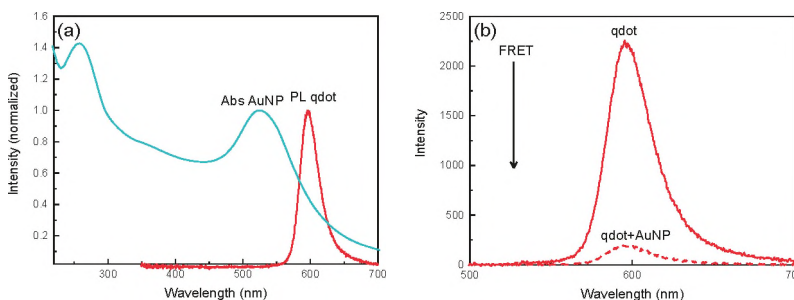


**Figure 5:** (a) Spectral overlap between the UV-vis of the AuNP acceptor and PL of the qdot donor (b) decrease in qdot PL in the presence of the AuNPs.

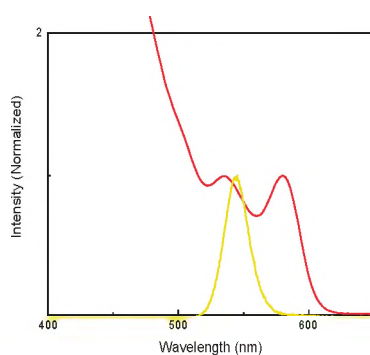


**Figure 6:** Spectral overlap between the PL of a qdot donor (qdot540) and the absorbance of a qdot acceptor (qdot600).

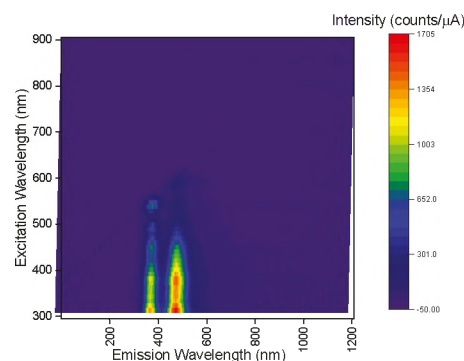


**Figure 7:** EEM for a qdot donor and acceptor pair.

## FY2020 Accomplishments

- Created AuNP-DNA and qdot-DNA conjugates
- Successfully measured FRET between qdots with a variety of different acceptors
- Designed FRET pairs for the detection of a sarin metabolite, methylphosphonic acid

## Future Directions

Follow up funding in a full LDRD project (LDRD-2021-00250) will build upon the results from this seedling work. Future work will focus on detection quantification using different FRET pairs. The development of biological and radiological/nuclear FRET pairs will be carried out on separate platforms before being combined for the simultaneous CBRN detection. The addition of multiple targeting ligands for the same analyte will also be investigated to decrease the risk of false positives.

## FY 2020 Peer-reviewed/Non Peer-reviewed Publications

One manuscript has been outlined, with SRNL as the primary research organization. The publication is slated to be completed by early FY21.

## References

1. Kalb, S. R.; Schieltz, D. M.; Becher, F.; Astot, C.; Fredriksson, S.-Å.; Barr, J. R., Recommended Mass Spectrometry-Based Strategies to Identify Ricin-Containing Samples. *Toxins* **2015**, *7* (12), 4881-4894.
2. Moshiri, M.; Hamid, F.; Etemad, L., Ricin Toxicity: Clinical and Molecular Aspects. *Rep. Biochem. Mol. Biol.* **2016**, *4*, 60-65.
3. (a) Berney, C.; Danuser, G., FRET or No FRET: A Quantitative Comparison. *Biophys. J.* **2003**, *84* (6), 3992-4010; (b) Beljonne, D.; Curutchet, C.; Scholes, G. D.; Silbey, R. J., Beyond Förster Resonance Energy Transfer in Biological and Nanoscale Systems. *J. Phys. Chem. B* **2009**, *113* (19), 6583-6599; (c) Singh, M. P., and Strouse G. F., Involvement of the LSPR Spectral Overlap for Energy Transfer between a Dye and Au Nanoparticle. *J. Am. Chem. Soc.* **2010**, *132*, 9383-9391; (d) Halivni, S., Sitt, A., Hadar I., and Banin, U., Effect of Nanoparticle Dimensionality on Fluorescence Resonance Energy Transfer in Nanoparticle-Dye Conjugated Systems. *ACS Nano* **2012**, *6* (3), 2758-2765; (e) Han, H.; Valle, V.; Maye, M. M., Probing Resonance Energy Transfer and Inner Filter Effects in a Quantum Dot-Large Metal Nanoparticle Clusters using a DNA-Mediated Quench and Release Mechanism. *J. Phys. Chem. C* **2012**, *116*, 22996-23003; (f) Han, M., Gao, X., Su, J. Z., and Nie, S., Quantum-Dot-Tagged Microbeads for Multiplexed Optical Coding of Biomolecules. *Nat. Biotech.* **2001**, *19*, 631-635; (g) Breshike, C. J., Riskowski, R. A., and Strouse, G. F., Leaving Förster Resonance Energy Transfer Behind: Nanometal Surface Energy Transfer Predicts the Size-Enhanced Energy Coupling between a Metal Nanoparticle and an Emitting Dipole. *J. Phys. Chem. C* **2013**, *117*, 23942-23949; (h) Chen, G.; Song, F.; Xiong, X.; Peng, X., Fluorescent Nanosensors Based on Fluorescence Resonance Energy Transfer. *Ind. Eng. Chem. Res.* **2013**, *52*, 11228-11245; (i) Lakowicz, J. R., *Principles of Fluorescence Spectroscopy*. Second ed.; Kluwer Academic/Plenum Publishers: New York, NY, 1999.
4. (a) Coopersmith, K.; Han, H.; Maye, M. M., Stepwise assembly and characterization of DNA linked two-color quantum dot clusters. *Langmuir* **2015**, *31*, 7463-7471; (b) Lee, J.; Lee, S.; Ragunathan, K.; Joo, C.; Ha, T.; Hohng, S., Single-molecule four-color FRET. *Angew Chem Int* **2010**, *49* (51), 9922-9925; (c) Clapp, A. R.; Medintz, I. L.; Uyeda, H. T.; Fisher, B. R.; Goldman, E. R.; Bawendi, M. G.; Mattoussi, H., Quantum Dot-Based Multiplexed Fluorescence Resonance Energy Transfer. *J. Am. Chem. Soc.* **2005**, *127*, 18212-18221.

5. Kuscu, M.; Akan, O. B., The Internet of Molecular Things Based on FRET. *IEEE Internet of Things Journal* **2016**, *3* (1), 4-17.
6. Kuscu, M.; Akan, O. B., Multi-Step FRET-Based Long-Range Nanoscale Communication Channel. *IEEE Journal on Selected Areas in Communications* **2013**, *31* (12), 715-725.
7. Jares-Erijman, E. A.; Jovin, T. M., FRET imaging. *Nature Biotechnology* **2003**, *21* (11), 1387-1395.
8. Rowland, C. E.; III, C. W. B.; Delehanty, J. B.; Medintz, I. L., Nanomaterial-based sensors for the detection of biological threat agents. *Mater. Today* **2016**, *19* (8), 464-477.
9. Bruno, J. G.; Carrillo, M. P.; Phillips, T.; Vail, N. K.; Hanson, D., Competitive FRET-aptamer-based detection of methylphosphonic acid, a common nerve agent metabolite. *J Fluoresc* **2008**, *18* (5), 867-76.

## Acronyms

A	Acceptor
AuNP	Gold nanoparticle
CBRN	Chemical, biological, radiological, nuclear
D	Donor
DNA	Deoxyribonucleic acid
EEM	Excitation Emission Matrix
FRET	Förster Resonance Energy Transfer
LD <sub>50</sub>	Median lethal dose
MePA	Methylphosphonic acid
MS	Mass spectroscopy
NSET	Nanometal surface energy transfer
PCR	Polymerase chain reaction
PL	Photoluminescence
Qdot	Quantum dot
QY	Quantum yield
UV-Vis	Ultraviolet-visible spectroscopy

## Novel Perovskite Semiconductors for the Detection of Special Nuclear Material

**Project Team:** Joy McNamara and Kaitlin Lawrence

**Project Start Date:** October 1, 2019

**Project End Date:** September 30, 2020

*Special nuclear material detection using portable, highly efficient detectors is of paramount importance to national security and environmental monitoring. Current neutron detectors, including gas proportional counters and scintillators, are not suitable for discrete or portable monitoring due to size, weight, and power limitations.*

*For example,  $^3\text{He}$  gas proportional detectors have significant drawbacks, including long absorption lengths, high voltage requirements, and dependence on the availability of  $^3\text{He}$ . The goal of this project is to synthesize a novel, boron-based perovskite semiconductor crystals to create a more efficient and more portable neutron detector. This innovative material will lead to a significant decrease in power and size requirements with higher operating temperatures than other traditional solid-state detectors. Directly incorporating  $^{10}\text{B}$  eliminates the need for a conversion layer and leads to high neutron absorption coefficients. In this seedling project, we used inverse temperature crystallization with boron precursors to create  $\text{CH}_3\text{NH}_3\text{PbI}_{3-x}(\text{BF}_4)_x$ . The crystals were analyzed with X-ray diffraction, but the results were inconclusive. Future work will focus on tailoring the solution growth and selecting appropriate solvents and precursors.*

### FY2020 Objectives

- Synthesis of boron perovskite crystals
- Characterization of boron perovskite properties

### Introduction

Perovskite photovoltaic devices ( $\text{CsPbX}_3$  and  $\text{CH}_3\text{NH}_3\text{PbX}_3$ ;  $X = \text{Cl, I, or Br}$ ) have experienced an unprecedented and meteoric rise in device efficiency due to their unique and tunable optoelectronic properties. These include exceptionally high carrier mobility-lifetime products ( $\mu\tau$ ; higher  $\mu\tau$  values lead to higher charge collection efficiencies), low defect density, long carrier diffusion lengths, larger band gap, and high absorption coefficients that match and even exceed most traditional solid-state detectors.<sup>1-5</sup> Typical  $\mu\tau$  products and band gaps for perovskites are 2-5 orders of magnitude larger than common solid state detectors, such as boron nitride (h-BN), high purity germanium (HPGe) and single crystal silicon.<sup>6</sup> Since the bias voltage required for efficient charge collection is inversely proportional to charge carrier mobility lifetime products, perovskites can be operated at lower bias voltages, utilizing less energy.<sup>7</sup> Additionally, traditional solid state detectors require expensive and time consuming fabrication techniques that can lead to interfacial strain due to lattice mismatch and require cryogenic cooling for efficient operation.<sup>6,8,9</sup> Depending on the composition, perovskites have a band gap that is 2–3 times larger than the band gap for HPGe, allowing for operation without active cooling due to the suppression of thermal excitation of charge carriers. The electronic and optical properties of perovskites lead to higher charge collection efficiencies and lower detection limits, which can be harnessed to create more efficient, smaller nuclear detection devices. Although there is extensive research from the photovoltaic community on the progress and achievements of perovskite based photovoltaic devices, radiation detection using perovskites is scarce and focused on gamma detection.<sup>10</sup>

The proposed neutron detecting perovskites also increase efficiency by directly incorporating boron ( $^{10}\text{B}$ ) into the perovskite unit cell. This combines both the neutron absorber and charge carrier generator in one material, eliminating the energy diminishing routes (e.g. self-absorption, interlayer energy transfer, etc.)

that can occur in indirect conversion materials. After  $^{10}\text{B}$  atoms capture incoming neutrons, the emission of charged particles (alpha particles,  $^7\text{Li}$ , and gamma rays) generates electron-hole pairs in the perovskite semiconductor. The density of boron atoms in a solid-state detector is an order of magnitude larger than that found in  $^3\text{He}$  gas detectors, which is much larger than the difference in neutron absorbing efficiency, since  $^3\text{He}$  is 28% more efficient than  $^{10}\text{B}$ . Additionally, since the atomic density is much lower for  $^3\text{He}$  compared to  $^{10}\text{B}$ , the thermal neutron absorption length is much larger for  $^3\text{He}$ . Therefore, at this replacement level, the fabricated crystals will exceed the sensitivity and performance of current  $^3\text{He}$  detectors with smaller size requirements. In this project, we attempted the synthesis and characterization of boron perovskite crystals using the inverse temperature crystallization (ITC) method.

## Approach

Solution crystal growth is traditionally accomplished through the process of cooling heated solutions, since solutes are typically more soluble at higher temperatures. Growth using this method is slow and time consuming and is dependent on the solubility of the precursors in the solvent. Using the appropriate solvent will allow more precursors to be dissolved when heated, and will induce supersaturation upon cooling the solution, thereby causing crystallization to occur. Choosing an appropriate solvent therefore determines the quality of crystal growth. For organo-metal halide perovskites ( $\text{CH}_3\text{NH}_3\text{PbX}_3$ , where  $X = \text{Br}, \text{Cl}, \text{ or } \text{I}$ ), solvents which lead to successful crystal growth are commonly  $\gamma$ -butyrolactone (GBL),  $N,N$ -dimethylformamide (DMF) and dimethylsulphoxide (DMSO). The solubility of the  $\text{PbX}_2$  precursor varies based on the specific halogen, and successful crystal growth is only achieved upon selecting the appropriate solvent. It has been reported that for perovskites with iodine, crystallization is more successful using GBL as the solvent.<sup>11</sup>

Interestingly, perovskite solution crystal growth exhibits retrograde solubility; that is, the precursors have a higher solubility at low temperatures, and a lower solubility at high temperatures.<sup>12</sup> This rare phenomenon that is only seen in a few materials,<sup>12</sup> is referred to as inverse temperature crystallization (ITC). The ITC method is capable of growing high-quality single crystals very rapidly in a matter of hours as opposed to days (Figure 1).<sup>13</sup> In this work, we have attempted the growth of  $\text{CsPbBr}_3$  (Figure 2) in FY19 and  $\text{CH}_3\text{NH}_3\text{PbI}_{3-x}(\text{BF}_4)_x$  in FY20, and we explored the use of different solvents for the growth of organometal halides with boron substitution.

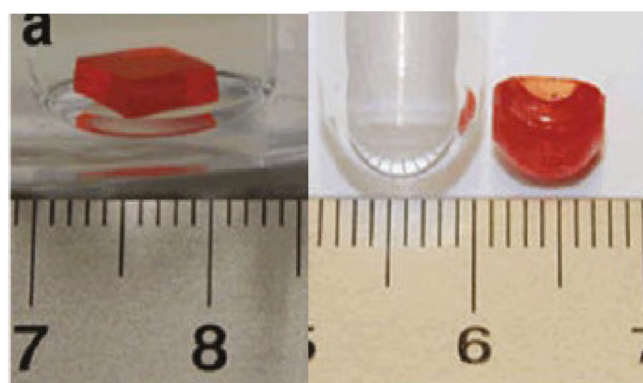


**Figure 1:** ITC-grown  $\text{CH}_3\text{NH}_3\text{PbBr}_3$  perovskite single crystals. Taken from Ref. 13.

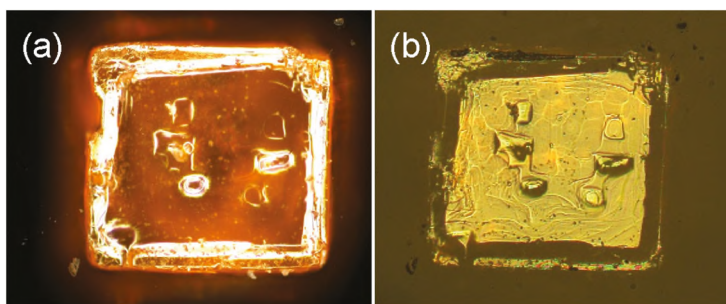


**Figure 2:** (a) Dark field and (b) polarized light micrographs of a  $\text{CsPbBr}_3$  perovskite crystal grown at SRNL using ITC.

## Results/Discussion

The goal of this work was to synthesize boron substituted perovskites with the elemental composition of  $\text{CH}_3\text{NH}_3\text{Pb}_{1-x}\text{(BF}_4)_x$ . This perovskite structure was grown in Ref. 1 using vapor deposition and solid-state synthesis. A perfunctory search of the literature does not reveal if this specific perovskite form has ever been grown using solution crystal growth methods.

Following the approach of Ref. 13, 1 molar (M) solutions of  $\text{PbI}_2$  and  $\text{CH}_3\text{NH}_3\text{BF}_4$  were prepared in GBL. The solutions were stirred at 60 °C until dissolved. Both solutions were filtered and combined into one solution, which was then heated to 110 °C for 2-3 hours. No observable crystallites formed even upon increasing the temperature to 140 °C. Since  $\text{PbI}_2$  did not readily dissolve in GBL, the synthesis was carried out in a GBL/DMF mixture to ensure the lead was dissolved. Small crystallites began to form after heating to 110 °C. After increasing the temperature to 140 °C, the crystallites rapidly grew to 1–2 millimeters in size and were bright orange colored (Figure 3). The crystals were rinsed with GBL and washed with ethanol to remove the solvent before drying overnight. These crystals were analyzed via X-ray diffraction (XRD). The data showed peaks for  $\text{PbI}_x$  structures, but peaks for the desired form of  $\text{CH}_3\text{NH}_3\text{Pb}_{1-x}\text{(BF}_4)_x$  were not observed (Figure 4). Upon analyzing the data, it was determined that  $\text{PbI}_x$  crystallites had most likely formed from the solution, since the  $\text{PbI}_2$  solute was not able to fully dissolve in the GBL.

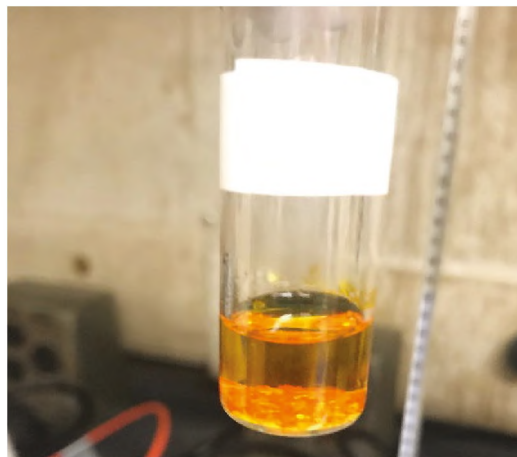


**Figure 3:** Vial containing presumed boron perovskite crystals after ITC growth.

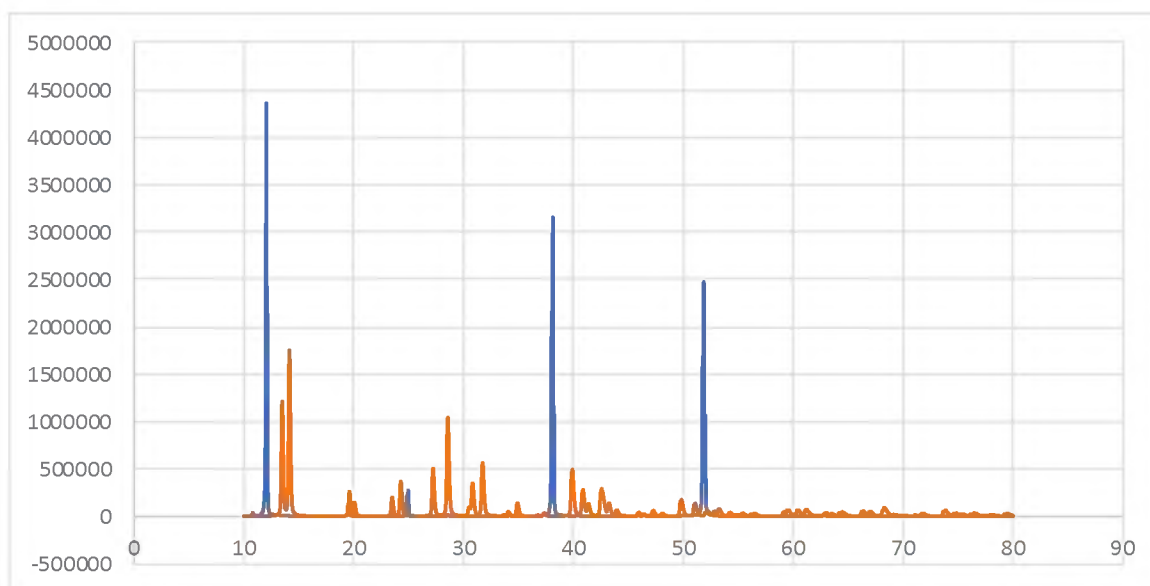


**Figure 4:** XRD graph of presumed boron perovskite structures (blue lines) compared to desired theoretical composition (orange lines).

It appears that the  $\text{PbI}_2$  crystallites are forming from the mixture of GBL and DMF solvents, since the individual boiling points of the two solvents is 153 °C for the DMF and 205 °C for the GBL. Thus, heating the mixture of these two solvents caused the  $\text{PbI}_2$  products to crystallize, indicating that DMF, the solvent responsible for dissolving the  $\text{PbI}_2$ , was evaporating faster than the GBL. This resulted in the

supersaturation of  $\text{PbI}_2$ , which caused crystallization of  $\text{PbI}_2$ . Future work may involve modeling the vapor liquid equilibrium curves for these two solutions or finding comparable systems from which comparisons can be made. Additional studies must be conducted on the appropriate solvents, since successful crystallization of similar perovskite structures in the literature was accomplished using only one solvent (e.g., GBL for iodine containing perovskites<sup>13</sup>). Alternatively, different precursors can be explored such as  $\text{CH}_3\text{NH}_3\text{BF}_4$  salts mixed with  $\text{PbBF}_4$  solutions to increase the boron density and reduce the need for halogen substitution. Again, a search of the literature does not reveal that this technique has ever been tested.

## FY2020 Accomplishments

- Determined the need for appropriate solvent and precursor usage in perovskite crystal growth
- Successfully relocated setup from W-area to A-area laboratory and revised hazard analysis package
- Procured materials and chemicals

## Future Directions

- Model vapor liquid equilibrium curves for solvents
- Optimize crystal growth by exploring the use of alternative precursors and solvents
- Optimize crystal growth by understanding time and temperature effect
- Partner with external sources (e.g., university) to grow reference crystal materials
- Carry out electrical and device characterization using current-voltage measurements to obtain expected device performance
- Examine the neutron absorption ability and stability of the crystals in a neutron source

## Acronyms

DMF	N,N-dimethylformamide
DMSO	Dimethylsulphoxide
GBL	$\gamma$ -butyrolactone
HPGe	High-purity germanium
ITC	Inverse temperature crystallization
$\mu\tau$	Mobility lifetime
XRD	X-ray diffraction

## References

1. Stranks, S. D.; Snaith, H. J. Metal-halide Perovskites for Photovoltaic and Light-Emitting Devices. *Nature Nanotech.* **2015**, *10*, 391-402.
2. Liu, M.; Johnston, M. B.; Snaith, H. J. Efficient Planar Heterojunction Perovskite Solar Cells by Vapor Deposition. *Nature* **2013**, *501*, 395-398.
3. Eperon, G. E.; Leijtens, T.; Bush, K. A.; Prasanna, R.; Green, T.; Wang, J. T.-W.; McMeekin, D. P.; Volonakis, G.; Milot, R. L.; May, R.; Palmstrom, A.; Slotcavage, D. J.; Belisle, R. A.; Patel, J. B.; Parrott, E. S.; Sutton, R. J.; Ma, W.; Moghadam, F.; Conings, B.; Babayigit, A.; Boyen, H.-G.; Bent, S.; Giustino, F.; Herz, L. M.; Johnston, M. B.; McGehee, M. D.; Snaith, H. J. Perovskite-Perovskite Tandem Photovoltaics with Optimized Band Gaps. *Science* **2016**, *354* (6314), 861-865.
4. Zhou, H.; Chen, Q.; Li, G.; Luo, S.; Song, T.-b.; Duan, H.-S.; Hong, Z.; You, J.; Liu, Y.; Yang, Y. Interface Engineering Of of Highly Efficient Perovskite Solar Cells. *Science* **2014**, *345* (6196), 542-546.
5. Huang, J.; Yuan, Y.; Shao, Y.; Yan, Y. Understanding the Physical Properties and Hybrid Perovskites for Photovoltaic Applications. *Nat Rev Mater* **2017**, *2* (17042).

6. Li, J.; Dahal, R.; Majety, S.; Lin, J. Y.; Jiang, H. X. Hexagonal Boron Nitride Epitaxial Layers as Neutron Detector Materials. *Nucl. Instrum. Methods Phys. Res. A* **2011**, *654* (1), 417-420.
7. Doan, T. C.; Li, J.; Lin, J. Y.; Jiang, H. X. Growth and Device Processing of Hexagonal Boron Nitride Epilayers for Thermal Neutron and Deep Ultraviolet Detectors. *AIP Advances* **2016**, *6* (7), 075213.
8. Yang, G.; Mei, H.; Guan, Y.; Wang, G.; Mei, D.; Irmscher, K. Study on the Properties of High Purity Germanium Crystals. *J. Phys.: Conf. Ser.* **2015**, *606*, 012013.
9. Shi, D.; Adinolfi, V.; Comin, R.; Yuan, M.; Alarousu, E.; Buin, A.; Chen, Y.; Hoogland, S.; Rothenberger, A.; Katsiev, K.; Losovyj, Y.; Zhang, X.; Dowben, P. A.; Mohammed, O. F.; Sargent, E. H.; Bakr, O. M., Low Trap-State Density and Long Carrier Diffusion in Organolead Trihalide Perovskite Single Crystals. *Science* **2015**, *347* (6221), 519-522.
10. Stoumpos, C. C.; Malliakas, C. D.; Peters, J. A.; Liu, Z.; Sebastian, M.; Im, J.; Chasapis, T. C.; Wibowo, A. C.; Chung, D. Y.; Freeman, A. J.; Wessels, B. W.; Kanatzidis, M. G. Crystal Growth of the Perovskite Semiconductor CsPbBr<sub>3</sub>: A New Material for High-Energy Radiation Detection. *Cry. Growth Des.* **2013**, *13* (7), 2722-2727.
11. Shi, D. et al. Low Trap-State Density and Long Carrier Diffusion in organolead trihalide perovskite single crystals. *Science* **2015**, *347*, 519-522.
12. Söhnel, O.; Novotný, P., *Densities of Aqueous Solutions of Inorganic Substances*. New York, **1985**; Vol. 22.
13. Saidaminov, M. I.; Abdelhady, A. L.; Murali, B.; Alarousu, E.; Burlakov, V. M.; Peng, W.; Dursun, I.; Wang, L.; He, Y.; Maculan, G.; Goriely, A.; Wu, T.; Mohammed, O. F.; Bakr, O. M. High-Quality Bulk Perovskite Single Crystals Within Minutes by Inverse Temperature Crystallization. *Nat. Commun.* **2015**, *65*, 7586.
14. Nagane, S.; Bansode, U.; Game, O.; Chhatreab, S.; Ogale, S. CH<sub>3</sub>NH<sub>3</sub>Pb<sub>1-*x*</sub>(BF<sub>4</sub>)<sub>*x*</sub>: Molecular Ion Substituted Hybrid Perovskite. *Chem. Commun.*, **2014**, *50*, 9741-9744.

## High Performance 3D Printable X ray Scintillators for Remote Radiation Sensing Applications

**Project Team:** Donald Benza and Aaron Washington

**Project Start Date:** March 1, 2020

**Project End Date:** September 30, 2020

*Unmanned vehicles represent an excellent tool for remote radiation sensing. CZT and other radiation detectors can be added to drones and other robots but come at a high monetary cost in addition to increasing payload. This limits the deployment time and puts a strain on available power reserves. To combat this, high strength 3D printable polymers that have encapsulated*

*X-ray scintillator could be used to manufacture structural components that act as a radiation detector. This method could save considerable cost as well as minimize the additional payload/power requirements. Polycarbonate and PETG mixtures were developed with various loading concentrations (10%, 20%, 30%). Mechanical properties were tested in addition to optimizing the optical clarity of printed parts.*

### FY2020 Objectives

- Develop 3D printable Polymer with strength, temperature resistance, and optical clarity
- Encapsulate X-ray scintillator into said polymer
- Characterize new material mechanical and optical properties for publishing
- Design and build a high frequency low power pulse counting circuit

### Introduction

Remote radiation sensing can be a valuable tool for the Department of Energy as well as other government offices such as the department of defense. Currently unmanned vehicles such as drones and robots are attaching commercially available detectors such as CZT to these craft. While effective as sensors, the added payload and cost limits the utility of these craft for long deployments. New methods and technologies are necessary to make unmanned vehicles an efficient cost-effective means of remote radiation sensing.

To solve this problem, work has centered on developing high performance 3D printable polymers with encapsulated X-ray scintillator. This new material will allow for rapidly and cheaply manufacturing structural components of drones and other robots that also possess radiation sensing capability. The added payload and power requirements of traditional detectors will be virtually eliminated which will allow for extended deployment times. It is critical that the materials developed possess sufficient strength and high optical clarity to extract as much light as possible. Materials characterization will include a full suite of both mechanical and optical experiments.

### Approach

As part of an FY19 seedling, X-ray scintillators were encapsulated into Poly-Ether-Terephthalate with a glycol modifier (PETG). While this was very successful, there was room for improvement. Polycarbonate (PC) is another 3D printable thermoplastic that is an excellent candidate to improve this technique due to its high strength, impact and temperature resistance, and relatively high optical clarity. However, PC suffers from relatively low ductility as well as relatively poor layer to layer adhesion. PETG on the other hand has excellent ductility and layer to layer adhesion at the expense of temperature resistance and some loss in clarity. To take advantage of the best properties of both "alloys" of PC/PETG were created.

Loading percentages of PETG were 10%, 20%, and 30%. Pellets were dried and extruded out of the Filabot system. The filament was printed into tensile bars and optical samples using the SRNL modified Stratasys Titan.

Once the optimum mixture is determined, Gadolinium Oxysulfide doped with Terbium will be coated onto the pellets prior to extrusion. The pellets will melt, and the extruder screw will incorporate the powder into the matrix. Optical experiments are to include X-ray and natural source irradiation which will gauge the performance as a detector. In the future, arms will be printed and installed into existing SRNL drones. The drones' flight performance as well as its ability to locate sources will then be tested.

## Results/Discussion

Tensile testing on dog bone geometries have been performed. Initially it appears that loading PC with 20% PETG by weight has the highest strength of the three concentrations though there is an anomaly in sample 3. This can be due to several factors including human error in setup or a possible random printing defect. Five samples of each concentration were tested. Ultimately more samples need to be tested to make any conclusions on the strength of the mixtures. Compression testing needs also be performed as well as 3-point bend tests.



Figure 1: Tensile testing of dog bone samples.

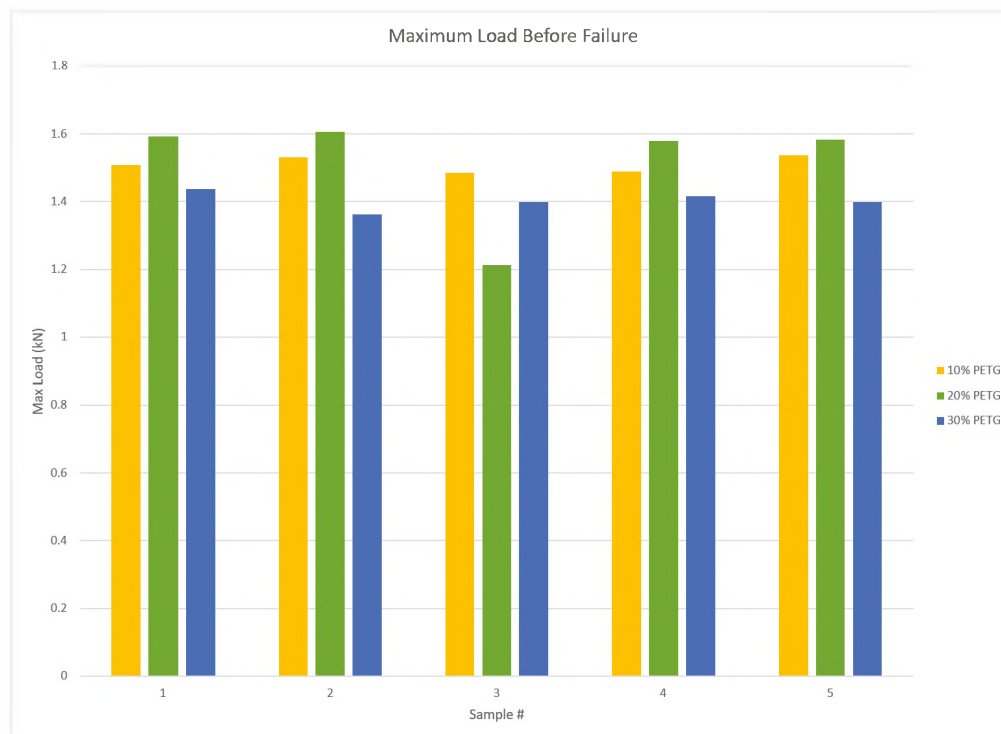
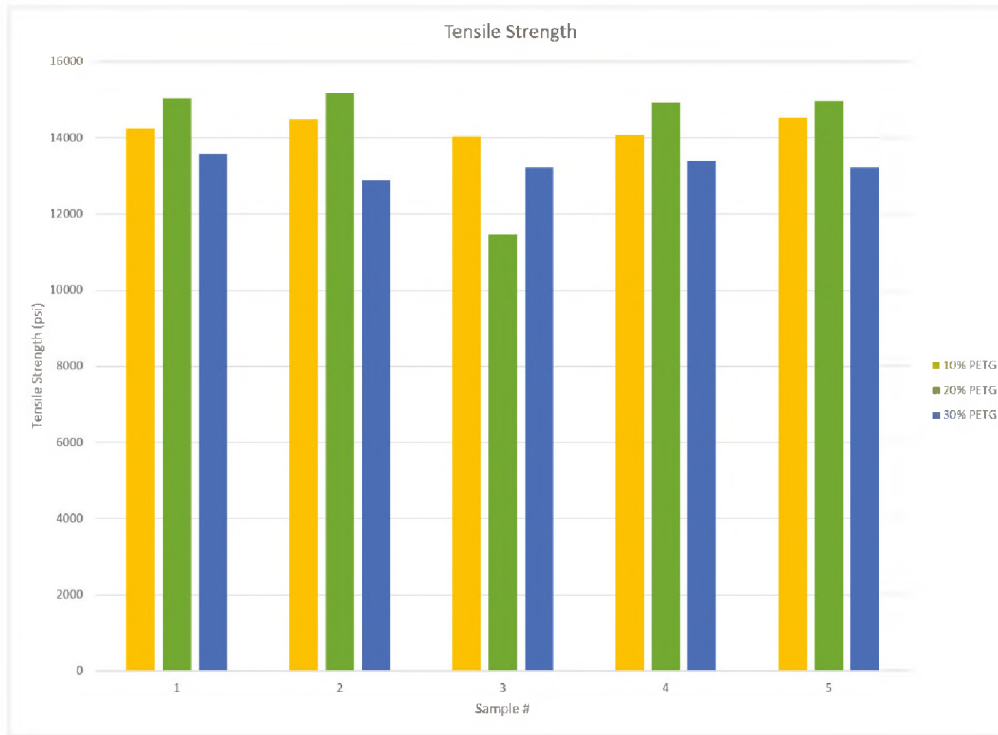
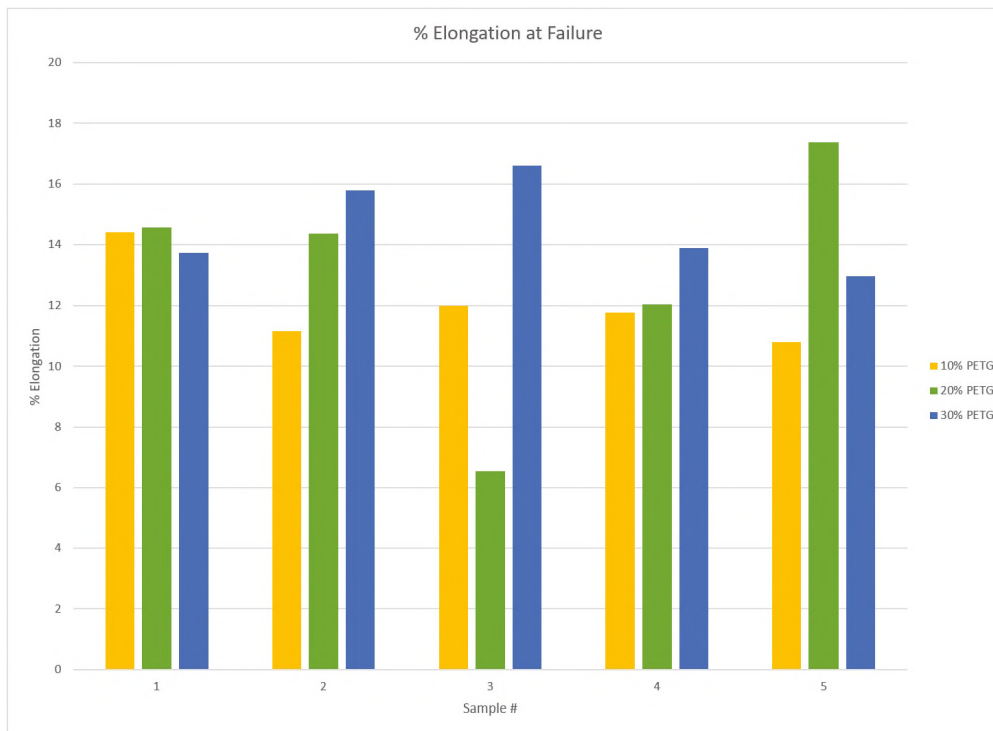


Figure 2: Graph of Max load before failure.



**Figure 3:** Graph of Tensile Strength.



**Figure 4:** Graph of % Elongation at failure.

FDM printing is generally very poor for making optically clear parts. This presents a problem for encapsulated scintillator as any light that is self-absorbed by the polymer matrix decreases the sensitivity as a detector. Initially it was thought that printing thick layers (300 microns) would limit the number of optical interfaces in parts and allow for greater light transmission. However, it was discovered that printing ultra-thin layers (20–30 microns) greatly increased light transmission through samples by eye. The hypothesis for this is that because the layers are so thin, the hot nozzle is much closer to the previous layer than when thick layers are printed. This allows the nozzle to not only melt the material in the nozzle but also re-melt the previous layer and allow for high fusion between layers. High fusion between layers eliminates optical boundaries created by the layering process. The highest printing temperature possible is used for this process.



**Figure 5:** Unpolished 10% PETG/ 90% PC Mixture printed at 20 micron layer height.

To capture data from the printed parts, a lightweight, low power, and high sensitivity light detector is necessary. For this a Hamamatsu micro PMT was selected. SRNL designed and manufactured a small low power counting circuit to detect pulses from the PMT. The number of pulses is directly proportional to signal intensity.

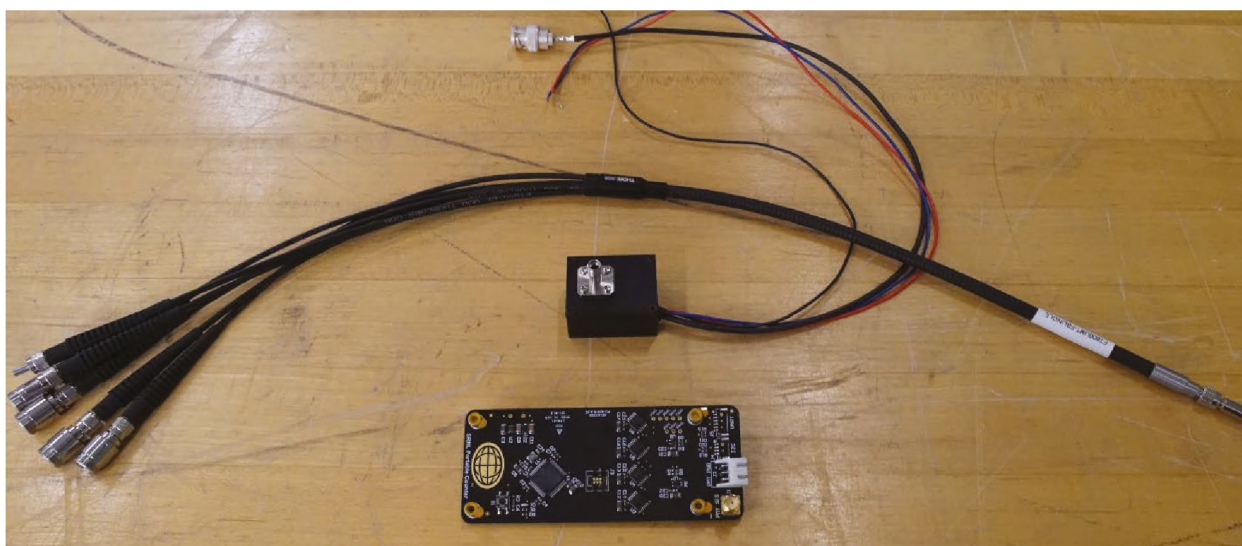


**Figure 6:** Micro PMT, Counting Circuit, and 6 to 1 fiber optic cable.

## FY2020 Accomplishments

- Developed new alloy by mixing PC and PETG at various loading percentages
- Testing of optical and mechanical properties
- Developed high frequency low power pulse counting circuit to read data output from a Hamamatsu micro PMT

## Future Directions

- Perform experiments with X-rays and natural sources
- Continue optimizing PC/PETG formula
- Incorporate into existing SRNL drone
- Demonstrate ability to locate sources and extend flight times

## Publications

Two materials characterization papers are in progress which outline the mechanical and optical properties of the developed materials

## Acronyms

PC Polycarbonate  
PETG Poly ether terephthalate Glycol modified  
PMT Photomultiplier Tube

## Intellectual Property

RS-19-015, Fabrication of Unmanned Systems Using 3D Printed Components Using Materials Sensitive to Radiation

## Crystal Growth and Material Development of CZTS for Radiation Detector Applications

**Project Team:** Utpal N Roy

**University of South Carolina at Columbia and Alabama A&M University**

**Collaborators:** Krishna C Mandal and Stephen U. Egarevwe

**Project Start Date:** April 1, 2020

**Project End Date:** September 30, 2020

*More than 90% of the required equipment has been ordered. This covers a fully functional self-sufficient laboratory for growth, cutting, polishing, characterization and detector testing at SRNL. The upcoming state-of-the-art nuclear detector development laboratory (especially for CdZnTeSe) is expected to have tremendous impact nationally and internationally. The CZTS material invented by the author and his team has already provided new R&D directions for several academic and industrial institutions (e.g., General*

*Electric) based on its advantages over present day CZT. The crystal growth facility is designed to be versatile for growth of different materials using different techniques, such as Traveling Heater method, Vertical Bridgman method, and Physical Vapor Transport.*

### FY2020 Objectives

- Develop crystal growth facility at SRNL
- Develop crystal cutting and polishing facility in house
- Develop detector fabrication laboratory
- Develop characterization facility at SRNL
- Install detector testing facility in house

### Introduction

The intent of the proposal was to establish a fully functional crystal growth and device fabrication facility at SRNL and develop state-of-the-art advanced materials for next-generation radiation detector applications. As opposed to semiconductor sensors for low-energy photons, nuclear radiation detectors need to be thick enough to ensure sufficient absorption of high-energy X- and gamma rays within the active volume of the detector. Thus, detector materials should have the lowest possible defects (charge trapping centers), so that the induced charge carriers can travel through the entire length of the detector without being trapped.

CdZnTe (CZT) has been the gold standard for more than two and a half decades; however, the material still suffers from many detrimental defects that limits widespread deployment of large-volume detectors. The material has the disadvantages of compositional inhomogeneity because of non-unity segregation coefficient of zinc, high concentrations of Te inclusions, and sub-grain boundary networks (dislocation walls). These defects result in spatial inhomogeneity of the charge-collection efficiency and are responsible for deterioration of detector performance, especially for large-volume devices. Thus, in order to increase the yield for high-quality devices, the ideal material demands very high spatial homogeneity of charge collection efficiency. Hence, to achieve high yield of superior quality detectors at lower cost of production, the material should be compositionally homogeneous and contain minimum concentrations of deleterious defects.

Recently, CdZnTeSe (CZTS) has been found to be a very promising material for radiation detector applications. All the defects, presently limited CZT-based detectors, were found to be greatly reduced in CZTS, which makes the material very promising towards achieving high-quality detectors at a much lower

cost of production. The energy resolution for Frisch-grid detectors was found to be about 1% at 662 keV for ~1-cm long devices. However, the extrinsic impurities responsible for deteriorating the device performance, such as Fe, Cr, etc., were found to be present in higher concentrations as compared to commercial-grade CZT. Thus, the energy resolution and yield of superior quality CZTS detectors are expected to be greatly augmented for purified material. After establishing the crystal growth laboratory, the growth of high-quality CZTS by the Traveling Heater method (THM) will be carried out after purification of the raw material to further improve the detector response, increase the yield, and open new pathways for applications. The results are expected to establish new global records for the performance of CZTS detectors.

## Approach

The overall objective was to establish a fully functional laboratory for detector development at SRNL, starting from crystal growth to detector fabrication and testing. To achieve the final goal, versatile three zone furnaces were designed and then fabricated from a leading furnace manufacturing company. In order to avoid any contamination due to an ampoule crack or other event during the growth, a furnace enclosure was also designed and built. The versatile furnaces were designed so that material can be grown by different techniques, such as Traveling Heater Method (THM), vertical Bridgman technique and Physical Vapor Transport (PVT). The upcoming laboratory will have the capability for cutting, polishing, characterization, detector fabrication and testing.

## Results/Discussion

We have designed and ordered two three-zone furnaces for crystal growth experiments; one of the furnaces is capable of growing three-inch diameter ingots. Various parts were ordered, including a turbomolecular pump to install the carbon-coating facility on the inner wall of the growth ampoules and sealing the loaded ampoules under dynamic vacuum. The parts necessary for ampoule lowering mechanism were also ordered. Completion of these tasks was critical for growth of up to three-inch diameter ingots.

A high-resolution optical microscope was installed to characterize the presence of secondary phases present in the grown ingots as well as to investigate the growth interface, which is very important for studies of the growth characteristics. A programmable wire saw, and polishing machines were ordered to cut and polish the grown ingots for characterization and detector fabrication. High input impedance electrometer with a built-in voltage source was ordered for current-voltage studies and resistivity measurements. Various components such as pre-amplifier, shaping amplifier, and multichannel analyzer were also ordered to build an operational detector testing station. All undelivered components are expected to be on-site before the middle of September 2020.

## FY2020 Accomplishments

- Designed multi-faceted crystal growth furnace capable of growing crystals by different techniques depending on the materials requirements
- Ordered various equipment to build a fully functional state-of-the art crystal growth lab, device fabrication facility and testing system at SRNL

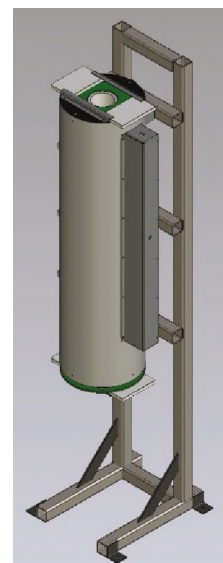


Figure 1: Schematic of a three-zone furnace for crystal growth operation.

## Future Directions

- We strongly believe purification of the raw CZTS material can improve the detector resolution down to 0.6–0.5% at 662 keV. The plan forward is to purify the synthesized CZTS material
- Growth of two and three-inch diameter CZTS ingots to fabricate very high-resolution gamma-ray detectors
- Establish new global records for CZTS energy resolution and efficiency

## FY 2020 Peer-reviewed/Non Peer-reviewed Publications

1. Drabo, M. L.; Egariyewe, S. U.; Roy, U. N.; Harrison, B. A.; Goree, C. A.; Savage, E. K.; James, R. B. Study of CdZnTeSe Gamma-Ray Detector under Various Bias Voltage. *Materials Sciences and Applications*, **2020**, *11*, 553.
2. Egariyewe, S. U.; Roy, U. N.; Agbalagba, E. O.; Harrison, B. A.; Goree, C. A.; Savage, E. K.; James, R. B. Optimizing CdZnTeSe Frisch-Grid Nuclear Detector for Gamma-Ray Spectroscopy. *IEEE Access*, **2020**, *8*, 137530.
3. Dědič, V.; Fridrišek, T.; Franc, J.; Kunc, J.; Rejhon, M.; Roy, U. N.; James, R. B. Mapping of Inhomogeneous Quasi-3D Electrostatic Vector Field in Electro-Optic Materials. Submitted to *Scientific Reports*.

## Presentations

- Roy, U. N.; Camarda, G.S.; Cui, Y.; James, R. B. CdZnTeSe: A promising room-temperature detector material for tomorrow. IEEE Room-Temperature Semiconductor Detector Conference (2020), Accepted for oral presentation.
- Sajjad, M.; Kleppinger, J. W.; Chaudhuri, S. K.; Roy, U. N.; James, R. B.; Mandal, K.C. Growth of Cd<sub>0.9</sub>Zn<sub>0.1</sub>Te<sub>0.95</sub>Se<sub>0.05</sub> Single Crystal for Room Temperature Gamma Ray Detection. IEEE Room-Temperature Semiconductor Detector Conference (2020), Accepted for oral presentation.
- Egariyewe, S. U.; Roy, U. N.; Alexander, P. L.; Israel, M. B.; Davis, A. H.; Agbalagba, E. O.; James, R. B. Characterization of CdZnTeSe Planar and Frisch-Grid Nuclear Detectors. IEEE Room-Temperature Semiconductor Detector Conference (2020), Accepted for oral presentation.
- Egariyewe, S. U.; Israel, M. B.; Davis, A.; McGuffie, M.; Hartage, K.; Alim, M.A.; Roy, U. N.; James, R. B. X-Ray Photoelectron Spectroscopy of CdZnTe and CdMnTe Materials for Nuclear Detectors. IEEE Room-Temperature Semiconductor Detector Conference (2020), Accepted for poster presentation.

## Acronyms

THM	Traveling Heater Method
CZT	CdZnTe
CZTS	CdZnTeSe
PVT	Physical Vapor Transport

## Student Researchers

University of South Carolina at Columbia: Joshua W. Kleppinger, Ph.D student

## External Collaborators (Universities, etc.)

Brookhaven National Laboratory: Giuseppe Camarda, Dr. Yonggang Cui

## Electric Field Imaging Small Scale Testing - Seedling

**Project Team:** James Nicholson and Vincent Ceysens

**Project Start Date:** April 16, 2020

**Project End Date:** July 10, 2020

*This research's goal was to test the ability of the electric field imager to detect a charged capacitor inside of varying enclosures. Testing was requested by NA-84 to demonstrate the imager's capability before providing follow-on funding.*

### FY2020 Objectives

- Build circuit with 3 kV charged capacitor and identify other commercial or readily available circuits to mimic customer relevant systems
- Test EFI against various enclosures (plastics and metal) at various standoff distances
- Document results for both LDRD program and interested customers

### Introduction

During FY19, an LDRD seedling (LDRD-2019-00202) was conducted in order to determine the proof of concept for imaging electric fields using standard off-the-shelf JFETs. This seedling was a resounding success, showing that a statically charged rubber mat could be detected by a 1-D array of JFETs in a sensing circuit. The potential applications of this technology, when further developed, are numerous and diverse.

The investigators during the previous FY's seedling presented their findings to some contacts at NA-84, and although they were very interested, more proof of capability of needed. Therefore, a test was developed to determine if the EFI could detect a 3 kV charged capacitor inside varying enclosures (two of varying aluminum thicknesses, and one of Lexan). This test was also a success, with the EFI able to ascertain the capacitor when charged inside of all three enclosures, both with and without an active power supply after charging. Dialogue is ongoing with NA-84 concerning future work and funding.

### Approach

There are several steps that were taken to achieve the project goal. First, all parts needed were collected or fabricated (high voltage power supply, high voltage capacitor, enclosures). Then a circuit was made to charge the capacitor to 3kV and allow for it to be disconnected from the power supply. Finally, tests were conducted, placing the capacitor inside of each enclosure with a lid, charging the capacitor with shielded wiring connected to the circuit, measuring the detectable fields at various standoffs while the power supply was active and after it was turned off, and collecting data generated by the EFI during the test.

### Results/Discussion

The circuit used for the test was designed in such a way that the capacitor could be charged, and then disconnected from the power supply through the ground path. This was done so that the power supply could be turned off, and the capacitor would not discharge through the power supply. The power supply was a noisy when on, and this setup increased the confidence that the EFI was not picking up noise from the power supply. The initial switch was a relay, but there was concern about noise generated by the coil

inside the relay, so a simple single pole single throw switch was used instead. A schematic of the circuit can be seen in Figure 1, and a picture of the actual circuit inside of an enclosure can be seen in Figure 2.

The EFI was used at multiple points on the enclosure to determine how standoff and geometry affected detection signal. Multiple materials were used for the housing to determine if a) metal thickness tracked with decrease in signal, and b) if the EFI was able to detect the charged system through a staticky plastic enclosure that had the possibility of swamping the detectors sensitivity. Results are shown in Figures 3–5 for each of the imaged regions as the EFI is moved from position to position with the relative field strength shown for the y-axis and data point number for the x-axis.

The three figures that follow demonstrate the EFI's ability to detect the presence of the capacitor inside of the varying enclosures and when held at varying positions around the enclosures. In each of these figures, there are sixteen sensors' data presented. Each data point (x-axis) is a "picture" taken by the EFI of what it is seeing in that position by each sensor. In Figure 3 for example, when the EFI is held by the hole in the enclosure, sensor 10 detects the strongest fields. This makes sense because sensor ten was the sensor closest to the hole during this phase of the test.

The EFI expectedly detected the capacitor best during the 1/8" aluminum test. The extra thickness from the 1/4" enclosure attenuates more of the fields, and the Lexan has a stronger static nature than aluminum. This data was considered a success by the NA-84 contacts.

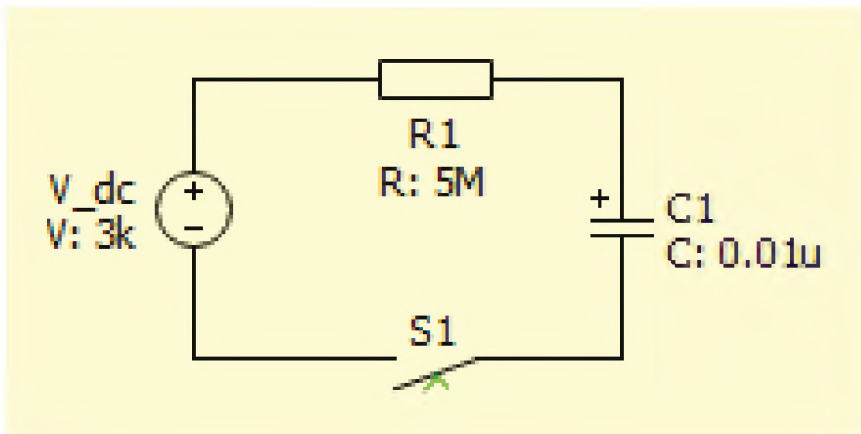


Figure 1: Circuit schematic for capacitor charging circuit.

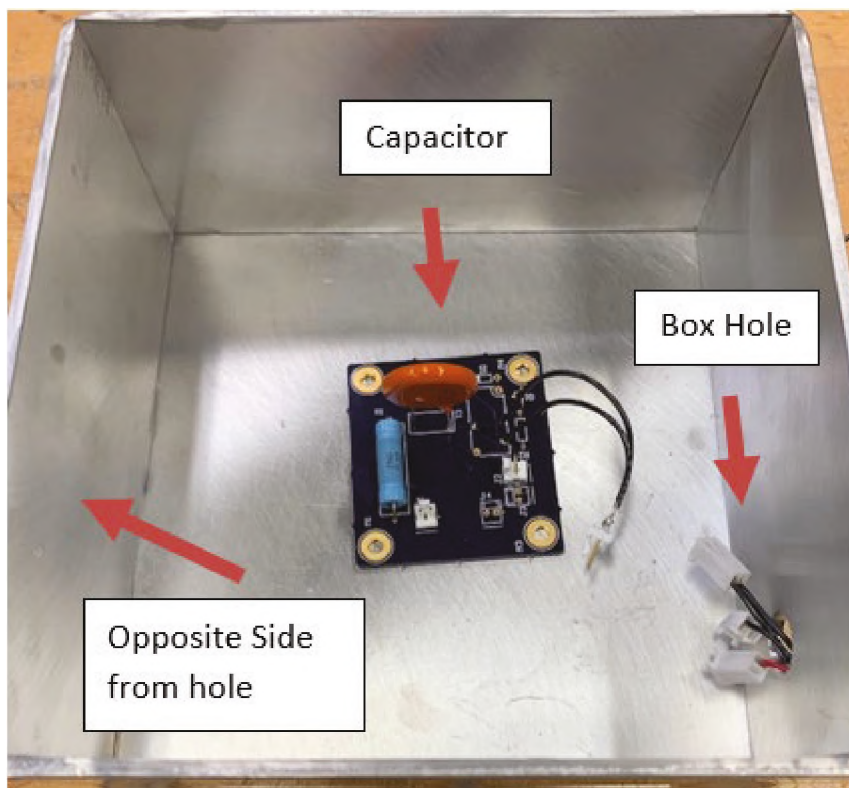


Figure 2: Capacitor charging circuit inside of an aluminum enclosure (enclosure lid not shown).

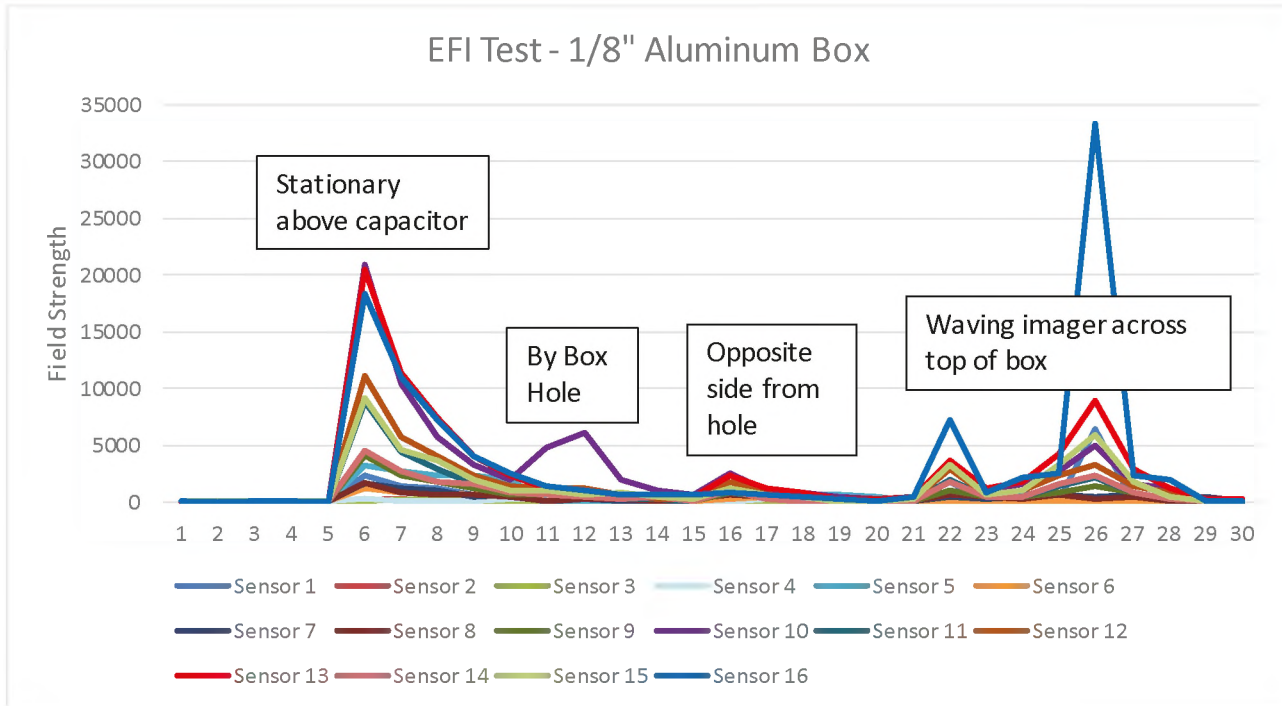


Figure 3: Results for 1/8" aluminum box test. Text boxes in figure describe varying sensor positions.

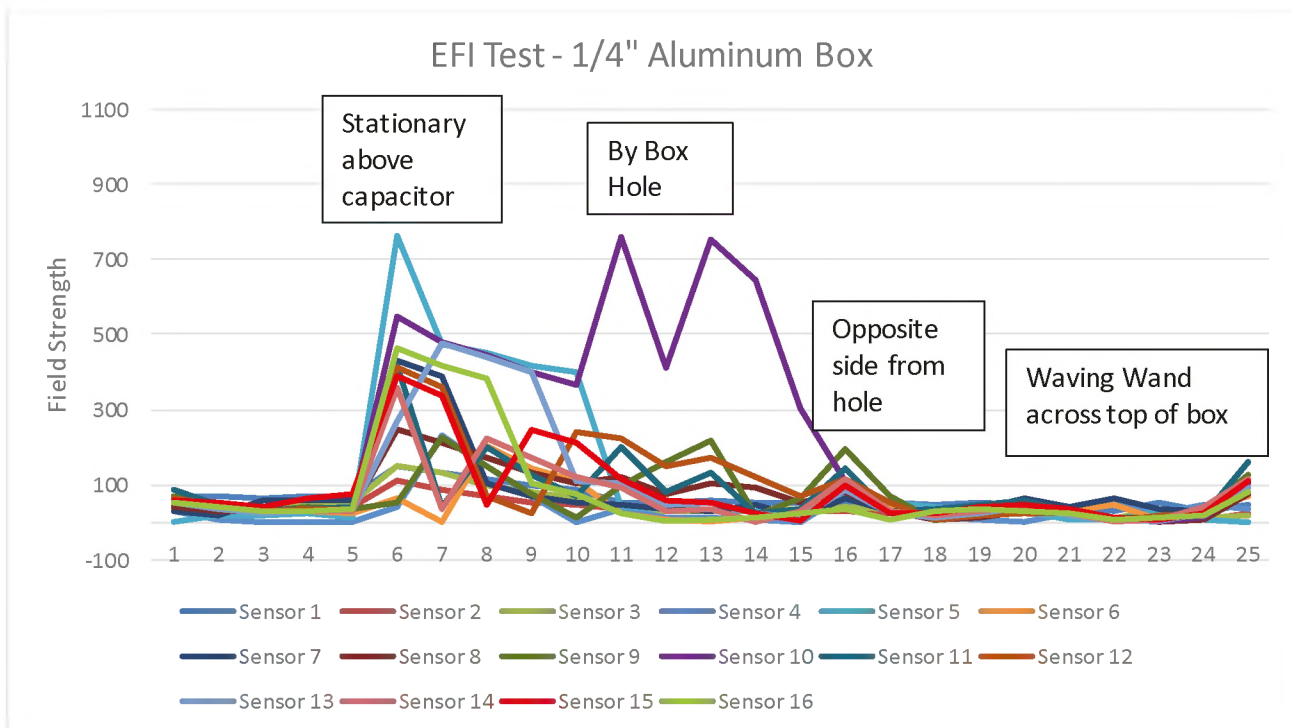


Figure 4: Results for 1.4" aluminum box test. Text boxes in figure describe varying sensor positions.

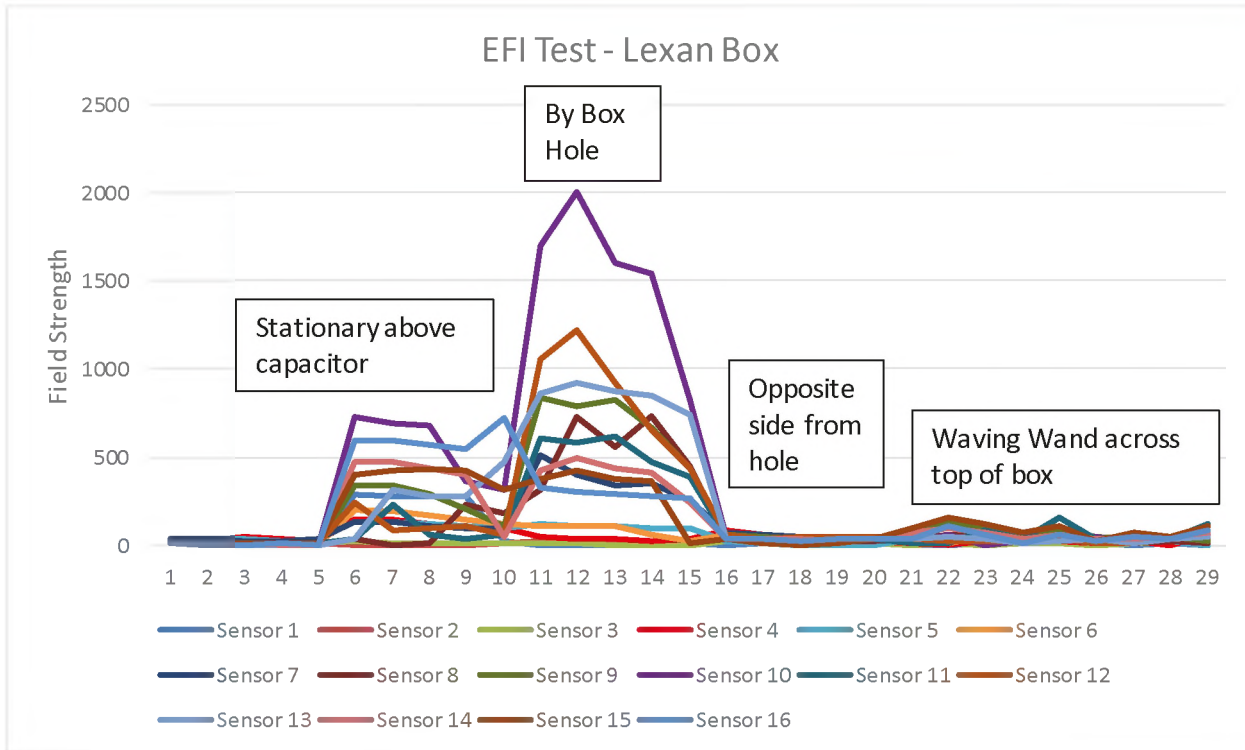


Figure 5: Results for 1/8" Lexan box test. Text boxes in figure describe varying sensor positions.

## FY2020 Accomplishments

- Built test circuit and prepared enclosures for benchmarking EFI's capabilities imaging through barriers
- Data showed that the capacitor could be measured within all three enclosures
- Presented findings to NA-84 contacts and put together report for LDRD administration team

## Future Directions

- The next immediate step is to show phenomenology by modeling electric fields emanating from a capacitor inside of an enclosure in COMSOL
- Following the successful modeling, the following stage is to work on increasing accuracy, range, and consistency of the sensors

## Presentations

Presentation given to NA-84 contacts on June 26 to display testing results and discuss.

## Acronyms

EFI Electric Field Imager  
 JFET Junction Field Effect Transistor

# SECURE ENERGY & MANUFACTURING

## PROJECTS

Novel Complex Hydride Flow Batteries for Grid Storage Applications

Metal Hydride Fuel Cell Powered UAV

Material Developments for 3D/4D Additive Manufacturing (AM) Technologies

Component Development for Alkaline URFCs

Advanced Photoelectrode Development to Produce Novel Solar Batteries

MAX Phase Materials and MXenes as Hydrogen Barrier Coatings

Solid State Ionics: Materials Development by Multiscale Modeling and Advanced Manufacturing Techniques

Robust, High-energy Density Supercapacitors for Portable Energy Storage

Low-Profile, Smooth-Walled Inner Pipe Sealing Insert for Low-Pressure Applications

Electronic Structure Calculations for Improving Catalyst Design for Use in the Hybrid Sulfur Cycle

High Temperature Water Electrolysis Testing of Gold-based Electrodes for H<sub>2</sub> Production

Development of High Capacity Energy Storage Materials

## Novel Complex Hydride Flow Batteries for Grid Storage Applications

**Project Team:** Ragaiy Zidan, Patrick Ward, Hector Colon-Mercado, Aaron Lando, Prabhu Ganesan

**California State University Northridge  
Subcontractor:** Joseph A. Teprovich Jr.

**Project Start Date:** October 1, 2018  
**Project End Date:** September 30, 2020

*A variety of complex metal hydride alanates were synthesized and investigated for their potential to develop high energy batteries in a redox flow cell configuration. Electrochemical analysis of various alkali metal and alkaline earth metal alanates were carried out with an array of differing metal hydride working electrodes and metal and graphite counter electrodes. Invesatget the intercalation of metallic ions in novel electrodes developed in past BES funded research to be leveraged for this project.*

### FY2020 Objectives

- Characterize an array of alkali and alkaline earth metal alanates and electrolytes and metal hydrides as anodes
- Evaluate various metal hydride electrodes (anodes) for compatibility with the proposed battery technology
- Carryout electrochemical analysis to determine the ideal combination of metal hydride anode, cathode material, alanate electrolyte, and electrolyte solvent
- Continue research related to novel anodes for lithium ion batteries that was started in a previous BES funded project

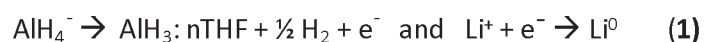
### Introduction

Electrical grid resiliency and effective deployment of large-scale renewable technologies such as photovoltaics and wind power require large scale electrical storage. Flow batteries offer several advantages to traditional energy storage such as high scalability and flexibility that can be applied to a wide range of applications in a diverse grid-energy market. Our proposal idea is based on using complex hydride materials that offer a high energy density alternative to state-of-the-art materials. In addition, this novel technology proposed herein has the advantage of operating at a higher voltage not available with current technology. Most metal alanates are much less costly than typically used vanadium oxide in current flow batteries technology. The proposed project seeks to develop novel complex hydride flow batteries for high energy density grid storage applications.

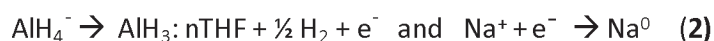
### Approach

A series of complex hydrides, called alanates (e.g.  $\text{LiAlH}_4$ ,  $\text{NaAlH}_4$ ,  $\text{KAlH}_4$ ,  $\text{Mg}(\text{AlH}_4)_2$ ,  $\text{Ca}(\text{AlH}_4)_2$ , etc.), dissolved in organic solvents such as ethers or amines will be examined to demonstrate their feasibility as an electrolyte for flow cell batteries. Previously obtained preliminary results illustrate the possibility of utilizing alanates in THF as an electrolyte. Since  $\text{AlH}_3 \bullet \text{Adduct}$  is an intermediate of the electrochemical reaction and the adduct is a solvent molecule, a suitable solvent or solvent combination must be carefully considered and chosen. It is well-known that the diethyl ether adducts of  $\text{AlH}_3$  (alane) is not stable over long periods of time and therefore would not be an appropriate choice. Once a solvent or combination of solvents with an appropriate alane stabilization effect, high ionic conductivity, and suitable operational conditions is selected, the ex-situ effort will focus on the appropriate alanate and electrode choice. The reduction of ions such as  $\text{Li}^+$  and  $\text{Na}^+$ , to metals requires different voltages depending on the metal and results in batteries with different operational voltages and differing numbers of charges transferred. In

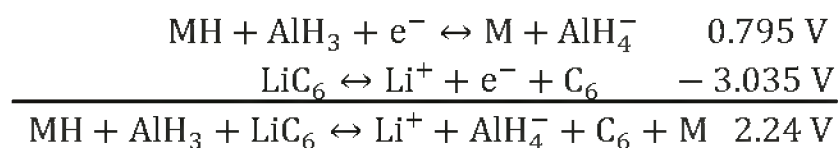
the case of  $\text{LiAlH}_4$  or  $\text{NaAlH}_4$  the electrolyte is ionized when potential is applied to the battery to produce a lithium or sodium ion ( $\text{Li}^+$ )/( $\text{Na}^+$ ) and an alanate ion ( $\text{AlH}_4^-$ ) at cathode and anode, respectively, as shown in equation (1) and (2). One electrode in this case is made to intercalate Li/Na based materials; the other electrode is made of metal hydride material or materials that have metal hydride embedded in it, (e.g.  $\text{AB}_5$ ,  $\text{AB}_2$ , metal hydrides embedded in graphite, etc.).



or



The charging-discharging of a  $\text{LiAlH}_4$  battery of this type can be summarized in the following equations:



Equation 1 and 2 show the evolution and release of hydrogen in THF during charging and discharging respectively. Therefore, a hydrogen absorbing and desorbing material for the electrode is needed and must be compatible with the electrolyte the same with the lithium electrode and must be compatible with the electrolyte as well. Once equation 1 and 2 can be translated in components and the best combinations of electrode is selected, a bench-scale flow battery system was supposed to be constructed. Figure 1 illustrates the ability to charge and discharge a non-aqueous electrochemical cell that has an alkali metal alanate dissolved in a polar, aprotic solvent and with at least one electrode in the zero-valence state that can form a hydride.

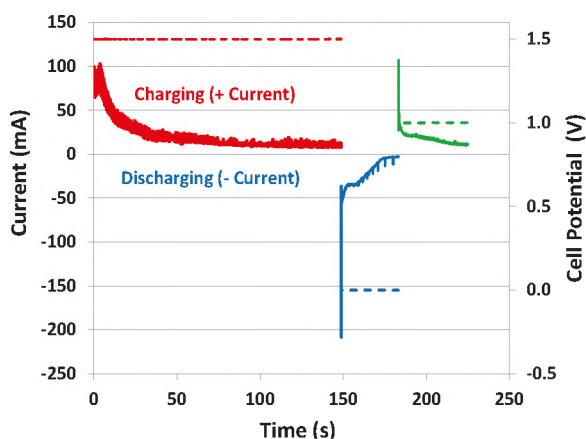


Figure 1: Charging and discharging curves for  $\text{LiAlH}_4$  in THF.

## Results/Discussion

A mischmetal-nickel alloy ( $\text{MmNi}_5$ ) electrode is capable of absorbing hydrogen.  $\text{MmNi}_5$  it is been used in commercial MH-nickel batteries but in our case

the electrodes are submerged in THF and needed to be test under this condition. Mesh metal nickel hydride (MmNiH<sub>x</sub>), obtained from a rechargeable C battery, was submerged in 150mL of Tetrahydrofuran (THF) and loaded into a Parr reactor. Qualitative experiments to verify the uptake of hydrogen by the metal hydride submerged in THF were carried out. The Parr reactor was charged with approximately 500 psi of hydrogen gas and allowed to equilibrate. The Parr reactor was quickly vented and then allowed to re-equilibrate for an hour to allow pressure build up from the absorbed hydrogen. Because THF also dissolves hydrogen, the same experiment was completed with only 150mL of THF in the Parr reactor. In both experiments the final pressure after venting and waiting an hour was recorded. The experiment was repeated twice for MmNiH<sub>x</sub>/THF and THF blank. Figure 2 clearly shows that significantly more hydrogen is absorbed in the experiments with MmNiH<sub>x</sub> in THF. Therefore, it is evident that MmNiH<sub>x</sub> is capable of absorbing hydrogen when submerged in THF. In addition, MmNiH<sub>x</sub> electrode did not have undesirable interaction with electrolyte. On the other hand, solid electrolyte interface (SEI) shown in figure 3 was made to prevent reaction of reduced metal with electrolyte (e.g. Li)

In order to verify the formation of products as shown in equation 1 and 2 such as the formation of alane adduct it was use decided to TEDA which as a white precipitant only when AlH<sub>3</sub>:TEDA is formed indicating the formation of AlH<sub>3</sub>:TEDA was then used and showed the formation of AlH<sub>3</sub>:TEDA validating mechanisms in equation 1 and 2. Figure 4 shows electrode on left before applying voltage and on right white deposition on electrode after applying voltage are TEDA: AlH<sub>3</sub> verifying mechanisms in 1 and 2.

NaAlH<sub>4</sub> was used as an electrolyte and a CV confirming mechanism was obtained where Reproducible peaks are showing the formation of AlH<sub>4</sub> and formation of THF: Alane(AlH<sub>3</sub>) adduct as shown in Figure 5.

LiCl in THF with LiAlH<sub>4</sub> electrolyte was used to reduce the formation of dendrites and proved. LiCl in THF with LiAlH<sub>4</sub> electrolyte doubled the amount of current in the cell under 5 volt operating voltage.

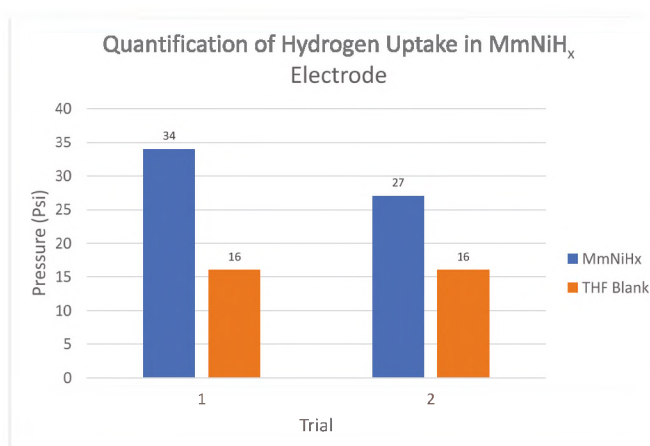


Figure 2: Final Pressure Comparison of Mm NiH<sub>x</sub>/THF and THF blank.

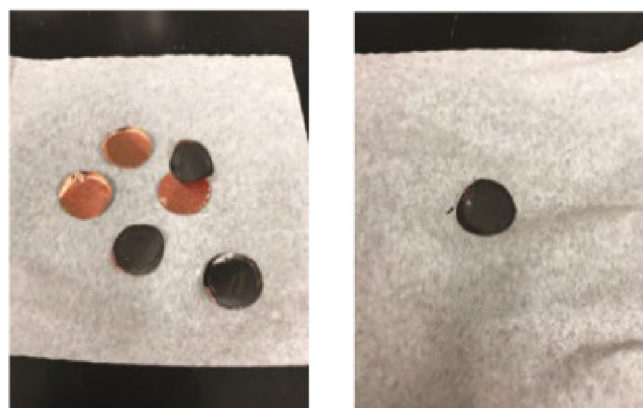
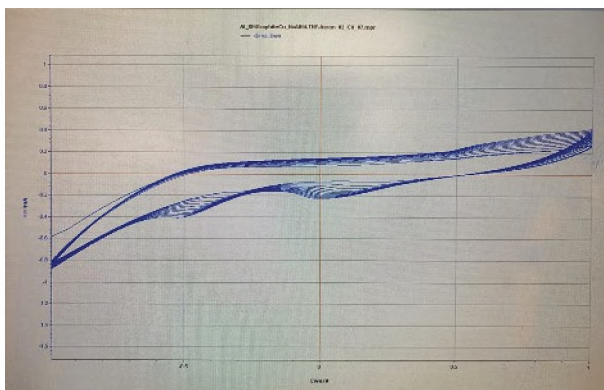


Figure 3: Solid state electrolyte Interface (SEI).



Figure 4: Show no TEDA:AlH<sub>3</sub> before applying voltage and the formation TADA:AlH<sub>3</sub> when voltage is applied.



**Figure 5:** CV data for Graphite with ESI/Aluminum electrochemical cell with NaAlH<sub>4</sub> in THF.

The design of a full flow battery has been done and components were tested, and a pressurized system would have been tested and operated.

In the case of solid-state electrolyte an alane (AlH<sub>3</sub>) is used as an electrode proved to successful. Scanning electron microscope images in figure 6 show electrode before cycling and after 9 cycles. In addition, a prototype battery was constructed powering an LED as shown in Figure 7.

Impedance of a Li/LiAlH<sub>4</sub>/Li cell based on LiAlH<sub>4</sub> solid electrolyte was measure. Figure 8 shows ion conductivity increases as the temperature increases in the system. The solid-state electrolyte also hinders dendrite formation.

## FY2020 Accomplishments

- Verification of mechanisms of how the battery works and mitigation of obstacles
- MmNiH<sub>x</sub> electrode immersed in THF absorbed H<sub>2</sub>
- (SEI) has been made to prevent reaction of reduced metal with electrolyte
- Alane (AlH<sub>3</sub>) use as electrode was successful in the solid-state battery version
- SEM shows stability of AlH<sub>3</sub> electrode with cycling solid-state battery
- A prototype was constructed powering an LED solid state battery
- H-C<sub>60</sub> is used as Li electrodes was successful
- TEDA was used and showed the formation of AlH<sub>3</sub>:TEDA validating mechanisms

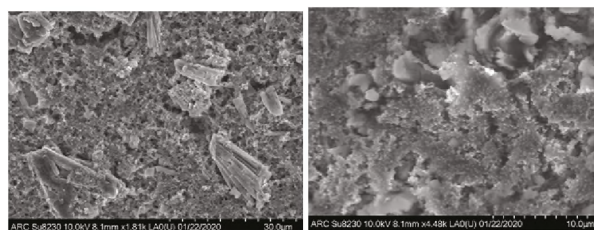


**Figure 6:** AlH<sub>3</sub> electrode on the right before cycling; AlH<sub>3</sub> on the left after 9 cycles.

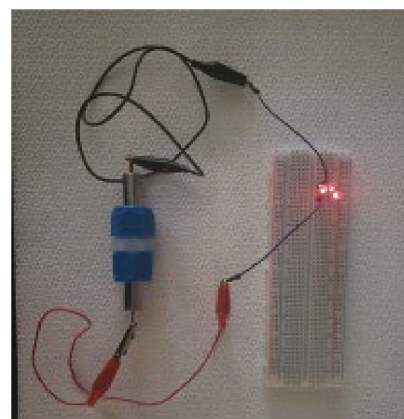


**Figure 7:** Prototype battery powering an LED.

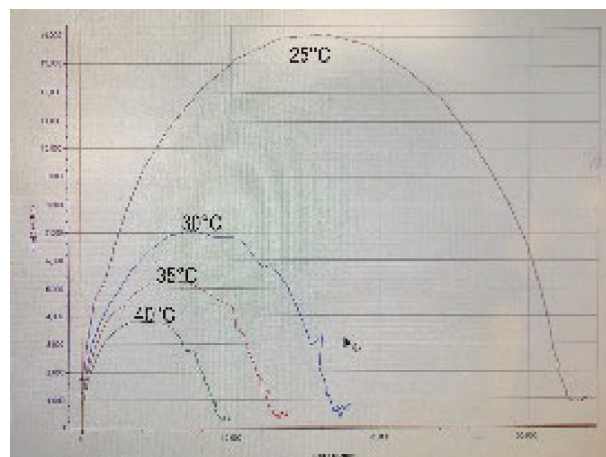


**Figure 8:** Impedance of a Li/LiAlH<sub>4</sub>/Li under varying temperature.

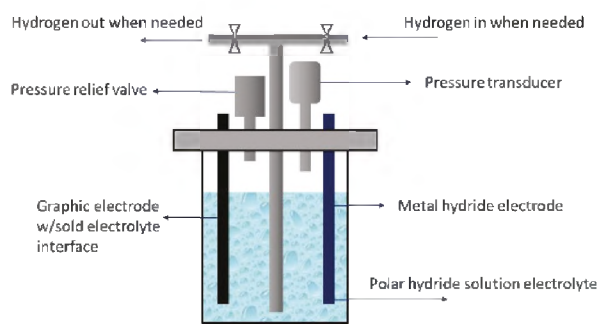


**Figure 9:** Design of the flow battery.

- NaAlH<sub>4</sub> was used; an electrolyte and a CV confirming mechanism was obtained
- Reducing dentaries by the use of LiCl in THF with LiAlH<sub>4</sub> electrolyte
- The design of a full flow battery (figure 9) has started and a pressurized system will be tested

## Future Directions

- Construct flow cell battery testing apparatus
- Optimize operating conditions
- Carryout testing of alanate based flow cell batteries

## FY 2020 Peer-reviewed/Non Peer-reviewed Publications

Jovy Ann Santos, Paulo Simon, Christopher Babasi, Anthony Bernot, Patrick A. Ward, Son-Jong Hwang, Ragaiy Zidan, and Joseph A. Teprovich Jr. Synergistic effect of nanoionic destabilization and partial dehydrogenation for enhanced ionic conductivity in MBH<sub>4</sub>-C<sub>60</sub> (M = Li<sup>+</sup>, Na<sup>+</sup>) nanocomposites, To be submitted by end of September.

## References

1. Wang, L.; Menakath, A.; Han, F.; Wang, Y.; Zavalij, P. Y.; Gaskell, K. J.; et. al. Identifying the components of the solid-electrolyte interphase in Li-ion batteries. *Nature Chemistry*, **2019**, *11*, 789-796.
2. Teprovich, J. A. Jr.; Weeks, J. A.; Ward, P. A.; Tinkey, S. C.; Huang, C.; Zhou, J.; Zidan, R.; Jena, P. Hydrogenated C<sub>60</sub> as High-Capacity Stable Anode Materials for Li Ion Batteries. *ACS Appl. Energy Mater.* **2019**, *2*, (9), 6453-6460.

## Acronyms

CV	Cyclic Voltammetry
DFT	Density Functional Theory
SEM	Secure Energy Manufacturing
SRNL	Savannah River National Laboratory
XRD	X-ray Diffraction

## Metal Hydride Fuel Cell Powered UAV

**Project Team:** Henry Sessions, Patrick Ward and Andrew Blanton

**Collaborator:** Kevin Kochersberger

**Project Start Date:** October 1, 2019

**Project End Date:** September 30, 2020

*Small Unmanned Aerial Systems (sUAS) have experienced tremendous growth in recent years. The ability of a multi-rotor sUAS to loiter at a fixed location has proven to be a valuable surveillance tool for a variety of applications, including military and life-saving first responder missions. SRNL successfully demonstrated increased sUAS flight times compared to battery powered unmanned aerial vehicles (UAVs) of the same size and weight, by using a hydrogen fuel cell (HFC), (proton exchange membrane) with hydrogen supplied from hydride materials.*

### FY2020 Objectives

- Develop light weight vessel to withstand required temperature and pressure
- Develop removeable cartridge with heaters to house hydride material
- Design and build electronic PID (Proportional, Integral, Derivative) heater system for controlled release of hydrogen
- Test and integrate components with commercially available UAV and flight test
- Obtained large UAV from Virginia Tech.
- Acquired 5kg alane for test flights.
- Developed SOW for Virginia Tech
- FRRB (DOE) Complete for ARC and P area
- Prepared Large Alane Pucks for Flight
- Large Aluminum Vessel Fabricated and Pressure Tested
- 800 Watt Fuel Cell Received
- Rapid Prototype Parts Complete for Mounting to UAV

### Introduction

Savannah River National Lab has initiated a small Unmanned Aircraft Systems (sUAS) program using commercially available remote-controlled aircraft. These aircraft are also referred to as Drones, Unmanned Aerial Vehicles (UAVs), and Birds.

UAVs have evolved into useful tools for surveillance of buildings, power lines, construction sites, farm crops, orchards, application of herbicides, and assisting first responders. A major issue with sUAS is the short flight duration, typically 20 minutes, due to battery life. An alternative to batteries is fuel cell powered sUAS using hydrogen. Hydrogen is stored in small lightweight cylinders and compressed to 7,000 to 10,000 psig to provide sufficient hydrogen for flight durations of approximately one hour. Battery powered UAVs have been in use for many years. The application of hydrogen supplied fuel cells for sUAS is just beginning and having compressed cylinders of hydrogen flying overhead is not always desirable.

The mission capability of small Unmanned Aerial Systems is limited by battery power density which dictates flight time. SRNL is proposing the use of Hydrogen Fuel Cells supplied with Hydrogen from the Metal Hydride Alane to extend sUAS flight times. An alternative to hydrogen stored in high pressure compressed gas cylinders is hydrogen stored at low pressure on metal hydrides. SRNL has decades of experience with metal hydrides.

## Approach

Fuel cells supplied with hydrogen from metal hydrides have the potential to increase flight time of UAVs from a nominal twenty minutes, based on batteries, to several hours.

## Results/Discussion

In September 2019, SRNL flew a quadcopter powered by a fuel cell supplied with hydrogen from the metal hydride alane (AlH<sub>3</sub>) (Figure 1). Alane contains 10 weight percent hydrogen. Fifty grams of Alane was available for this flight and it provided five grams of hydrogen. For the weight and configuration of the quadcopter shown in the photographs below the flight time was increased by five minutes. It was a modest increase in flight time but proved the feasibility of the application. The continuation of the LDRD in 2020 was to demonstrate extended flight of 2 hours using 1 kilogram of alane, (100 grams of hydrogen). This report documents the accomplishments in FY2020 towards that goal.

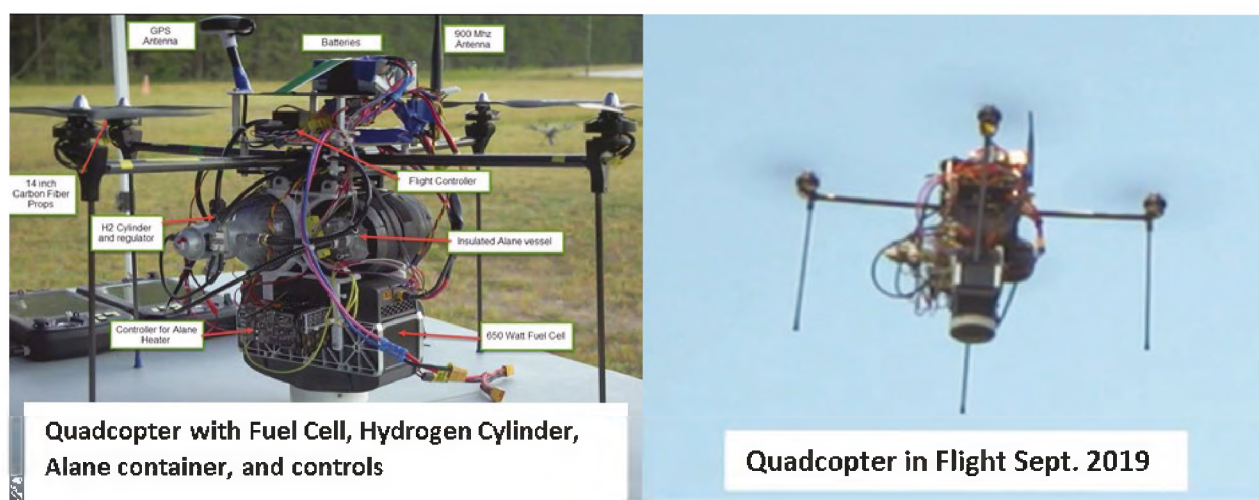


Figure 1: Photographs of quadcopters.

## FY2020 Accomplishments

SRNL partnered with Va. Tech. to produce an efficient hex-copter that could provide sufficient lift for 1 kilogram of Alane and the required components for containment, controlled heating, and hydrogen delivery to the hydrogen fuel cell (Figure 2).

A lightweight vessel to house the hydride material was developed. It is capable of withstanding the temperature required to release hydrogen from the hydride material and containing the hydrogen pressure. It is envisioned that the hydride material will be housed in a cartridge that can be easily exchanged. An electrical/electronic heater control system for controlling the release of hydrogen from hydride material and regulating the hydrogen flow to the fuel cell was designed. This circuit functioned as a PID



Figure 2: Hexacopter fabricated by VA Tech's Unmanned Systems Lab.

control and was integrated with the UAV flight controls. All the subcomponents have been tested and integrated with a commercially available UAV and flight tested.

Alane ( $\text{AlH}_3$ ) is a powdery, granular substance and must be heated to 150 degrees Celsius to liberate hydrogen. In order to aid in heat transfer, alane is pressed into a puck. Enhanced Natural Graphite (ENG) is mixed with the alane prior to pressing. ENG acts a binder to maintain the puck shape and reduce pressing force required to produce and maintain the puck shape. Eightygrams of ENG is mixed with 1 kg of alane. A Die Set was purchased from Materials Testing Inc. Corporation. Fortunately a Huboldt Compression Test Machine, typically used for concrete testing, capable of supplying 300,000 lbs. of pressure was available in building 999-1W. It along with the die set was used to press 100 gram alane pucks. to press 100 gram pucks of Alane. The pucks were pressed using 150 tons of force.

The pressed alane pucks are stacked in the aluminum vessel and surrounded with insulation to minimize heat transfer to the wall of the vessel. The initial location of the alane heater was the bottom of the aluminum vessel. However preliminary tests indicated an insufficient heating rate. Therefore the heater was moved to the middle of the stack. The heater is a thin ceramic wafer and heat flows out of both sides of the heater. This configuration maximizes use of the heating power. Hollow ceramic rods were used to insulate the electrical wires that supply power to the heaters.

## Future Directions

Test and integrate components with commercially available UAV and flight test.

## Acronyms

HFC	Hydrogen Fuel Cell
PID	Proportional, Integral, Derivative
sUAS	Small Unmanned Aircraft Systems
UAVs	Unmanned Aerial Vehicles

## Intellectual Property

Two invention disclosures were generated.

## Material Developments for 3D/4D Additive Manufacturing (AM) Technologies

**Project Team:** Simona Hunyadi Murph, Henry Sessions, Patrick Ward, John Bobbitt and Ray Belliveau

**Project Start Date:** October 1, 2019  
**Project End Date:** September 30, 2020

*Additive Manufacturing (AM), or 3D printing, is a unique technology in which structurally complex objects can be easily manufactured. While AM allows for the creation of intricate 3D objects, these objects are inactive and motionless. With recent incorporation of a “pre-programmed functionality” to the 3D printed objects, a new concept has emerged, 4D printing. Specifically, the 4D printing technology enables a static*

*3D printed object to change its shape, functionality or property over time upon exposure to a specific stimulus such as heat, stress, light, pH, and moisture, etc. We designed and produced compact 3D/4D printable materials that can be used as (a) structural components of the unmanned aerial vehicles (UAVs), and (b) as hydrogen storage materials that supply hydrogen to a fuel cell to expand the operational reach, namely flight time, and endurance of the UAVs.*

### FY2020 Objectives

- Design and print 3D/4D hydride materials
- Evaluate and optimize the 3D/4D printed hydride materials as hydrogen storage material

### Introduction

Additive Manufacturing (AM), or 3D printing (Figure 1), is a unique technology in which structurally complex objects can be easily manufactured. While AM allows for the creation of intricate 3D objects, these objects are inactive and motionless. With recent incorporation of a “pre-programmed functionality”

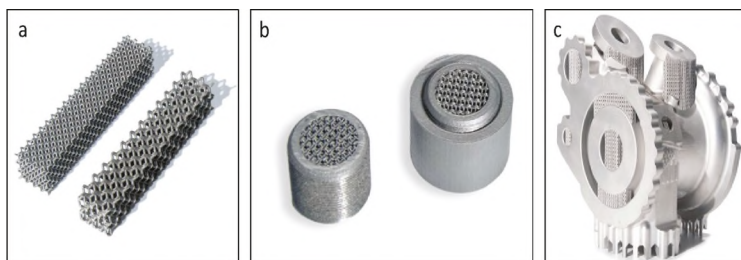


**Figure 1:** 3D printed objects via selective laser melting process.

to the 3D printed objects, a new concept has emerged, 4D printing. Specifically, the 4D printing technology enables a static 3D printed object to change its shape, functionality or property over time upon exposure to a specific stimulus such as heat, stress, light, pH, and moisture, etc. One area of interest that can greatly benefit from the implementation of the 3D/4D printed objects is the field of unmanned aerial vehicles (UAV).

Unmanned aircraft systems (UASs) have experienced explosive growth in recent years and have proved to be an invaluable resource in military and first responders’ missions, agricultural surveillance, deliveries, telecommunications, etc. In recent years, the need for improved UAS’s operational reach and endurance has been echoed across all DOE’s and DoD’s levels of leadership. (Note: Operational reach is defined as the distance and duration across which a unit can successfully employ its capabilities).

The development and implementation of the 3D/4D hydride materials as structural components for hydrogen fuel cells operated UAV's proposed here will have a significant impact in expanding their operational reach and endurance (Figure 2). This project developed Smart/Enabling Tools, in the form of 3D/4D materials and components, that will enhance SRNL's drone and additive manufacturing programs while expanding SRNL's leadership role in scientific discovery and innovation. The research and development technologies addressed here will align with the SRNL's and DOE's and DOD's vision to encourage initiatives that will support national defense, and energy security programs.

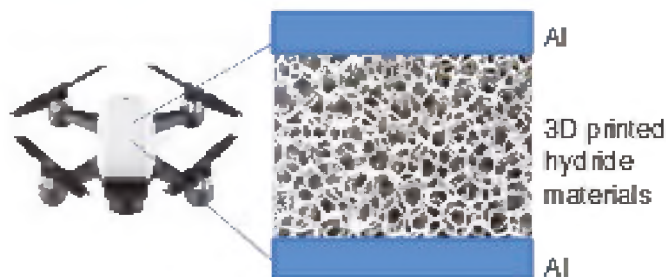


**Figure 2:** Simple illustration of the concept of 3D/4D hydride material.

## Approach

- Design and produce a 3D/4D hydride materials via additive manufacturing technologies that could be used as parts of the unmanned aerial vehicles (UAV)
- 3D printing (e.g. selective laser melting) will be used to produce sandwich hydride foam materials (novel feeding stock materials) to create UAV parts, e.g. body, landing gear, and motor supports

## Results/Discussion

Hydrogen storage materials has been the subject of an intense research effort in the last decades. However, this is the first study demonstrating the successful creation of 3D printed hydride materials via additive manufacturing approaches.

The first task of the project focused on the design and material production of a library of 3D/4D hydride-based materials that could be used as structural components of the unmanned aerial vehicles (UAV). Metal hydrides selection is based on decades of intensive and extensive explorations at SRNL in this field. In the initial phase of this task, we engineered and designed hydride materials based on various composition additive metals. Aluminum served as an inert scaffolding material in these architectures. The following alloy compositions were explored: (a) powders: Al, Ti, Fe, Mn, V, Cr, Mg, Pd, Zr, Sc, Ni, Pd, Si, La, etc. and/or (b) nano-microscale additive: Ti, TiO<sub>2</sub>, Pd, Fe<sub>2</sub>O<sub>3</sub> as numerous studies shows improved strengths, kinetics, and favorable thermodynamics based on these compositions.

Selection of the hydride materials must meet the following specifications: (a) contains light metals as strength-to-weight ratio is important in aircraft applications, (b) has favorable hydrogen gas storage capabilities, (c) made of porous structures, e.g. foams, with regular/irregular arrays of pores having



**Figure 3:** 3D/4D printed metal hydride objects.

tunable dimensions at the microscale. Porous hydride materials are of particular interest because they can increase the penetration depth of hydride reaction and decrease the hydrogen absorption time. The pore size affects hydrogen storage capacity and kinetics, as well as thermal stability. Smaller pores impart larger surface areas of interaction at the gas/solid interface, allowing hydrogen to diffuse harmlessly out of the solid. The bulk hydride materials often decrepitate or break down into smaller particles under repetitive reaction cycles, usually hundreds of cycles. The reduced size material may be advantageous since previous studies show that nanophase metal hydrides have enhanced kinetics for reversible hydrogen storage relative to the bulk materials. The hydride material alloyed with specific additive of interest were successfully 3D/4D printed by a laser sintering 3D printing technique. The laser sintering 3D printing uses a high-power laser to fuse powdered material by scanning cross-sections on the surface of a powder bed which is the preferred technique for our materials (Figure 3).

Once produced the 3D/4D printed materials were characterized by a series of analytical tools to evaluate their physico-chemical properties (Figure 4). This includes SEM, EDS, EDS mapping, ICP-MS, UV-Vis spectroscopy, surface charge, etc. Data shows that the materials retain their properties upon additive manufacturing. A number of the feeding stock materials were also produced and characterized by the aforementioned techniques (Figure 5a inset).

Hydrogen absorption isotherms adsorption and desorption kinetics (Figure 5 a, b), capacity, thermodynamic were collected using the automated, patent pending Sieverts apparatus at various temperatures available in our lab at SRNL/ARC. This patent pending technology is based on a novel automatic gas absorption-desorption apparatus that can be used to collect isotherm measurements and evaluate the kinetics and thermodynamic behavior of hydride material at

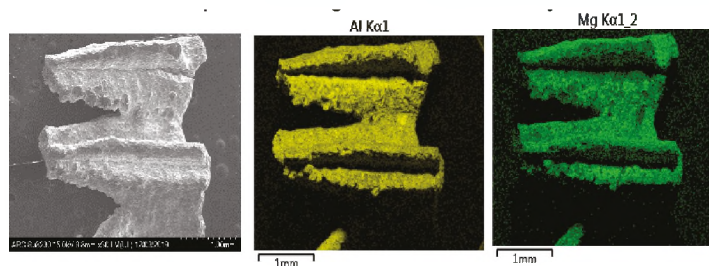


Figure 4: EDS mapping of the 3D printed Mg-Al based alloys.

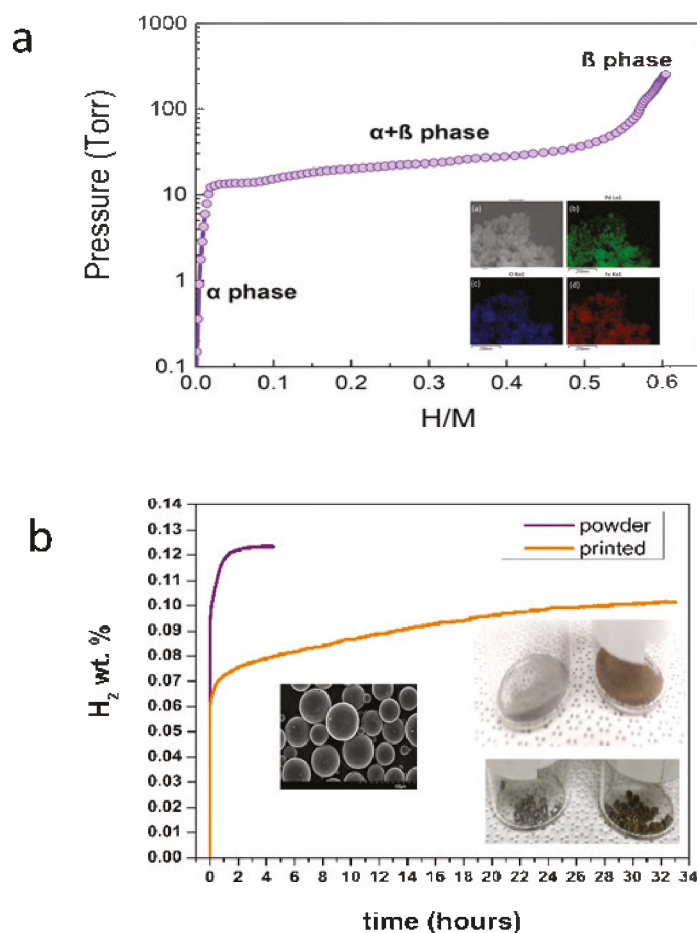


Figure 5: Hydrogen absorption isotherm absorption on (a) Pd-Fe/FeO<sub>x</sub>; inset showing EDS mapping; and (b) TiAl<sub>6</sub>V<sub>4</sub> alloy. Inset shows photograph of feeding stock alloy samples before (gray) and after (brown) hydrogenation. The kinetics are far slower for printed TiAl<sub>6</sub>V<sub>4</sub>.

various temperatures and pressures. This automated apparatus is capable of collecting data on multiple absorption-desorption cycling experiments to study long-term cycling effects on capacity and kinetics. It is composed of automated valves that are remotely controlled using LabVIEW. The apparatus can process two samples concurrently for determination of equilibrium temperatures, pressures, and thermodynamics. It can be coupled with any PCTPro or magnetic induced heating systems available on the market for automatization. Isotherms can be collected unattended in less than 8 hours on two hydride samples. The initial testing assessed the system's performance under a variety of process conditions (temperature, pressure, composition), physical design, transient heat and mass transfer. Data collected will be used to compare the material capacity and plateau pressure for the 3D/4D printed samples.

## FY2020 Accomplishments

- Designed and produced 3D/4D hydride materials via additive manufacturing technologies that could be used as parts of the UAV
- Acquired and/or 3D printed a number of hydride-based materials of various compositions: Al, Ti, Fe, Mn, V, Cr, Mg, La, and/or Pd - based materials coupled with other additives
- Evaluated and characterized both hydrogen storage materials feeding stocks and 3D printed materials -isotherms, SEM, EDS, ICP-MS, EDS mapping, ICP-MS, UV-VIS, collected isotherms on selected feed stock & 3D printed hydride materials
- Initiated modeling studies on hydride materials
- Demonstrated for the first time that we can 3D print hydride materials for hydrogen storage capabilities. Preliminary measurements indicate small variation and responses in the hydride absorption kinetics
- Developed a very unique automated, patent pending Sieverts apparatus at various temperatures available in our lab that can be used to collect isotherm measurements and evaluate the kinetics and thermodynamic behavior of hydride material at various temperatures and pressures
- Two patent applications were filled with the US Patent and Trademark Office
- Published one manuscript in the ACS Materials & Interfaces
- A second manuscript was submitted to the International Journal of Hydrogen Research – Special Issue
- One book chapter accepted for publication
- Delivered two conference presentations – The Mineral, Metals and Materials Symposium and Technology and Environmental Business Association (ETEBA) Conferences

## Future Directions

- Continue to evaluate and optimize the 3D/4D printed hydride materials as hydrogen storage material
- Produce structural components of the UAVs made of 3D/4D printed materials
- Technology integration of UAV's components with the aircraft and maturation

## FY 2020 Peer-reviewed/Non Peer-reviewed Publications

- Efficient Thermal Processes using Alternating Electromagnetic Field for Methodical and Selective Release of Hydrogen Isotopes, International Journal of Hydrogen Energy, Special Issue, 2020 submitted; SRNL – corresponding and first author.
- Controlled Release of Hydrogen Isotopes from Hydride-Magnetic Materials, ACS Applied Materials & Interfaces, 2020, 12, 9478-9488; SRNL – corresponding and first author.

- Analytical Method for Measuring Total Protium and Total Deuterium in a Gas Mixture Containing H<sub>2</sub>, D<sub>2</sub>, and HD via Gas Chromatography, 2020, Metal-Matrix Composites: Advances in Analysis, Measurement and Observations, Springer, accepted; SRNL – corresponding and first author.

## Presentations

- Efficient Heating Processes Using Nanomaterials and Alternating Electromagnetic Fields, Energy, Technology and Environmental Business Association (ETEBA) Conference
- State-of-the-Art Materials at SRNL: From Innovation to Marketplace, The Minerals, Metals and Materials Society (TMS)

## Acronyms

ARC	Applied Research Center
SRNL	Savannah River National Laboratory
AM	Additive Manufacturing
3D	Three Dimensional
4D	Four dimensional
UAVs	Unmanned Aerial Vehicles
SEM	Scanning Electron Microscopy
EDS	Energy Dispersive X-ray Spectroscopy
ICP-MS	Inductively coupled plasma mass spectrometry
UV-Vis	ultraviolet - visible
ETEBA	Energy, Technology and Environmental Business Association

## Intellectual Property

- Structural Components for UAVs Made of 3D/4D Printable Materials - U.S. Patent Application
- Automatic Gas Absorption-Desorption Apparatus - U.S. Patent Application

## Post-Doctoral Researchers

Ray Belliveau (SRNL)

## Component Development for Alkaline URFCs

**Project Team:** Héctor Colón-Mercado, Aaron Lando, William Mustain

**University of South Carolina Collaborator:** William Mustain

**Project Start Date:** October 1, 2019  
**Project End Date:** September 30, 2021

*Performance, cost, and durability of the catalyst materials are the key factors that govern the commercialization of H<sub>2</sub>-based energy devices such as unitized regenerative fuel cells (URFCs). URFCs offer the advantage of high energy density vs. existing battery systems. In addition, with the use of an alkaline URFC system, lower system costs can be achieved through the use of platinum group metal-free (PGM-free) materials. This project seeks to address the major obstacles faced in*

*URFC systems and establish a URFC technical capability through the strategic partnership between USC and SRNL. The research focuses on the development of low-PGM and PGM-free based bifunctional oxygen catalysts and electrodes, as well as the development of a URFC testing capability at SRNL.*

### FY2020 Objectives

- Establish *ex-situ* baseline performance of state-of-the-art bifunctional catalysts
- Establish in-situ discrete baseline performance of state-of-the-art bifunctional catalysts
- Low-PGM bifunctional catalyst development and *ex-situ* evaluation
- Design of URFC testing facility
- Facility construction/evaluation

### Introduction

The development of high-performance and low-cost bifunctional electrodes for oxygen evolution reaction (OER) and oxygen reduction reaction (ORR) is critical for enabling the use of electrochemical energy storage devices based on O<sub>2</sub> chemistries such as metal–air batteries and URFCs. URFCs are superior to existing battery systems with respect to energy density and performance over prolonged operation, making them the preferred choice for applications such as stationary renewable energy storage for utility power, other large power applications (e.g. rail), and surveillance systems. By developing low PGM or PGM-free catalysts we are able to move towards more efficient and lower-cost URFC operation.

URFCs are capable of operating in both power production (fuel cell, FC) and energy storage (electrolysis cell, EC) modes. URFCs are seen as a key enabler of intermittent renewable energy technologies, as they are able to store and convert chemical energy to electrical energy depending on supply and demand. The attractiveness of URFCs is that the theoretical energy density is approximately an order of magnitude higher than commercial lithium ion batteries. However, as is typical with low TRL technologies, URFCs are currently too expensive to compete with existing energy storage technologies. A major contributor to URFCs high cost is their incorporation of platinum group metal (PGM) catalysts in the electrodes. This reliance on PGMs is because they are currently the only catalysts that show both high activity and stability in the acidic environment of proton exchange membrane (PEM) based URFCs. To circumvent the electrode material cost in PEM systems, alkaline systems enable the use of PGM-free electrodes. However, until recently, alkaline system performance has been negatively impacted by poor membrane and ionomer stability. Recent improvements to performance and stability in state-of-the-art alkaline anion exchange membranes (AEMs), has opened the doors to new technology development within low cost URFCs, capable of competing with existing energy storage technologies.

## Approach

Highly active and stable catalysts are needed to achieve high round trip thermodynamic efficiency ( $\epsilon_{RT} > 50\%$ , Figure 1) and long system life for URFC systems. To meet these objectives, this project will focus on three main areas:

1. Increasing  $\epsilon_{RT}$  through the development of stable catalysts with improved overall ORR and OER kinetics
2. Electrode development capable of efficient operation at the conditions required in energy production and energy delivery modes, and
3. Establish a functional test facility capable of analyzing various operating energy cycles.

## Results/Discussion

Due to the slow kinetics for both oxygen reactions (OER and ORR), the primary barrier to achieving high  $\epsilon_{RT}$  is the oxygen electrode performance. To compensate for this inefficiency, typical URFCs combine the best electrocatalysts for the ORR (namely Pt based catalysts) and OER catalyst (namely Ir, Ru and their oxides) to prepare a bifunctional oxygen electrode. However, most of these catalysts are non-supported and the cell suffer from high precious metal loadings. To lower the cost of the bifunctional electrode, SRNL is producing supported PGM. Figure 2 shows the *ex-situ* testing of commercial electrocatalyst and SRNL synthesized bifunctional catalysts. Figure 3 shows the short-term *ex-situ* cycle stability for various of the catalysts. As observed in the figures the prepared catalyst not only has comparable activity to commercial catalysts, but also has comparable stability.

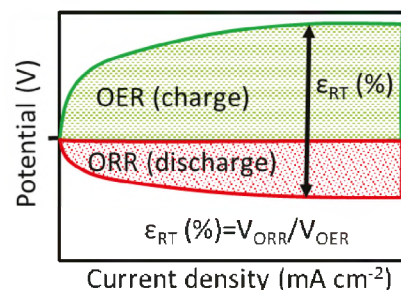


**Figure 1:** Representative performance curve of an URFC. Kinetic improvements are needed to minimize separation between the charge and discharge curves.

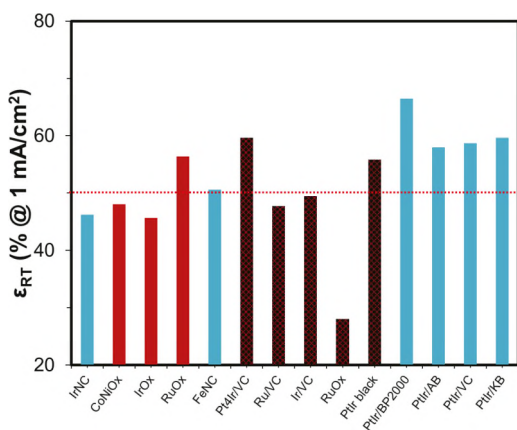


**Figure 2:** Round trip efficiency comparison of commercial and synthesized catalysts.

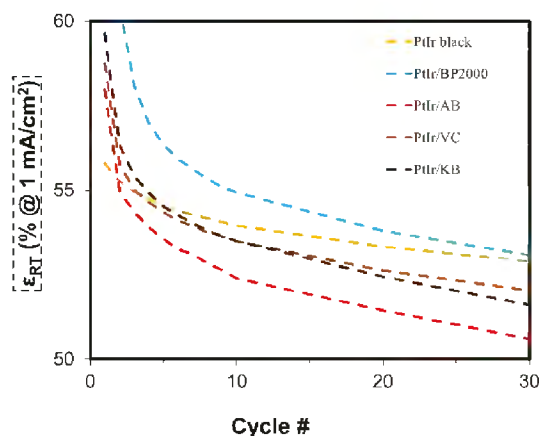


**Figure 3:** Short-term cycle stability of PtIr on various carbon supports.

*In-situ* cell electrode optimization was performed at USC in an electrolysis cell using commercial electrocatalysts. Figure 4 shows the performance test of the electrolysis cell using standard electrode fabrication. Finally, figure 5 shows the modified test station at SRNL to initiate in-house URFC testing.

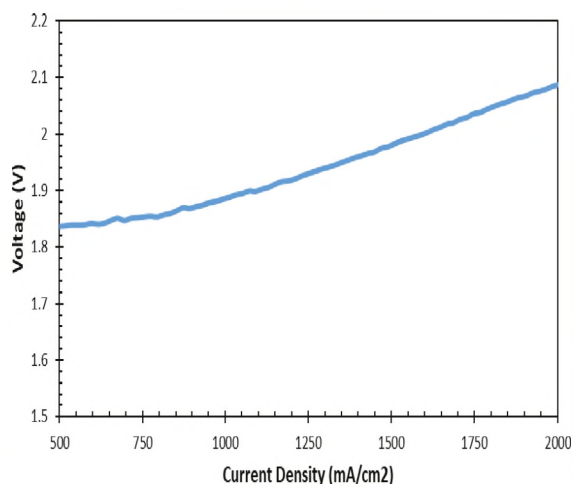


**Figure 4:** Electrolysis cell test using commercial electrocatalysts.



**Figure 5:** In-situ testing set up completed and SRNL inspected.

## FY2020 Accomplishments

- Optimized and decreased synthesis time by moving to a polyol microwave synthesis technique
- Found PtIr on BP2000 to have the highest OER and ORR activity
- Initiated electrode optimization at USC
- Built and SRNL approved URFC Station

## Future Directions

- Create an operational baseline for the URFC Station
- Development of PGM-free bifunctional catalysts as electrodes
  - PGM-free catalysts based on metal oxides and pyrolyzed organic frameworks will be prepared and characterized
  - Catalysts prepared will be down selected for electrode optimization via ORR and OER cycling measurements and compared to PtIr on BP2000
  - Systematically optimizing the anionomer:carbon:catalyst ratio, catalyst loading, hydrophilicity/hydrophobicity, cell temperature, and reactant flowrates for the optimization of water flow and overall FC performance

## Acronyms

EC	Electrolysis cell
FC	Fuel cell
PGM	Platinum group metals
$\epsilon_{RT}$	Round trip efficiency
OER	Oxygen evolution reaction
ORR	Oxygen Reduction Reaction
URFC	Unitized regenerative fuel cell

## Student Researchers

Noor Ul Hassan, University of South Carolina

## Advanced Photoelectrode Development to Produce Novel Solar Batteries

**Project Team:** Patrick A. Ward, Simona Murph, Aziz Boulesbaa (CSUN)

**University of South Carolina Aiken Collaborator:** Nicholas Marshall

**California State University Northridge Collaborators:** Joseph Teprovič, Aziz Boulesbaa

**Project Start Date:** October 1, 2020  
**Project End Date:** September 30, 2021

*Energy storage solutions are critical for our nation's electrical grid in order to provide reliable power using intermittent renewable energy technologies such as wind and photovoltaics. Herein, fundamental research was carried out to control and determine electron transfer pathways in order to develop broadband multicomponent photoelectrodes. These photoelectrodes were developed with the application of directly charging a redox flow battery in mind. This allows for an integration of solar energy conversion and storage in one device to reduce the cost and footprint associated with renewable energy deployment.*

### FY2020 Objectives

- Synthesize novel multicomponent photoelectrode materials
- Characterize materials for photoelectrode
- Determine electron transfer pathways utilizing femtosecond transient absorption spectroscopy
- Evaluate produced photoelectrodes

### Introduction

The necessity of grid storage for reliable and dispatchable power intensifies as more photovoltaic systems are deployed. To address this issue and lower the overall cost of solar power, our team is investigating an integrated photovoltaic and electrochemical storage system that simultaneously increases solar spectrum utilization. By leveraging systematically grown multicomponent materials, wavelengths spanning from the ultraviolet to the near infrared

can be utilized to directly store electrochemical energy. The long-lived charge separated state of this composite allows for the transfer of electrons through a current collector to the cathode as well as oxidation of electrolyte molecules by holes on the photoanode. Separation of these anionic and cationic species by a semipermeable membrane provides electrochemical storage in a redox flow cell type battery.

### Approach

The investigation of this fundamentally new idea provides solutions to grid scale energy storage as well as solar spectrum utilization efficiency. This idea couples a photoelectrode, capable of utilizing solar irradiation over a wide portion of the solar spectrum, with a redox flow battery. In this configuration, the absorbed solar energy is used to directly charge the redox flow battery. Absorbed solar irradiation excites

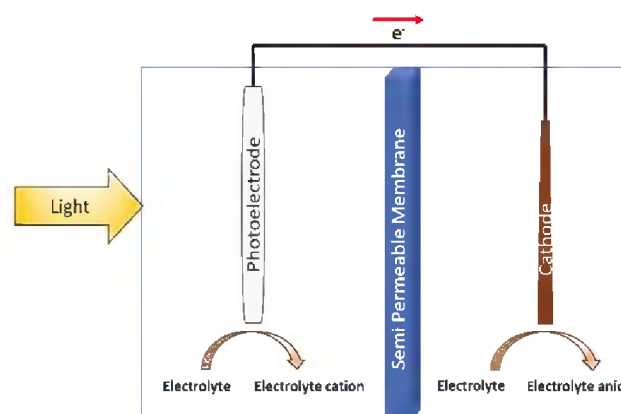


**Figure 1:** Graphical illustration of the photoelectrochemical redox flow battery.

electrons from various components of the multicomponent photoelectrode to generate holes and free electrons. These free electrons and holes then oxidize/reduce the electrolytes in a redox flow cell battery design. The electrons generated from the solar excitation will be transferred to the cathode to drive the reduction of electrolyte molecules on the other side of a semipermeable membrane. Figure 1 shows the fundamental cell operation and design. The proposed design pathway has the advantage of utilizing a large portion of the solar spectrum. The separation of these cationic and anionic species by a semipermeable membrane effectively stores the electrochemical energy. Only recently have other research groups begun to explore the concept of developing photoelectrochemical cells in a redox flow battery configuration. Previous work on this type of concept has utilized TiO<sub>2</sub> photoelectrodes which are only capable of exciting electrons into the conduction band with the absorption of UV radiation.<sup>1,2</sup> Other recent work has demonstrated the use of CdS as a direct semiconductor photoelectrode to charge a vanadium redox flow battery.<sup>3</sup> The current state-of-the-art in this technology has been limited to employing semiconductor substrates which absorb relatively small portions of the electromagnetic spectrum and have shorter-lived charge separation states.

## Results/Discussion

Multicomponent photoelectrode materials were evaluated to ensure proper electron transfer mechanistic behavior. Components were interfaced particularly to inject electrons into the conduction band of the base material from absorbing wavelengths of light in the visible spectrum. Figure 2 below provided transient absorption spectroscopy measurements which confirm electron ejection into the conduction band of a higher energy using visible light excitation. Figure 3 below also supports charge transfer due to the faster relaxation of the visible excited state when the components are appropriately interfaced. Electron transfer mechanisms were supported by photoelectrochemical UV/Vis measurements of one of the visible excited components. This data was used in conjunction

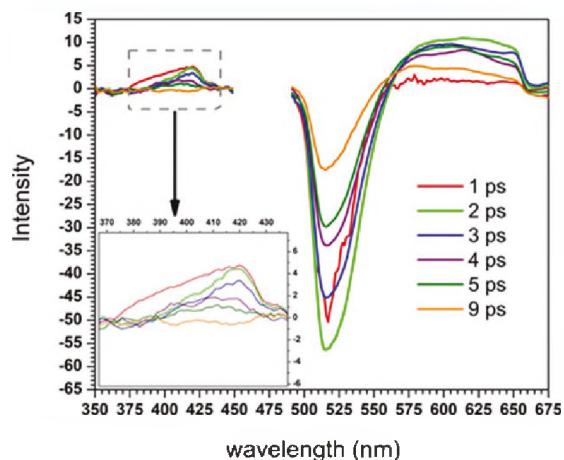


Figure 2: Transient absorption spectroscopy of multicomponent photoelectrode materials used for photoelectrodes.

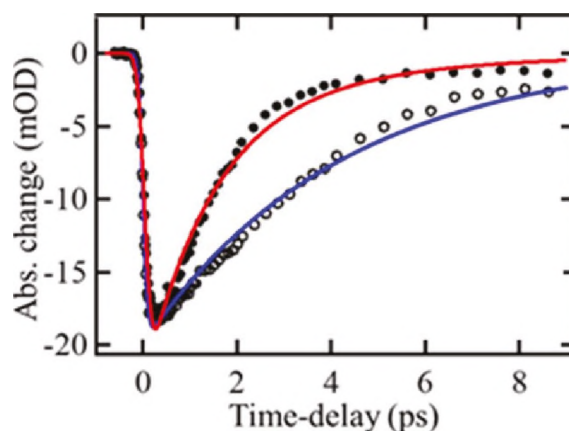


Figure 3: Transient absorption spectroscopy illustrating relaxation dynamics of one of the charge transfer components.

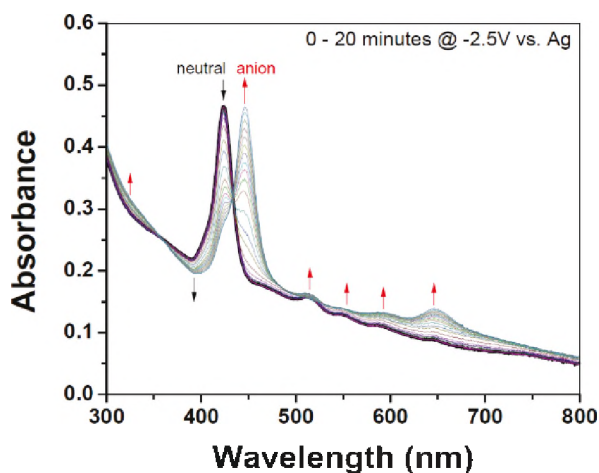


Figure 4: Photoelectrochemical UV/Vis of a component of the multicomponent photoelectrode showing the electronic transition from neutral to anionic state.

with DFT calculations to identify the state of the component after visible excitation of the electronic transition. If the component is in an anionic state, electrons were transfer to it. If the component is in a cationic state, electrons were donated from it. Figure 4 provides photoelectrochemical UV/Vis measurements of one of the components. Due to the pending invention disclosure on these materials, they cannot be released at this time.

## FY2020 Accomplishments

- Experimentally confirm electron transport suitable for broad band photoelectrode development
- Synthesized and characterized a series of novel multi-component photoelectrode materials
- Studied the ionic and neutral states of photoelectrode components by employing photoelectrochemical UV/Vis, DFT calculations, and transient absorption spectroscopy to understand the underlying mechanistic photoexcitation behavior of the materials

## Future Directions

- Develop methodologies for photoelectrode production and compare
- Demonstrate operation of the full photoelectrochemical redox flow cell under simulated solar irradiation
- Cycle the full system greater than 10 times to demonstrate reversibility

## References

1. Wei, Z.; Liu, D.; Hsu, C.; Liu, F. *Electrochemistry Communications*, **2014**, *45*, 79-82.
2. Wei, Z.; Almakrami, H.; Lin, G.; Agar, E.; Liu, F. *Electrochimica Acta*, **2018**, *263*, 570-575.
3. Azevedo, J.; Seipp, T.; Burfeind, J.; Sousa, C.; Bentien, A.; Araujo, J. P.; Mendes, A. *Nano Energy*, **2016**, *22*, 396-405.

## Acronyms

CSUN	California State University Northridge
DFT	Density Functional Theory
PI	Principal Investigator
SRNL	Savannah River National Laboratory
USCA	University of South Carolina Aiken
UV/Vis	Ultraviolet / Visible

## Post-Doctoral Researchers

Michael Thomas - SRNL

## MAX Phase Materials and MXenes as Hydrogen Barrier Coatings

**Project Team:** D. Hitchcock, T. Krentz, M. Drory, B. Garcia-Diaz

**Georgia Institute of Technology**  
**Collaborators:** E. Vogel, K. Young

**Project Start Date:** October 1, 2019  
**Project End Date:** September 30, 2021

*Hydrogen and its isotopes play an important role in nuclear applications, but their permeation and radioactivity lead to degradation of materials. Therefore, hydrogen isotope permeation barriers are an important supporting technology. Unfortunately, most permeation barriers that perform well in the laboratory fail when placed in radiation environments. The goal of this work is to begin the development of next generation permeation barriers with materials known to have good stability under neutron irradiation, and then tailor their*

*composition and structure to maximize their barrier properties. In particular MAX phase materials and their two-dimensional analogues (MXenes) have been chosen due their excellent stability under neutron irradiation.*

### FY2020 Objectives

- Coating deposition
- Structural characterization of deposited films
- Permeation measurements

### Introduction

Hydrogen and its isotopes play an important role in nuclear applications, but their permeation and radioactivity lead to degradation of materials. During tritium production, permeation release rates from Tritium Producing Burnable Absorbing Rods (TPBARs) exceed expected levels. Moreover, surface interactions, particularly with stainless steel, demand high performance hydrogen isotope permeation barrier coatings (HIPBs). Additionally, tritium retention in both plasma facing and process components is a major issue facing the demonstration and widespread use of fusion energy. The development of permeation barriers capable of operation in a fusion environment would greatly alleviate this concern.

Barrier materials display bulk hydrogen isotope permeabilities as low as 10 orders of magnitude below structural materials. Therefore, very thin coatings, on the order of microns, can reduce the permeation through structural materials drastically. Current candidates for HIPBs include oxides such as  $\text{Al}_2\text{O}_3$  or  $\text{Er}_2\text{O}_3$ , carbides such as  $\text{SiC}$ , and aluminides. Previous work has shown that though some hydrogen isotope permeation barrier materials display very low permeability<sup>2</sup> most barrier materials which perform well in laboratory experiments fail when placed in radiation environments.<sup>3</sup> Furthermore, permeation reduction factors (PRFs) vary significantly in literature. For example oxide and carbide barriers have PRFs varying from  $\sim 10$  -

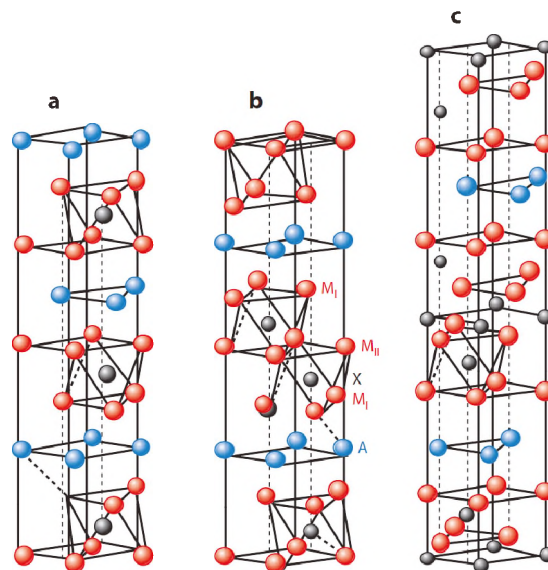


**Figure 1:** MAX phase unit cells: (a) 211, (b) 312, and (c) 413 phases.<sup>1</sup>

1000<sup>4</sup> while aluminide PRFs can also span 10 - 10,000 (though the general PRF value for gaseous H<sub>2</sub> is <1000).<sup>5</sup> In-reactor permeation measurement on aluminides show PRFs as low as 3.4 and as high as 80.<sup>6</sup> SiC coatings are another alternative, but are brittle which leads to coating failure during thermal cycling and delamination issues.

MAX phase materials have a layered structure with the general formula M<sub>n+1</sub>AX<sub>n</sub> where M is an early transition metal, A is an A group element from group 13-16, and X is carbon or nitrogen. The carbide or nitride octahedra layers are alternated with single atomic layers of metallic A atoms (Figure 1). MAX phases are currently being investigated for fission applications due to their excellent stability under neutron irradiation. These materials have mixed ceramic and metallic characteristics due to their layering and have displayed excellent barrier properties to hydrogen and stability under elevated temperature, aggressive chemistries, and high neutron fluence, making them attractive for cladding materials in nuclear reactors.<sup>7</sup>

## Approach

The goal of this work is to begin the development of next generation permeation barriers with materials known to have good stability under neutron irradiation, and then tailor their composition and structure to maximize their barrier properties. In particular MAX phase materials and their two-dimensional analogues (MXenes) have been chosen due their excellent stability under neutron irradiation.

In addition to studying the barrier mechanisms for MAX phase/MXene materials and identify/synthesizing specific formulations which are hydrogen/irradiation resistant in extreme environments, routes to lower temperature depositions were also explored. Current deposition strategies for MAX phases and MXenes, namely sputtering followed by high temperature annealing, are not suitable for structural materials in many nuclear environments due to the need for heat treatments outside of the operating temperatures of the alloys of interest. Strategies for deposition of MAX phases at moderate temperatures are an important innovation which will enable the use of MAX phases in wide range of commercial applications.

## Results/Discussion

Recent work has explored the use of chemical vapor deposition on liquid metal substrates to controllably synthesize transition metal carbides,<sup>8</sup> and early results from this work confirmed that Mo<sub>2</sub>C can be grown on Cu substrates at temperatures above 1000 °C. However, this elevated temperature is unacceptable for many applications which has led to recent studies using Cu alloy substrates such as Cu-Sn to lower the growth temperature.<sup>9</sup> In this work the effects of using a Ag-Cu alloy as a substrate for Mo<sub>2</sub>C synthesis by chemical vapor deposition (CVD) were systematically analyzed. The results conclusively demonstrated that synthesis of Mo<sub>2</sub>C is controlled by Mo diffusion through the liquid alloy (Figure 2). Utilizing a Ag-Cu alloy as a substrate successfully reduced the necessary synthesis temperature below the melting point of Cu; however, Mo<sub>2</sub>C coalescence was limited and directly proportional to Cu content due to the separation of the Ag and Cu components in the alloy upon cooling (Figure 3). Ag alone is not a suitable substrate for Mo<sub>2</sub>C synthesis, likely due to the inability of Ag to dehydrogenate methane effectively. Thus, an optimal substrate for Mo<sub>2</sub>C synthesis should be able to dehydrogenate methane, have a low melting temperature, and, if an alloy, demonstrate solid solubility.<sup>10</sup>

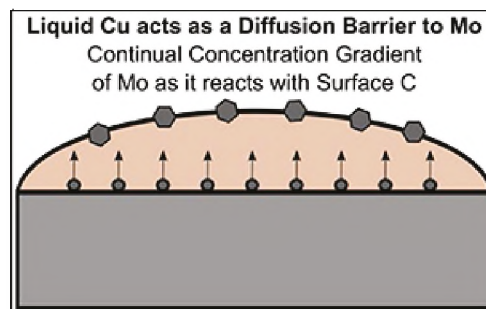


**Figure 2:** Proposed mechanism where Cu melts on the Mo foil surface. Mo atoms diffuse through the liquid Cu until they reach the surface, where they either react with surface C or CH<sub>4</sub> to form Mo<sub>2</sub>C.

Though the  $\text{Mo}_2\text{C}$  synthesis temperature is decreased when using a Ag-Cu alloy vs Cu-alone, there were still some challenges with the Ag-Cu alloy as a substrate. One of the major challenges with using a Ag-Cu alloy as substrate for  $\text{Mo}_2\text{C}$  synthesis is that there is separation of the alloy components upon cooling. This prevents the  $\text{Mo}_2\text{C}$  from coalescing fully. Thus, an alloy that can remain mixed or that does not separate except at low temperatures, could solve this problem. In-Cu alloys have greater mixing, even at lower temperatures, than Ag-Cu alloys. Though uniform coverage across the entire sample is still a challenge, there is much higher  $\text{Mo}_2\text{C}$  coalescence for an In-Cu alloy substrate (Figure 3) compared to the Ag-Cu alloy substrate.

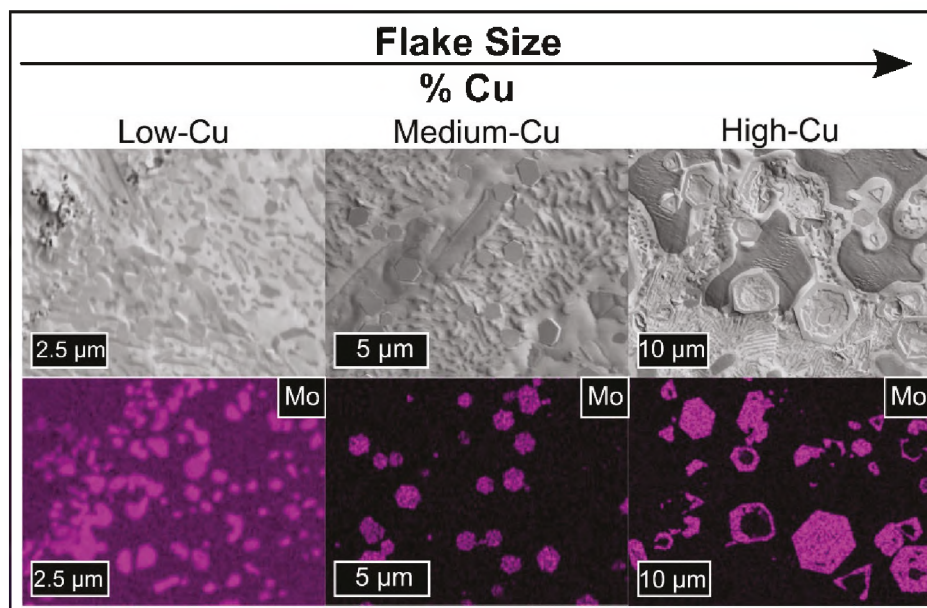


**Figure 3:** SEM images and EDS maps comparing the  $\text{Mo}_2\text{C}$  flake sizes on Low-, Medium-, and High-Cu alloys.

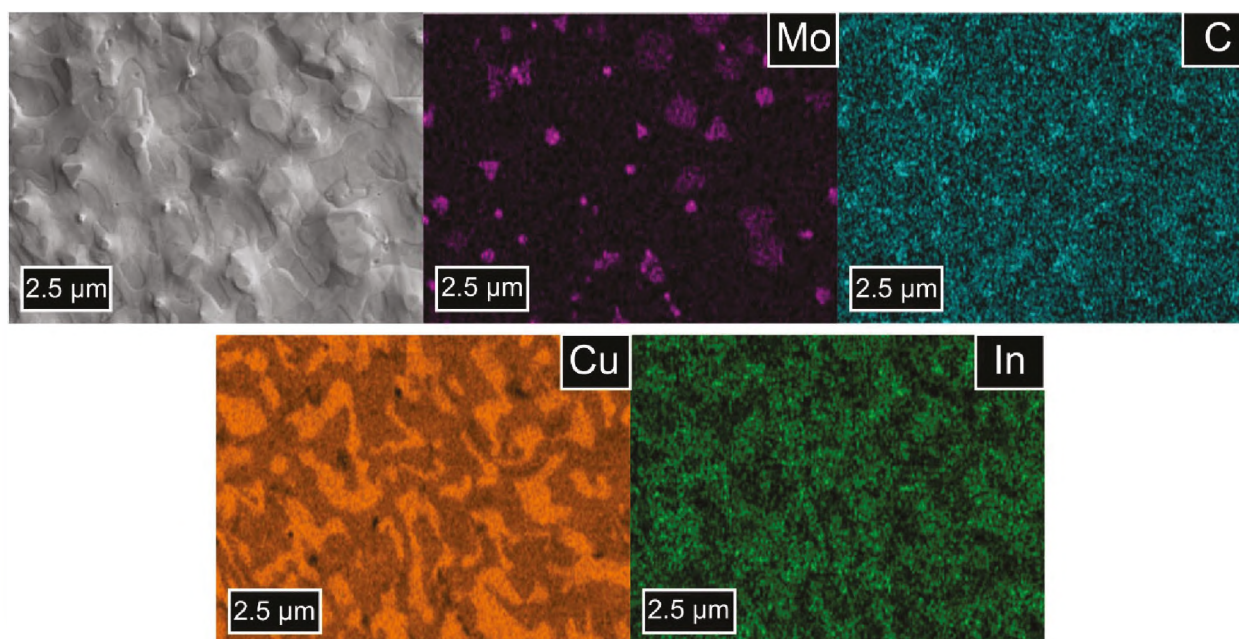


**Figure 4:**  $\text{Mo}_2\text{C}$  synthesis on an In-Cu alloy substrate at 800 °C.

Another challenge with using Cu alloy substrates for  $\text{Mo}_2\text{C}$  synthesis as a substitute for Cu-alone is that the alloy may not dehydrogenate  $\text{CH}_4$  as effectively as Cu. The inability of Ag to efficiently dehydrogenate  $\text{CH}_4$  is likely what causes a decrease in  $\text{Mo}_2\text{C}$  flake size with increasing Ag composition in the alloy substrate. Unlike Ag, In substrates have had some success in dehydrogenating  $\text{CH}_4$  for CVD graphene

synthesis. Thus, alloys with lower Cu composition could still successfully synthesize  $\text{Mo}_2\text{C}$  with large flake sizes and/or coalescence. In the case of In-Cu alloys, the melting temperature tends to decrease with increasing In composition. Thus, synthesis temperatures that are even lower than  $1000\text{ }^\circ\text{C}$  may be possible. Chaitoglou, et al., were able to synthesize  $\text{Mo}_2\text{C}$  at  $880\text{ }^\circ\text{C}$  using a Sn-Cu alloy substrate; however, no  $\text{Mo}_2\text{C}$  was synthesized at temperatures below  $880\text{ }^\circ\text{C}$ .<sup>11</sup> However, in the current study,  $\text{Mo}_2\text{C}$  was synthesized at  $800\text{ }^\circ\text{C}$  when using an alloy with 40 wt% In and 60 wt% Cu (Figure 4). Though the flakes are smaller and less coalesced, these are promising results for synthesizing two-dimensional transition metal carbides by CVD at lower temperatures.

To test the ability of the SRNL permeation system to resolve the effects of monolayer coatings on bulk substrates, permeation measurements were performed on monolayer graphene coated copper samples synthesized using CVD. Since the graphene was synthesized directly onto the Cu, the permeation experiments were able to be performed over a large area ( $16.62\text{ mm}^2$ ) without the

detrimental impact of transfer-induced tears and holes that is common in previous studies. Thus, permeation through intrinsic defects of the chemical vapor deposited graphene was probed. The graphene-coated copper showed a reduction in permeation by a factor of  $\sim 28$  compared to copper alone (Figure 5a). The permeation results were modeled with a composite permeation model where the graphene coating is in series with the Cu. The permeation through the composite system displayed surface-controlled behavior, and the graphene permeance followed Arrhenius behavior, suggesting permeation is in the activated regime. The room temperature pore permeation coefficients for the small and large grain graphene samples are  $\sim 7.0 \times 10^{-28} \pm 5.0 \times 10^{-28}$  and  $\sim 1.9 \times 10^{-27} \pm 1.4 \times 10^{-27}$  mol/s MPa, respectively, which are lower than what is normally observed in literature. The experimental results and associated modeling strongly suggest that single C vacancy intrinsic defects (Figure 5b) are limiting permeation through the graphene. Thus, the results provide a fundamental understanding of the intrinsic permeation of chemical vapor deposited graphene, as well as the use of graphene in hydrogen isotope permeation barrier applications.

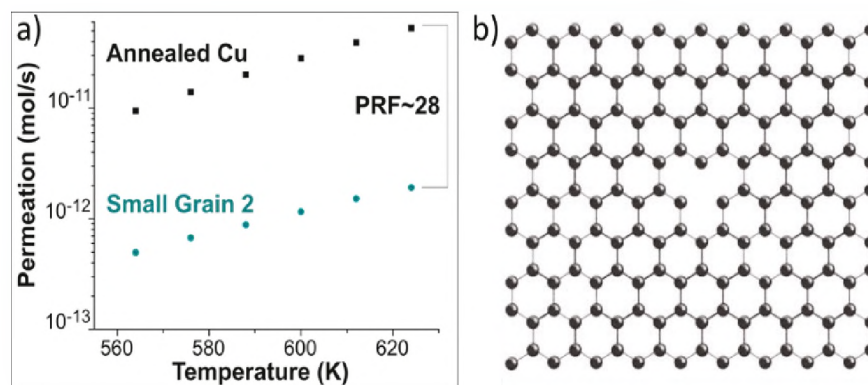


**Figure 5:** a) Comparison of the permeation data between the annealed Cu and small grain graphene. The PRF at 624 K is  $\sim 28$  and b) Schematic of a C vacancy in graphene.

## FY2020 Accomplishments

- Deposition of  $\text{Mo}_2\text{C}$  on multiple substrates
  - Deposition on Cu-In alloy at  $800\text{ }^\circ\text{C}$  is the lowest reported growth temperature for  $\text{Mo}_2\text{C}$  using CVD
- Permeation measurement system configured to work with thin film permeation barriers
- Permeation measurements performed on graphene coated Cu
  - Mention that the PRF may be the highest reported if scaled for thickness

## Future Directions

- Magnetron sputtering of MAX phase coatings
- Atomic Layer Deposition of MAX phases
- Permeation measurements on MAX phase and MXene coated substrates
- Transfer of MXenes films

## FY 2020 Peer-reviewed/Non Peer-reviewed Publications

- “The Synthesis Mechanism of Mo<sub>2</sub>C on Ag-Cu Alloy Substrates by Chemical Vapor Deposition and the Impact of Substrate Choice”, K. Young, C. Smith, D. Hitchcock, T. Walters, C. Voigt, and E. Vogel *2D Materials* **2020**, 7 (3), 035022.
- “Graphene Synthesized by Chemical Vapor Deposition as a Hydrogen Isotope Permeation Barrier” K. Young; C. Smith; T. M. Krentz; D. A. Hitchcock, and E. M. Vogel *Carbon* submitted, SRNL co-corresponding author
- “Measurement of Gas-Concentration-Driven Permeation for the Examination of Permeability, Solubility, and Diffusivity in Varying Materials” K. Young, T. Krentz, A. d'Entremont, E. Vogel, and D. Hitchcock *Review of Scientific Instruments* submitted SRNL corresponding author

## Presentations

- “The Effects of Graphene and its Defects on Hydrogen Permeation in Cu” Katie Young, MRS Fall Meeting, Boston MA Dec. 2019
- “Fusion Fuel Cycle Science and Technology” Dave Babineau, Steve Xiao, and Dale Hitchcock, Technical Seminar, MIT Plasma Science and Fusion Center, Cambridge MA Dec. 2019

## References

1. Barsoum, M. W.; Radovic, a. M., Elastic and Mechanical Properties of the MAX Phases. *Annual Review of Materials Research* **2011**, 41, 195-227.
2. Perujo, A.; Forcey, K. S., Tritium Permeation Barriers for Fusion Technology. *Fusion Engineering and Design* **1995**, 28 (2), 252-257.
3. Causey, R. A.; Karnesky, R. A.; San Marchi, C., Tritium barriers and tritium diffusion in fusion reactors. *Comprehensive Nuclear Materials* **2012**, 4, 511-549.
4. (a) Li, Q.; Wang, J.; Xiang, Q.-Y.; Tang, T.; Rao, Y.-C.; Cao, J.-L., Thickness impacts on permeation reduction factor of Er<sub>2</sub>O<sub>3</sub> hydrogen isotopes permeation barriers prepared by magnetron sputtering. *International Journal of Hydrogen Energy* **2016**, 41 (4), 3299-3306; (b) Li, Q.; Wang, J.; Xiang, Q.-Y.; Yan, K.; Yao, W.-Q.; Cao, J.-L., Study on influence factors of permeation reduction factor of Al<sub>2</sub>O<sub>3</sub>-hydrogen isotopes permeation barriers. *International Journal of Hydrogen Energy* **2016**, 41 (7), 4326-4331; (c) Nakamura, H.; Isobe, K.; Nakamichi, M.; Yamanishi, T., Evaluation of deuterium permeation reduction factor of various coatings deposited on ferritic/martensitic steels for development of tritium permeation barrier. *Fusion engineering and design* **2010**, 85 (7-9), 1531-1536; (d) Nemanič, V., Hydrogen permeation barriers: Basic requirements, materials selection, deposition methods, and quality evaluation. *Nuclear Materials and Energy* **2019**, 19, 451-457.

5. Xiang, X.; Wang, X.; Zhang, G.; Tang, T.; Lai, X., Preparation technique and alloying effect of aluminide coatings as tritium permeation barriers: a review. *International Journal of Hydrogen Energy* **2015**, *40* (9), 3697-3707.
6. (a) Conrad, R.; Debarberis, L.; V, V. C.; al, e., Irradiation of liquid breeder material Pb17Li with in situ tritium rease masurements in the LIBRETTO 2 eperiment. *Journal of Nuclear Materials* (**1991**), *179*, 875-878. ; (b) Conrad, R.; Futterer, M. A.; Giancarli, L.; al., e., LIBRETTO-3 - Performance of tritium permeation barriers under irradiation at the HFR Petten. *Journal of Nuclear Materials* **1994**, *215*, 998-1002; (c) Magielsen, A. J.; Bakker, K.; Chabrol, C.; al., e., In-pile performance of a double-walled tube and a tritium permeation barrier. *Journal of Nuclear Materials* **2002**, *307*, 832-836; (d) Proust, E.; Leroy, P.; Franenberg, H. W., Preliminary interpretation of the LIBRETTO-2 experimental results in terms of tritium permeation barrier efficiency. *Journal of Nuclear Materials* **1992**, *191*, 186-189.
7. (a) al., E. N. H. e., MAX phase carbides and nitrides: Properties for future nuclear power plant in-core applications and neutron transmutation analysis. *Nuclear Engineering and Design* **2012**, *244*, 17-24; (b) al., D. J. T. e., Effect of neutron irradiation on select MAX phases. *Acta Materialia* **2015**, *85*, 32-143.
8. Zhe Kang, Z. Z., Helin Wei, Zhi Zhang, Xinyu Tan, Lun Xiong, Tianyou Zhai, and Yihua Gao, Controlled Growth of an Mo2C—Graphene Hybrid Film as an Electrode in Self-Powered Two-Sided Mo2C—Graphene/Sb2S0.42Se2.58/TiO2 Photodetectors. *Sensors (Basel)* **2019**, *15* (5).
9. Chaitoglou S, G. T., Speliotis A, Vavouliotis A, Trapalis C and Dimoulas A Mo2C/graphene heterostructures: low temperature chemical vapor deposition on liquid bimetallic Sn-Cu and hydrogen evolution reaction electrocatalytic properties *Nanotechnology* **2019** *30*
10. Katherine T Young, C. S., Dale A Hitchcock, Todd Walters, Cooper Voigt and Eric M Vogel, The synthesis mechanism of Mo2C on Ag-Cu alloy substrates by chemical vapor deposition and the impact of substrate choice. *2D Materials* **2019**, *7* (3).
11. Stefanos Chaitoglou, T. G., Thanassis Speliotis, Antonios Vavouliotis, Christos Trapalis, Athanasios Dimoulas, Mo2C/graphene heterostructures: low temperature chemical vapor deposition on liquid bimetallic Sn—Cu and hydrogen evolution reaction electrocatalytic properties. *Nanotechnology* **2019**, *30* (12), 125401.

## Acronyms

CVD	Chemical Vapor Deposition
HIPB	Hydrogen Isotope Permeation Barriers
PRF	Permeation Reduction Factor
TPBAR	Tritium Producing Burnable Absorbing Rods

## Student Researchers

Graduate student Katie Young, Georgia Institute of Technology

## External Collaborators

Dr. Eric Vogel, Department of Materials Science and Engineering, Georgia Institute of Technology

## Solid State Ionics: Materials Development by Multiscale Modeling and Advanced Manufacturing Techniques

**Project Team:** Lindsay Roy and Dale Hitchcock

**Clemson University Collaborators:** Kyle Brinkman, Lindsay Shuller-Nickles

**Project Start Date:** October 1, 2019

**Project End Date:** September 30, 2021

*Solid-state ionic materials are an important enabling technology for energy conversion and storage. Solid-state batteries would be a safer and higher energy density alternative to commercially available lithium ion batteries (LIB), however their implementation requires ion conduction in solids at room temperature to occur on the same level as the current generation of liquid electrolytes. Microstructural modifications have been demonstrated to play a major role on ion transport through the control of grain boundary interfaces, which*

*traditionally serve as “blocking” layers. Ultimately, these materials will be fabricated in thin films form as electrolytes in order to minimize ohmic losses in electrochemical devices. This work uses advanced manufacturing techniques (e.g., 3D printing followed laser processing) in combination with theoretical modeling to implement a science-based approach in the deposition of thin films ion conductors with controlled microstructures used in ceramic energy conversion and storage devices.*

### FY2020 Objectives

- Synthesis and densification of bulk and doped LLZO materials, and solid-state laser sintering thin films of doped LLZO
- Experimental thermochemical characterization, structural characterization of doped LLZO
- Computational thermodynamic stability and structure evaluation of bulk and doped LLZO
- Defect incorporation and mobility calculations in LLZO

### Introduction

Solid-state ionic materials are an important enabling technology for energy conversion and storage. Solid-state batteries would be a safer and higher energy density alternative to commercially available lithium ion batteries (LIB), however their implementation requires ion conduction in solids at room temperature to occur on the same level as the current generation of liquid electrolytes. Microstructural modifications have been demonstrated to play a major role on ion transport through the control of grain boundary interfaces, which traditionally serve as “blocking” layers. Ultimately, these materials will be fabricated in thin films form as electrolytes in order to minimize ohmic losses in electrochemical devices. This work uses advanced manufacturing techniques (e.g., 3D printing followed laser processing) in combination with theoretical modeling to implement a science-based approach in the deposition of thin films ion conductors with controlled microstructures used in ceramic energy conversion and storage devices.

Specific focus has been on dopants in the garnet-like structure  $\text{Li}_7\text{La}_3\text{Zr}_2\text{O}_{12}$  (LLZO).<sup>1</sup> The thermodynamically stable tetragonal phase of LLZO exhibits relatively low  $\text{Li}^+$  conductivity, but dopants such as  $\text{Ga}^{3+}$  in the Li sites or  $\text{Ta}^{5+}$  in the Zr sites stabilize a cubic phase of LLZO, resulting in increased Li vacancies for charge compensation and conductivity by two orders of magnitude.<sup>2,3</sup> However, preparation of dopant LLZO materials remains challenging because conductivity is dependent upon the dopant concentration in the structure and conditions to suppress Li sublimation during sintering are dependent upon variables that are difficult to quantify or control. In order to overcome these challenges, research this year focused on tailoring the appropriate microstructure with fast manufacturing techniques and computational evaluations to enable significant progress toward understanding and controlling the

microstructure of LLZO. Specifically, results have shown that advanced quantum calculations can predict the precise dopant concentration necessary for rapid Li<sup>+</sup> migration and techniques such as solid-state reactive sintering (SSRS) enable enhanced materials processing at lower temperatures.

Overall, this project addresses key scientific issues identified by the Department of Energy (DOE) – Basic Energy Science (BES), Fusion Energy Science (FES) and Energy Efficiency and Renewable Energy (EERE) program that limit the present understanding and implementation of solid state ionic materials and devices in separations and energy conversion and storage applications. The key issues include an understanding of ionic transport in the bulk of materials and across interfaces (grain boundaries, surfaces and layers of functional devices) by experimental and computational methods. Since polycrystalline material microstructures are likely to dominate low cost and scalable energy conversion devices, an understanding and ability to tailor the appropriate microstructure with fast manufacturing routes is essential to the development and implementation of new materials.

## Approach

This project incorporates a three-pronged approach as summarized in Figure 1. Task A focuses on novel synthetic and characterization methods such as solid-state reaction synthesis (SSRS) and solution combustion synthesis (SCS) for rapid and efficient materials production. Task B utilizes quantum mechanical calculations to help inform the experimental thrust by correlating thermodynamic stability of doped LLZO with observables such as X-ray diffraction (XRD) and X-ray absorption spectroscopy. Task C sets out to fabricate 3D thin films of dense and doped LLZO followed by rapid laser sintering. Each box represents a subtask in the project and the items highlighted in green were completed this FY while those in light green are in progress.

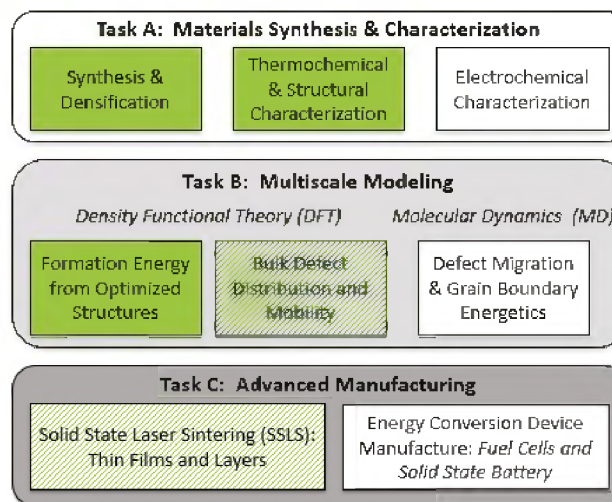


**Figure 1:** Pictorial representation of the approach used in this project.

## Results/Discussion

The synthesis of single-phase cubic LLZO powder is complicated by the high volatility of Li. Solid-state ceramic processing, which involves the mixing, milling, and calcination of oxide and/or carbonate precursors, is a well-established and relatively simple technique that is highly amenable to up-scaling and mass production. However, the lack of intermixing on the molecular level (when compared to wet chemical routes) leads to an increase in the atomic diffusion distance necessary for crystallization. To overcome the larger diffusion distance and ensure adequate crystallinity, higher calcination temperatures are often needed. Such elevated temperatures serve to enhance Li loss and increase the percentage of lower conductivity secondary phases (e.g., La<sub>2</sub>Zr<sub>2</sub>O<sub>7</sub>) in the final product. These difficulties have spurred research into the synthesis of cubic LLZO by wet chemistry techniques, which have the advantages of excellent cation intermixing and a reduction in Li loss due to the lower peak temperatures necessary for crystallization.

In this work, the feasibility of synthesizing single-phase cubic LLZO via SCS without the need for extensive post-annealing was investigated. SCS involves the initiation of a thermodynamically favorable, self-sustaining redox reaction between metal nitrates (oxidizers) and suitable fuels. The intermixing of molecular components in solution allows for excellent compositional control, while the simplicity of the process facilitates ease of scalability and the use of modular components. Preliminary experiments to synthesize LLZO were conducted with cation nitrates as oxidizers and urea as the fuel. In a typical procedure, an aqueous solution of lanthanum nitrate hexahydrate ( $\text{La}(\text{NO}_3)_3 \cdot 6\text{H}_2\text{O}$ ), zirconium(IV) nitrate pentahydrate ( $\text{Zr}(\text{NO}_3)_4 \cdot 5\text{H}_2\text{O}$ ), and urea was first prepared by magnetic stirring at 80 °C for 1 h. Trivalent nitrates (e.g., Ga, Al) were also introduced into the La/Zr nitrate solution for doped LLZO compositions. Anhydrous  $\text{LiNO}_3$  was then weighed out in a glovebox according to the targeted LLZO stoichiometry; various excess amounts of  $\text{LiNO}_3$  were utilized in certain experiments to account for any loss of Li during processing. Here, the desired mass of  $\text{LiNO}_3$  removed from the glovebox and dissolved in DI water, at which point urea was added. Ultimately, the two separate nitrate-urea mixtures were combined into one solution and allowed to stir on a hot plate at 80 °C to yield an SCS precursor. The starting LLZO precursors were then either used directly in liquid form or evaporated to a gel prior to combustion. Direct microwave heating of the precursors in quartz vials was utilized to induce combustion. Both undoped and Ga-doped LLZO synthesized by SCS displayed a high-symmetry cubic phase and a secondary pyrochlore phase  $\text{La}_2\text{Zr}_2\text{O}_7$ . Figure 2 shows an XRD spectrum for Ga-doped LLZO powder grown using SCS. Optimization of processing parameters and re-design of experiment are needed to produce a single phase LLZO via microwave SCS.

Experimental results demonstrated that Tantalum doped LLZO powders can be densified by Spark Plasma Sintering (SPS). Powders were purchased from Ampcera with two different particle sizes 150mesh (<5 microns) and ~100um. Due to the volatility of Li the heating rate was maintained below 100 C/min to avoid off gassing. Initial tests were performed with the small particle size material because literature results suggest sinterability and particle size are inversely related for LLZO. Tests using the smaller particle size material all displayed significant off gassing during heating which led to several runs being aborted early. Tests with the larger particle size powder showed much less off gassing and were therefore the basis of the remainder of the studies. Samples were successfully densified using 950 and 1000C in less than 30 minutes. The rapid densification at relatively low temperatures suggests that SPS may be a promising technique for the densification of LLZO powders.

Experimental results showed that the SSRS process and the addition of CuO were beneficial for the preparation of dense Ta-doped LLZO electrolytes. Applying the SSRS process and adding 1 wt% CuO lowered the sintering temperature for LLZTO pellets with over 90% density from 1250°C to 1100°C. Whereas 5 wt% CuO additions resulted in the appearance of Cu-related secondary phases, 1 wt% CuO

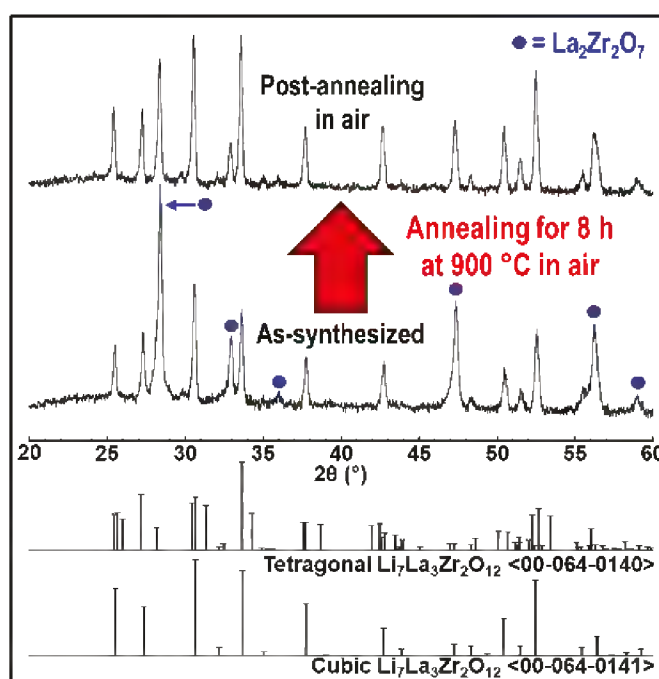


**Figure 2:** XRD pattern of as-synthesized Ga-doped powder shows two-phase structure consisting of cubic LLZO and  $\text{La}_2\text{Zr}_2\text{O}_7$  pyrochlore.

additions resulted in no secondary phases detected at the XRD level and no electronic conduction below 100°C. Table 1 shows excellent conductivity for 1 wt% CuO-mixed Ta-doped LLZO pellets. The formation of the  $K_2NiF_4$ -type  $La_2Cu_{0.5}Li_{0.5}O_4$  intermediate phase during heating indicates that CuO works as a sintering aid by enabling liquid-phase sintering and promoting the decomposition of LiOH. The combined SSRS process along with optimized CuO sintering aid addition is a one-step process that is a practical technique to enhance the preparation of LLZO-based electrolyte for all-solid-state lithium-ion batteries.

**Table 1.** Temperature-dependent AC/DC conductivities and transference numbers of the 1 wt% CuO-mixed LLZTO pellet sintered at 1100 C and 2 wt% CuO-mixed LLZWO reported by Zhang and Sun. <sup>4</sup>

Materials	Temperature (°C)	AC total conductivity ( $S \cdot cm^{-1}$ )	DC conductivity ( $S \cdot cm^{-1}$ )	Li <sup>+</sup> transference number
1wt% CuO-mixed LLZTO (this work)	25	$1.06 \times 10^{-4}$	$< 5.70 \times 10^{-6}$	1.00
	50	$3.62 \times 10^{-4}$	$< 5.70 \times 10^{-6}$	1.00
	100	$2.51 \times 10^{-3}$	$< 5.70 \times 10^{-6}$	1.00
	150	$1.29 \times 10^{-2}$	$7.47 \times 10^{-5}$	0.994
	200	$3.16 \times 10^{-2}$	$2.36 \times 10^{-4}$	0.993
2wt% CuO-mixed LLZWO (Zhang and Sum)	25	$1.88 \times 10^{-4}$	$1.338 \times 10^{-8}$	1.00

Computational work consisted of identifying initial configurations for cubic LLZO where the partially occupied model utilized Ga and Ta as the dopant. In the Ga-doped models, we employed a supercell program written by Okhotnikov et al. to determine the total coulomb interactions of the structure. <sup>5</sup> The supercell approach can be applied for very large and complex system for approximation of materials with point disorder. In addition, it can derive multiple structures with desired properties such as creating each individual structure with different coulomb energy. In this case, 24 possible structures were identified based on the substitution of Li for Ga

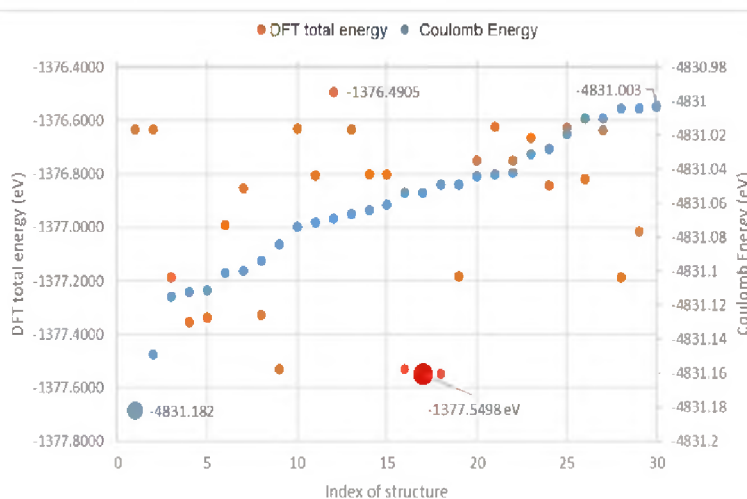


**Figure 3:** The relation between coulomb energy in supercell program and DFT total energy in 30 Li1-11 models with minimized coulomb energy.

in the Li1 site. Then, based on the Ga occupancy, 30 structures with the minimized coulomb energy were investigated in DFT total energy analysis. From the finding the change of total energy is quite small, the gap between the highest and minimized total energy is 0.9018 eV. The minimized total energy from the DFT modeling is structure index #17 with a total energy of -1377.5498 eV (Figure 3). In Ta-doped models, several dopant concentrations were calculated and formation greater than 50% showed very little change in the cubic structure, suggesting higher Ta concentrations may enable facile Li+ transport within the material (Figure 4).

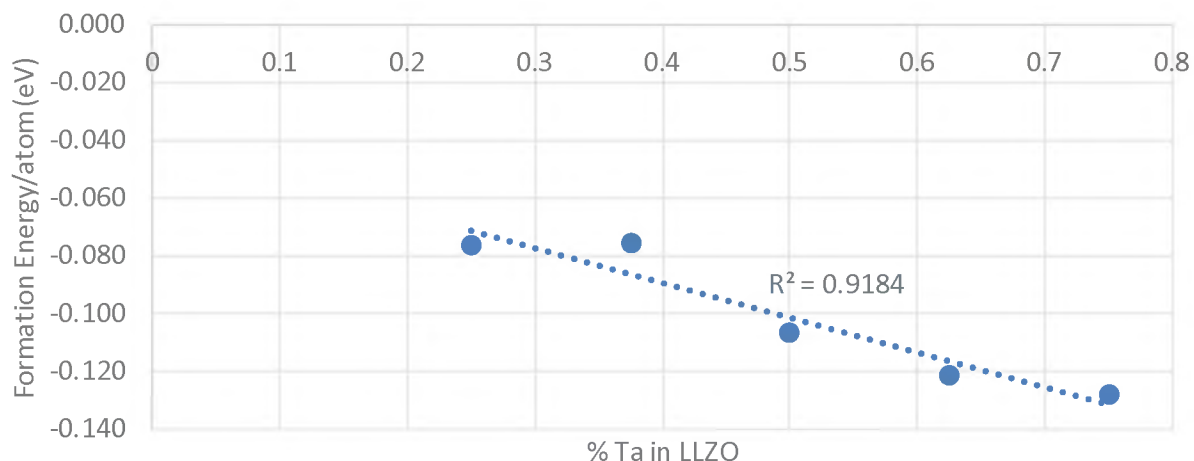


**Figure 4:** DFT-calculated formation energy/atom vs. %Ta in LLZO.

## FY2020 Accomplishments

As mentioned earlier, project work was divided into three tasks to show progress in all areas, outlined below along with their milestones for FY20. Results and accomplishments are presented under each milestone:

- TaskA: Materials Synthesis and Characterization
  - M1: Synthesis and densification of bulk materials and solid-state laser sintering thin films (Feb 2020)
    - TMS conference presentation: “Protonic Ceramic Fuel Cells and Solid-State Ionics: Materials and Device Development”
    - Microwave solution combustion synthesis (SCS) of pure and Ga-doped LLZO led to a high-symmetry cubic phase and a secondary pyrochlore phase  $\text{La}_2\text{Zr}_2\text{O}_7$ . Optimization of processing parameters and re-design of experiment are needed to produce a single phase LLZO via microwave SCS
  - M2: Experimental thermochemical characterization, structural characterization (June 2020)
    - Manuscript accepted at Journal of Materials Science: “Solid-State Reactive Sintering of Dense and Highly Conductive Ta-Doped  $\text{Li}_7\text{La}_3\text{Zr}_2\text{O}_{12}$  Using CuO as a Sintering Aid”. Pure and CuO-mixed Ta-doped LLZO was prepared via conventional and solid-state reactive sintering (SSRS). Results show that SSRS and CuO were effective in decreasing the sintering temperature and providing high conductivity

- Task B: Multiscale Modeling
  - M3: Computational thermodynamic stability and structure evaluation (June 2020)
    - Drafted peer-reviewed manuscript to be submitted August 2020. Paper identified dozens of Li-ion configurations in undoped and Ga-doped LLZO, quantified enthalpy of formation and reaction energies with respect to solid-state Ga concentration, probed the onset of nano-domain formation and potential for phase separation at high Ga concentration (conclusion pending final results)
    - Peer-reviewed manuscript in preparation to be submitted December 2020. Paper will outline the computed energies and structural changes within the Ta-doped LLZO ranging from 25% to 75%. Systems doped around 50% Ta retain the symmetry needed for facile Li<sup>+</sup> mobility; higher doped systems are lower in energy but break the necessary symmetry needed for Li<sup>+</sup> mobility
- Task C: Advanced Manufacturing
  - M4: Defect incorporation and mobility calculations (Ongoing - March 2021)
    - Initial calculations on Li<sup>+</sup> mobility in 50% Ta-doped LLZO suggest a low energy barrier of ~4 eV
    - Initial experimental work shows laser sintering of Ta-doped LLZO films have a relative density of ~98%

## Future Directions

Next year will focus on continued parallel execution of the various tasks, as listed below:

- Task A: Materials Synthesis and Characterization
  - Microwave SCS of pure cubic phase LLZO
  - Electrochemical characterization of bulk and laser sintered LLZO
- Task B: Multiscale Modeling
  - Bulk defect incorporation and Li<sup>+</sup> ion mobility calculations
  - Defect migration and grain boundary energetics
- Task C: Advanced Manufacturing
  - Solid state laser sintering of Ga-doped and Ta-doped LLZO
  - Energy conversion device manufacturing

## FY 2020 Peer-reviewed/Non Peer-reviewed Publications

- “Solid-state reactive sintering of dense and highly conductive Ta-doped Li<sub>7</sub>La<sub>3</sub>Zr<sub>2</sub>O<sub>12</sub> using CuO as a sintering aid,” Changlong Li, Akihiro Ishii, Lindsay Roy, Dale Hitchcock, Yuqing Meng, Kyle Brinkman, Journal of Materials Science, accepted for publication, Clemson lead institution.
- “Thermodynamic stability and Li<sup>+</sup>/vacancy distribution of Ga-doped LLZO: Insight into dopant-enhanced Li<sup>+</sup> mobility,” Changlong Li, Lindsay Roy, and Lindsay Shuller-Nickles, manuscript in preparation, Clemson lead institution.

## Presentations

“Protonic ceramic fuel cells and solid state ionics: Materials and device development,” Akihiro Ishii and Kyle Brinkman, Invited talk at TMS Conference, San Diego, CA, Feb 2020.

## References

1. Han, F.; Zhu, Y.; He, X.; Mo, Y.; Wang, C., Electrochemical Stability of  $\text{Li}_{10}\text{GeP}_2\text{S}_{12}$  and  $\text{Li}_7\text{La}_3\text{Zr}_2\text{O}_{12}$  Solid Electrolytes. *Advanced Energy Materials* **2016**, 6 (8), 1501590.
2. Wagner, R.; Redhammer, G. J.; Rettenwander, D.; Senyshyn, A.; Schmidt, W.; Wilkening, M.; Amthauer, G., Crystal Structure of Garnet-Related Li-Ion Conductor  $\text{Li}_{7-3x}\text{Ga}_x\text{La}_3\text{Zr}_2\text{O}_{12}$ : Fast Li-Ion Conduction Caused by a Different Cubic Modification? *Chem. Mater.* **2016**, 28 (6), 1861-1871.
3. Gu, W.; Ezbiri, M.; Prasada Rao, R.; Avdeev, M.; Adams, S., Effects of penta- and trivalent dopants on structure and conductivity of  $\text{Li}_7\text{La}_3\text{Zr}_2\text{O}_{12}$ . *Solid State Ionics* **2015**, 274, 100-105.
4. Zhang, W.; Sun, C., Effects of CuO on the microstructure and electrochemical properties of garnet-type  $\text{Li}_{6.3}\text{La}_3\text{Zr}_{1.65}\text{W}_{0.35}\text{O}_{12}$  solid electrolyte. *J. Phys. Chem. Solids* **2019**, 135, 109080.
5. Okhotnikov, K.; Charpentier, T.; Cadars, S., Supercell program: a combinatorial structure-generation approach for the local-level modeling of atomic substitutions and partial occupancies in crystals. *Journal of Cheminformatics* **2016**, 8 (1), 17.

## Acronyms

DFT	Density functional theory
Ga	Gallium
LLZO	Lithium lanthanum zirconium oxide $\text{Li}_7\text{La}_3\text{Zr}_2\text{O}_{12}$
LLZTO	Lithium lanthanum zirconium tantalum oxide $\text{Li}_{6.5}\text{La}_3\text{Zr}_{1.5}\text{Ta}_{0.5}\text{O}_{12}$
LLZWO	Lithium lanthanum zirconium tungsten oxide $\text{Li}_{6.3}\text{La}_3\text{Zr}_{1.4}\text{W}_{0.35}\text{O}_{12}$
SCS	Solution combustion synthesis
SPS	Spark plasma sintering
SSRS	Solid-state reactive synthesis
Ta	Tantalum
XRD	X-ray diffraction

## Post-Doctoral Researchers

Akihiro Ishii, Clemson University, Advisor K. Brinkman

## Student Researchers

Changlong Li, Clemson University, Advisors K. Brinkman and L. Shuller-Nickles

## Robust, High-energy Density Supercapacitors for Portable Energy Storage

**Project Team:** Jay Gaillard, Héctor Colón-Mercado, Mark Elvington, Spencer Tinky, Aaron Lando

**Project Start Date:** October 1, 2019

**Project End Date:** August 14, 2020

The 2017 DOE BES Workshop on Basic Research Needs for Electric Energy Storage (EES)<sup>1</sup> concluded that supercapacitor (SC) research, in parallel with battery research, is a critical area for meeting future EES needs. The technology is needed to improve the resiliency and reliability of “critical facilities” such as transportation, communications, and emergency response infrastructure. The US Army have already begun

exploring flexible supercapacitors as a means to supply energy for battery applications such as wearable electronics, soldier-borne energy-harvesting technologies, and exoskeleton power/control electronics due to their high-power density, long lifetimes (~20-100 years), and fast charging (~60-120 secs). Although power density for most SCs is enormous, broad application of these devices has suffered from low energy density. To solve this problem, SRNL pursued concepts to significantly increase energy density while retaining high power output. The work was performed in partnership with an already funded team between Mainland Solutions (MS) and the Army’s Natick Soldier Research, Development and Engineering Center (NSRDEC). SRNL intended to investigate localized ion/electron charge distribution and charge-compensation behavior of high surface area nanoporous MnO<sub>2</sub> coated graphene/nanotube hybrids with the goal of translating the scientific mechanisms to enhanced energy density in device-level portable EES for ensuring energy security and developing portable EES for soldiers.

### FY2020 Objective

- Produce SCs with specific capacitance >500 F/g

### Introduction

Supercapacitors, or electro-chemical double layer capacitors (EDLCs), are expected to play a significant role in future power systems (as both in use with batteries or as the battery) due to:

- *Low equivalent series resistance (ESR).* Compared to batteries, EDLCs have a low internal resistance, hence providing high power density capability (Figure 1)
- *Low temperature performance.* They are capable of delivering energy down to -40°C
- *Fast charge/discharge.* Due to extraordinarily low ESR which is not available with conventional batteries
- *Long lifetimes.* SCs have very long lifetimes (~20-100 years) with no maintenance and high durability

To impact the development of future energy storage, supercapacitors require improvements in one key metric: energy density. Purely graphitic or graphene-like materials have shown great promise as the SC active layer but has yet to get close to battery-like energy density. Leveraging previous SC research at SRNL, our team’s proposed solution was to add pseudocapacitive metal oxides coatings (e.g., MnO<sub>2</sub> - 1380 F/g theoretical capacitance – values that would provide battery-like energy density) onto graphitic

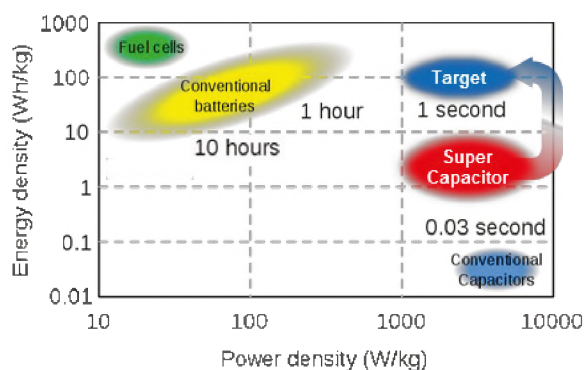


**Figure 1:** Ragone chart showing general performance target.<sup>2</sup>

nanocarbon supports such as *edge-rich graphene*. Combining these materials hold the potential for high energy density SCs with stable, long-lifetime operation.<sup>2</sup>

**Edge-rich graphene:** It was shown experimentally<sup>3</sup> that the graphene edge has specific areal capacitance 5 orders of magnitude ( $10^5 \mu\text{F}/\text{cm}^2$ ) larger than the basal plane ( $4 \mu\text{F}/\text{cm}^2$ ). Experimentally unzipped 30-nm multi-walled carbon nanotubes (MWCNTs) as the SC electrode material (Figure. 2-bottom) at SRNL<sup>4</sup> showed more than 100X higher maximum specific capacitance and more than 10X higher specific energy than the original nanotubes (after 25 cycles at 2 mV/s with 1M TEABF<sub>4</sub> in acetonitrile electrolyte).

**Pseudocapacitive coatings:** Theoretical pseudocapacitance of metal oxides is very high, with values such as 1380, 2120, 2584, 3560 F g<sup>-1</sup> for MnO<sub>2</sub>, V<sub>2</sub>O<sub>5</sub>, NiO, Co<sub>3</sub>O<sub>4</sub>, respectively. However, the demonstrated practical capacitances are far lower ( $\sim 10$ -400 F g<sup>-1</sup>) due to limitations such as low conductivity, low surface area and porosity, and poor long-term stability. For these reasons, many studies of pseudocapacitive materials have focused on coating small particles or thin layers of the material onto conductive carbon frameworks to mitigate these effects. For example, Li *et al.* prepared MnO<sub>2</sub>-MWCNTs composites through a modified one-pot reaction process.<sup>5</sup> The cross-linked MnO<sub>2</sub> nanoflakes-MWCNTs structure showed a good specific capacitance of 201 F g<sup>-1</sup> and good cycle stability (no obvious decay after 10,000 cycles). Nanocomposites of V<sub>2</sub>O<sub>5</sub> nanowires and MWCNTs<sup>6</sup> showed a specific capacitance peaked at 530 F g<sup>-1</sup> when loaded at 33 wt% MWCNTs compared to solely V<sub>2</sub>O<sub>5</sub> nanowires (146 F g<sup>-1</sup>). Wang *et al.* prepared a Co<sub>3</sub>O<sub>4</sub>@MWCNT nanocable using MWCNTs as the core cable.<sup>7</sup> Compared to the pristine Co<sub>3</sub>O<sub>4</sub>, with a low specific capacitance less than 130 F g<sup>-1</sup>, the prepared Co<sub>3</sub>O<sub>4</sub>@MWCNT nanocomposite showed a specific capacitance of 590 F g<sup>-1</sup> at 15 A g<sup>-1</sup> and 510 F g<sup>-1</sup> at 100 A g<sup>-1</sup>.

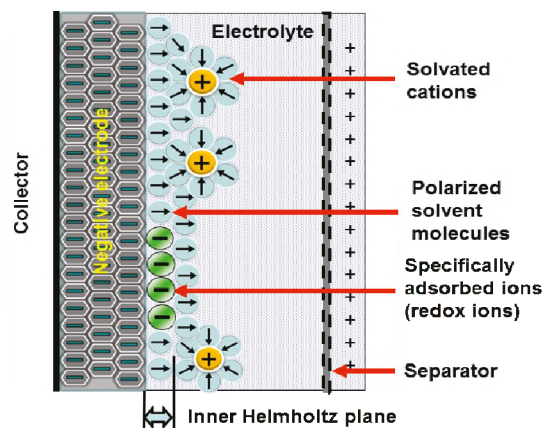


**Figure 2:** Faradaic charge-transfer of pseudocapacitance (may contribute 100x capacitance as compared to the double-layer<sup>2</sup>).

## Approach

In this project, we combined two promising avenues for increasing energy density ( $E = CV^2$ ): (1) maximizing EDLC capacitance (C) via high-surface-area, edge-rich graphene electrode frameworks with porous high surface area pseudocapacitive metal oxide (e.g. MnO<sub>2</sub>) coatings (little scientific research has focused on increased metal oxide surface area) and (2) investigated low viscosity ionic liquids (ILs) for high operating voltage (V) and high ion mobility. In order to achieve the above objectives, the following tasks were followed:

- **Task 1: SElectrode material synthesis/fabrication** – The primary technical challenge in the proposed work was to develop methods to incorporate the metal oxide onto 1D carbon nanomaterial with 3D surface structures with sharp edges (e.g., see Fig. 3), high surface areas, and optimal pores. We synthesized expanded CNT/MnO<sub>2</sub> hybrid materials for producing new architectures by metal oxide coating the expanded CNTs followed by activation techniques to increase surface area. Importantly, we explored techniques to add nanopore structure on the metal oxide surface. Specifically, we investigated chemical etching of the MnO<sub>2</sub> surface using etchants such as ceric ammonium nitrate and sulfuric acid to increase specific surface area. MnO<sub>2</sub> was chosen as the metal oxide due to its good chemical and thermal stability, natural abundance, environmental benignity and low cost.

- **Task 2: SC testing in organic and ionic liquid electrolytes** – Ionic liquids offer several advantages, including high ionic conductivity (up to  $10^{-2}$  S  $\text{cm}^{-1}$ ), large liquid phase range ( $-100$ – $400$  °C), wide electrochemical window (4–6V). We first used organic electrolytes (SRNL has recently used 1M TEABF<sub>4</sub> in acetonitrile and ethylene carbonate) to screen the electrode performance, then ionic liquids (particularly imidazolium tetrafluoroborate), and IL diluted with ethylene carbonate (reduce viscosity).
- **Task 3: Characterization** – Materials and synthesis methods were characterized using high resolution scanning electron microscopy, Raman and Fast-Fourier transform spectroscopy, high resolution transmission spectroscopy, and BET specific surface area along with 3-electrode rotating disk measurements.

## Results/Discussion

Work executed during the project focused on supercapacitive material synthesis/fabrication and characterization of these materials. Pseudocapacitive metal oxides (e.g. MnO<sub>2</sub>, RuO<sub>2</sub>, NiMoO<sub>4</sub>, Ni(OH)<sub>2</sub>)

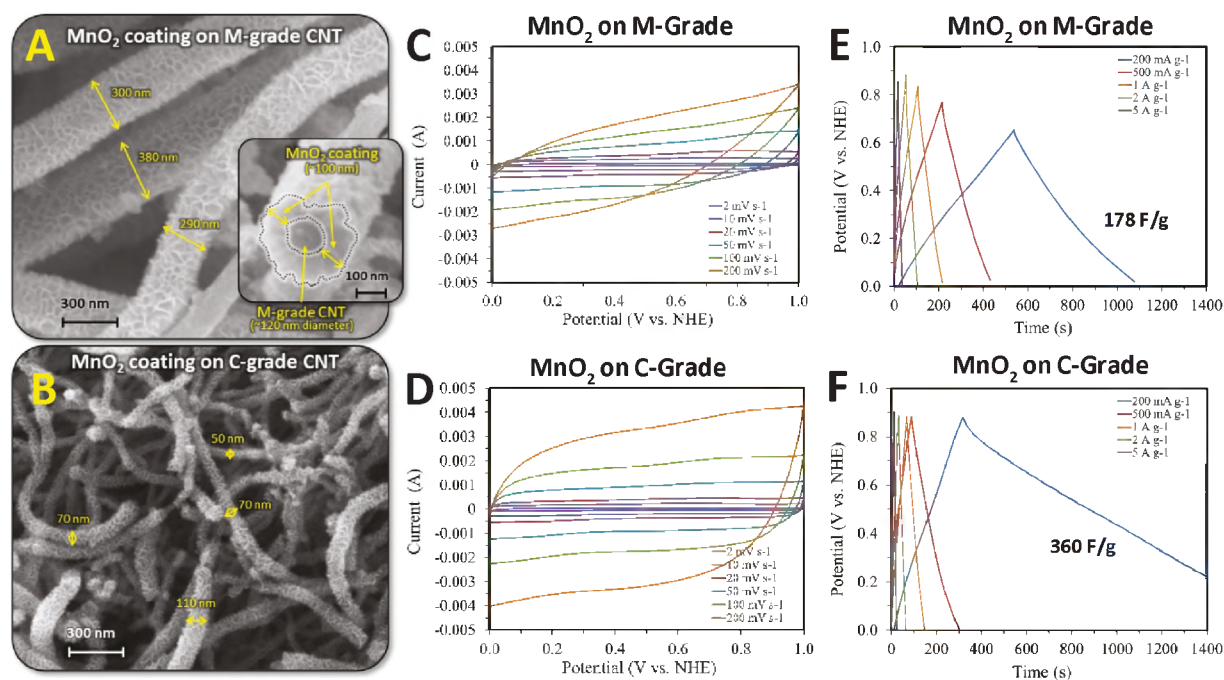


**Figure 3:** SEM images of MnO<sub>2</sub> on (A) large diameter M-grade CNTs, (B) small diameter C-grade CNT; cyclic voltammetry measurements for (C) large diameter M-grade CNTs, (D) small diameter C-grade CNTs; three electrode constant current charge/discharge capacitive electrochemical measurements for (E) large diameter M-grade CNTs, (F) small diameter C-grade CNT.

and their composites were successfully synthesized on expanded CNTs, M-grade and C-grade MWCNTs. Novel MnO<sub>2</sub>/carbon composites composed of a MnO<sub>2</sub> nanoarchitected coating on (i) large diameter CNTs (M-grade; ~120 nm diameter) (ii) small diameter CNTs (C-grade; ~30 nm diameter) and (iii) expanded nanotubes (large diameter CNTs following thermal exfoliation) were prepared. SEM images show a comparison of the MnO<sub>2</sub>/CNT composites including a cross-section analysis to determine layer thickness. The images show MnO<sub>2</sub> coatings of ~90 to 140 nm and ~10 to 40 nm thick on the large and small diameter CNTs, respectively (Figure 3A and 3B). This equates to average MnO<sub>2</sub>/C mass ratios of 12.0 and 10.1 for the large and small diameter CNTs. Coating thickness influences both specific capacitance and power

density. Due to the relatively poor conductivities within the metal oxide layer, it is important to incorporate the maximum utilizable volume of  $\text{MnO}_2$  without overloading, which would result in electrically inaccessible material creating “dead weight” and thus lowering specific capacitance, while also reducing conductivity and therefore power density as well. Even with similar mass loadings of  $\text{MnO}_2$  for the two CNT composites, the  $\text{MnO}_2$  on C-grade cyclic voltammogram shows superior conductivity (Figure 3C and 3D) and specific capacitance, 360 F/g compared to 178 F/g at 200 mA/g (Figure 3E and 3F), which is not unexpected considering the shorter average pathlength from the  $\text{MnO}_2$  redox site and the CNT current collector. The cross section and electrochemical analyses can be used to guide future loading optimization. Finally, we report on the  $\text{MnO}_2$ /expanded nanotube composite. Figure 4 shows an SEM image of the  $\text{MnO}_2$  coated composite, which clearly shows the signature  $\text{MnO}_2$  nanoarchitecture, with an inset showing the initial seeding of an individual carbon nanoribbon. This prospective pseudocapacitive material shows promise due to the high surface area of the base material ( $\sim 500 \text{ m}^2/\text{g}$ ) combined with the 1D macroscale nature of the expanded nanotube, meaning it retains high long-distance electron mobility like a wire. Future work will analyze the morphological and electrochemical characteristics and optimize the  $\text{MnO}_2$  loading.

Other metal oxides investigated during the project include  $\text{RuO}_2$ ,  $\text{NiMoO}_4$ , and  $\text{Ni}(\text{OH})_2$ .  $\text{RuO}_2$  showed an excellent specific capacitance of  $\sim 600 \text{ F/g}$  (Figure 5A). Future work will include preparing  $\text{RuO}_2$ /carbon composites to increase specific capacitance and power density. A solution combustion synthesis (SCS) approach was used to fabricate  $\text{NiMoO}_4$  nanoparticles. Using combustion synthesis avoids the need for calcination and is a faster synthesis method overall compared to the sol-gel and hydrothermal synthesis methods. Figure 5B shows the Cyclic Voltage curve of the synthesized  $\text{NiMoO}_4$  with the distinct pseudocapacitive oxidation and reduction peaks equating to a specific capacitance of 136 F/g. Future work for  $\text{NiMoO}_4$  includes using the solution combustion synthesis approach to prepare  $\text{NiMoO}_4$  in the presence of a combustion inert support such as an  $\text{MnO}_2$  coated C-grade CNTs. This composite is expected to take advantage of the high conductivity of the  $\text{MnO}_2$ /C-grade composites as a 3D-architected support and the high theoretical capacitance of the  $\text{NiMoO}_4$ .

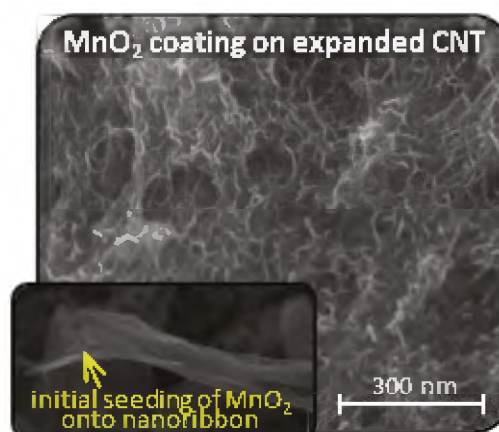


Figure 4: SEM images of  $\text{MnO}_2$  on ribbon portion of expanded nanotube.

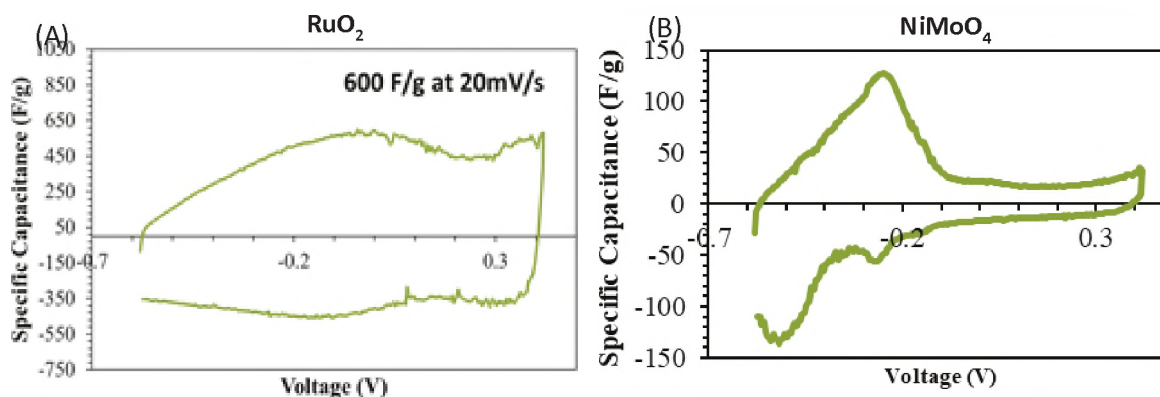


Figure 5: Cyclic voltammetry measurements for (A)  $\text{RuO}_2$  unsupported, (B)  $\text{NiMoO}_4$  unsupported, at 20 mV/s.

## FY2020 Accomplishments

- Achieved 600 F/g specific capacitance with RuO<sub>2</sub>
- Successfully synthesized MnO<sub>2</sub> on large diameter CNTs, small diameter CNTs and expanded nanotubes
- Successful synthesis of NiMoO<sub>4</sub> and Ni(OH)<sub>2</sub> on MWCNTs as proof of concept for synthesis on expanded CNTs

## Future Directions

- Synthesize NiMoO<sub>4</sub> and MnO<sub>2</sub> on expanded CNTs/graphene like structures
- Use microscopy techniques and Rotating Disk Electrode measurements to identify the most optimal specific capacitance and highest energy density nanostructure
- Study the localized ion/electron charge distribution and charge-compensation behavior via EQCM
- Prepare metal oxide/carbon nanostructured composites that have a specific capacitance of 80 Wh/kg

## References

1. Grabtree et al., Report of the Basic Research Needs Workshop on Next Generation Electrical Energy Storage, **2017**, 11.
2. [https://commons.wikimedia.org/wiki/File:Supercapacitors\\_chart.svg](https://commons.wikimedia.org/wiki/File:Supercapacitors_chart.svg)
3. Yuan et al., The edge- and basal-plane-specific electrochemistry of a single-layer graphene sheet, *Sci. Rep.* **2013**, 3(2248), 1-7.
4. J. Gaillard, H. C. Mercado, R. Czerw, High Specific Capacitance Graphene Nanoribbon Electrodes for Supercapacitors, Hilton Clearwater Beach Resort, Clearwater, FL, Materials Challenges in Alternative & Renewable Energy Feb. 17-20, **2014**.
5. Li, L. et al., Facile synthesis of MnO<sub>2</sub>/CNTs composite for supercapacitor electrodes with long cycle stability, *J. Phys. Chem. C*, **2014**, 118(40), 22865–22872.
6. Z. Chen, V. Augustyn, X. Jia, Q. Xiao, B. Dunn, Y. Lu High-performance sodium-ion pseudocapacitors based on hierarchically porous nanowire composites, *ACS Nano*, **2012**, 6, 4319-4327.
7. Wang, X., et al., Co<sub>3</sub>O<sub>4</sub>@ MWCNT nanocable as cathode with superior electrochemical performance for supercapacitors, *ACS Applied Materials & Interfaces*, **2015**, 7(4), 2280–2285.
8. Beasley, C., Sassin, M., Long, J., Extending Electrochemical Quartz Crystal Microbalance Techniques to Macroscale Electrodes: Insights on Pseudocapacitance Mechanisms in MnOx-Coated Carbon Nanofoams. *J. Electrochem. Soc.*, **2015**, 162(5), A5060-A5064.

## Acronyms

EES	Electric Energy Storage
EDLCs	Electro-Chemical Double Layer Capacitors
ESR	Low equivalent series resistance
MWCNTs/CNTs	Multi-Walled Carbon Nanotubes/Carbon Nanotubes
ILs	Ionic Liquids

## Post-Doctoral Researchers

Dr. Joseph Meany, SRNL post-doc researcher

## External Collaborators

Richard Czerw, PhD, Mainland Solutions

## Low-Profile, Smooth-Walled Inner Pipe Sealing Insert for Low-Pressure Applications

**Project Team:** Patrick Ward, Carina Grady, David Tamburello

**Project Start Date:** October 1, 2019

**Project End Date:** September 30, 2020

*This is a low-pressure (above ambient pressure) sealing insert for use inside smooth-walled piping where the pipe walls are too thin to have threads turned. It is installed inside the piping because some applications cannot clamp to the outside of the pipe. It is low profile because some applications cannot have their pipe lengths extended. The low-pressure plug developed in this work*

*was determined to hold pressures of at least 1000 psig at room temperature in a 2-inch diameter pipe.*

### FY2020 Objectives

- Create various plug designs that will be tested to determine their maximum pressure capability
- Reach 200 psi in maximum rated pressure (600 psi burst pressure). If the plug reaches this goal, it is deemed effective for a predetermined low-pressure application

### Introduction

The current market of pipe sealing technologies includes being high profile (pipe seal extends past or wraps around the length of the pipe) and having a modified inner pipe wall (the inner pipe walls are fabricated to have threads for the seal) designs. However, there are applications where a pipe sealing technology must be low-profile (pipe seal does not extend past or clamp around the length of the pipe) and have a smooth-walled inner pipe (the inner pipe walls may not have threads or be modified).

Therefore, the design of a low-profile, smooth-walled, single-use inner pipe sealing technology for low-pressure applications was designed. This design has commercial potential in any industry that has a need for similar design constraints. Since a concept of a plug insert for a low-profile, smooth-walled, thin-walled, low-pressure application does not exist, the design by SRNL can be patented and can be used for commercial purposes to fill this application gap.

Before patenting the design, experimental tests must be conducted to prove the effectiveness of the design. This report will detail the designs and pressure burst test results to determine its effectiveness.

### Approach

To test the effectiveness of the pipe sealing technology, experimental tests must be performed to determine the maximum pressure inside the sealed pipe before the seal bursts or leaks. Like Figure 1, various designs of the pipe sealing technology (“plug”) have been drawn and fabricated to determine

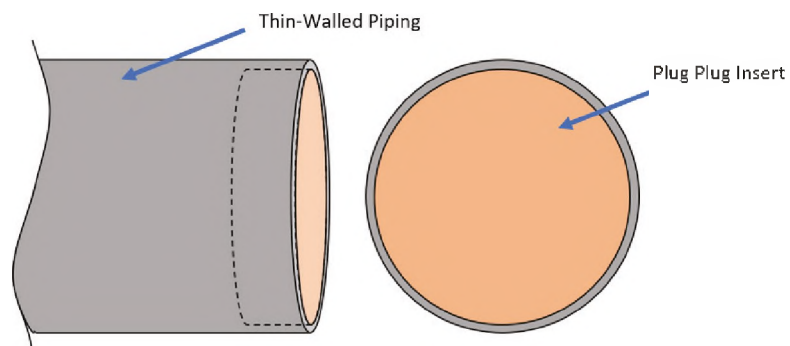


**Figure 1:** Plug inside thin-walled tube with undisclosed fitting.

which design will be the most effective. With the designs, each pressure bursting test will be repeated to confirm consistent results.

## Results/Discussion

Due to a pending patent, the specifics of the plug design are not disclosed in this report. Specifically, the details omitted include the variations of the design that lead to how the plug fits into the tube. Instead, ten different design parameters were consolidated into a legend with their appropriate pressure reading, as seen in Figure 2.

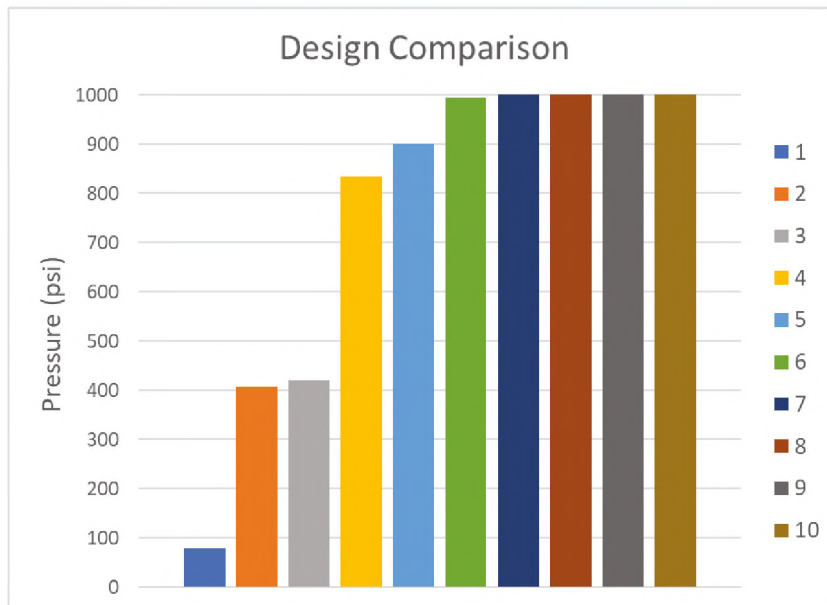


**Figure 2:** Visual comparison of design effectiveness.

Legend	Pressure (psig)
1	79.68
2	405.88
3	421.81
4	835.29
5	900.63
6	995.37
7	1001.02
8	1001.07
9	1000.20
10	1001.01

**Table 1:** Maximum pressure of 10 designs.

The designs can be fabricated, assembled, then tested for a pressure burst. This is done by enclosing the pipe with an inert gas such as nitrogen or argon, then stop the test when there is a drop of pressure indicating a plug burst or leak. After testing, the maximum pressure of the plug design is found to be 1000 psig, as seen in Table 1.

The initial project goal is to reach 200 psig, but the plug design exceeds this target by five times, thereby concluding this project to be a success. Since the testing set-up was not built to exceed a pressure of 1000 psig, the test is stopped if the pressure exceeds that. Because of this, Designs 7 through 10 likely have a maximum pressure exceeding 1000 psig. The pressure versus time graph of Design 10 is seen in Figure 3.

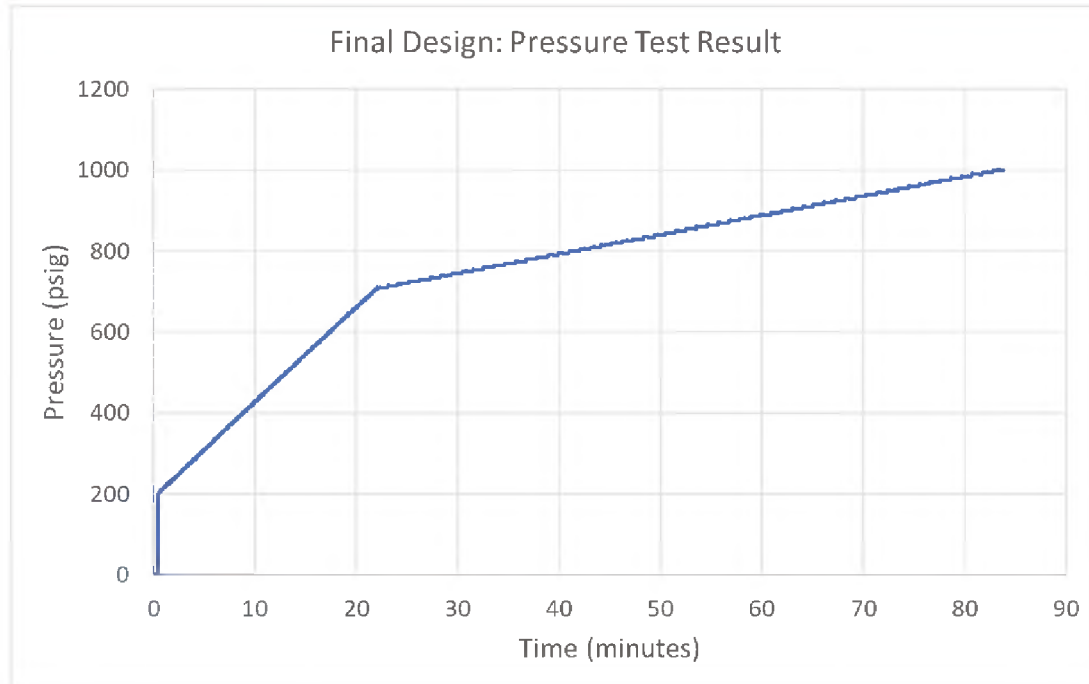


Figure 3: Maximum pressure of plug with the final chosen design parameters.

## FY2020 Accomplishments

- Designed a low-profile, smooth-walled, inner pipe sealing plug with a maximum pressure of 1000 psig, far exceeding the original goal of 200 psig rated pressure for low-pressure applications

## Future Directions

- File patent and reevaluate potential for originally designed purpose.
- Engage customers which potential use of the developed design for further study or implementation.
- Continue evaluation of plug design for higher pressure and non-ambient temperature applications.

## Intellectual Property

Patent review pending per OSR 3-188.

## External Collaborators

- Richard Douglas (Douglas Fluid & Integration Technology, LLC) performed the pressure burst tests
- Michael Brown (SRNL, R&D Engineering) created the LabView program for pressure burst testing

## Electronic Structure Calculations for Improving Catalyst Design for Use in the Hybrid Sulfur Cycle

**Project Team:** Thomas Danielson and Lindsay Roy

**Project Start Date:** October 1, 2019

**Project End Date:** September 30, 2020

*The hybrid sulfur cycle is a promising means for efficient production of large quantities of hydrogen with a small carbon footprint. However, many challenges remain in designing catalysts that are stable at high temperatures and have high sulfur tolerance. Theoretical calculations can provide fundamental insights at the electronic scale to improve our understanding of reaction mechanisms*

*and surface energetics, thereby facilitating improved catalyst design. Here, density functional theory was used to explore the reaction energetics of the hybrid sulfur cycle on Pt, Au, and Pt - Au surfaces. A database of information has been built that contains calculations from which adsorption energetics and density of states information can be extracted.*

### FY2020 Objectives

- Run density functional theory calculations for various HyS steps on the Pt – Au catalyst surface
- Run density functional theory calculations with applied electric fields
- Expand the calculation database from FY2019's LDRD seedling

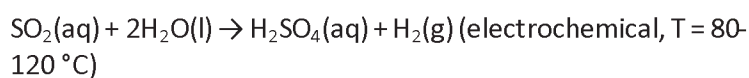
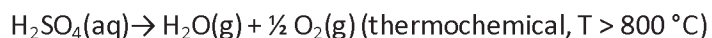
### Introduction

Catalytic materials are used in nearly 80% of all chemical processes and yet are largely developed through trial and error methods of synthesis and evaluation. In order to take a more scientific approach to catalyst design, this work has constructed a database of density functional theory (DFT) calculations (expanding on those completed in FY19) that can be examined to gain a deeper understanding of how the structure of Pt, Au, and Pt – Au catalyst systems affects reactivity in the hybrid sulfur cycle (HyS). Design and control of catalyst structures used in HyS will enable the synthesis of specialty materials at the nanometer scale. Controls in design will help further elucidate the impact of spatial defects in atomic structure to enable the synthesis of new highly reactive species. This will further the understanding of how carbon supported Pt/Au catalysts interact to accelerate SO<sub>2</sub> oxidation. Understanding the mechanism of catalytic processes can be improved by determining deactivation rates, changes in chemical structure involved in each step, and macroscopic rates of conversion.

Incorporating advanced modeling and simulation to our knowledge base for HyS builds upon the research efforts in nano-particulate catalytic material systems to develop methods of fine-tuning catalyst reactivity at the molecular level. This seedling LDRD focused on expanding the database of calculations that were performed in FY2019 and is comprised of systematic investigations that demonstrate how the electronic structure of Pt/Au catalysts affect the adsorption energetics and catalytic activity at the surface.

## Approach

Density functional theory as implemented in the VASP code<sup>1-3</sup> was used to calculate the electronic structure and energetics of Pt/Au systems. The two reactions in the HyS cycle are:



A systematic approach was taken to build a database of theoretical calculations containing information that will allow exploration of favorable reaction configurations and the electronic structural changes that promote them. In this approach, the catalyst surfaces and the molecules were structurally optimized in their pure states. Next, various steps in the HyS reaction pathways were iteratively explored by introducing a single molecular species to the surface and subsequently multiple species from various primary and intermediate reaction steps.

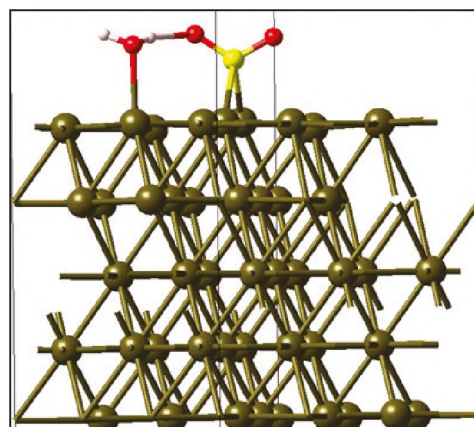


Figure 1: Stabilized structure of SO<sub>2</sub> and H<sub>2</sub>O on Pt(111).

## Results/Discussion

The primary result of this research effort is a database of 80 structurally optimized density functional theory calculations that have explored various configurations of the primary steps in the HyS reaction pathways. From this, the most stable states can be identified and compared against less stable states to extract configuration-dependent changes in the adsorption energetics and the accompanying electronic structure of both the molecular species and the catalyst surface.

Two key outputs from these models are the total system energies and the partial density of states. Total system energies can be combined in order to compute reaction energetics for the various steps and compare the stability of different configurations. In addition to guiding experiments, the database of energetics can be used to parameterize larger-scale chemical kinetics models. The partial density of states between different configurations containing the same species can be compared to identify, for example, a shift in the d-band states that might promote increased stability or reactivity.

## FY2020 Accomplishments

- Construction of a database of 80 density functional theory calculations that can be used to understand various steps in the HyS on Pt, Au, and Pt – Au catalyst surfaces

## Future Directions

- Applying the database of information to experimental catalyst design by more precisely analyzing simulation results and identifying key phenomena that promote reactivity
- Identifying and filling in critical gaps of the database (e.g., the inclusion of surface defects)

## References

1. Kresse, G.; Furthmüller, J., Efficiency of ab-initio total energy calculations for metals and semiconductors using a plane-wave basis set. *Computational Materials Science* **1996**, *6* (1), 15-50.
2. Kresse, G.; Furthmüller, J., Efficient iterative schemes for ab initio total-energy calculations using a plane-wave basis set. *Physical Review B* **1996**, *54* (16), 11169-11186.
3. Perdew, J. P.; Burke, K.; Ernzerhof, M., Generalized Gradient Approximation Made Simple. *Phys. Rev. Lett.* **1996**, *77*(18), 3865-3868.

## Acronyms

DFT	Density Functional Theory
HyS	Hybrid Sulfur
VASP	Vienna ab initio Simulation Package

## High Temperature Water Electrolysis Testing of Gold-based Electrodes for H<sub>2</sub> Production

**Project Team:** H. Colón-Mercado, M. Gorenssek, A. Lando, C. Fujimoto

**University of South Carolina**  
**Collaborator:** B. Meekins

**Start Date:** February, 2020

**End Date:** September, 2020

*The Hybrid Sulfur (HyS) process is a promising thermochemical water-splitting cycle with global scale hydrogen production potential. The SO<sub>2</sub>-depolarized electrolyzer (SDE) is a critical component of the cycle. At the core of the SDE is the membrane-electrode assembly (MEA), which consists of a polymer electrolyte membrane (PEM) sandwiched between two electrocatalyst layers. New electrocatalyst and membrane materials are being developed with the goals of improving the electrolyzer performance and extending the lifetime of the MEA. In*

*this work, we evaluated the performance of three different membranes and optimized operating conditions, resulting in one of the highest performances in the literature.*

### FY20 Objectives

- Electrolyzer Performance Evaluation under various operating conditions
- Write manuscript

### Introduction

There exists a significant and growing need for clean, efficient, and large-scale hydrogen production. Using high temperature heat, thermochemical cycles can provide an energy-efficient route for hydrogen production. The HyS process is a promising thermochemical water-splitting cycle with significant scalability. The HyS process, one of the most researched thermochemical cycles, is a sulfur-based water-splitting cycle which contains a low temperature electrolysis step, and thus can be considered an electrochemical and thermochemical hybrid process.

The electrolysis step must be maintained at the highest possible conversion fraction to minimize unreacted SO<sub>2</sub> and obtain high H<sub>2</sub>SO<sub>4</sub> concentration. Unreacted SO<sub>2</sub> must be recycled, and water must be removed prior to the high temperature decomposition step. Both of these are energy intensive steps and must be minimized to keep process efficiency high. Operation of the electrolyzer at the target conditions, however, is unfeasible using the current state-of-the-art materials. Therefore, new materials will be required to achieve the electrolysis performance goals. This project is focused on the development of new membranes and their effect on process efficiency, with the goals of improving the electrolyzer performance and extending the lifetime of the MEA.

### Approach

A collaborative effort between SRNL, USC, and SNL was continued to develop novel materials designed to operate under the HyS process conditions with superior performance compared to the state-of-the-art. SRNL is utilizing its expertise in electrode design along with SNL's expertise in membrane development and USC in electrolyzer modeling to achieve improvements in the HyS and meet DOE-EERE's hydrogen production goals. The work is a conclusion of previous funded LDRD work. The final approach takes the optimized materials and characterizes the electrolyzer conditions to achieved high performance. Flowrates, temperatures, and water input locations were evaluated for three MEAs fabricated with N212, N115 and SDAPP MEAs.

## Results/Discussion

The electrochemical performance of various MEAs were evaluated in an electrolysis cell. Figure 1, shows the SO<sub>2</sub> electrooxidation performance of the various MEA using different membranes. As observed the highest performance is observed for the SDAPP based membrane. Figure 2 shows the effect of temperature for the different MEAs under constant current. As observed, all MEAs show an increase in performance with an increase of temperature until 105 °C. However, the performance using the SDAPP remains superior to that of commercial Nafion® membranes.

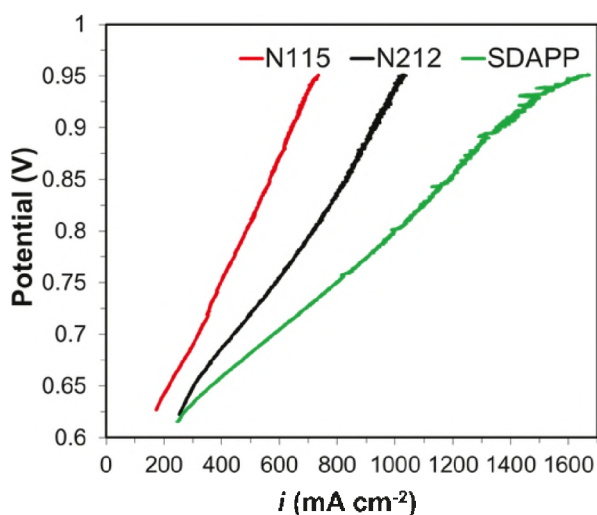


Figure 1: Performance comparison at 95 °C.

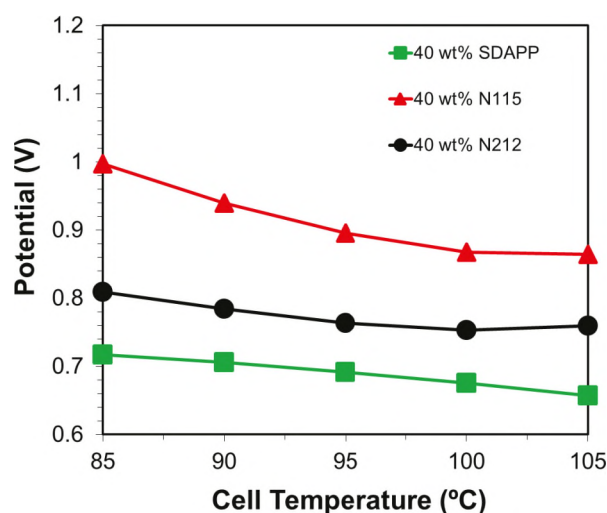


Figure 2: Constant Current performance as a function of cell temperature.

## FY20 Accomplishments

- Completed constant current measurements, impedance measurements, cell operation effects, and long duration testing on N212, N115 and SDAPP based MEAs

## Future Directions

- Publish results and apply for funding at various DOE-EERE solicitations

## Acronyms

DOE-EERE	Department of Energy-Office of Energy Efficiency and Renewable Energy
HyS	Hybrid Sulfur
MEA	Membrane electrode assembly
N212	Nafion® 212
N115	Nafion® 115
PEM	Polymer electrolyte membrane
SDE	SO <sub>2</sub> -depolarized electrolyzer
SNL	Sandia National Laboratory
SRNL	Savannah River National Laboratory
USC	University of South Carolina

## Development of High Capacity Energy Storage Materials

**Project Team:** Patrick A. Ward, Hector Colon-Mercado, Alicia Fessler

**Project Start Date:** March 1, 2020

**Project End Date:** September 30, 2021

*Hydrogen fuel cells offer energy and power density advantages over lithium ion batteries in automotive and portable power applications when paired with an appropriate hydrogen storage system. Current fuel cell vehicles utilize 700 bar carbon fiber reinforced tanks due to a variety of limitations across the range of hydrogen storage materials. Many high capacity*

*hydrogen storage materials suffer from high expense, impurity release in the desorbed hydrogen, and poor reversibility. Herein, we develop methodologies to address impurity release in high capacity hydrogen storage materials.*

### FY2020 Objectives

- Demonstrate methodologies to mitigate ammonia release from alkali metal amides
- Evaluate the effect of Iridium doping in lithium amide-based materials to decompose ammonia
- Develop methodologies to capture and utilize borane-based impurities from borohydride hydrogen storage materials

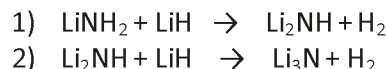
### Introduction

The development of high capacity hydrogen storage materials has been of studied for hydrogen fuel cell vehicles for decades. Most of the typical high capacity materials have limitations in reversibility, cost, operational temperature, and the evolution of other gaseous species which poison the fuel cell catalyst or membrane. Recent advances in fuel cells combined with nontraditional operational configurations provide promising pathways to significantly enhance the energy density needed for many defense applications.

Lithium nitride provides a promising pathway toward storing hydrogen due to its high gravimetric hydrogen density upon hydrogenation, reversibility, and relatively low operating temperatures (200–270 °C).<sup>1-4</sup>  $\text{Li}_3\text{N}$  reacts with gaseous hydrogen by direct hydrogenation according to the following overall equation:



Hydrogen release is known to occur in two distinct dehydrogenation steps as



Although ammonia is known to react spontaneously with LiH to produce  $\text{LiNH}_2$ ,<sup>5</sup>  $\text{NH}_3$  evolution is still observed in the  $\text{Li}_3\text{N}$  system during desorption. Ammonia readily reacts with the acidic groups found in Nafion proton exchange membranes to significantly reduce fuel cell performance. Previous researchers have demonstrated the addition of  $\text{N}_2$  to hydrogen used for rehydrogenation mitigates the nitrogen loss from  $\text{NH}_3$  emission resulting in virtually negligible hydrogen capacity losses after 516 cycles.<sup>6</sup> Therefore, decomposition of ammonia to prevent fuel cell damage and rehydrogenation with hydrogen:nitrogen mixtures to regenerate the material provides a promising pathway for the utilization of this material in practice.

## Approach

Lithium amide and lithium amide/lithium hydride samples were doped with varying amounts of Iridium black by ball milling. These samples were then used to determine the effectiveness of ammonia impurity decomposition during hydrogen release from the samples. Thermogravimetric Analysis (TGA) coupled with residual gas analysis (RGA) was employed to determine the weight capacity loss from the sample at a given temperature and identify the decomposition gases. Gas chromatography was employed to quantitatively determine the amount of ammonia decomposition observed from the Iridium doped samples. Kissinger plots of the decomposition thermograms were derived from TGA thermograms to determine the catalytic effect on hydrogen release from the samples.

Methodologies to effectively mitigate boron-based impurities were identified and methodologies to produce impurity resistance fuel cells theorized. These methodologies will be employed to provide additional techniques for the utilization of other high capacity hydrogen storage materials.

## Results/Discussion

Lithium amide samples were doped with Iridium black (99.99% purity) by SPEX milling to provide samples with varying amounts of Iridium. These samples were evaluated by TGA/RGA to qualitatively determine their effectiveness in ammonia impurity removal from the gas stream. Ammonia impurities have detrimental effects on the performance of proton exchange membrane (PEM) fuel cells due to the acid/base neutralization reaction which occurs with the Nafion membrane. Additionally, ammonia contains hydrogen from the material which lowers the amount of useable hydrogen released from the storage material. TGA/RGA data illustrates the significant amount of ammonia release from the decomposition of  $\text{LiNH}_2$  as shown in Figure 1. Upon addition of 2 wt. % Iridium, a significant reduction in ammonia release is observed as demonstrated in Figure 2. While additional reduction of ammonia is observed from the addition of 5 wt. % and 10 wt. % of Iridium, as shown in Figures 3 and 4, the improvement is not as dramatic. The increase in observed nitrogen is consistent with the decomposition of ammonia into nitrogen and hydrogen. This suggests that ammonia is being decomposed after release during higher temperature decomposition where nitrogen release is observed. On the other hand, ammonia appears to be sequestered through a catalytic mechanism during the decomposition of lithium amide in the initial onset of decomposition. Additionally, the quantity of hydrogen release during the initial decomposition increases with increasing Ir content. These findings present pathways towards the decomposition of ammonia impurities in hydrogen streams and potential mechanisms to provide catalytic mechanisms to reduce the release of ammonia from lithium amide systems. Further investigation is currently underway to provide additional mechanistic insight into the impact of Iridium incorporation in metal amide systems for hydrogen storage applications.

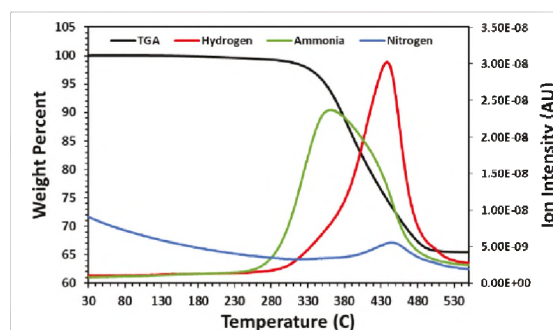


**Figure 2:** TGA/RGA of SPEX milled  $\text{LiNH}_2$  at a ramp rate of  $5^\circ\text{C}/\text{minute}$ .

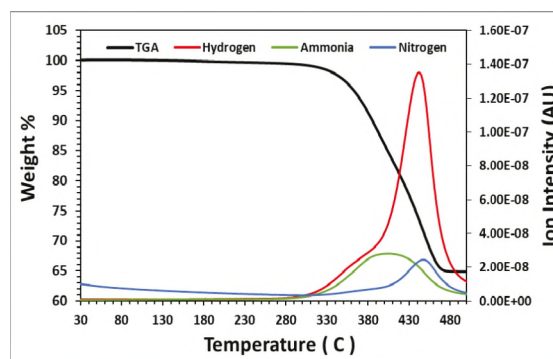


**Figure 1:** TGA/RGA of SPEX milled  $\text{LiNH}_2$  with 2 wt. % Ir at a ramp rate of  $5^\circ\text{C}/\text{minute}$ .

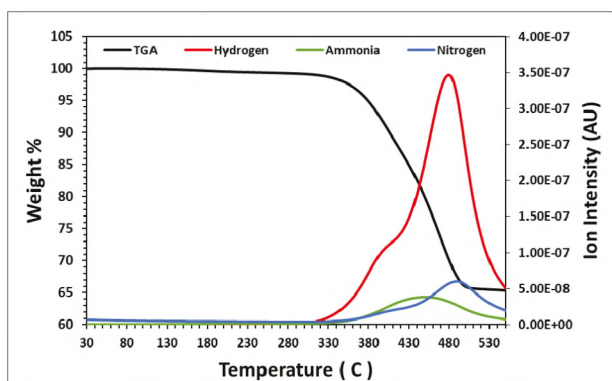


**Figure 3:** TGA/RGA of SPEX milled  $\text{LiNH}_2$  with 5 wt. % Ir at a ramp rate of  $5^\circ\text{C}/\text{minute}$

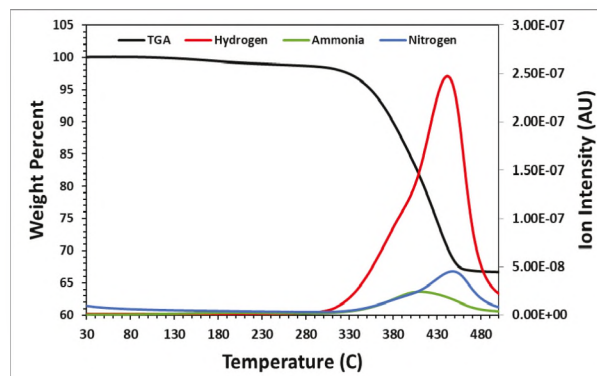


**Figure 4:** TGA/RGA of SPEX milled  $\text{LiNH}_2$  with 10 wt. % Ir at a ramp rate of  $5^\circ\text{C}/\text{minute}$

## FY2020 Accomplishments

- Demonstrated catalytic decomposition of ammonia into hydrogen and nitrogen from lithium amide-based hydrogen storage materials
- Identified aspects of the mechanistic behavior of ammonia decomposition in the lithium amide system
- Acquired materials and fuel cell components needed to demonstrate boron impurities removal techniques and impurity resistant fuel cell methodologies

## Future Directions

- Demonstrate impurity scrubbing/utilization technologies for boron-based impurities
- Evaluate the impurity resistance of constructed fuel cells
- Obtain additional insight into the mechanism and behavior of Iridium in alkali metal amide hydrogen storage materials

## References

1. Chen, P.; Xiong, Z.; Luo, J.; Lin, J.; Tan, K. L. Interaction of hydrogen with metal nitrides and imides. *Nature*, **2002**, *420*, 302-304.
2. Hao, T.; Matsuo, M.; Nakamori, Y.; Orimo, S. Impregnation method for the synthesis of Li-N-H systems. *Journal of Alloys and Compounds* **2008**, *458*, L1-L5.
3. Hu, Y. H.; Yu, N. Y.; Ruckenstein, E.; Hydrogen Storage in  $\text{Li}_3\text{N}$ : Deactivation Caused by a High Dehydrogenation Temperature. *Ind. Eng. Chem. Res.* **2005**, *44*, 4304-4309.
4. Hu, Y. H.; Ruckenstein, E.  $\text{H}_2$  Storage in  $\text{Li}_3\text{N}$ . Temperature-Programmed Hydrogenation and Dehydrogenation. *Ind. Eng. Chem. Res.* **2003**, *42*, 5135-5139.
5. Hu, Y. H.; Ruckenstein, E. Ultrafast Reaction between  $\text{LiH}$  and  $\text{NH}_3$  during  $\text{H}_2$  Storage in  $\text{Li}_3\text{N}$ . *J. Phys. Chem. C* **2003**, *107*, (46), 9737-9739.
6. Lamb, J.; Chandra, D.; Chien, W.; Phanon, D.; Penin, N.; Cerny, R.; Yvon, K. Mitigation of Hydrogen Capacity Losses during Pressure Cycling of the  $\text{Li}_3\text{N}$ -H System by the Addition of Nitrogen. *J. Phys. Chem. C* **2011**, *115*, 14386-14391.

## Acronyms

GC Gas Chromatography  
RGA Residual Gas Analysis  
SPEX A brand of high energy ball mill used to homogenize samples  
TGA Thermogravimetric Analysis

## Post-Doctoral Researchers

Willis Jones and Dustin Olsen

# PIONEERING SCIENCE



## PROJECTS

Quantum Fields on Driven Plasmonic Nanostructures

Molecular and Microstructural Bases for Understanding Microplastic Origin, Transport and Fate

Patterning of Magneto-Optical Nanomaterials

## Quantum Fields on Driven Plasmonic Nanostructures

**Project Team:** Patrick O'Rourke, Lindsay Roy, Robert Lascola, Simona Murph, Michael Thomas

**Project Start Date:** October 1, 2019

**Project End Date:** August 30, 2020

This work explores electromagnetic radiation coupling to plasmonic nano-particles, and its redistribution throughout a symmetric mesoscale nanostructure of the plasmonic particles. The goal was to identify coherent EM oscillations associated with groups of nano-particles that could be interpreted as quasi-particles, and seek to stabilize the quasi-particles by introducing asymmetric

'traps' in the structure.

### FY2020 Objectives

- Develop modeling approach for multiple nanoparticle coupling
- Fabricate SEM/FIB nanostructures
- Observe optical effects of nanostructures on optical substrates

### Introduction

Energy absorbed by a system is eventually distributed throughout the system according to the laws of thermodynamics. Thermodynamics does not, however, address the mechanisms whereby a non-equilibrium state approaches equilibrium. Understanding the quantum mechanical mechanisms responsible for energy redistribution are complicated by the huge number of kinetic and electromagnetic interactions involved.

It may be possible to separate kinetic and electromagnetic interactions responsible for energy redistribution in plasmonic arrays because the array elements are fixed in space and only interact electromagnetically. In addition, the array elements can be arranged in one- and two-dimensional geometries greatly simplifying simulations and experimental interpretation.

This work explores electromagnetic radiation coupling to plasmonic nanoparticles, and its redistribution throughout a symmetric mesoscale nanostructure of the plasmonic particles. We hope to identify coherent electro-magnetic oscillations associated with groups of nano-particles that could be interpreted as quasi-particles and seek to stabilize the quasi-particles by introducing asymmetric 'traps' in the structure.

### Approach

Time dependent density functional (TD-DFT) and time-dependent density functional tight binding (TD-DFTB) calculations are used to simulate electro-magnetic field interactions with individual gold nano-particles<sup>1</sup> (Figure 1). Finite-Difference Time-Domain (FDTD) calculations are used to simulate

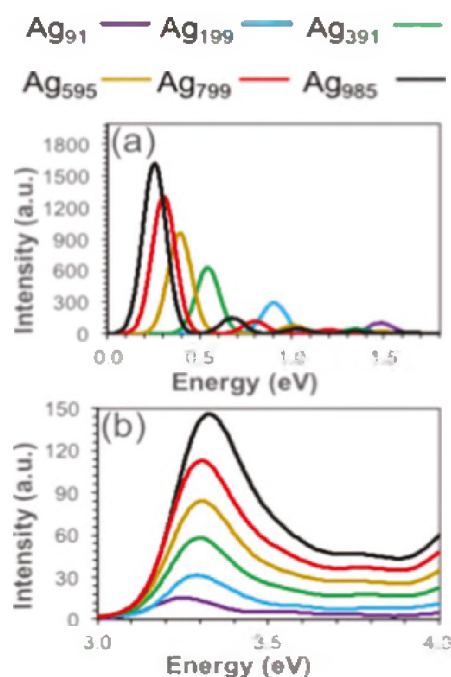


**Figure 1:** From Alkan et al, J Phys Chem C, 2018, 122, 23639 TD-DFTB calculated absorption spectra for silver nanorods (a) Longitudinal peak for various length nanorods (b) Transverse peak for the same systems.

electro-magnetic near-field dynamics arising from 1-dimensional chains of Au NPs with 100 nm diameter and interparticle distance of 15 nm.

Focused ion beam milling was used to create nano-island structures in a thin gold and silver films deposited on prism surfaces (Figure 2).

An optical scattering apparatus was constructed to facilitate evanescent wave coupling of electro-magnetic fields into nano-structures fabricated onto prism surfaces (Figure 3).

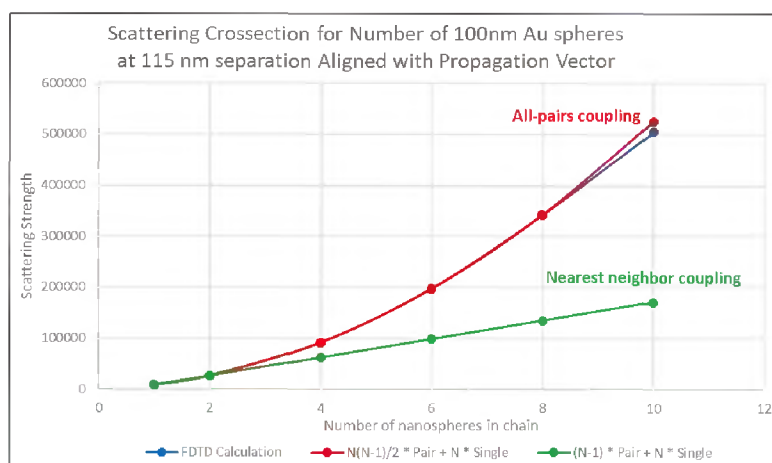
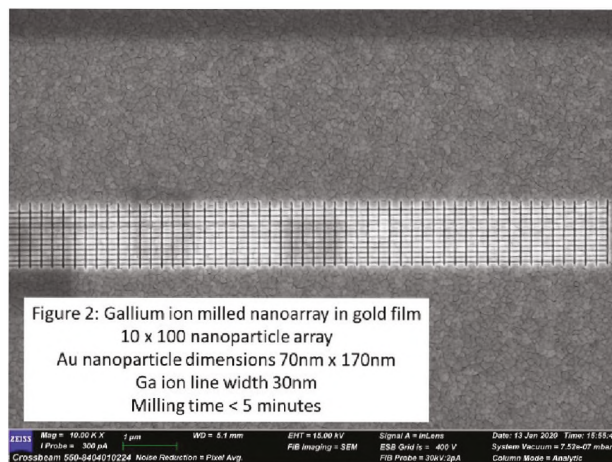


Figure 4: FDTD simulation of chains of nanospheres.

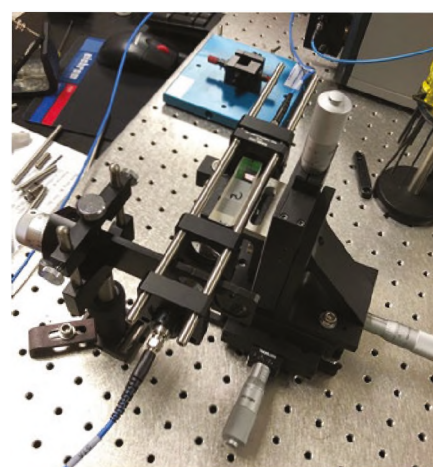


Figure 3: Optical scattering apparatus.

## Results/Discussion

Computer simulations show that light scattering from chains of nanospheres have much greater scattering strength than expected from the individual particles and suggests that pair coupling between particles extends to much greater distances than nearest neighbor (Figure 4).

## FY2020 Accomplishments

- Nano particle simulation software was procured and installed at SRNL to simulate plasmon interactions with electromagnetic fields and shows novel unexpected scattering strength from chains of nano spheres
- A combination (Scanning Electron Microscope) and (Focused Ion Beam) (SEM-FIB) instrument was installed at SRNL and methods to fabricate nano-scale features in thin metal films were developed.
- A light scattering apparatus was constructed which will allow observation of light scattering phenomena from mesoscale nanostructures

## Future Directions

Nanostructure simulations will be extended to two dimensional structures and will include symmetry breaking features to stimulate novel light scattering effects. These simulated structures will be fabricated in the SEM-FIB and light scattering from the structures will be observed.

## References

1. Alkan et al, *J Phys Chem C*, **2018**, 122, 23639.

## Acronyms

FDTD	(Finite Difference) - (Time Domain)
SEM-FIB	(Scanning Electron Microscope) – (Focused Ion Beam)
TD-DFT	Time dependent density functional theory
TD-DFTB	Time-dependent density functional tight binding

## Post-Doctoral Researchers

Michael Thomas started work on the project in May of 2020 as a post-doctoral researcher in the Analytical Development Section of SRNL.

## Molecular and Microstructural Bases for Understanding Microplastic Origin, Transport and Fate

**Project Team:** G. Larsen, K. Lawrence, D. Benza, T. Guin

**Project Start Date:** November 1, 2019

**Project End Date:** August 21, 2020

*The ubiquitous use of plastics has led to one of the worst human created environmental disasters of our time, leading to millions of tons of plastic waste per year. Plastics generally are not biodegradable and accumulate in vast amounts in the form of micro- and nanoplastics in ocean water, freshwater, soil, and the atmosphere.<sup>1-3</sup> The primary mechanism for microplastic formation from larger structures is thought to be photochemical degradation in ultraviolet light.<sup>4-5</sup> The goal of this research is to investigate the breakdown of plastic particulates in the presence of different stressors (e.g. UV light, water, oxidative stress, etc.) to unravel the role these play in the formation of nanoplastics. The effect of UV damage on the thermal and physical properties of different types polymer micro and bulk particulates was investigated. Nylon showed the largest decrease in crystallinity and melting temperature after UV damage, which is attributed to the presence of more reactive amine groups. As the particulate size decreased, polyethylene crystallinity decreased with UV exposure.*

### FY2020 Objectives

- Print test pieces and evaluate residual stresses
- Aging experiments of bulk samples
- Microplastic Adsorption Experiments
- Bulk polymer and microplastic characterization

### Introduction

The goal of this project is to investigate the role that different physicochemical properties and different stressors play on the creation of microplastics. The primary mechanism for microplastic formation from larger structures is through photochemical degradation in ultraviolet light.<sup>5</sup> While this degradation process has been studied extensively in the context of bulk mechanical behavior of polymers,<sup>6</sup> there is little to no work relating the polymeric molecular and microstructural effects on the photochemical production of micro- or nanoplastics. Since photochemical degradation is generally localized to the surface due to limits from molecular diffusion and light penetration depths, the correlation between bulk stability and microplastic production may be weak, non-existent, or even negative. In addition to the inherent stability of the polymer, processing effects and additives can also substantially alter the photochemical processes in the final product, increasing the complexity of subsequent analyses.

### Approach

#### Technical Approach:

##### *1. Relationships between Molecular Structure, Microstructure and Microplastic Formation*

The effect of molecular structure and chemical functionalities on plastic degradation was evaluated. Bulk plastics were printed using additive manufacturing, which offers an ideal solution to initiate a scientific study into microplastic formation from bulk degradation. A single processing technique can be employed across a set of different thermoplastics, and the same feedstock can be used for varying processing parameters to allow for the isolation of the effects of the different properties of polymers (e.g., glass transition temperature, oxygen and water permeability). In this portion of the project, additively manufactured test pieces of thermoplastics (HDPE, PET, PS) were produced with varying degrees of

residual stresses and then subsequently aged using UV irradiation. Both bulk and particulate samples were characterized by electron microscopy, thermal analysis, FTIR, Raman spectroscopy, and polarized light microscopy to assess any molecular and microstructural changes throughout the process.

## 2. Relationship between Molecular Structure and Tracer Uptake and Analysis

In this portion of the project, pristine and artificially weathered plastic particles were evaluated for metal capture (Pb). As stated above, these different thermoplastics have unique properties (e.g., glass transition temperature, crystallinity, permeabilities) due to their different molecular groups and polymeric microstructure (e.g., chain entanglement), and therefore, enable a molecular-based investigation. The proportion of different functional group will evolve as these materials degrade as well.

## Results/Discussion

### UV Exposure

Different types of plastics were exposed to UV light and analyzed via scanning electron microscopy (SEM), differential scanning calorimetry (DSC) and Fourier transform infrared spectroscopy (FTIR). As shown in

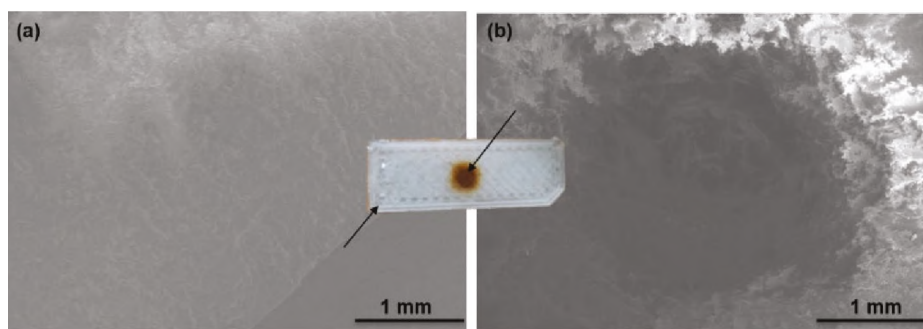


Figure 1: SEM of PET-G bulk plastic (a) with no UV exposure and (b) after UV exposure.

Figure 2, the UV light burned through 3D printed PET-G, leading to a decrease in FTIR absorbance intensity (Figure 2) and disappearance of peaks in the fingerprint region.

The effect of polymeric structure on the UV induced damage for different microparticles was investigated. Figure 3 shows the DSC results for high density polyethylene microspheres (HDPE) before and after UV exposure. The crystallinity was calculated from the measured enthalpy and compared to the enthalpy of melting for a completely crystalline form of the polymer. For the HDPE microparticles, a decrease in crystallinity was measured after UV exposure, along with a decrease in melting temperature. A secondary,

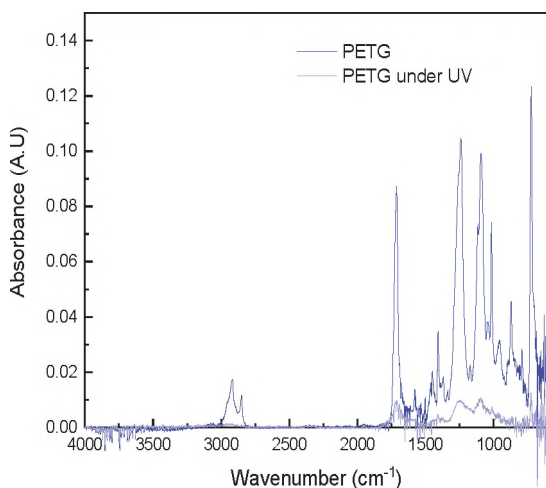


Figure 2: DSC of HDPE microspheres before and after UV exposure.

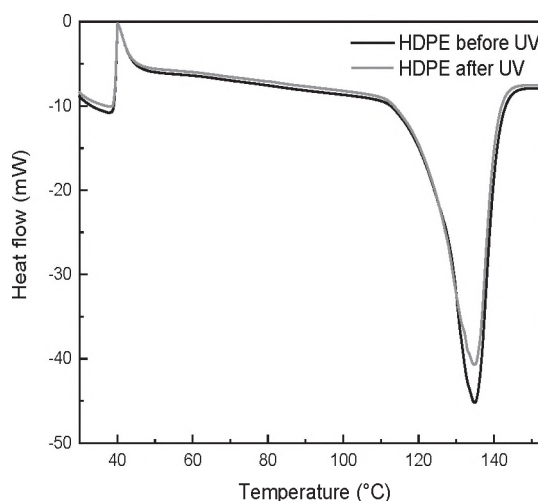
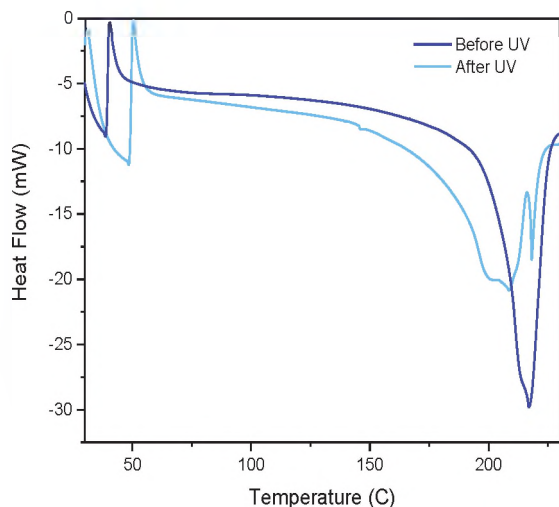


Figure 3: FTIR of PET-G before and after UV exposure.

lower melting temperature was observed as well, indicating a weakening of the polymeric structure.

Polyamide microspheres were also investigated, as shown in the DSC in Figure 4. A decrease in melting temperature and the appearance of a lower melting temperature peak was observed which is consistent with the HDPE data. A decrease in the crystallinity again was observed. As shown in the FTIR spectra in Figure 5, there weren't any significant changes to the peaks; however, a decrease in crystallinity was observed based on the ratio of the crystalline and amorphous peaks.



**Figure 4:** DSC of polyamide microspheres before and after UV exposure.

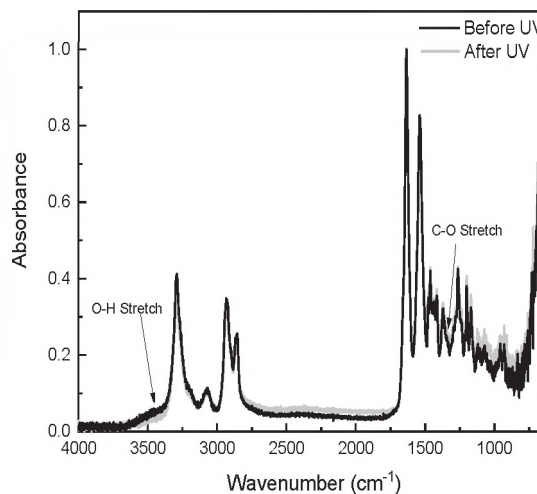


**Figure 5:** FTIR of polyamide microspheres before and after UV exposure.

A summary of the thermal properties of the different types of plastics that were analyzed are shown in Table 1. The polyamide microparticles showed the largest change in the melting temperature and crystallinity. This is attributed to the presence of the more reactive amine groups. Additionally, the

Sample	$T_m$ [°C, peak]	$T_m'$ (°C)	$\Delta H @ T_m$ (J/g)	$x_c$ (%)
Polyamide No UV	216.98		97.18	42.3
Polyamide after UV	218.4	208.76	0.53	0.23
HDPE before UV	131.27		232.1	80.9
HDPE after UV	131.75	127.74	228.9	79.8
PE before UV	116.72		231.1	80.6
PE after UV	114.94		218.8	76.3

**Table 1:** Effect of UV exposure on the thermal properties of different types of micro sized plastics.

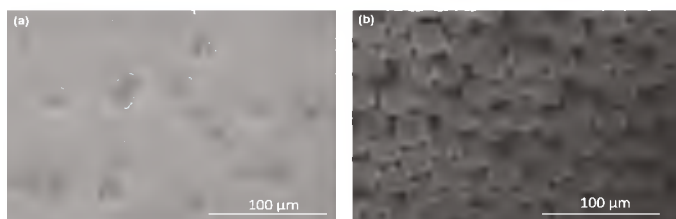


**Figure 6:** SEM of (a) polyamide and (b) polyethylene microspheres.

polyamide microparticles are smaller and have a more anisotropic shape (Figure 6) that can lead to more reactive surface groups that will respond to the UV damage.

The effect of UV damage to polyethylene microspheres was measured for different particle sizes. As shown in Figure 7, the smaller particles showed a larger change in crystallinity after UV exposure.

### Metal Uptake

The printed plastics were evaluated for metal uptake to see if UV exposure affected the uptake. Both non-illuminated and UV-illuminated plastics exhibited Pb uptake from solution, as measured by XRF.

## FY2020 Accomplishments

- Developed processes to extrude and 3D print from pure polymer feedstock
- Developed process to incorporate varying amounts of residual stress into printed polymer pieces
- Characterized the material properties of microplastics
- Observed metal uptake in microplastics
- Awarded CINT user facility proposal

## Future Directions

- Conduct CINT user facility research
- Investigate environmental microplastics
- Understand biological effects on microplastics

## References

1. Lebreton, L.; Slat, B.; Ferrari, F.; Sainte-Rose, B.; Aitken, J.; Marthouse, R.; Hajbane, S.; Cunsolo, S.; Schwarz, A.; Levivier, A.; Noble, K.; Debeljak, P.; Maral, H.; Schoeneich-Argent, R.; Brambini, R.; Reisser, J., Evidence that the Great Pacific Garbage Patch is rapidly accumulating plastic. *Scientific Reports* **2018**, *8* (1), 4666.

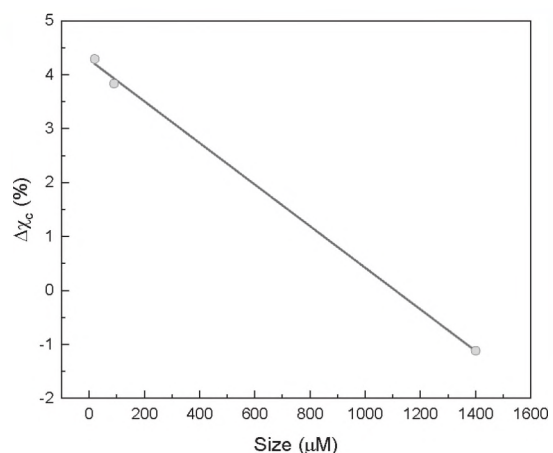


**Figure 7:** Effect of UV damage on change in crystallinity for different sized polyethylene microspheres.

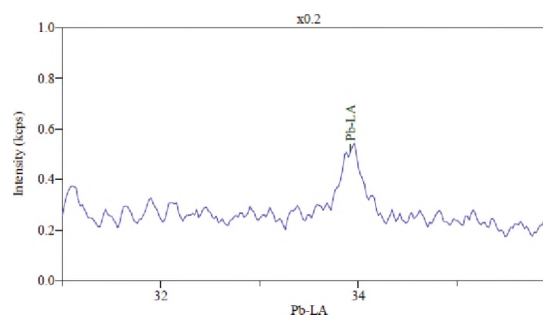


**Figure 8:** XRF of lead plastic before UV exposure.

2. Andrady, A. L., The plastic in microplastics: A review. *Marine Pollution Bulletin* **2017**, *119* (1), 12-22.
3. Rochman, C. M., Microplastics research—from sink to source. *Science* **2018**, *360* (6384), 28-29.
4. Gigault, J.; Pedrono, B.; Maxit, B.; Ter Halle, A., Marine plastic litter: the unanalyzed nano-fraction. *Environmental Science: Nano* **2016**, *3* (2), 346-350.
5. Gewert, B.; Plassmann, M. M.; MacLeod, M., Pathways for degradation of plastic polymers floating in the marine environment. *Environmental Science: Processes & Impacts* **2015**, *17* (9), 1513-1521.
6. White, J. R., Polymer ageing: physics, chemistry or engineering? Time to reflect. *Comptes Rendus Chimie* **2006**, *9* (11), 1396-1408.

## Acronyms

CINT	Center for Integrated Nanotechnologies
DSC	Differential Scanning Calorimetry
FTIR	Fourier Transform Infrared Spectroscopy
HDPE	High Density Polyethylene
PET	Polyethylene Terephthalate
PETG	Polyethylene Terephthalate Glycol
PE	Polyethylene
PS	Polystyrene
SEM	Scanning Electron Microscopy
UV	Ultraviolet
XRF	X-ray fluorescence

## Patterning of Magneto-optical Nanomaterials

**Project Team:** Simona Hunyadi Murph, Henry Sessions, Tyler Guin and Ray Belliveau

**Project Start Date:** October 1, 2019  
**Project End Date:** September 30, 2020

*Patterning of colloidal particles in precisely organized architectures has attracted intense research interest for decades. This is due to their potential applications in flexible electronics, magnetic and optical devices, sensors, biotechnology, communications, etc. However, creation of mesoscale assemblies at commercial scale received less attention. The mesoscale systems reside between the micro- and macro-scopic scales, with length*

*dimensions from  $\approx 100\mu\text{m}$  to 5mm. One way to create mesoscale materials is to leverage decades of experimental and theoretical research in nanomaterials field that allows us to precisely create and control the placement of nanoscale materials. We developed a versatile and automatic mesoscale patterning technology that provide precise and consistent control and special arrangement of functional nanomaterials. The versatility of the strategy is demonstrated by patterning nanoparticles with different dimensions, shapes and compositions, tethered with various functionalities and subjected to different external stimuli. Nanomaterials were created via the patent pending automated flow-throughput domain process (AFTDP), aka nano-additive manufacturing approach, recently developed by us, based on a unique small-scale fluidics concept, that enables a uniform reaction environment for production of high-quality materials in large quantities.*

### FY2020 Objectives

- Fabrication of novel magneto-optical nanomaterials of various sizes, shapes, and compositions via AFTDP technology
- Preparation and characterization of novel nanomaterials: mono-metallic and/or bimetallic Au/Fe/FeXO<sub>y</sub>; Au-TiO<sub>2</sub>, Au-SiO<sub>2</sub> and various shapes: spheres, stars, rods, triangular plates, etc.
- Large scale (mesoscale) patterning

### Introduction

Patterning of colloidal particles in precisely organized architectures has attracted intense research interest for decades. This is due to their potential applications in flexible electronics, magnetic and optical devices, sensors, biotechnology, communications, etc.

The most common surface patterning techniques, including nanoimprinting, nanografting, or a combination of nanolithography techniques coupled with chemical approaches, generate micrometer and submicrometer-sized architectures. Unfortunately, these approaches either lack the required surface coverage or a specialized and costly print/stamp technology is necessary in achieving the patterning of nanoparticle arrays on surfaces. However, creation of mesoscale assemblies at commercial scale received less attention. The mesoscale systems reside between the micro- and macro-scopic scales, with length dimensions from  $\approx 100\mu\text{m}$  to 5mm.

One way to create mesoscale materials is to leverage decades of experimental and theoretical research in nanomaterials field that allows us to precisely create and control the placement of nanoscale materials. The key to the production of mesoscale systems is tailoring nanomaterials' chemical functionality as a way of controlling and tuning their molecular interactions and at their interfaces in ways that can be used to couple materials together to develop new capabilities and architectures.

We proposed to develop a versatile and automatic mesoscale patterning technology that will provide precise and consistent control and special arrangement of functional nanoparticles. The versatility of the strategy was demonstrated by patterning nanoparticles with different dimensions, shapes and compositions, tethered with various functionalities and subjected to different external stimuli.

## Approach

Nanomaterials created via the patent pending automated flow-throughput domain process (AFTDP) recently developed by us, aka nano-additive manufacturing approach based on a unique small-scale fluidics concept, that enables a uniform reaction environment for production of high-quality materials in large quantities.

Spatial assembly and distribution of nanoparticles in various architectures was achieved by surface functionalization/recognition, template directed self-assembly, external electric or magnetic fields, among others.

## Results/Discussion

Nanomaterials of various sizes (1-100 nm), shapes (rods, spheres, triangular plates, stars, etc.) and compositions (Au/Fe/FeXO<sub>y</sub>; Au-TiO<sub>2</sub>, Au-SiO<sub>2</sub>) were prepared through a solution chemistry, through the reduction of molecular precursors in the presence/absence of surfactants, and capping agents (Figure 1). The ligands on the surface are used to stabilize the NPs and change the surface energy at certain facets through preferential adsorption to achieve shape control. The reduction rates of the metal precursors, reductant-to-precursor ratio, ligands and strength of reductant all were used to manipulate the final product which affect the optical and physical properties. By automatically varying the amount, volumetric flow rates, timing, location, size of the capillaries/tubings, etc. of the injected reagents, highly reliable and uniform nanomaterials were produced. Continuous operation of the system allows production of nanomaterials in large quantities. Once produced, nanomaterials

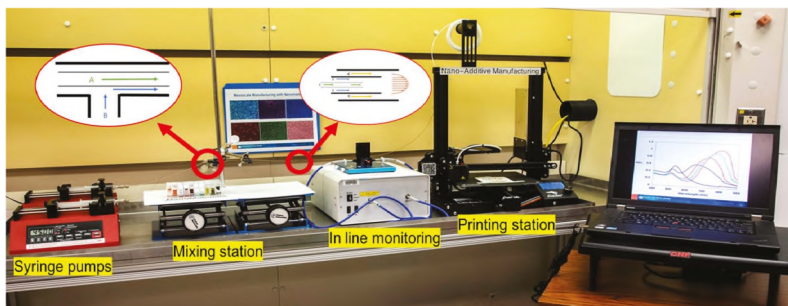


**Figure 1:** Automated flow-throughput domain process (AFTDP) recently developed by us, aka nano-additive manufacturing approach.

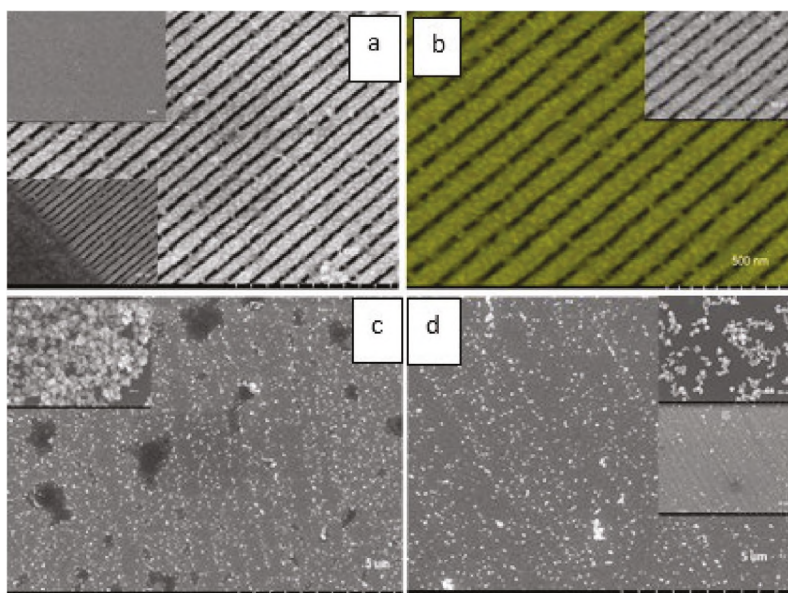


**Figure 2:** Mesoscale assemblies nanostructures (a, b) gold nanostructures into parallel line patterns on the surface of gold /silver surfaces or (c, d) Au-FeO<sub>x</sub> on patterned magnetic medium.

were deposited in various patterns generating two dimensional printed surfaces.

A number of different support compositions were used for deposition, including quartz, gold/silver supports, stainless steel, copper, longitudinal and transverse magnetic media. The mesoscale surfaces were characterized through a series of analytical tools to elucidate materials physico-chemical properties. This includes electron microscopy, spectroscopy, UV-Vis spectroscopy, dynamic light scattering, PALS surface charge, etc. Data shows that the materials retain their properties upon additive manufacturing in 2D patterns.

Depending on the Nps properties (concentration, size, shape, surface functionalization, etc.) different assemblies and patterns were produced. Factors affecting the magnetic and non-magnetic nanostructure assembly include nanoparticle's properties, e.g. magnetic susceptibility, surface chemistry, size, etc., media magnetic gradient strength, solvent ionic strength, factors in preserving self-assembled structure, wetting properties of the solvent, possibly solvent volatility, surface tension can disturb assembled nanoparticles.

## FY2020 Accomplishments

- Mesoscale Printing: Nanomaterials produced by our automated flow-throughput domain process (AFTDP) recently developed by us, aka nano-additive manufacturing approach were printed on various surfaces through reliable surface functionalization/ patterning approaches
- Assemblies and patterns dependent on the Nps properties (concentration, size, shape, surface functionalization, etc.
- One patent application was filled with the US Patent and Trademark Office.
- One manuscript in preparation
- One book chapter accepted for publication.
- Hired one postdoc researcher
- Technology presented to the Honorable Paul Dabbar, Undersecretary for Science

## Future Directions

A multifactorial experimental design will be used to (i) explore the correlation between the processing parameters that govern both production and 3D nano-additive printing of advanced nanomaterials, and (ii) elucidate the fundamental understanding of the process-structure-property relationships of these technologies.

## FY 2020 Peer-reviewed/Non Peer-reviewed Publications

- Iron-oxide-gold composite nanoparticles and nanogap junctions for sensing applications using Surface Enhanced Raman Scattering, 2020, Metal-Matrix Composites, Springer Publisher.

## Acronyms

ARC – Applied Research Center  
SRNL – Savannah River National Laboratory  
AM - Additive Manufacturing  
3D – Three Dimensional  
4D – Four dimensional  
UAVs - Unmanned Aerial Vehicles  
SEM – Scanning Electron Microscopy  
EDS – Energy Dispersive X-ray Spectroscopy

ICP-MS - Inductively coupled plasma mass spectrometry

UV-Vis – ultraviolet - visible

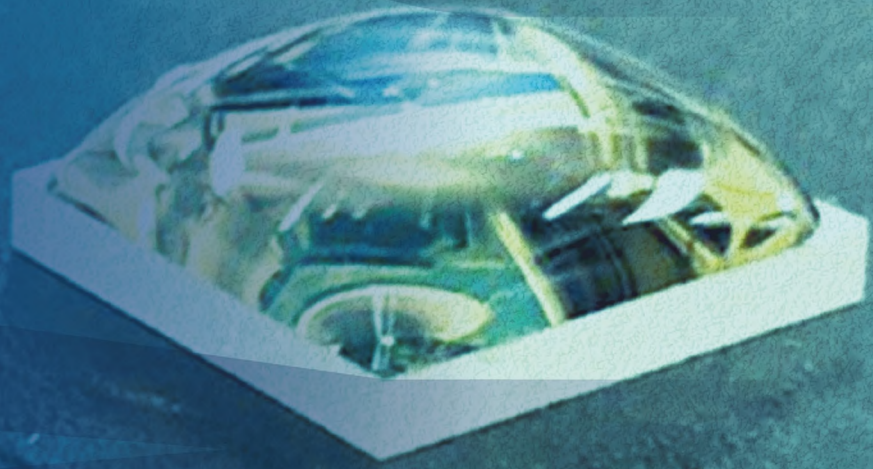
ETEBA - Energy, Technology and Environmental Business Association

## **Intellectual Property**

System and Methods for Manufacturing Nano-Scale Materials

## **Total Number of Post-Doctoral Researchers**

Ray Belliveau (SRNL)



 **SRNL**<sup>®</sup>  
SAVANNAH RIVER NATIONAL LABORATORY

 **LDRD**  
LABORATORY DIRECTED  
RESEARCH & DEVELOPMENT